

Antibody targeting of HIV-1 Env:  
A structural perspective

Thesis by  
Morgan E. Abernathy

In Partial Fulfillment of the Requirements for  
the Degree of  
Doctor of Philosophy

The Caltech logo, featuring the word "Caltech" in a bold, orange, sans-serif font, centered within a light orange rectangular background.

CALIFORNIA INSTITUTE OF TECHNOLOGY  
Pasadena, California

2022  
(Defended December 3, 2021)

© 2022

Morgan E. Abernathy  
ORCID: 0000-0001-9959-7713

## ACKNOWLEDGEMENTS

First, I need to thank my advisor Pamela Bjorkman, mostly for training and mentoring me academically, but also for convincing me not to quit grad school in 2019. I very literally would not be here without her support. When I first started at Caltech, I was most interested in Pamela's lab because she had a reputation for supporting female mentees unequivocally, and I am so grateful to have benefited from that support, even when it meant awkwardly standing up and presenting my one slide of data from the back of the room during our lab's presentation to a scientific advisory board because "Why on earth would you want a man to present your research for you??" Under her mentorship, I have grown into a better scientist.

I also want to thank my committee for helping me along the way: Professors Doug Rees, Dave Tirrell, and Bil Clemons. I am so grateful for the time and advice you have shared with me.

I want to say a special thank you to our collaborators: Michel Nussenzweig, Amelia Escolano, Malcolm Martin, and Florian Klein. I never dreamed I would work on such far-reaching and collaborative projects, and I'm grateful for all that I have learned from you all.

I'm also extremely grateful for the Caltech Cryo-EM facility including Songye Chen and specifically Andrey Malyyutin, who trained me and was forced to repeatedly assure me that I had not broken the microscope every single time it made a new noise.

In March of 2021, Pamela asked me if I wanted to help set up a Covid-19 surveillance testing lab on campus, and I'm so glad I said yes. I worked with passionate people at the CCSL, including Professor Barbara Wold, George Tolomiczenko, Jost Vielmetter, Mike Anaya, Erica Lee, Justin Ho, and Marta Murphy. I also had the opportunity to work a bit with Jennifer Howes, Assistant Vice President for Student Affairs and Wellness, and am so appreciative that I was able to learn from and observe such an inspirational leader.

Before Caltech, I worked in the lab of Dr. Zach Ball at Rice University. This experience was what encouraged me to pursue research and graduate school, and I'm so grateful for it. All of the Ball lab members helped me learn what it meant to do science, but now-Professor Jun Ohata deserves a special shout-out for teaching and managing me on the day-to-day, and making research truly fun. We learned that I am pretty ok at Western blots but *very* bad at peptide synthesis. I also need to thank Dr. Jeanine Conklin, my high school chemistry teacher, for inspiring the curiosity about chemistry and the world that led me into science in the first place.

In the Bjorkman lab, my first and most aggressive thanks go to Marta Murphy. You name it and Marta has calmed me down from a panic by helping me figure out how to do it: edit figures, pay open access fees, carefully coordinate scheduling a committee meeting. She has also been a great friend and supporter of me as a scientist and as a person. I also need to say a very large TY to Kim Dam for being a great friend and labmate, and also for proofreading the introduction to this thesis (!). Additionally, Harry Gristick and Christopher Barnes spent so much time training me and helping me understand the process of doing research when I joined the lab, for which I'm so grateful. So many others in the lab have helped me over the years, including Dr. Jennifer Keeffe, my bay-mate Dr. Anthony West, Claudia Jette, Zhi Yang, Erica Lee, Andy DeLaisch, Nick Koranda, Dr. Alex Cohen, Dr. Magnus Hoffmann, Dr. Andrew Flyak, Dr. Chengcheng Fan, Dr. Haoqing Wang, Beth H-T, Han Gao, Pri Gnanapragasam, Dr. Beth Stadtmueller, Dr. Semi Rho, Leesa Kakutani, Pauline Hoffman, Alisa Voll, Stormy Ruiz, Tiffany Luong, and Annie Lynch.

A special thanks goes to my neighbors on North Wilson that have kept me safe, supported, and well-fed since 2018: Jess, Waffles, Paul, Ann, Sharon, Lupita, and Bruce. I have really flourished in the presence of such great neighbors, and I hope to be as good of a neighbor in the future as you all have been to me.

To Claire Bonnyman: our walk-n-talks give me life! Thank you for being such a great friend and listener; our friendship means so much to me. In addition, there are so many other Caltech and Rice friends I won't list but that have helped me be a human during this time.

To my parents and family: thank you for your love and support, and for reassuring me that this thesis does not define me.

Finally, I want to thank my partner Veeral, who has been literally on the other side of the wall—whenever I’ve needed to talk through a point or take a break—the entire time I’ve been writing this thesis. This thesis is a part of the life that we have built together, and I’m so excited for the life that we will continue to create after.

## ABSTRACT

A key component of contemporary efforts toward a human immunodeficiency virus 1 (HIV-1) vaccine is the use of structural biology to understand the structural characteristics of antibodies elicited both from human patients and animals immunized with engineered ‘immunogens,’ or early vaccine candidates. This thesis will report on projects characterizing both types of antibodies against HIV-1. Chapter 1 will introduce relevant topics, including the reasons HIV-1 is particularly capable of evading the immune system in natural infection and after vaccination, the 20+ year history of unsuccessful HIV-1 vaccine large-scale efficacy trials, an introduction to broadly neutralizing antibodies (bNAbs), and a review of common strategies utilized in HIV-1 immunogen design today. Chapter 2 describes the isolation, high-resolution structural characterization, and in vitro resistance profile of a new bNAb, 1-18, that is both very broad and potent, as well as able to restrict HIV-1 escape in vivo. Chapter 3 reports the results of an epitope-focusing immunogen design and immunization experiment carried out in wild type mice, rabbits, and non-human primates where it was shown that B cells targeting the desired epitope were expanded after a single prime immunization with immunogen RC1 or a variant, RC1-4fill. Chapter 4 describes Ab1245, an off-target non-neutralizing monoclonal antibody isolated in a macaque that had been immunized with a series of sequential immunogens after the prime immunization reported in Chapter 3. The antibody structure describes a specific type of distracting response as it binds in a way that causes a large structural change in Env, resulting in the destruction of the neutralizing fusion peptide epitope. Chapter 5 is adapted from a review about how antibodies differentially recognize the viruses HIV-1, SARS-CoV-2, and Zika virus. This review serves as an introduction to the virus SARS-CoV-2, which is the topic of the final chapter, Chapter 6. In this chapter, structures of many neutralizing antibodies isolated from SARS-CoV-2 patients were used to define potentially therapeutic classes of neutralizing receptor-binding domain (RBD) antibodies based on their epitopes and binding profiles.

## PUBLISHED CONTENT AND CONTRIBUTIONS

1. **Abernathy, M.E.**, Gristick, H.B, Vielmetter, J., Keeffe, J.R., Gnanapragasam, P.N.P, Lee, Y.E., Escolano, A., Gautam, R., Seaman, M.S., Martin, M.A., Nussenzweig, M.C., Bjorkman, P.J. Antibody elicited by HIV-1 immunogen vaccination in macaques displaces Env fusion peptide and destroys a neutralizing epitope. *npj Vaccines*, **6**, 126 (2021). <https://doi.org/10.1038/s41541-021-00387-4>

M.E.A designed the research, performed experiments, analyzed results, and wrote the manuscript.

2. **Abernathy, M.E.\***, Dam, K.A.\*, Esswein, S.R.\*, Jette, C.A.\*, Bjorkman, P.J. How antibodies recognize pathogenic viruses: Structural correlates of antibody neutralization of HIV-1, SARS-CoV-2, and Zika. *Viruses*, **13**, 2106 (2021). <https://doi.org/10.3390/v13102106>

M.E.A. participated in writing and editing the review, with a particular emphasis on HIV-1 and SARS-CoV-2 material.

3. Barnes, C.O., Jette, C.A., **Abernathy, M.E.**, Dam, K-M.A., Esswein, S.R., Gristick, H.B., Malyutin, A.G., Sharaf, N.G., Huey-Tubman, K.E., Lee, Y.E., Robbiani, D.F., Nussenzweig, M.C., West, A.P., Bjorkman, P.J. SARS-CoV-2 neutralizing antibody structures inform therapeutic strategies. *Nature*, **588**, 682–687 (2020). <https://doi.org/10.1038/s41586-020-2852-1>

M.E.A. processed and interpreted structural data for both cryo-EM and crystallographic structures.

4. Schommers, P.\*, Gruell, H.\*, **Abernathy, M.E.\***, Tran, M-K., Dingens, A.S., Gristick, H.B., Barnes, C.O., Schoofs, T., Schlotz, M., Vanshyla, K., Kreer, C., Weiland, D., Holtick, U., Scheid, C., Valter, M.M, van Gils, M.J., Sanders, R.W., Vehreschild, J.J., Cornely, O.A., Lehmann, C., Fatkenheuer, G., Seaman, M.S., Bloom, J.D., Bjorkman, P.J., and Klein, F. Restriction of HIV-1 escape by a highly broad and potent neutralizing antibody. *Cell*, **180**, 1-19 (2020). <https://doi.org/10.1016/j.cell.2020.01.010>

M.E.A. collected, processed, and interpreted cryo-EM data and participated in writing the manuscript.

5. Escolano, A.\*, Gristick, H.B.\*, **Abernathy, M.E.**, Merckenschlager, J., Gautam, R., Oliveira, T.Y., Pai, J., West, A.P., Barnes, C.O., Cohen, A.A., Wang, H., Golijanin, J., Yost, D., Keeffe, J.R., Wang, Z., Zhao, P., Yao, K-H., Bauer, J., Nogueira, L., Gao, H., Voll, A.V., Montefiori, D.C., Seaman, M.S., Gazumyan, A., Silva, M., McGuire, A.T., Stamatatos, L., Irvine, D.J., Wells, L., Martin, M.A., Bjorkman, P.J., Nussenzweig, M.C. Immunization expands HIV-1 glycan patch-specific B-cells in mice and macaques. *Nature*, **570**: 468-73 (2019). <https://doi.org/10.1038/s41586-019-1250-z>

M.E.A. collected, processed, and interpreted cryo-EM data and participated in writing the manuscript.

\* Equal Contributions

## TABLE OF CONTENTS

Acknowledgements .....	iii
Abstract.....	vi
Published Content and Contributions.....	vii
Table of Contents .....	ix
Chapter 1: Introduction .....	1
Section 1: HIV-1 is the virus that causes AIDS .....	1
Section 2: HIV-1 vaccine challenges .....	1
2.1: HIV-1 is a retrovirus that persists in patients for life .....	1
2.2: HIV-1 mutates frequently, resulting in a large diversity of strains ..	2
2.3: HIV-1 virions are uniquely evolved to evade the immune system ..	3
2.4: Effective bNAbs have features that are hard to elicit.....	5
Section 3: Unsuccessful HIV-1 vaccine attempts.....	6
Section 4: Broadly neutralizing antibodies against HIV-1 .....	9
Section 5: Common strategies utilized in HIV-1 immunogen design.....	13
5.1: Stabilized Env trimer immunogens .....	15
5.2: Germline-targeting immunogens.....	17
5.3: Epitope-focusing immunogens.....	20
5.4: Lineage-based immunogens.....	22
Scope of Work.....	23
References.....	25
Chapter 2: Restriction of HIV-1 escape by a highly broad and potent neutralizing antibody.....	39
Summary .....	39
Introduction .....	40
Results.....	41
Discussion .....	62
Methods .....	65
Data and Code Availability .....	81
Acknowledgements.....	81
References.....	83
Supplemental Material .....	96
Chapter 3: Immunization expands B cells specific to HIV-1 V3 glycan in mice and macaques.....	109
Summary .....	109
Introduction .....	110
Results & Discussion .....	111
Conclusions .....	122
Methods .....	124
Data Availability.....	133
Acknowledgements.....	134

References.....	135
Extended Data Figures and Tables.....	140
Chapter 4: Antibody elicited by HIV-1 immunogen vaccination in macaques displaces Env fusion peptide and destroys a neutralizing epitope.....	152
Summary.....	152
Introduction.....	152
Results & Discussion.....	154
Methods.....	164
Data Availability.....	169
Acknowledgements.....	169
References.....	171
Supplemental Material.....	177
Chapter 5: How antibodies recognize pathogenic viruses: Structural correlates of antibody neutralization of HIV-1, SARS-CoV-2, and Zika.....	179
Summary.....	179
1. Introduction.....	179
2. Main Body.....	184
3. Conclusions.....	198
Methods.....	198
Acknowledgements.....	199
References.....	200
Chapter 6: SARS-CoV-2 neutralizing antibody structures inform therapeutic strategies.....	223
Summary.....	223
Introduction.....	224
Results & Discussion.....	225
Conclusions.....	237
Methods.....	238
Data Availability.....	245
Acknowledgements.....	245
References.....	247
Extended Data Figures and Tables.....	253

## Chapter 1

### INTRODUCTION

#### **Section 1. HIV-1 is the virus that causes AIDS**

First described in 1981<sup>1</sup>, Acquired ImmunoDeficiency Syndrome (AIDS) is a life-threatening disease that describes a state of extreme immunodeficiency. The cause of AIDS was later identified to be a virus named human immunodeficiency virus 1 (HIV-1), which has eluded vaccine efforts for the last 35+ years. While antiretroviral therapy (ART) and pre-exposure prophylaxis (PrEP) have reduced the spread of the virus and greatly extended the life expectancies of those living with HIV-1, an effective vaccine is still necessary as there is currently no cure for HIV-1, and PrEP has thus far not been widely adopted to levels necessary to significantly reduce global transmission. Unlike with many other viruses, the human body cannot clear or rid itself of the virus once infected, so preventing transmission and acquisition is crucial to controlling the HIV-1 epidemic, which in 2020 affected 38 million people globally<sup>2</sup>.

#### **Section 2. HIV-1 vaccine challenges**

##### **2.1 HIV-1 is a retrovirus that persists in patients for life**

HIV-1 is a member of the RNA virus family *Retroviridae*; viral strains therein are commonly referred to as ‘retroviruses.’ As such, HIV-1 inserts a copy of its RNA genome into the host’s genomic DNA via the enzymes reverse transcriptase and integrase. Once incorporated, the host cell transcribes and translates the viral DNA sequences into proteins along with its own. Immature viral particles then bud off of the host cell membrane and mature into infectious virions that continue to propagate the infection<sup>3</sup>. Because of this integration, it is not possible for a natural infection to be cleared by the body as in many other common infections, such as influenza, SARS-CoV-2, or even in some cases Hepatitis C. As leading HIV-1 vaccine researchers Glenda Gray and Lawrence Corey wrote in May 2021, “HIV vaccine

development has become a process of stepwise learning of how to make a vaccine that induces an immune response that is markedly better than the human immune response to HIV.”<sup>4</sup> Because of this ability to integrate into the host genome and establish a ‘latent reservoir’ of infected cells that can resist immune responses and viral therapies, it is believed that an ideal HIV-1 vaccine would provide sterilizing protection from infection<sup>5</sup>. By contrast, effective vaccines against SARS-CoV-2 and other non-retroviruses do not need to provide sterilizing protection; even if circulating short-lived plasma B cell titers wane and breakthrough infections and disease occur, vaccination can still protect against severe disease and death through stimulation of pre-existing memory B cells and long-lived plasma cells<sup>6</sup>. In HIV-1, there is no recourse once the initial DNA integration occurs (within a few hours of infection)<sup>7</sup>. This means that an ideal vaccine would need to provide this immediate protection continuously in the long-term, which is an incredible challenge. Other theoretical avenues that a less ideal vaccine candidate might take include allowing the infection and then promoting viral clearance, allowing the infection but controlling viremia to below the limit of detection, and allowing the infection but reducing initial peak viremia and viral load set point<sup>5</sup>. In addition to the question of whether these other avenues could even be met with a real vaccine candidate and whether they would be clinically valuable, designing trials to assess these outcomes is not trivial<sup>5</sup>.

## **2.2 HIV-1 mutates frequently, resulting in a large diversity of strains**

HIV-1 has an incredible degree of viral diversity, which is implicated in a variety of the HIV-1 specific challenges to vaccine design. While the main sources of viral diversity in HIV-1 are rapid viral turnover and very high mutation rates, other factors include retroviral recombination, selection from the host immune system, and genetic/phenotypic constraints on variation<sup>8</sup>. This viral diversity is observed at both the individual and global levels, and both have implications for HIV-1 vaccine design.

At the individual level, rapid generation of mutations combined with a life-long, persistent infection result in a massive diversity of strains within a single HIV-1-positive patient. It has been estimated that the diversity of global influenza sequences in a given year is

approximately equal to the diversity of HIV-1 sequences observed in a single individual captured at one time point<sup>9</sup>. This is incredible considering that most HIV-1 transmission events are believed to have been initiated by a single viral particle from what is referred to as a transmitted/founder (T/F) strain<sup>10</sup>. When combined with the host humoral immune system, this persistent generation of new variants results in a co-evolution of both viruses and antibodies. In some rare patients, antibodies develop that can neutralize a variety of these strains; these are the human broadly neutralizing antibodies (bNAbs) that are commonly studied. Over years, the antibodies mature by accruing somatic hypermutations including insertions or deletions that improve breadth and potency<sup>11</sup>. HIV-1 neutralizing antibodies are, in general, far more mutated than antibodies that neutralize other viruses<sup>12</sup>. This poses a great challenge to HIV-1 vaccine design, which aims to re-elicite these types of protective responses in naïve individuals, and is the topic of Section 2.4: *Effective bNAbs have features that are hard to elicit*. Unfortunately, the competitive co-evolution that results in these bNAbs also generates viral species that are resistant to them, and thus evolved bNAbs do not actually protect their own host from progression to lower CD4+ T cell counts and higher viral load, at which point ART is usually initiated to prevent progression to AIDS<sup>13</sup>.

At the population level, HIV-1's incredible viral diversity poses a great challenge to vaccine design because vaccines need to be designed to protect from a large number of strains, rather than just one or a few as in other vaccines. The current predominant strategy for HIV-1 vaccine design is the elicitation of broadly neutralizing antibodies that can neutralize many of these circulating strains (discussed further in Section 3: *HIV-1 Vaccine Failures*).

### **2.3 HIV-1 virions are uniquely evolved to evade the immune system**

HIV-1 viral particles exhibit distinctive features that make them particularly challenging for the human immune system to thwart. The most obvious instance of this is the virus's target cell: CD4+ T cells, which are often referred to as 'helper T cells' and form a critical arm of the immune response to any foreign antigen. In reality, HIV-positive patients that have progressed to AIDS die not directly from the virus but from opportunistic infections that their bodies would have been able to clear if HIV-1 had not depleted their CD4+ T cell reserves.

Therefore, HIV-1 infects the very cells that would otherwise be working to help clear it. Furthermore, the Env spikes on HIV-1 are far more sparse on the surface of the virion than on other viruses, which likely contributes to immune evasion because bivalent IgG antibodies cannot bind with both Fab arms, thus losing any advantage of avidity effects<sup>14</sup>. Because the IgG molecule is bound at one site rather than two, it is more sensitive to mutations that cause decreases in affinity at those sites<sup>14</sup>.

The Env spike protein contains other distinctive features that contribute to challenges in HIV-1 neutralization. Env is the protein responsible for fusion with the host cell membrane; furthermore, it is the only antigenic target that antibodies can be raised against on the surface of a virion<sup>12</sup>. It is a type I fusion protein consisting of a trimer of heterodimeric protomers containing gp120 and gp41, which are enzymatically cleaved after translation of a full gp160 construct. The three protomers can adopt a range of conformations relative to each other, from the fully 'closed' pre-fusion state, to an 'open' conformation that is triggered when CD4 binds to gp120, wherein the variable 1 & 2 (V1V2) loops and variable 3 (V3) loops dramatically change position in preparation for co-receptor binding by CCR5 or CXCR4<sup>15</sup>. These conformational changes, which require binding to the host cell receptor, serve to mask conserved epitopes necessary for viral function from antibodies during maturation<sup>16</sup>. The surface of the Env protein is also decorated with glycans attached to a median of 30 potential N-linked glycosylation sites (PNGSs) per protomer<sup>17</sup>. These glycans are poorly immunogenic because they are processed using host-cell machinery, and thus also serve to mask the important protein epitopes underneath them from the immune system<sup>11</sup>. Glycans also add another layer of mutability to the presentation of Envs in regard to 3-dimensional immune recognition<sup>18</sup>. Additionally, most PNGSs are conserved across HIV-1 strains, but some viruses contain mutations that abolish specific PNGSs<sup>17</sup>. These missing glycans create what are called 'glycan hole' epitopes, which are highly immunodominant but strain-specific patches of polypeptide that only elicit autologous neutralizing antibodies<sup>19</sup>. Antibodies to these epitopes are commonly the dominant component of any neutralizing activity observed in the serum of animals immunized with stabilized native Env immunogens<sup>19</sup>, as discussed in Section 5.1.

## 2.4 Effective bNAbs have features that are hard to elicit

Another hindrance to the development of an HIV-1 vaccine is that the types of antibodies believed to be necessary and elicited by the vaccine, bNAbs, frequently bear unique and highly derived features that make them harder to elicit. These include high levels of somatic hypermutation (SHM), including insertions and deletions, as well as the tendency for these bNAbs to exhibit poly- or auto-reactivity, which makes them susceptible to clonal deletion via tolerance mechanisms<sup>11,20,21</sup>. On average, top neutralizers present about 40-70 nucleotide mutations in the VH domain, compared to 15-20 nucleotide mutations in naïve, healthy donors<sup>22,23</sup>. While there are exceptions, the level of SHM is correlated with the breadth and potency of individual bNAbs<sup>22</sup>. This means that a similarly high number of mutations, occurring over a long period of time, will likely also be required for bNAbs elicited by vaccine candidates.

Furthermore, the inferred germlines (iGLs) of known bNAbs do not usually bind to native Env proteins<sup>24</sup>. This means that immunogens are often selected and/or designed to bind with detectable affinity to these iGLs in order to activate the correct pool of precursor B cells. Sequential immunization with engineered Envs with more and more native-like features will likely be necessary to guide the maturation of iGLs to bNAbs<sup>25</sup>. Additionally, B cells encoding for these iGLs are often found to be very rare in the human repertoire, which presents another great challenge in designing immunogens that engage them to mature at sufficient levels<sup>26</sup>.

Finally, the enzyme that is responsible for somatic mutation, activation-induced cytidine deaminase (AID), has been shown to preferentially mutate specific positions in an antibody sequence<sup>27</sup>. Subsequently, it was shown that many of the critical mutations that are responsible for a bNAb's functionality occur in locations that are less likely to be mutated. Therefore, bNAbs are enriched with low-probability mutations that are also key to their function<sup>28</sup>. Engineering immunogens that can guide antibody maturation to these specific improbable mutations is a focus of lineage-based immunogen design, which will be discussed in Section 5.4.

### Section 3. Unsuccessful HIV-1 vaccine attempts

Since the first in 1998, there have been nine large-scale efficacy trials of HIV-1 vaccine candidates initiated. Of these, one is still in progress, one showed modest efficacy, and the other seven have been deemed abject failures.

The first two efficacy trials, VAX004 and VAX003, were phase III and sponsored by VaxGen, with the goal of inducing protective neutralizing antibody responses<sup>7</sup>. They tested variants of the AIDSVAX® vaccine, which were composed of bivalent recombinant gp120s (rgp120s) of different circulating transmitted/founder strains adjuvanted with alum. VAX004 evaluated a bivalent clade B/B vaccine in people at risk for sexual transmission in North America and the Netherlands<sup>29</sup>, and VAX003 a B/E vaccine in people who inject drugs in Thailand<sup>30</sup>. For both trials, participants received seven injections of either vaccine or placebo over 30 months, and the primary endpoint was HIV-1 acquisition at 36 months. The trials were initiated in 1998 and 1999, and analyses of results for both were completed in 2003. The conclusion of both trials was that the vaccine did not prevent HIV-1 infection, with estimated vaccine efficacy (VE) figures of 6% and 0.1%, for VAX004 and VAX003, respectively<sup>29,30</sup>.

The next two completed trials were known as STEP (HVTN 502) and Phambili (HVTN 503), and were sponsored by the HIV Vaccine Trials Network (HVTN), in an effort to elicit protective immunity mediated by T cells<sup>31</sup>. These phase IIb trials tested a protocol of three injections of Merck's MRKAd5® trivalent vaccine, which consisted of a replication-deficient adenovirus type-5 vector carrying HIV-1's gag, pol, and nef genes. The STEP trial began in 2004 at many global sites, but ended early in 2007 when preliminary results indicated that vaccinated trial participants may be more likely to contract HIV-1 than those that received the placebo<sup>32</sup>. Consequently, Phambili was terminated at the same time, but since it had only begun enrolling earlier in 2007, very few of the planned participants were actually vaccinated<sup>33</sup>. Later studies confirmed that vaccinated men who were Ad5-seropositive and/or uncircumcised did indeed have higher rates of HIV-1 acquisition than the placebo group<sup>34</sup>. It is thought that Ad5-specific CD4+ T cells from prior Ad5 exposure were

recruited at mucosal sites in these participants, which increased the pool of available CD4+ HIV-1 target cells in exactly the tissues that would be exposed to the virus during sexual contact<sup>33</sup>.

The fifth completed trial, RV144, is the only HIV-1 vaccine efficacy trial that has shown any level of protection from infection<sup>7</sup>. The trial took place in Thailand beginning in 2003, and was overseen by the US Military and the Thai Ministry of Public Health<sup>7</sup>. RV144 was designed to elicit both B and T cell responses using a heterologous prime-boost combination of four immunizations of ALVAC® HIV (vCP1521 canarypox vector expressing env, gag, and pro) followed by two immunizations of the bivalent AIDSVAX® B/E vaccine tested in the VAX003 trial<sup>35</sup>. Participants were monitored for three years following immunization, and in 2009, results were released assigning a modest 31.2% efficacy to the trial<sup>35</sup>. Later studies investigated the correlates of protection, which were determined to be non-neutralizing V1V2 IgGs, Env IgG3s, and CD4+ T cells expressing multiple cytokines<sup>36–38</sup>. Furthermore, neutralizing antibodies were not found to be a correlate of protection, which initiated a shift in focus to the elicitation of non-neutralizing antibodies that could induce antibody dependent cell-mediated cytotoxicity (ADCC) for vaccine candidates<sup>31</sup>. This was formally acknowledged as a goal for HIV-1 vaccine trials by HVTN in 2014, which informed the final three large-scale efficacy trials: Uhambo (HVTN 702), Imbokodo (HVTN 705), and Mosaico (HVTN 706)<sup>4</sup>.

HVTN 505 was a phase IIb trial that was carried out at many sites in the United States starting in 2008, and was the sixth efficacy trial to release results in 2013 when it was halted for lack of efficacy<sup>39</sup>. Similar to RV144, the vaccine regimen was designed to elicit both cellular and humoral responses using a combination of a DNA plasmid prime (three injections) and an rAd5 boost, where the vectors expressed three clades (A, B, and C) of the B cell target env gene in addition to T cell epitope genes gag, pol, and nef<sup>39</sup>. Due to the increased risk of infection observed for Ad5 seropositive and/or uncircumcised men in the STEP trial, the study only enrolled male participants who were circumcised and negative for Ad5 antibodies, as this group was shown to be at no higher risk than the placebo group<sup>33</sup>. With these

precautions, no increase in transmission risk was observed, but the vaccine was not effective<sup>39</sup>.

Beginning in 2016, Uhambo (HVTN 702) was a phase IIb/III trial that was conducted in South Africa and was designed as a follow-up to RV144<sup>4</sup>. Participants received a similar ALVAC® HIV prime (two injections) and AIDSVAX® boosts (four injections), but with a bivalent rgp120 clade C/C vaccine to match currently circulating strains in South Africa. The adjuvant was also changed to MF59 from alum, which had been shown to elicit stronger responses<sup>40</sup>. The study's primary endpoint was HIV-1 infection after 24 months. Unfortunately, the trial was halted early in late January 2020 due to a lack of efficacy, although high levels of gp120-binding antibodies and ADCC activity (thought to be important correlates of protection from the RV144 trial) were observed<sup>40</sup>.

The final two efficacy trials are parallel studies designed to test an adenovirus-vectored mosaic prime followed by recombinant Env protein boosts with the goal of eliciting protective non-neutralizing antibodies<sup>41</sup>. Imbokodo (HVTN 705) was a phase IIb study recruiting women in sub-Saharan Africa beginning in 2017, and Mosaico (HVTN 706) is a phase III study that began in late 2019 in South America, Mexico, and the United States<sup>4</sup>. In these trials' vaccine candidates, the adenovirus vector used is Ad26, which was developed with the goal of improving on the issues associated with Ad5's seroprevalence<sup>42</sup>. The studies use a tetravalent prime (two injections) vaccine (Ad26.Mos4.HIV) that contains two mosaic gag-pol Ad26 vectors and two mosaic env Ad26 vectors followed by two boosts of Ad26.Mos4.HIV combined with mosaic Env gp140 protein (monovalent in Imbokodo, bivalent in Mosaico)<sup>41</sup>. 'Mosaic' refers to the generation of recombinant antigens that have been computationally designed to maximize coverage of potential T cell epitopes, while maintaining resemblance of the wild type protein<sup>43</sup>. Gray and Corey of the HVTN wrote in early 2021 that these two studies "will be critical in the quest to understand whether non-neutralizing antibodies are capable of inducing protection against HIV."<sup>4</sup> Sadly, Imbokodo was halted prematurely in late August 2021, shedding doubt on the hope that eliciting

protective non-neutralizing antibodies is the path to an effective HIV-1 vaccine, and suggesting that eliciting bNAbs may be the necessary next path forward<sup>44</sup>.

#### **Section 4. Broadly neutralizing antibodies against HIV-1**

bNAbs are antibodies isolated from HIV-1-infected human patients that display breadth and potency against a panel of HIV-1 viral strains. Breadth refers to the percentage of strains on an experimental panel of HIV-1 strains that are neutralized by the antibody at a half maximal inhibitory concentration ( $IC_{50}$ )  $< 50 \mu\text{g/mL}$ ; the standard of the last several years for new bNAbs is about 50% breadth, although there are still less broad bNAbs with interesting features described, as well as several bNAbs that are near ‘pan-neutralizing,’ meaning they neutralize up to 99% of strains tested<sup>45</sup>. Potency refers to the median  $IC_{50}$  of neutralization, with lower  $IC_{50}$ s describing more potent bNAbs (less antibody is required to neutralize the virus)<sup>11</sup>. In these neutralization assays, a range of viruses can be tested. Strains that are most sensitive to neutralization are categorized as ‘tier 1;’ these strains can be lab-adapted and are easier to neutralize than a majority of circulating HIV-1 strains<sup>46</sup>. ‘Tier 2’ strains are harder to neutralize and more representative to real circulating variants. It is widely accepted that only tier 2 neutralization has the potential to protect from infection in animal models, and is thus the goal in vaccination experiments<sup>47</sup>. Additionally, in vaccination experiments, ‘heterologous’ neutralization refers to an animal’s ability to neutralize viruses beyond what it was exposed to by immunization, and ‘autologous’ neutralization describes only strain-specific neutralizing responses. Therefore, an effective vaccine would need to elicit heterologous tier 2 neutralizing antibodies, and this is the ultimate goal of many animal immunization experiments discussed in Section 5.

In terms of discovery, bNAbs are only isolated in a very small percentage of infected people (termed ‘elite neutralizers’), and only after years of untreated infection during which the viral population and antibodies co-evolve<sup>48</sup>. The process by which bNAbs (and all antibodies) mature in response to specific pathogens is called affinity maturation<sup>49</sup>. To start, germline-encoded V, D, and J genes recombine in humans to create a diverse array of heavy and light chains that make up germline precursor antibodies, which are expressed on the surface of B

cells as B cell receptors (BCRs). This recombination allows for many germline antibody sequences to be encoded by a relatively small number of genes. These germline B cells circulate in naïve humans, and are recruited into the germinal centers for iterative rounds of SHM and selection when they bind with even low affinity to a specific antigen. This process iteratively selects for antibodies with higher affinity to the antigen present, and years of co-evolution with circulating viruses can result in potent bNAbs<sup>49</sup>. The sequences of these bNAbs can be derived from B cells found in the serum or plasma of human patients after screening their samples for neutralizing activity and sorting/sequencing single B cells based off of their binding to viral protein ‘baits’<sup>50</sup>. Once a bNAb has been isolated and characterized, the sequence of the precursor germline antibody that matured into the bNAb can be estimated using bioinformatic approaches that assess likely V, D, and J genes as well as their likely junctions<sup>51</sup>. This is what is referred to as the ‘inferred germline’<sup>52</sup>, and is crucial to the germline-targeting immunogen design approach discussed in Section 5.2.

In total, bNAbs isolated from human patients serve three roles in the HIV-1 field: treatment, prevention, and as templates for HIV-1 vaccine design. Frequently, individual bNAbs are better suited for either treatment/prevention or vaccine design. In general, highly mutated, very potent pan-neutralizers are desirable for treatment and prevention, but would be harder to elicit by immunogen design because their highly evolved features are what make them effective. On the other hand, less broad and potent bNAbs with features that might be easier to elicit, like the IOMA class of bNAbs<sup>53</sup>, are better suited to be templates for vaccine design. This thesis will explore two of these three roles: mAb 1-18 was tested for treatment potential in animal models and reported in Chapter 2, and immunogen design attempts to elicit V3-glycan patch bNAbs are discussed in Chapters 3 & 4.

The use of bNAbs for HIV-1 treatment has been explored in a number of phase I clinical trials (a recently updated list of which can be found in Hsu et al.<sup>54</sup>). More recent studies have incorporated so-called ‘LS’ mutations in the Fc regions of bNAb IgGs to increase in vivo half-life and therefore confer better activity<sup>55-57</sup>. In most cases, the treatments have been deemed safe and well-tolerated<sup>54</sup>. bNAb monotherapy usually causes reductions in HIV-1

RNA of about  $1.5 \log_{10}$  copies/mL<sup>54</sup>. Unfortunately, monotherapy quickly leads to ‘viral rebound’ where HIV-1 viruses gain resistance to the bNAb treatment and return to baseline levels after a period of several weeks<sup>58</sup>. Additionally, a patient’s circulating strains may already be resistant to the bNAb, in which case patients are typically not enrolled in the trials<sup>59</sup>. Combination therapy with multiple highly potent bNAbs or combination therapy of bNAbs and ART treatment are thought to be potential future avenues for treatment research<sup>54</sup>.

Two recently completed large-scale efficacy trials gave great insight into the use of bNAbs for HIV-1 prevention. These studies are referred to as the Antibody Mediated Protection (AMP) trials, and were instigated by the HVTN in an effort to understand if neutralizing antibodies could even be protective, thus making them a potential target for future vaccine work<sup>4</sup>. The studies investigated the efficacy of bNAb VRC01<sup>60</sup> infusion every 8 weeks for 20 months. They found that while overall VRC01 infusion did not prevent HIV-1 infection, it was ~75% effective against viruses that were highly sensitive to it ( $IC_{80}$  of  $<1 \mu\text{g/mL}$ ), implying that a pan-neutralizing bNAb, or a bNAb specifically targeted to local circulating strains, could be protective<sup>61</sup>. Furthermore, bNAbs elicited by a vaccine, so long as they are sensitive to circulating strains, are still possible candidates for vaccine design. It is worth noting that while VRC01 was one of the most potent and broad bNAbs when it was discovered<sup>60</sup> and is thus what is used in many treatment and prevention studies that began years ago, it is not particularly potent in comparison to more recently discovered bNAbs<sup>62</sup>.

The final role that bNAbs play in HIV-1 research is as templates for vaccine design. This process has been coined ‘reverse vaccinology 2.0,’ derived from the concept that ‘reverse vaccinology’ generates vaccines using information derived from studies of antibodies, rather than the initial concept of creating antibodies from vaccines<sup>63,64</sup>. From there, a molecular and structural understanding of the antibodies’ mechanisms is considered to be key to facilitating immunogen design (‘2.0’)<sup>25</sup>. This conceptualization fundamentally underpins of all of the immunogen design strategies discussed in Section 5, where immunogens are designed to re- elicit the types of bNAbs that have been isolated in HIV-1-infected patients.

There are a variety of possible mechanisms through which bNAbs are thought to neutralize. Almost all posited mechanisms can be categorized as prevention of viral fusion through either steric (blocking CD4) or allosteric (preventing the rearrangements necessary for fusion) means. For instance, CD4bs and other classes of bNAbs sterically block the CD4 binding site, preventing receptor binding, while V3-glycan patch bNAbs bind to the unextended V3 loop, allosterically preventing it from being exposed as necessary for co-receptor binding<sup>65</sup>. Another bNAb, 3BC315, is proposed to neutralize by causing trimers on virions to disassociate into protomers that are clearly fusion-incompetent<sup>66</sup>. It is important to note that there is not a clear, obvious, and proven mechanism for each bNAb class<sup>11</sup>, but generally all have plausible mechanisms in this steric/allosteric context.

Newly-isolated bNAbs are categorized by their epitope (the specific 3D location that they bind to on HIV-1 Env protein), which can be approximated by binding assays and definitively determined using structural biology techniques such as X-ray crystallography and cryo-electron microscopy (cryo-EM). These epitopes often include conserved functional regions that bNAb binding would either sterically or allosterically hinder<sup>67</sup>. HIV-1 bNAb epitopes are typically divided into the following categories: (1) the V1V2 loops at the apex of the trimer that make a dramatic rearrangement upon CD4 binding and trimer opening<sup>68</sup>, (2) the V3-glycan patch, which includes the co-receptor binding V3 loop and the highly conserved <sub>324</sub>GDIR<sub>327</sub> motif its base, as well as several surrounding N-linked glycans<sup>46,69</sup>, (3) the CD4bs, which is the receptor binding site<sup>70</sup>, (4) residues only accessible in the CD4-induced (CD4i) open state<sup>71</sup>, (5) the glycan-rich ‘silent face’ of gp120 that sits opposite to the CD4bs on an intact trimer<sup>72,73</sup>, (6) the gp120/gp41 interface, which includes the fusion peptide (FP)<sup>74,75</sup>, and (7) the membrane proximal external region (MPER) epitope which resides at the base of gp41 and also usually includes interactions with the lipid bilayer<sup>76,77</sup>.

Finally, as a primer to Chapter 2, which describes the isolation and characterization of CD4bs bNAb 1-18, CD4bs bNAbs will be discussed in more detail. This category of bNAbs is often divided into four classes: VH1-2 gene segment restricted (‘VRC01-like’), VH1-46 gene

segment restricted ('8ANC131-like'), IOMA-like, and CDRH3 dominated ('loop binders')<sup>53,70</sup>.

Historically, VRC01-like bNAbs have been the most potent of the CD4bs bNAbs. They are characterized by VH1-2 variable heavy (VH) gene segment use and an unusually short, five-residue CDRL3 loop that accommodates the N276<sub>gp120</sub> glycan<sup>78</sup>. bNAbs of this class have been elicited from many different patients, and all bind with a very similar pose, utilizing the same conserved residue contacts between the bNAb and Env<sup>70,78</sup>. 8ANC131-like antibodies utilize the VH1-46 gene segment, and until the publication of 1-18 (Chapter 2), were thought to be categorically less potent than the VRC01 class<sup>50,70</sup>. IOMA-class antibodies are VH1-2 derived, but have a longer eight-amino acid CDRL3s, which are much more common in the human germline repertoire<sup>26,53</sup>. Both VH1-2 (including the IOMA class) and VH1-46 derived antibodies act as mimics of CD4 by contacting the same residues on Env using the same immunoglobulin domain backbone secondary structure as CD4<sup>79</sup>. Finally, loop binders make contact primarily with their CDRH3 loops, and can adopt a range of poses from a variety of germline genes, but are not usually very potent in comparison to other CD4bs antibodies<sup>70</sup>.

### **Section 5. Common strategies utilized in HIV-1 immunogen design**

The past 20+ years of dismal efficacy trials have led many to the conclusion that the necessary next goal of the HIV-1 vaccine field should be the elicitation of bNAbs that can protect humans from infection by a wide range of circulating strains. Because the iGL precursor antibodies of many known bNAbs do not bind to native Env proteins, there is a general consensus in the field that a sequential immunization strategy will be necessary to activate these B cells and shepherd their development into bNAbs<sup>25</sup>. Broadly, 'prime' immunogens would be specifically engineered to bind to these precursor antibodies, and would be followed by several 'boosts' of immunogens that incorporate increasingly more native-like features over a course of months, causing affinity maturation of the antibodies in a guided manner. This process would theoretically mimic the co-evolution of both antibody and virus that led to the original bNAbs discovered in infected patients<sup>80</sup>. The exact process and priorities of this strategy can vary, causing the methodologies taken by different groups

tend to categorize into three broad approaches: germline-targeting, epitope-focusing, and lineage-based. Additionally, earlier generations of non-sequential native Env trimer immunogens will be discussed for their historical value, although none have elicited heterologous tier 2 neutralizing antibody responses in animal models, and thus are not thought to be strong candidates for a widely effective human HIV-1 vaccine.

Stabilized pre-fusion native Env trimer immunogens that are not necessarily delivered as a part of a sequential immunization protocol were the first trimeric Env-based protein immunogens. One such immunogen, BG505 SOSIP.664<sup>81</sup>, was the first Env protein immunogen to elicit tier 2 neutralizing responses in animal models, although these neutralizing antibodies were only active against the immunogen's HIV-1 strain<sup>82</sup>. The three general approaches to later sequential immunization protocols designed to elicit specific bNAbs or heterologous tier 2 responses can be defined by their focus. In the germline-targeting approach, immunogens are engineered with the goal of expanding and activating B cells with specific inferred germline genes that are known to have matured into specific bNAb classes in humans. The epitope-focusing approach is geared toward eliciting precursor antibodies of any germline toward a specific bNAb epitope. Finally, lineage-based immunogen design proposes to design immunogens that will elicit bNAbs via the same evolutionary pathways as those whose development has been studied longitudinally, including the development of necessary but improbable mutations.

While each of these methodologies prioritize different aspects of the bNAb maturation process, there are a variety of general immunogen design strategies used across the categories. These tools are utilized to combat some of the unique challenges that HIV-1 poses to vaccine design, such the low or lack of affinity of precursor antibodies to native Envs, the wide strain diversity of HIV-1, and the frequency of antibodies elicited against non-conserved, immunodominant 'hole' epitopes that are only ever able to neutralize the strain that was used in the immunization. A commonly-used tool is directed evolution using yeast or mammalian cell surface to select for engineered Env immunogen proteins that bind to precursor antibodies. Rational immunogen design can also be used to test hypotheses about

changes to the immunogens that might make them more effective. In particular, the addition or removal of potential N-linked glycosylation sites is commonly used to either mask non-desired exposed protein epitopes or increase accessibility to desired epitopes, respectively. For example, the most advanced prime immunogen of the project discussed in Chapter 3, RC1-4fill, was rationally designed relative to the starting immunogen by incorporating both the removal of a PNGS at position N156<sub>gp120</sub> to increase accessibility to the desired V3-glycan patch epitope, and the addition of four PNGSs at positions 230, 241, 289, and 344 to decrease accessibility to the ‘glycan hole,’ which is a distracting epitope<sup>83</sup>. Multimerization of antigens onto nanoparticles (NPs) or virus-like particles (VLPs) has also been used to mask distracting epitopes at the ‘hole’ and ‘base’ epitopes of the trimer due to steric occlusion when Envs are projected outward and tightly packed on particles<sup>83</sup>. Furthermore, multimerization is thought to increase germinal center responses due to the avidity effects of multiple receptors on a B cell binding to multiple antigens on a multimerized particle at the same time, thus increasing the apparent affinity, which is an important factor in germinal center selection and affinity maturation<sup>84,85</sup>. Mosaic antigens, as discussed in reference to the Imbokodo and Mosaico trials, are designed in silico to optimize coverage of potential global HIV-1 T cell epitopes.<sup>86</sup> Consensus antigens have also been designed in an effort to increase the breadth of responses. These are antigens that are derived from the consensus sequence of a collection of Env strains, such as ConM and ConC, which are based on group M and clade C sequences, respectively<sup>87,88</sup>. Finally, there has been some recent work showing that antigens which are administered via antigen retention strategies either through continuous delivery mechanisms, dose escalation strategies, or the use of linkers to conjugate antigens to alum for antigen retention at the injection site for up to two weeks, have higher antigen-specific B cell responses in germinal centers<sup>89,90</sup>.

### **5.1 Stabilized Env trimer immunogens**

The design of stabilized, pre-fusion Env immunogens was a major leap forward in the effort toward eliciting bNAbs because earlier work was carried out using either non-native monomeric gp120s or gp120-gp41 Env trimer immunogens that adopted more open

conformations that exposed non-neutralizing epitopes<sup>91</sup>. So-called ‘foldon’ trimers have also been designed that include a trimerization domain, but production of these constructs results in a heterogeneous mixture of trimers and higher oligomers, the latter of which are not native-like prefusion states<sup>92,93</sup>. Native flexibly linked (NFL) trimers and uncleaved prefusion optimized (UFO) trimers have also been designed that incorporate a linker between gp120 and gp41 instead of the furin cleavage site and adopt the native pre-fusion conformation<sup>94,95</sup>. Although uncleaved, these constructs also elicit tier 2 autologous neutralizing responses, implying that the native pre-fusion conformation is more relevant to neutralizing responses than furin cleavage per se<sup>96,97</sup>.

In 2013, the first stabilized, pre-fusion Env trimer was published, which was known as the BG505 SOSIP.664 gp140 trimer<sup>81</sup>. The impact of this construct, both as a basis for future immunogens as well as for its use as a tool in structural studies, cannot be overstated. BG505 is a clade A strain of HIV-1 whose Env was particularly stable and amenable to further engineered stabilization<sup>98</sup>; SOSIP.664 refers to the mutations inserted into the BG505 Env sequence, which future work would show could also be inserted into many other Env sequences to create so-called ‘SOSIP trimers’ from many strains<sup>99</sup>. These mutations include the addition of an engineered disulfide bond between gp120 and gp41 (‘SOS’), while retaining the active furin cleavage site to stabilize the pre-fusion trimeric conformation<sup>100</sup>. Additionally, the helix-breaking mutation I559P (‘IP’) was incorporated to prevent the extension of gp41 alpha helix HR1 that occurs during fusion<sup>100</sup>. The construct is truncated after residue 664, which removed the MPER from the previously truncated ectodomain construct<sup>81,100</sup>. Immunogenicity studies showed that the trimer recapitulated native binding profiles well: bNAbs bound to the trimer, but non-neutralizing antibodies directed toward distracting epitopes had reduced or no binding<sup>81</sup>. Structural studies later showed that it recapitulated the structure of a native, un-stabilized Env ectodomain<sup>101,102</sup>. Later versions of these SOSIP constructs have continued to improve stability, decrease flexibility, and reduce immunodominance of non-neutralizing epitopes<sup>99</sup>. As stated previously, BG505 SOSIP.664 was the first Env protein immunogen to elicit autologous tier 2 responses in animal models<sup>82</sup>. Unfortunately, heterologous tier 2 responses have not been observed; the immunodominant

but strain-specific ‘glycan hole’ epitope centered around gp120 residue 241 is a major target of these autologous responses<sup>19</sup>.

While non-sequential native Env immunogens were the focus of research in animal models for several years, current studies are actually surveying these constructs in Phase I human trials. It should be noted that none of these Phase I trials are expected to elicit heterologous tier 2 responses in humans. Instead, the trials are designed to study the safety profile of the regimens as well as to see if the autologous tier 2 neutralizing responses seen in animals can be translated to humans<sup>41</sup>. BG505 SOSIP.664 gp140 trimer is being assessed in two trials: IAVIW001 (NCT03699241) and HVTN137 (NCT04177355). IAVI W001 is studying the immunogen in combination with the AS01<sub>B</sub> adjuvant, and HVTN137 is comparing the responses of the immunogen with a variety of adjuvants. Another phase I study, 19-I-0031 (NCT03783130), assessed a further-stabilized variant of BG505 SOSIP.664 referred to as DS-SOSIP<sup>103</sup>, or the 4571 trimer, which was designed with an additional intramolecular disulfide bond in gp120 designed to prevent ‘open’ conformations of Env and reduced V3 loop exposure (considered a distracting epitope). Additionally, in an effort to overcome immunodominance caused by strain-specific determinants (residues, glycans, glycan holes, etc.), an Env SOSIP was developed from the consensus sequence of HIV-1 group M, which encompasses all global epidemic strains<sup>9</sup>. ACTHIVE-001 (NCT03961438) is a phase I trial studying this ConM SOSIP.v7 trimer, which also incorporates further pre-fusion stabilizing mutations<sup>87</sup>. A final trial, HVTN122 (NCT03382418), studied the C.6980 gp145 trimer<sup>104</sup>, which is the only trimer immunogen in phase I trials that does not contain pre-fusion stabilizing mutations. The results of these trials are expected to help frame the translation of responses between animal models and humans, but these immunogens are unlikely to elicit the heterologous tier 2 neutralizing responses needed to continue as an HIV-1 vaccine candidate.

## **5.2 Germline-targeting immunogens**

Germline-targeting immunogens are typically designed as a series that introduces more native-like features over time, but always start with a ‘prime’ immunogen engineered to bind

with high or very high affinity to the iGLs of whatever class of bNAbs they are being designed to elicit. One major reason this strategy exists is that the iGLs of human bNAbs generally do not bind native Env immunogens<sup>24,52,105</sup>. Therefore, priming with a native Env immunogen might activate some B cells, but not necessarily those known to mature into bNAbs. Unfortunately, these sought-after bNAb iGLs are quite rare in the human repertoire, so expanding them has posed a challenge<sup>26,106</sup>.

An additional challenge for studying these types of responses is that different animal models have different V, D, and J gene segment repertoires, as well as different patterns of signature recombination features, such as CDR loop lengths. Therefore, if the goal is to elicit a specific sequence of neutralizing antibody rather than just a neutralizing response, an animal model may not be able to faithfully report if this is possible because they often lack the target germline genes found in humans. For this reason, ‘knock-in’ animal models can be utilized that are produced to express B cells with a specific V-gene segment or iGL sequence<sup>107</sup>. While these animal models can describe if an immunogen effectively primes a pool of the intended B cells, the starting proportion of these B cells is often unrealistically high compared to the human repertoire, so the same result should not be expected in humans or animals with a polyclonal immune response. More recently, adoptive transfer experiments have been used in an attempt to bridge this gap by transferring a known and representative amount of iGL B cells to the animal model<sup>106</sup>. Additionally, sorts of naïve (HIV-1 negative) human B cell repertoires have helped to quantify proportions of specific iGLs as well as identify which immunogens will be able to activate human B cells in their native context<sup>26,106</sup>. Deep sequencing of these repertoires can also be used to identify new iGL antibody sequences for immunogen design<sup>106,108</sup>.

The most popular bNAb target of germline-targeting immunogens has been the VRC01 class of CD4bs bNAbs, in part because bNAbs belonging to this well-defined class have been isolated from multiple donors and shown to bind in an extremely similar fashion<sup>70,78</sup>. This class of bNAb is broadly defined by VH1-2 gene usage and an unusually short 5-amino acid CDRL3<sup>78</sup>.

The most advanced germline-targeting immunogen designed to elicit the VRC01 class of bNAbs is the eOD-GT8 60mer<sup>109</sup>, which is currently being assessed in a phase I clinical trial (IAVI G001; NCT03547245). eOD-GT8 is an immunogen consisting of an engineered outer domain (eOD) of gp120 that was designed to have extremely high affinity to VRC01-class iGLs<sup>105</sup>. Prior work in knock-in and adoptive transfer mouse models suggested that eOD-GT8 60mer could activate rare VRC01-class precursors in humans<sup>109-111</sup>. In February 2021, preliminary results of the trial presented at the HIVR4P conference showed that 97% of vaccinated participants developed detectable VRC01-class IgG+ B cells<sup>112</sup>. This is the first time a specific class of iGL B cells has been primed in humans and is an exciting development. However, a boosting protocol that can guide these specific precursor B cells into VRC01-class bNAbs is still necessary for this approach to mature into an HIV-1 vaccine. Recent work on a boosting protocol in knock-in mice elicited VRC01-class antibodies that could neutralize up to 54% of a 208-strain panel<sup>113</sup>. If this boosting protocol could be improved and translated to humans, it would be a major advance in the HIV-1 vaccine space.

Another germline-targeting immunogen focused on the VRC01 class of bNAbs is the BG505 SOSIP GT1.1 trimer, which is also being evaluated in a phase I trial (NCT04224701). This construct is again based on BG505 SOSIP.664, but also incorporates germline-targeting mutations within two different epitopes: the CD4bs and the V1V2 apex<sup>114</sup>. In a knock-in mouse model, mice immunized with BG505 SOSIP GT1 (a slight variant of GT1.1) elicited CD4bs antibodies while mice immunized with non-germline-targeting BG505 SOSIP did not. In contrast to the high affinity eOD-GT8 60mer, BG505 SOSIP GT1 exhibits relatively weak binding to VRC01 iGLs<sup>109,114</sup>. A lingering question in the field is: exactly how high affinity do effective germline-targeting prime immunogens need to be? The phase I trials for these two VRC01-targeting immunogens may help to answer this question<sup>41</sup>.

The final VRC01-class germline-targeting immunogen is known as the 426c Core (or TM4ΔV1-3), and is a gp120 core immunogen from the clade C strain 426c, which includes both the inner and outer domains of gp120, but does not include the V1, V2, or V3 loops or the PNGSs at N276<sub>gp120</sub>, N460<sub>gp120</sub>, or N463<sub>gp120</sub><sup>115</sup>. This immunogen was shown to elicit

cross-reactive VRC01-like antibodies that can still bind in the presence of the notoriously difficult-to-accommodate glycan at position N276<sub>gp120</sub> when followed by a boost with N276<sub>gp120</sub>-containing HxB2 WT Core, although these antibodies were only autologously neutralizing<sup>116</sup>. Phase I trials for this immunogen are planned to begin in 2021<sup>117</sup>.

The second epitope that has been targeted via the germline-targeting approach is the V3-glycan patch; specifically, germline-targeting immunogens have been designed to activate and mature the precursors of V3 bNAbs PGT121<sup>118</sup> and BG18<sup>106</sup>. Initially, the BG505-10MUT trimer was engineered to bind germline-reverted precursors of PGT121-like antibodies using mammalian display directed evolution<sup>118</sup>. When injected into knock-in mice as a part of a sequential immunization protocol, this immunogen caused the development of the first broadly neutralizing antibodies (heterologous tier 2 responses) observed in animal models after immunization<sup>107</sup>. A further-engineered variant of BG505-10MUT, known as 11MUTB, was also designed to bind with even higher affinity to the germline precursors<sup>118</sup>. 11MUTB then became the starting-point immunogen for the BG18-targeting N332-GT2 series, as well as our lab's RC1 V3-glycan patch immunogen, which will be discussed in Section 5.3: *Epitope-Focusing Immunogens* (as well as Chapter 3). The BG18-directed, germline-targeting immunogen N332-GT2 Env trimer was shown to activate precursor B cells in an adoptive transfer mouse model with a low proportion of those precursor B cells when multimerized. Additionally, it was used to capture BG18-like naïve precursor B cells from HIV-1-negative human donors, thus suggesting that it could be used as an effective priming immunogen in a phase I human trial<sup>106</sup>.

### **5.3 Epitope-focusing immunogens**

The epitope-focusing immunogen design approach has also been referred to as the 'germline agnostic' approach because its goal is to elicit bNAbs to a certain neutralizing epitope, not bNAbs that mature from a certain precursor germline antibody<sup>49</sup>. In this view, so long as bNAbs mature, it does not so much matter if they faithfully recapitulate the germline genes, unique features, or lineage evolution of different bNAb classes. One challenge of the germline-targeting approach is that the desired precursor B cells are incredibly rare; in the

epitope-focusing approach the number of potentially mature-able B cells is not so severely limited in the initial step. Alternatively, one challenge that epitope-focusing sequential immunization protocols have encountered is determining whether the primed precursor B cells have the capacity to eventually mature into bNAbs. Epitope-focusing immunogens have been designed to target many epitopes, including the V3-glycan patch<sup>83</sup>, the V2 apex<sup>119</sup>, the MPER<sup>119</sup>, and the fusion peptide<sup>120</sup>.

The RC1 immunogen will be discussed in detail in Chapter 3, but briefly, it was rationally designed to target the V3-glycan patch with just a single amino acid change from 11MUTB—the removal of the PNGS that encodes for the N156<sub>gp120</sub> glycan<sup>83</sup>. This change was rationalized as a way to increase accessibility to the protein component of the V3-glycan patch epitope, as well as reduce negative charges (from sialic acids on the N156<sub>gp120</sub> glycan) to facilitate binding of the mostly neutrally charged precursor antibody. From there, further mutations were introduced to add PNGSs that would abolish the ‘glycan hole’ epitope at gp120 positions 230, 241, 289, and 344. This construct, named RC1-4fill, was multimerized on VLPs and then injected as part of a sequential immunization protocol in non-human primates (NHPs). Single B cell sorting and cloning from these NHPs allowed for the discovery of monoclonal antibodies that were shown by cryo-EM and enzyme-linked immunosorbent assays (ELISAs) to bind at the V3-glycan patch epitope, including the <sup>324</sup>GDIR<sup>327</sup> peptide motif and gp120 N332/N301 glycans<sup>83</sup>.

An epitope-focusing immunogen called the MT145K SIV Env trimer was engineered to target the V2 apex epitope, which is a quaternary epitope at the apex (‘top’) of the trimer<sup>119</sup>. The immunogen is a minimally-engineered SOSIP.664 construct derived from the simian immunodeficiency virus (SIV) strain MT145 Env. In line with the goal of epitope-focusing immunogen design, an SIV, rather than HIV-1, Env was chosen because the V2 apex epitope is the only common epitope between the two, so other off-target HIV-1 epitopes would not be exposed. Furthermore, the MT145K trimer binds the iGLs of several V1V2 bNAbs, but not the iGLs of bNAbs to other epitopes. A sequential immunization protocol with this

immunogen in a knock-in mouse model elicited heterologous neutralizing serum responses<sup>119</sup>.

Another epitope that has been targeted using epitope-focusing immunogen design is the MPER of HIV-1, where antibodies recognize a highly conserved, non-glycan, linear epitope at the C-terminal end of the trimer ectodomain<sup>121</sup>. Unfortunately, this is considered a particularly challenging epitope due to the fact that MPER bNAbs often bind the virus's lipid bilayer as well and can therefore exhibit polyreactivity that makes them vulnerable to deletion by immune tolerance mechanisms<sup>21</sup>. One epitope-focusing MPER immunogen is the MPER-656 liposome, in which a liposome displays a peptide of MPER gp41 residues 656-683<sup>122</sup>. In a sequential immunization protocol in NHPs using MPER-656 liposomes, it was reported that the desired 2F5-like precursor antibodies were not able to overcome tolerance mechanisms, and were either clonally deleted or never attained sufficient affinity to be potently neutralizing<sup>123</sup>. A phase I clinical trial (NCT03934541) evaluating MPER-656 liposomes in humans concluded in May 2021 but has not yet released results.

The fusion peptide at the N-terminus of gp41 is the final epitope targeted by the epitope-focusing approach. A sequential immunization series including an immunogen composed of multimerized fusion peptides conjugated to a keyhole limpet hemocyanin (KLH) carrier protein (FP-KLH), and followed by boosts with DS-SOSIPs, is the most advanced version of this FP epitope-focusing approach<sup>124</sup>. It is the only immunogen series yet to elicit tier 2, heterologous neutralizing antibodies in wild type mice, guinea pigs, and NHPs<sup>120,124</sup>. It would be an advance in the HIV-1 vaccine world if these results could be directly translated to humans, although that should not necessarily be expected from previous work in the field.

#### **5.4 Lineage-based immunogens**

The lineage-based approach is similar to the germline-targeting approach in that the goal is to recreate features of known bNAbs; however, the lineage-based approach focuses more specifically on mimicking the entire development pathway of these bNAbs, specifically the development of mutations that are considered key and improbable, rather than just the

recruitment of the correct germline B cells<sup>125,126</sup>. This is enabled by longitudinal tracking of both virus and bNAb co-evolution from transmitted/founder virus and germline antibody, respectively, in HIV-1-positive patients over the course of years<sup>80</sup>. A component of this strategy involves designing prime immunogens from the Envs of T/F viruses known to be the founding virus in the infection of a person who later developed bNAbs<sup>125</sup>. Unlike most native Envs, the CH505 T/F Env was found to bind to the iGLs of two bNAb lineages, the CH103 and CH235 lineages, observed in the same patient, and thus was thought to be an appropriate starting immunogen for inducing these types of bNAbs<sup>127</sup>. However, initial studies showed immunizations with CH505 TF gp120 and sequential CH505 TF lineage gp120s as well as a chimeric CH505 TF gp120:BG505 gp41 SOSIP did not elicit tier 2 neutralizing antibody responses in animal models<sup>128,129</sup>. In 2019, two lineage-based immunogens, CH848 10.17DT Env and M5.G458Y SOSIP, were published that target the DH270 (V3-glycan patch) and CH235 (CD4bs) bNAb lineages, respectively<sup>126</sup>. These immunogens were specifically developed to elicit antibodies that contained the specific, key, improbable mutations that were observed in the maturation of the DH270 and CH235 bNAbs. The immunogens were shown to bind with higher affinity to the bNAb precursors that had acquired the improbable mutations than those that had not<sup>126</sup>. Studies showed that NHPs immunized with multimerized M5.G458Y SOSIP gp140 nanoparticles elicited high titers of antibodies that could neutralize modified CH505 viruses (either a glycan GnTI<sup>-/-</sup> mutant or G458Y mutant)<sup>126</sup>. Additionally, two phase I trials (HVTN 115 and HVTN 135) are currently studying CH505 TF gp120 immunogens. HVTN 115 (NCT03220724) was designed to test a sequential immunization series with CH505 TF lineage gp120s similar to a previous NHP study<sup>128</sup>, and HVTN 135 (NCT04607408) will study the immunogenicity of CH505 TF gp120 in infants, who may generate bNAb responses more reliably and quickly than adults<sup>130</sup>.

### **Scope of Work**

Structural biology has been key to the advancement of HIV-1 immunogen design, both in terms of characterizing the desirable features of human bNAbs that immunogens are then

designed to elicit, as well as in evaluating the humoral responses of animals that have been immunized with designed immunogens. This thesis reports on several projects that relate to the themes explored in this introduction, such as bNAb isolation and characterization (Chapter 2), immunogen design (Chapter 3), and the structural study of a non-neutralizing, off-target monoclonal antibody (Chapter 4). Chapter 2 describes the isolation, high-resolution structural characterization, and in vitro resistance profile of a new bNAb, 1-18, that is both very broad and potent, as well as able to restrict HIV-1 escape in vivo. Chapter 3 reports the results of an epitope-focusing immunogen design and immunization experiment carried out in wild type mice, rabbits, and non-human primates where it was shown that B cells targeting the desired epitope were expanded after a single prime immunization with immunogen RC1 or a variant, RC1-4fill. Chapter 4 describes Ab1245, an off-target non-neutralizing monoclonal antibody isolated in a macaque that had been immunized with a series of sequential immunogens after the prime immunization reported in Chapter 3. The antibody structure describes a specific type of distracting response as it binds in a way that causes a large structural change in Env, resulting in the destruction of the neutralizing fusion peptide epitope.

Additionally, when the SARS-CoV-2 pandemic began to unfold in 2020, many of the researchers (including myself) that were familiar with HIV-1 structural biology analyses of antibodies were uniquely positioned to shift to working on analogous antibodies elicited in response to SARS-CoV-2 infection and vaccination. Chapter 5 is adapted from a review about how antibodies differentially recognize the viruses HIV-1, SARS-CoV-2, and Zika virus. This review serves as an introduction to the virus SARS-CoV-2, which is the topic of the final chapter, Chapter 6. In this chapter, structures of many neutralizing antibodies isolated from SARS-CoV-2 patients were used to define potentially therapeutic classes of neutralizing receptor-binding domain (RBD) antibodies based on their epitopes and binding profiles.

## References

1. Center for Disease Control. Pneumocystis Pneumonia --- Los Angeles. *Morbidity and Mortality Weekly Report : MMWR*. **30**, 1–3 (1981).
2. Global HIV & AIDS statistics — Fact sheet.
3. Engelman, A. & Cherepanov, P. The structural biology of HIV-1: mechanistic and therapeutic insights. *Nat Rev Microbiol* **10**, 279–290 (2012).
4. Gray, G. E. & Corey, L. The path to find an HIV vaccine. *J Int AIDS Soc* **24**, (2021).
5. Shapiro, S. Z. Clinical Development of Candidate HIV Vaccines: Different Problems for Different Vaccines. *AIDS Research and Human Retroviruses* **30**, 325–329 (2014).
6. Akkaya, M., Kwak, K. & Pierce, S. K. B cell memory: building two walls of protection against pathogens. *Nat Rev Immunol* **20**, 229–238 (2020).
7. Robinson, H. L. HIV/AIDS Vaccines: 2018. *Clin. Pharmacol. Ther.* **104**, 1062–1073 (2018).
8. Smyth, R. P., Davenport, M. P. & Mak, J. The origin of genetic diversity in HIV-1. *Virus Research* **169**, 415–429 (2012).
9. Korber, B. *et al.* Evolutionary and immunological implications of contemporary HIV-1 variation. *British Medical Bulletin* **58**, 19–42 (2001).
10. Keele, B. F. *et al.* Identification and characterization of transmitted and early founder virus envelopes in primary HIV-1 infection. *Proceedings of the National Academy of Sciences* **105**, 7552–7557 (2008).
11. Burton, D. R. & Hangartner, L. Broadly Neutralizing Antibodies to HIV and Their Role in Vaccine Design. *Annu. Rev. Immunol.* **34**, 635–659 (2016).

12. Burton, D. R. & Mascola, J. R. Antibody responses to envelope glycoproteins in HIV-1 infection. *Nat Immunol* **16**, 571–576 (2015).
13. Moore, P. L. *et al.* Potent and Broad Neutralization of HIV-1 Subtype C by Plasma Antibodies Targeting a Quaternary Epitope Including Residues in the V2 Loop. *J Virol* **85**, 3128–3141 (2011).
14. Klein, J. S. & Bjorkman, P. J. Few and Far Between: How HIV May Be Evading Antibody Avidity. *PLoS Pathog* **6**, e1000908 (2010).
15. Wang, H. *et al.* Cryo-EM structure of a CD4-bound open HIV-1 envelope trimer reveals structural rearrangements of the gp120 V1V2 loop. *Proc Natl Acad Sci USA* **113**, E7151–E7158 (2016).
16. Parren, P. W. H. I., Burton, D. R. & Sattentau, Q. J. HIV-1 antibody — debris or virion? *Nat Med* **3**, 366–367 (1997).
17. Wagh, K., Hahn, B. H. & Korber, B. Hitting the sweet spot: exploiting HIV-1 glycan shield for induction of broadly neutralizing antibodies. *Current Opinion in HIV and AIDS* **15**, 267–274 (2020).
18. Wei, X. *et al.* Antibody neutralization and escape by HIV-1. *Nature* **422**, 307–312 (2003).
19. McCoy, L. E. *et al.* Holes in the Glycan Shield of the Native HIV Envelope Are a Target of Trimer-Elicited Neutralizing Antibodies. *Cell Reports* **16**, 2327–2338 (2016).
20. Liu, M. *et al.* Polyreactivity and Autoreactivity among HIV-1 Antibodies. *J. Virol.* **89**, 784–798 (2015).
21. Yang, G. *et al.* Identification of autoantigens recognized by the 2F5 and 4E10 broadly neutralizing HIV-1 antibodies. *Journal of Experimental Medicine* **210**, 241–256 (2013).

22. Cizmeci, D. *et al.* Distinct clonal evolution of B-cells in HIV controllers with neutralizing antibody breadth. *eLife* **10**, e62648 (2021).
23. Tiller, T. *et al.* Autoreactivity in Human IgG+ Memory B Cells. *Immunity* **26**, 205–213 (2007).
24. Hoot, S. *et al.* Recombinant HIV Envelope Proteins Fail to Engage Germline Versions of Anti-CD4bs bNAbs. *PLoS Pathog* **9**, e1003106 (2013).
25. Burton, D. R. What Are the Most Powerful Immunogen Design Vaccine Strategies?: Reverse Vaccinology 2.0 Shows Great Promise. *Cold Spring Harb Perspect Biol* **9**, a030262 (2017).
26. Havenar-Daughton, C. *et al.* The human naive B cell repertoire contains distinct subclasses for a germline-targeting HIV-1 vaccine immunogen. *Sci. Transl. Med.* **10**, eaat0381 (2018).
27. Betz, A. G., Rada, C., Pannell, R., Milstein, C. & Neuberger, M. S. Passenger transgenes reveal intrinsic specificity of the antibody hypermutation mechanism: clustering, polarity, and specific hot spots. *Proceedings of the National Academy of Sciences* **90**, 2385–2388 (1993).
28. Schramm, C. A. & Douek, D. C. Beyond Hot Spots: Biases in Antibody Somatic Hypermutation and Implications for Vaccine Design. *Front. Immunol.* **9**, 1876 (2018).
29. The rgp120 HIV Vaccine Study Group. Placebo-Controlled Phase 3 Trial of a Recombinant Glycoprotein 120 Vaccine to Prevent HIV-1 Infection. *J INFECT DIS* **191**, 654–665 (2005).

30. Pitisuttithum, P. *et al.* Randomized, Double-Blind, Placebo-Controlled Efficacy Trial of a Bivalent Recombinant Glycoprotein 120 HIV-1 Vaccine among Injection Drug Users in Bangkok, Thailand. *J INFECT DIS* **194**, 1661–1671 (2006).
31. Esparza, J. A brief history of the global effort to develop a preventive HIV vaccine. *Vaccine* **31**, 3502–3518 (2013).
32. Buchbinder, S. P. *et al.* Efficacy assessment of a cell-mediated immunity HIV-1 vaccine (the Step Study): a double-blind, randomised, placebo-controlled, test-of-concept trial. *The Lancet* **372**, 1881–1893 (2008).
33. Fauci, A. S., Marovich, M. A., Dieffenbach, C. W., Hunter, E. & Buchbinder, S. P. Immune Activation with HIV Vaccines. *Science* **344**, 49–51 (2014).
34. Duerr, A. *et al.* Extended Follow-up Confirms Early Vaccine-Enhanced Risk of HIV Acquisition and Demonstrates Waning Effect Over Time Among Participants in a Randomized Trial of Recombinant Adenovirus HIV Vaccine (Step Study). *Journal of Infectious Diseases* **206**, 258–266 (2012).
35. Rerks-Ngarm, S. *et al.* Vaccination with ALVAC and AIDSVAX to Prevent HIV-1 Infection in Thailand. *N Engl J Med* **361**, 2209–2220 (2009).
36. Haynes, B. F. *et al.* Immune-Correlates Analysis of an HIV-1 Vaccine Efficacy Trial. *N Engl J Med* **366**, 1275–1286 (2012).
37. Yates, N. L. *et al.* Vaccine-Induced Env V1-V2 IgG3 Correlates with Lower HIV-1 Infection Risk and Declines Soon After Vaccination. *Sci. Transl. Med.* **6**, (2014).
38. Lin, L. *et al.* COMPASS identifies T-cell subsets correlated with clinical outcomes. *Nat Biotechnol* **33**, 610–616 (2015).

39. Hammer, S. M. *et al.* Efficacy Trial of a DNA/rAd5 HIV-1 Preventive Vaccine. *N Engl J Med* **369**, 2083–2092 (2013).
40. Gray, G. E. *et al.* Vaccine Efficacy of ALVAC-HIV and Bivalent Subtype C gp120–MF59 in Adults. *N Engl J Med* **384**, 1089–1100 (2021).
41. Lee, J. H. & Crotty, S. HIV vaccinology: 2021 update. *Seminars in Immunology* 101470 (2021) doi:10.1016/j.smim.2021.101470.
42. Abbink, P. *et al.* Comparative Seroprevalence and Immunogenicity of Six Rare Serotype Recombinant Adenovirus Vaccine Vectors from Subgroups B and D. *J Virol* **81**, 4654–4663 (2007).
43. Fischer, W. *et al.* Polyvalent vaccines for optimal coverage of potential T-cell epitopes in global HIV-1 variants. *Nat Med* **13**, 100–106 (2007).
44. Johnson & Johnson and Global Partners Announce Results from Phase 2b Imbokodo HIV Vaccine Clinical Trial in Young Women in Sub-Saharan Africa. *PRNewswire* (2021).
45. Huang, J. *et al.* Identification of a CD4-Binding-Site Antibody to HIV that Evolved Near-Pan Neutralization Breadth. *Immunity* **45**, 1108–1121 (2016).
46. Mouquet, H. *et al.* Complex-type N-glycan recognition by potent broadly neutralizing HIV antibodies. *Proceedings of the National Academy of Sciences* **109**, E3268–E3277 (2012).
47. Montefiori, D. C., Roederer, M., Morris, L. & Seaman, M. S. Neutralization tiers of HIV-1. *Current Opinion in HIV and AIDS* **13**, 128–136 (2018).
48. Simek, M. D. *et al.* Human Immunodeficiency Virus Type 1 Elite Neutralizers: Individuals with Broad and Potent Neutralizing Activity Identified by Using a High-

- Throughput Neutralization Assay together with an Analytical Selection Algorithm. *J Virol* **83**, 7337–7348 (2009).
49. Remmel, J. L. & Ackerman, M. E. Rationalizing Random Walks: Replicating Protective Antibody Trajectories. *Trends in Immunology* **42**, 186–197 (2021).
50. Schommers, P. *et al.* Restriction of HIV-1 Escape by a Highly Broad and Potent Neutralizing Antibody. *Cell* **180**, 471–489.e22 (2020).
51. Georgiou, G. *et al.* The promise and challenge of high-throughput sequencing of the antibody repertoire. *Nat Biotechnol* **32**, 158–168 (2014).
52. Slieden, K. *et al.* Binding of inferred germline precursors of broadly neutralizing HIV-1 antibodies to native-like envelope trimers. *Virology* **486**, 116–120 (2015).
53. Gristick, H. B. *et al.* Natively glycosylated HIV-1 Env structure reveals new mode for antibody recognition of the CD4-binding site. *Nat Struct Mol Biol* **23**, 906–915 (2016).
54. Hsu, D. C., Mellors, J. W. & Vasan, S. Can Broadly Neutralizing HIV-1 Antibodies Help Achieve an ART-Free Remission? *Front. Immunol.* **12**, 710044 (2021).
55. Ko, S.-Y. *et al.* Enhanced neonatal Fc receptor function improves protection against primate SHIV infection. *Nature* **514**, 642–645 (2014).
56. Zalevsky, J. *et al.* Enhanced antibody half-life improves in vivo activity. *Nat Biotechnol* **28**, 157–159 (2010).
57. Gaudinski, M. R. *et al.* Safety and pharmacokinetics of broadly neutralising human monoclonal antibody VRC07-523LS in healthy adults: a phase 1 dose-escalation clinical trial. *The Lancet HIV* **6**, e667–e679 (2019).
58. Caskey, M. *et al.* Antibody 10-1074 suppresses viremia in HIV-1-infected individuals. *Nat Med* **23**, 185–191 (2017).

59. Scheid, J. F. *et al.* HIV-1 antibody 3BNC117 suppresses viral rebound in humans during treatment interruption. *Nature* **535**, 556–560 (2016).
60. Wu, X. *et al.* Rational Design of Envelope Identifies Broadly Neutralizing Human Monoclonal Antibodies to HIV-1. *Science* **329**, 856–861 (2010).
61. Corey, L. *et al.* Two Randomized Trials of Neutralizing Antibodies to Prevent HIV-1 Acquisition. *N Engl J Med* **384**, 1003–1014 (2021).
62. Sok, D. & Burton, D. R. Recent progress in broadly neutralizing antibodies to HIV. *Nat Immunol* **19**, 1179–1188 (2018).
63. Burton, D. R. Antibodies, viruses and vaccines. *Nat Rev Immunol* **2**, 706–713 (2002).
64. Rappuoli, R., Bottomley, M. J., D’Oro, U., Finco, O. & De Gregorio, E. Reverse vaccinology 2.0: Human immunology instructs vaccine antigen design. *Journal of Experimental Medicine* **213**, 469–481 (2016).
65. Shaik, M. M. *et al.* Structural basis of coreceptor recognition by HIV-1 envelope spike. *Nature* **565**, 318–323 (2019).
66. Lee, J. H. *et al.* Antibodies to a conformational epitope on gp41 neutralize HIV-1 by destabilizing the Env spike. *Nat Commun* **6**, 8167 (2015).
67. West, A. P. *et al.* Structural Insights on the Role of Antibodies in HIV-1 Vaccine and Therapy. *Cell* **156**, 633–648 (2014).
68. Gorman, J. *et al.* Structures of HIV-1 Env V1V2 with broadly neutralizing antibodies reveal commonalities that enable vaccine design. *Nat Struct Mol Biol* **23**, 81–90 (2016).
69. Barnes, C. O. *et al.* Structural characterization of a highly-potent V3-glycan broadly neutralizing antibody bound to natively-glycosylated HIV-1 envelope. *Nat Commun* **9**, 1251 (2018).

70. Zhou, T. *et al.* Structural Repertoire of HIV-1-Neutralizing Antibodies Targeting the CD4 Supersite in 14 Donors. *Cell* **161**, 1280–1292 (2015).
71. Kwong, P. D. *et al.* Structure of an HIV gp120 envelope glycoprotein in complex with the CD4 receptor and a neutralizing human antibody. *Nature* **393**, 648–659 (1998).
72. Zhou, T. *et al.* A Neutralizing Antibody Recognizing Primarily N-Linked Glycan Targets the Silent Face of the HIV Envelope. *Immunity* **48**, 500-513.e6 (2018).
73. Schoofs, T. *et al.* Broad and Potent Neutralizing Antibodies Recognize the Silent Face of the HIV Envelope. *Immunity* **50**, 1513-1529.e9 (2019).
74. Kong, R. *et al.* Fusion peptide of HIV-1 as a site of vulnerability to neutralizing antibody. *Science* **352**, 828–833 (2016).
75. Scharf, L. *et al.* Antibody 8ANC195 Reveals a Site of Broad Vulnerability on the HIV-1 Envelope Spike. *Cell Reports* **7**, 785–795 (2014).
76. Huang, J. *et al.* Broad and potent neutralization of HIV-1 by a gp41-specific human antibody. *Nature* **491**, 406–412 (2012).
77. Zwick, M. B. *et al.* Broadly Neutralizing Antibodies Targeted to the Membrane-Proximal External Region of Human Immunodeficiency Virus Type 1 Glycoprotein gp41. *J Virol* **75**, 10892–10905 (2001).
78. West, A. P., Diskin, R., Nussenzweig, M. C. & Bjorkman, P. J. Structural basis for germ-line gene usage of a potent class of antibodies targeting the CD4-binding site of HIV-1 gp120. *Proc Natl Acad Sci USA* **109**, E2083–E2090 (2012).
79. Scheid, J. F. *et al.* Sequence and Structural Convergence of Broad and Potent HIV Antibodies That Mimic CD4 Binding. *Science* **333**, 1633–1637 (2011).

80. NISC Comparative Sequencing Program *et al.* Co-evolution of a broadly neutralizing HIV-1 antibody and founder virus. *Nature* **496**, 469–476 (2013).
81. Sanders, R. W. *et al.* A Next-Generation Cleaved, Soluble HIV-1 Env Trimer, BG505 SOSIP.664 gp140, Expresses Multiple Epitopes for Broadly Neutralizing but Not Non-Neutralizing Antibodies. *PLoS Pathog* **9**, e1003618 (2013).
82. Sanders, R. W. *et al.* HIV-1 neutralizing antibodies induced by native-like envelope trimers. *Science* **349**, aac4223 (2015).
83. Escolano, A. *et al.* Immunization expands B cells specific to HIV-1 V3 glycan in mice and macaques. *Nature* **570**, 468–473 (2019).
84. Victora, G. D. & Nussenzweig, M. C. Germinal Centers. *Annu. Rev. Immunol.* **30**, 429–457 (2012).
85. Marcandalli, J. *et al.* Induction of Potent Neutralizing Antibody Responses by a Designed Protein Nanoparticle Vaccine for Respiratory Syncytial Virus. *Cell* **176**, 1420–1431.e17 (2019).
86. Barouch, D. H. *et al.* Mosaic HIV-1 vaccines expand the breadth and depth of cellular immune responses in rhesus monkeys. *Nat Med* **16**, 319–323 (2010).
87. Slieden, K. *et al.* Structure and immunogenicity of a stabilized HIV-1 envelope trimer based on a group-M consensus sequence. *Nat Commun* **10**, 2355 (2019).
88. Killick, M., Capovilla, A. & Papathanasopoulos, M. A. Generation and Characterization of an HIV-1 Subtype C Transmitted and Early Founder Virus Consensus Sequence. *AIDS Research and Human Retroviruses* **30**, 1001–1005 (2014).

89. Cirelli, K. M. *et al.* Slow Delivery Immunization Enhances HIV Neutralizing Antibody and Germinal Center Responses via Modulation of Immunodominance. *Cell* **177**, 1153-1171.e28 (2019).
90. Moyer, T. J. *et al.* Engineered immunogen binding to alum adjuvant enhances humoral immunity. *Nat Med* **26**, 430–440 (2020).
91. Yasmeen, A. *et al.* Differential binding of neutralizing and non-neutralizing antibodies to native-like soluble HIV-1 Env trimers, uncleaved Env proteins, and monomeric subunits. *Retrovirology* **11**, 41 (2014).
92. Kovacs, J. M. *et al.* Stable, uncleaved HIV-1 envelope glycoprotein gp140 forms a tightly folded trimer with a native-like structure. *Proc Natl Acad Sci USA* **111**, 18542–18547 (2014).
93. AlSalmi, W. *et al.* A New Approach to Produce HIV-1 Envelope Trimers. *Journal of Biological Chemistry* **290**, 19780–19795 (2015).
94. Kong, L. *et al.* Uncleaved prefusion-optimized gp140 trimers derived from analysis of HIV-1 envelope metastability. *Nat Commun* **7**, 12040 (2016).
95. Sharma, S. K. *et al.* Cleavage-Independent HIV-1 Env Trimers Engineered as Soluble Native Spike Mimetics for Vaccine Design. *Cell Reports* **11**, 539–550 (2015).
96. He, L. *et al.* HIV-1 vaccine design through minimizing envelope metastability. *Sci. Adv.* **4**, eaau6769 (2018).
97. Pauthner, M. *et al.* Elicitation of Robust Tier 2 Neutralizing Antibody Responses in Nonhuman Primates by HIV Envelope Trimer Immunization Using Optimized Approaches. *Immunity* **46**, 1073-1088.e6 (2017).

98. Hoffenberg, S. *et al.* Identification of an HIV-1 Clade A Envelope That Exhibits Broad Antigenicity and Neutralization Sensitivity and Elicits Antibodies Targeting Three Distinct Epitopes. *Journal of Virology* **87**, 5372–5383 (2013).
99. de Taeye, S. W. *et al.* Immunogenicity of Stabilized HIV-1 Envelope Trimers with Reduced Exposure of Non-neutralizing Epitopes. *Cell* **163**, 1702–1715 (2015).
100. Sanders, R. W. *et al.* Stabilization of the Soluble, Cleaved, Trimeric Form of the Envelope Glycoprotein Complex of Human Immunodeficiency Virus Type 1. *J Virol* **76**, 8875–8889 (2002).
101. Lee, J. H., Ozorowski, G. & Ward, A. B. Cryo-EM structure of a native, fully glycosylated, cleaved HIV-1 envelope trimer. *Science* **351**, 1043–1048 (2016).
102. Pancera, M. *et al.* Structure and immune recognition of trimeric pre-fusion HIV-1 Env. *Nature* **514**, 455–461 (2014).
103. Do Kwon, Y. *et al.* Crystal structure, conformational fixation and entry-related interactions of mature ligand-free HIV-1 Env. *Nat Struct Mol Biol* **22**, 522–531 (2015).
104. Wiczorek, L. *et al.* Comparable Antigenicity and Immunogenicity of Oligomeric Forms of a Novel, Acute HIV-1 Subtype C gp145 Envelope for Use in Preclinical and Clinical Vaccine Research. *J Virol* **89**, 7478–7493 (2015).
105. Jardine, J. *et al.* Rational HIV Immunogen Design to Target Specific Germline B Cell Receptors. *Science* **340**, 711–716 (2013).
106. Steichen, J. M. *et al.* A generalized HIV vaccine design strategy for priming of broadly neutralizing antibody responses. *Science* **366**, eaax4380 (2019).
107. Escolano, A. *et al.* Sequential Immunization Elicits Broadly Neutralizing Anti-HIV-1 Antibodies in Ig Knockin Mice. *Cell* **166**, 1445–1458.e12 (2016).

108. Ward, A. B. & Wilson, I. A. Innovations in structure-based antigen design and immune monitoring for next generation vaccines. *Current Opinion in Immunology* **65**, 50–56 (2020).
109. Jardine, J. G. *et al.* Priming a broadly neutralizing antibody response to HIV-1 using a germline-targeting immunogen. *Science* **349**, 156–161 (2015).
110. Huang, D. *et al.* B cells expressing authentic naive human VRC01-class BCRs can be recruited to germinal centers and affinity mature in multiple independent mouse models. *Proc Natl Acad Sci USA* **117**, 22920–22931 (2020).
111. Abbott, R. K. *et al.* Precursor Frequency and Affinity Determine B Cell Competitive Fitness in Germinal Centers, Tested with Germline-Targeting HIV Vaccine Immunogens. *Immunity* **48**, 133-146.e6 (2018).
112. Fact sheet: Understanding the results from IAVI G001 presented at HIV R4P // Virtual 2021. (2021).
113. Chen, X. *et al.* Vaccination induces maturation in a mouse model of diverse unmutated VRC01-class precursors to HIV-neutralizing antibodies with >50% breadth. *Immunity* **54**, 324-339.e8 (2021).
114. Medina-Ramírez, M. *et al.* Design and crystal structure of a native-like HIV-1 envelope trimer that engages multiple broadly neutralizing antibody precursors in vivo. *Journal of Experimental Medicine* **214**, 2573–2590 (2017).
115. McGuire, A. T. *et al.* Specifically modified Env immunogens activate B-cell precursors of broadly neutralizing HIV-1 antibodies in transgenic mice. *Nat Commun* **7**, 10618 (2016).

116. Parks, K. R. *et al.* Overcoming Steric Restrictions of VRC01 HIV-1 Neutralizing Antibodies through Immunization. *Cell Reports* **29**, 3060-3072.e7 (2019).
117. Lin, Y.-R. *et al.* HIV-1 VRC01 Germline-Targeting Immunogens Select Distinct Epitope-Specific B Cell Receptors. *Immunity* **53**, 840-851.e6 (2020).
118. Steichen, J. M. *et al.* HIV Vaccine Design to Target Germline Precursors of Glycan-Dependent Broadly Neutralizing Antibodies. *Immunity* **45**, 483–496 (2016).
119. Andrabi, R. *et al.* The Chimpanzee SIV Envelope Trimer: Structure and Deployment as an HIV Vaccine Template. *Cell Reports* **27**, 2426-2441.e6 (2019).
120. Xu, K. *et al.* Epitope-based vaccine design yields fusion peptide-directed antibodies that neutralize diverse strains of HIV-1. *Nat Med* **24**, 857–867 (2018).
121. Muster, T. *et al.* A conserved neutralizing epitope on gp41 of human immunodeficiency virus type 1. *J Virol* **67**, 6642–6647 (1993).
122. Dennison, S. M. *et al.* Stable Docking of Neutralizing Human Immunodeficiency Virus Type 1 gp41 Membrane-Proximal External Region Monoclonal Antibodies 2F5 and 4E10 Is Dependent on the Membrane Immersion Depth of Their Epitope Regions. *J Virol* **83**, 10211–10223 (2009).
123. Zhang, R. *et al.* Initiation of immune tolerance–controlled HIV gp41 neutralizing B cell lineages. *Sci. Transl. Med.* **8**, (2016).
124. Kong, R. *et al.* Antibody Lineages with Vaccine-Induced Antigen-Binding Hotspots Develop Broad HIV Neutralization. *Cell* **178**, 567-584.e19 (2019).
125. Bonsignori, M. *et al.* Antibody-virus co-evolution in HIV infection: paths for HIV vaccine development. *Immunol Rev* **275**, 145–160 (2017).

126. Saunders, K. O. *et al.* Targeted selection of HIV-specific antibody mutations by engineering B cell maturation. *Science* **366**, eaay7199 (2019).
127. Bonsignori, M. *et al.* Maturation Pathway from Germline to Broad HIV-1 Neutralizer of a CD4-Mimic Antibody. *Cell* **165**, 449–463 (2016).
128. Williams, W. B. *et al.* Initiation of HIV neutralizing B cell lineages with sequential envelope immunizations. *Nat Commun* **8**, 1732 (2017).
129. Saunders, K. O. *et al.* Vaccine Induction of Heterologous Tier 2 HIV-1 Neutralizing Antibodies in Animal Models. *Cell Reports* **21**, 3681–3690 (2017).
130. Goo, L., Chohan, V., Nduati, R. & Overbaugh, J. Early development of broadly neutralizing antibodies in HIV-1–infected infants. *Nat Med* **20**, 655–658 (2014).

*Chapter 2*RESTRICTION OF HIV-1 ESCAPE BY A HIGHLY BROAD AND  
POTENT NEUTRALIZING ANTIBODY

Schommers, P.\* , Gruell, H.\* , **Abernathy, M.E.\*** , Tran, M-K., Dings, A.S., Gristick, H.B., Barnes, C.O., Schoofs, T., Schlotz, M., Vanshylla, K., Kreer, C., Weiland, D., Holtick, U., Scheid, C., Valter, M.M, van Gils, M.J., Sanders, R.W., Vehreschild, J.J., Cornely, O.A., Lehmann, C., Fatkenheuer, G., Seaman, M.S., Bloom, J.D., Bjorkman, P.J., and Klein, F. Restriction of HIV-1 Escape by a Highly Broad and Potent Neutralizing Antibody. *Cell*, **180**, 1-19 (2020). doi: 10.1016/j.cell.2020.01.010

*\* Equal Contributions*

**Summary**

Broadly neutralizing antibodies (bNAbs) represent a promising approach to prevent and treat HIV-1 infection. However, viral escape through mutation of the HIV-1 envelope glycoprotein (Env) limits clinical applications. Here we describe 1-18, a new V<sub>H</sub>1-46-encoded CD4 binding site (CD4bs) bNAb with outstanding breadth (97%) and potency (GeoMean IC<sub>50</sub> = 0.048 µg/mL). Notably, 1-18 is not susceptible to typical CD4bs escape mutations and effectively overcomes HIV-1 resistance to other CD4bs bNAbs. Moreover, mutational antigenic profiling uncovered restricted pathways of HIV-1 escape. Of most promise for therapeutic use, even 1-18 alone fully suppressed viremia in HIV-1-infected humanized mice without selecting for resistant viral variants. A 2.5 Å cryo-EM structure of a 1-18–BG505SOSIP.664 Env complex revealed that these characteristics are likely facilitated by a heavy-chain insertion and increased inter-protomer contacts. The ability of 1-18 to effectively restrict HIV-1 escape pathways provides a new option to successfully prevent and treat HIV-1 infection.

## Introduction

Broadly neutralizing antibodies (bNAbs) targeting the HIV-1 envelope protein (Env) can prevent infection in animal models and are under investigation for passive immunization in clinical trials (Balazs et al., 2011; Gautam et al., 2016; Julg and Barouch, 2019; Moldt et al., 2012; Shingai et al., 2014). Moreover, bNAbs have been demonstrated to suppress viremia and delay viral rebound after interruption of antiretroviral therapy (ART) in HIV-1-infected individuals (Bar et al., 2016; Bar-On et al., 2018; Caskey et al., 2015, 2017; Lynch et al., 2015a; Mendoza et al., 2018; Scheid et al., 2016). Although these results highlight the significant clinical potential of bNAbs, pre-existing or *de novo* HIV-1 resistance cause treatment failure and can strongly limit bNAb applications in humans (Bar et al., 2016; Bar-On et al., 2018; Caskey et al., 2015, 2017; Lynch et al., 2015a; Mendoza et al., 2018; Scheid et al., 2016). Strategies to prevent and overcome viral escape are therefore critical to effectively implement bNAb-mediated approaches for HIV-1 prevention and therapy (Caskey et al., 2019; Gruell and Klein, 2018).

In recent years, potent bNAbs have been isolated from HIV-1-infected donors that target distinct vulnerable epitopes on the Env trimer. These epitopes include the CD4 binding site (CD4bs), the V1/V2 loop, the V3 loop glycan patch, the membrane-proximal external region (MPER), and the interface between the gp120 and gp41 subunits (Gama and Koup, 2018; Sok and Burton, 2018; Walker and Burton, 2018). Among these sites, the CD4bs is of particular interest because CD4 serves as the primary receptor for viral entry (Kwong et al., 1998; Maddon et al., 1986; Zhou et al., 2007).

Most potent CD4bs bNAbs are characterized by use of the immunoglobulin heavy-chain gene segment IGHV1-2\*02, high levels of somatic hypermutation, a five-residue complementarity-determining region 3 of the light chain (CDRL3), and mimicry of the CD4-Env interaction (West et al., 2012; Zhou et al., 2010, 2013, 2015). Named after the prototypical antibody, these antibodies are referred to as VRC01-class bNAbs (Wu et al., 2010). Additional members of this class include 3BNC117, NIH45-46, N49-P7, N6, and VRC07-523 (Huang et al., 2016a; Rudicell et al., 2014; Sajadi et al., 2018; Scheid et al.,

2011). Other bNAbs that mimic CD4 binding are derived from the VH1-46 gene segment. However, compared with VH1-2-derived bNAbs, the VH1-46 bNAbs reported to date have lower potencies and breadth, which limits their potential for clinical use (Bonsignori et al., 2016; Gao et al., 2014; Scheid et al., 2011). For example, CH235.12, one of the best VH1-46-derived CD4bs antibodies, is less broad and more than 10-fold less potent than the VRC01-class bNAb N6 when tested against a large panel of HIV-1 strains (Bonsignori et al., 2016).

Accordingly, all CD4bs bNAbs that have advanced into clinical testing are members of the VRC01 class (3BNC117, N6, VRC01, and VRC07-523) (Bar et al., 2016; Bar-On et al., 2018; Caskey et al., 2015, 2019; Cohen et al., 2018a; Crowell et al., 2019; Gaudinski et al., 2018, 2019; Gruell and Klein, 2018; Ledgerwood et al., 2015; Lynch et al., 2015a; Mayer et al., 2017; Mendoza et al., 2018; Riddler et al., 2018; Scheid et al., 2016). However, although escape from VRC01 has been associated with a reduction in viral fitness (Lynch et al., 2015b), the effects of VRC01-class monotherapy are only transient and associated with emergence of viral escape variants (Bar et al., 2016; Caskey et al., 2015; Horwitz et al., 2013; Klein et al., 2012; Lynch et al., 2015a; Scheid et al., 2016).

Here we describe bNAb 1-18, a VH1-46-derived CD4bs antibody that exceeds the potency and breadth of most classical VH1-46- and VH1-2-derived bNAbs. The structural basis of its high activity was revealed by a single-particle cryo-electron microscopy (cryo-EM) structure of a 1-18 Fab-BG505 SOSIP.664 Env trimer complex solved at 2.5 Å resolution. Of particular interest, compared with 3BNC117 and VRC01, the two most clinically advanced CD4bs bNAbs, 1-18 effectively restricts viral escape and maintains both neutralizing activity against VRC01-class escape variants and full viral suppression when tested in HIV-1<sub>YU2</sub>-infected humanized mice. Therefore, 1-18 is a highly promising candidate for antibody-mediated strategies to effectively treat and prevent HIV-1 infection.

## **Results**

### **Identification of Potent VH1-46-Derived bNAbs**

To identify individuals with elite HIV-1-neutralizing activity, we screened HIV-1-infected subjects. From each individual, purified serum or plasma immunoglobulin G (IgG) was tested for neutralizing activity in a TZM-bl cell assay against a multiclade screening panel of 12 HIV-1 pseudoviruses (deCamp et al., 2014; Sarzotti-Kelsoe et al., 2014; Figure 1A). We identified IDC561, a clade B-infected long-term non-progressor (Walker and Yu, 2013), as ranking among the top 1% of a cohort of 2,274 individuals (HIV-1-neutralizing activity at a geometric mean  $IC_{50}$  [50% inhibitory concentration] of 41.7  $\mu$ g IgG/mL; Figures 1A and S1A–S1C). To characterize the epitope specificity of the IgG response, we performed neutralization fingerprinting and detected VRC01-like activity (Doria-Rose et al., 2017; Figure S1D). However, virus obtained from IDC561 was sensitive to 3BNC117 and N6, suggesting that the HIV-1-neutralizing antibodies in IDC561 differ from VRC01-class antibodies (Figure S1E).

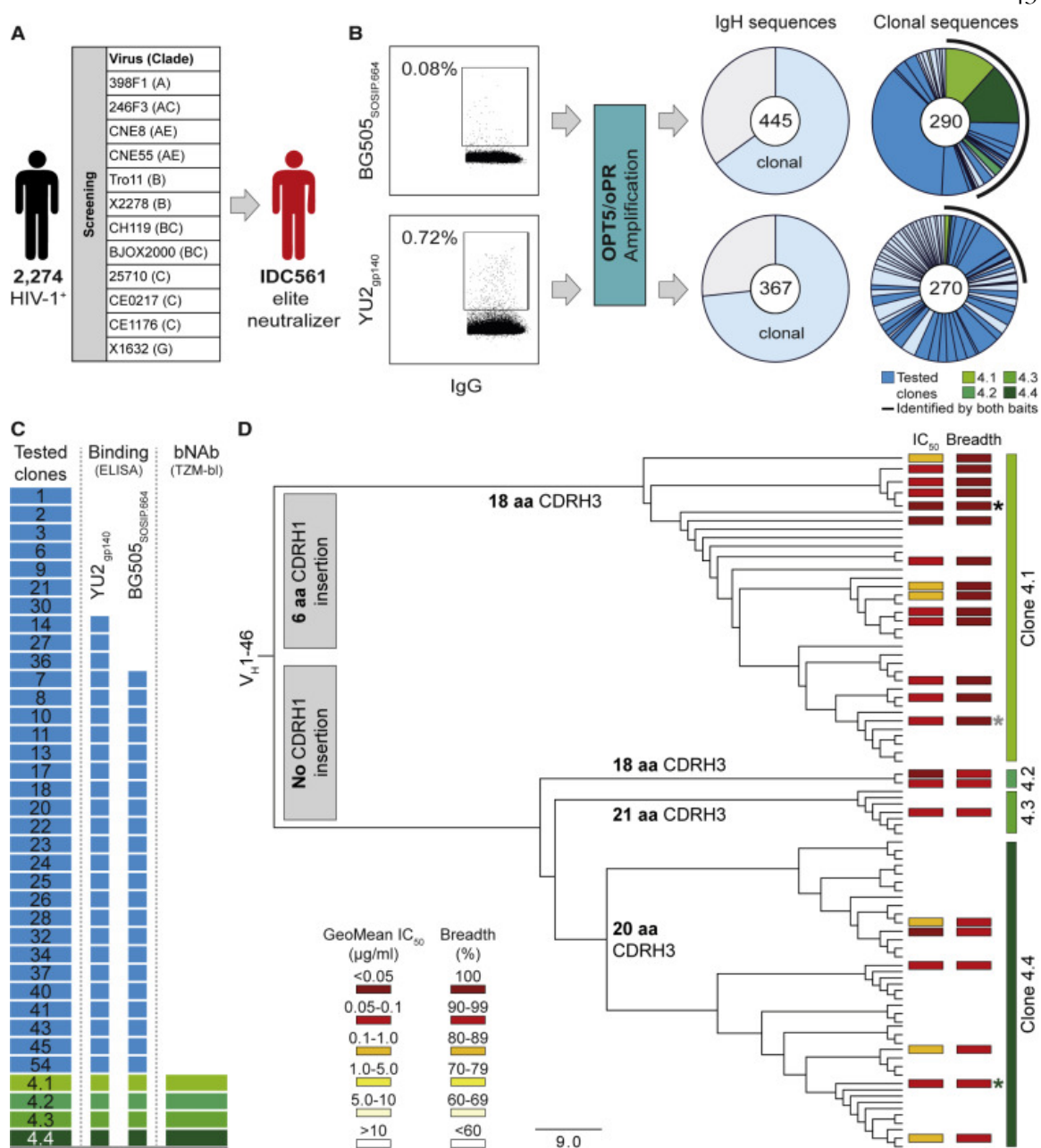


**Figure 1.** Identification of Broad and Potent Antibodies in Donor IDC561 (A) Identification of the elite neutralizer IDC561. (B) Single BG505<sub>SOSIP.664</sub>- (top) or YU2<sub>gp140</sub>-reactive (bottom) B cells were sorted, and antibody sequences were amplified using OPT5/oPR primers. Left pie charts showing the numbers of heavy-chain sequences identified, with clonal sequences indicated in light blue; right pie charts showing the numbers of clonal heavy-chain sequences, with individual clones represented by slices. Antibodies of members of clones in dark blue and green were tested. A black line indicates clones identified by both HIV-1 Env-sorting strategies. (C) Monoclonal antibodies were produced from members of

33 clones (clone 4 comprised subclones 4.1–4.4) (left). Boxes in the middle and on the right correspond to the left panel and show antibodies binding to YU2<sub>gp140</sub> or BG505<sub>SOSIP.664</sub> or neutralizing more than 90% of the global panel HIV-1 strains, respectively. (D) Phylogenetic tree of clone 4 members. Boxes indicate GeoMean IC<sub>50</sub> and breadth against the global panel. aa, amino acids. Black, gray, and green asterisks indicate antibodies 1-18, 1-55, and 2-12, respectively. See also Figures S1 and S2 and Tables S1, S2, S3, and S4.

To identify antibodies that accounted for the potent neutralizing activity of IDC561, we performed single-cell sorting of Env-reactive B cells that bound to native-like BG505 SOSIP.664 (Sanders et al., 2013; Sliepen et al., 2015) (0.08% of IgG+ B cells) or to YU2<sub>gp140</sub> (Scheid et al., 2009; Yang et al., 2000) (0.72% of IgG+ B cells) (Figure 1B). Using a new amplification strategy with primer sets optimized for precise detection of highly mutated IgG gene segments (OPT5/oPR; Kreer et al., 2019), we obtained and analyzed 812 IgG heavy-chain sequences (BG505 SOSIP.664, n = 445; YU2<sub>gp140</sub>, n = 367) (Figure 1B). Compared with the total IgG+ B cell reservoir of IDC561, Env-reactive B cells carried slightly longer CDRH3s (median length of 17 versus 16 amino acids, p < 0.001), had higher levels of somatic mutation (median VH gene nucleotide germline identity of 88.4% versus 95.3%, p < 0.001), and were enriched for the VH gene segments 1-46, 1-69, and 4-4 (Figures S1F–S1H). Among Env-reactive B cells, we identified 80 B cell clones with two or more members (Figure 1B).

Following production of monoclonal antibodies (Table S1), binding of both BG505 SOSIP.664 and YU2<sub>gp140</sub> was detected by ELISA for 70% of the tested antibody clones (Figure 1C; Table S2). The antibodies of most clones showed no or minimal neutralizing activity when analyzed against the 12-strain global panel, suggesting that they play a limited role in the serum activity of IDC561 (Figure 1C; Table S3A). In contrast, all tested members (23 antibodies) of B cell clone 4 (comprising subclones 4.1–4.4) neutralized 92%–100% of viruses in the screening panel with remarkable potency (GeoMean IC<sub>50</sub> of 0.032–0.198 µg/mL; Figure 1D; Table S3A). B cell clone 4, derived from the VH1-46 and VK3-20 gene segments, included members with different CDRH3 lengths of 18 (subclones 4.1 and 4.2), 20 (subclone 4.4), or 21 (subclone 4.3) amino acids (Table S1). Subclone 4.1 showed the highest breadth and potency and was characterized by a six-amino-acid CDRH1 insertion

that lengthened the CDRH1 from 8 to 14 amino acids (Figure 1D; Tables S1 and S4). We conclude that antibodies of the VH1-46-derived B cell clone 4 are highly potent, broadly active, and likely mediate the neutralizing serum activity of the elite neutralizer IDC561.

### **1-18: A CD4bs bNAb with Near-Universal Breadth and Outstanding Potency**

We selected antibodies 561\_01\_18 and 561\_01\_55 (hereafter referred to as 1-18 and 1-55), two representative members of clone 4.1, for further analyses (Figure 2A). Both antibodies are highly mutated, with heavy and light chain V gene germline nucleotide sequence identities of 68% and 78%–79%, respectively (Figure 2A; Table S4). Notably, the neutralizing activities of 1-18 and serum IgG of IDC561 against 42 pseudoviruses strongly correlated, suggesting that members of clone 4.1 are main contributors to the serum activity of IDC561 (Figure S2A). To determine binding of 1-18 and 1-55 to the BG505 SOSIP.664 trimer in the presence of other HIV-1 bNAbs, we performed competition ELISAs and detected interference with 3BNC117, N6, and VRC01 (Figures 2A; S2B). However, compared with these VRC01-class CD4bs antibodies, a different binding pattern was detected for 1-18 and 1-55 when tested by ELISA against several Env proteins. For example, whereas 3BNC117, N6, and VRC01 bound similarly to YU2<sub>gp120</sub>, YU2<sub>gp140</sub>, and BAL<sub>gp140</sub> and were reactive to the V1-V3 loop-deficient gp120 variant RSC3 (Wu et al., 2010), bNAbs 1-18 and 1-55 showed lower (YU2<sub>gp120</sub>, YU2<sub>gp140</sub>, and BAL<sub>gp140</sub>) or no (RSC3) binding to these proteins (Figure S2C). Therefore, 1-18 and 1-55 target the CD4bs but recognize this epitope differently than VRC01-class antibodies.

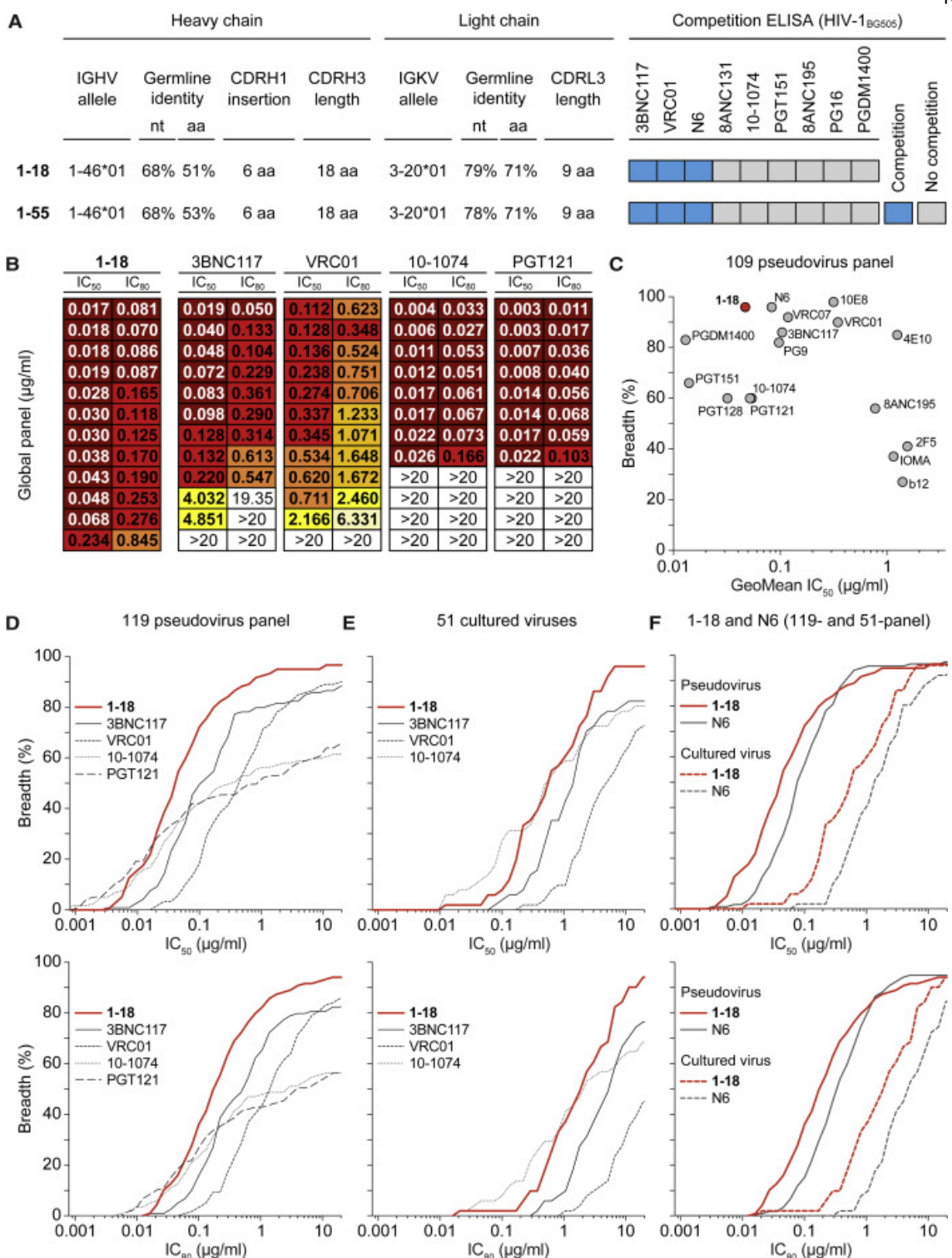


**Figure 2.** bNab 1-18 Demonstrates Highly Potent and Near-Pan HIV-1-Neutralizing Activity (A) Characteristics of antibodies 1-18 and 1-55. (B) Activity of 1-18 against the

global panel compared with bNAbs in advanced stages of clinical testing, individually sorted by increasing  $IC_{50}$  values for each bNAb. Data for 3BNC117, VRC01, 10-1074, and PGT121 were derived from CATNAP (Yoon et al., 2015). (C) Activity of 1-18 compared with a selection of bNAbs against an identical set of 109 pseudovirus strains (Yoon et al., 2015). For N6, neutralization data were determined in the same laboratory as for 1-18. (D) Activity against the 119-pseudovirus multiclade panel. Data for 3BNC117, VRC01, 10-1074, and PGT121 were derived from CATNAP (Yoon et al., 2015). (E) Activity against patient-derived bulk culture outgrowth virus. (F) Activity of 1-18 compared with N6 against the 119-pseudovirus multiclade panel and patient-derived bulk culture outgrowth viruses. In (D)–(F),  $IC_{50}$  values are shown at the top and  $IC_{80}$  values at the bottom. See also Figure S2 and Tables S3 and S5.

We next evaluated the neutralizing activity of 1-18 in detail. In comparison with four bNAbs in advanced stages of clinical investigation (3BNC117, VRC01, 10-1074, and PGT121), 1-18 demonstrated superior activity with high potency (GeoMean  $IC_{50}$  of 0.035  $\mu\text{g}/\text{mL}$ , GeoMean  $IC_{80}$  [80% inhibitory concentration] of 0.155  $\mu\text{g}/\text{mL}$ ) against all viruses of the 12-strain global screening panel (deCamp et al., 2014; Figure 2B; Table S3A). Although 1-18 competed with other CD4bs bNAbs for binding to BG505 SOSIP.664 by ELISA, no reduction in neutralizing activity was detected when 1-18 and 3BNC117 were combined (Figure S2D). To confirm the results of the screening panel, we evaluated the activity of 1-18 on extended pseudovirus panels. Overall, 1-18 ranked among the best bNAbs that are currently available (Figure 2C). When tested against a 119-strain multiclade panel, 1-18 showed highly potent activity (GeoMean  $IC_{50}$  of 0.048  $\mu\text{g}/\text{mL}$ , GeoMean  $IC_{80}$  of 0.183  $\mu\text{g}/\text{mL}$ ) with a breadth of 97% (Figure 2D; Table S5A). In addition, 1-18 demonstrated high potency (GeoMean  $IC_{50}$  of 0.074  $\mu\text{g}/\text{mL}$ , GeoMean  $IC_{80}$  of 0.279  $\mu\text{g}/\text{mL}$ ) and breadth (90%) when tested against a 100-strain clade C panel (Table S5B). Finally, we determined the activity of 1-18 against culture-derived primary HIV-1 strains that are generally more difficult to neutralize than pseudoviruses (Cohen et al., 2018b). Against viruses obtained from 51 HIV-1-infected individuals, 1-18 demonstrated higher breadth and/or potency (GeoMean  $IC_{50}$  of 0.56  $\mu\text{g}/\text{mL}$ , GeoMean  $IC_{80}$  of 1.57  $\mu\text{g}/\text{mL}$ , 96% breadth) than 3BNC117, VRC01, 10-1074, and PGDM1400 (Figure 2E; Table S5C) and was superior to the near-pan-neutralizing VH1-2-derived CD4bs bNAb N6 (Huang et al., 2016a; Figure 2F; Table S5C).

We conclude that 1-18 is a highly broad and potent VH1-46-derived antibody that rivals or exceeds the activity of CD4bs bNAbs described to date.

### **1-18 Targets the CD4bs and Regions of the Adjacent gp120 Protomer**

To characterize Env recognition by the 1-18 family of bNAbs, we solved cryo-EM structures of 1-18 and 1-55 Fabs in complex with soluble native-like Env trimers and the V3-targeting bNAb 10-1074 at resolutions of 2.5 Å (1-18 complexed with BG505 SOSIP.664) and 3.9 Å (1-55 complexed with RC1, a designed immunogen that is a derivative of BG505 SOSIP.664; Escolano et al., 2019) (Figures 3A and S3; Table S6). Notably, at 2.5 Å resolution, the 1-18 complex is the highest resolution view yet obtained of an HIV-1 Env trimer (Figure S3A; Table S6). Both complexes contained three 1-18 family Fabs and three 10-1074 Fabs interacting with three-fold symmetry with a SOSIP Env trimer. 1-18 and 1-55 recognized the CD4bs similarly to other VH1-46-derived bNAbs, including 8ANC131 and CH235.12 (Bonsignori et al., 2016; Zhou et al., 2015), with interactions encompassing contacts with the N276<sub>gp120</sub> and N197<sub>gp120</sub> glycans, the CD4bs loop via the CDRH2, the V5 loop via the CDRH2, and loop D via the CDRL3 (Figures 3A, 3B, S4A, and S4B). However, in addition, 1-18 contacts Env by residue F54<sub>HC</sub>, which is buried in the gp120 ‘Phe43 pocket’, and by residue R64<sub>HC</sub>, which makes a salt bridge with V5 residue D457<sub>gp120</sub> (Figure S4B). These interactions mimic analogous gp120 contacts made by CD4 residues F43<sub>CD4</sub> and K35<sub>CD4</sub>, respectively, and the VH1-2-derived bNAb N6 also buries an aromatic residue (Y54<sub>HC</sub>) in the ‘Phe43 pocket’ (Huang et al., 2016a; Kwong et al., 1998; Figure S4B).

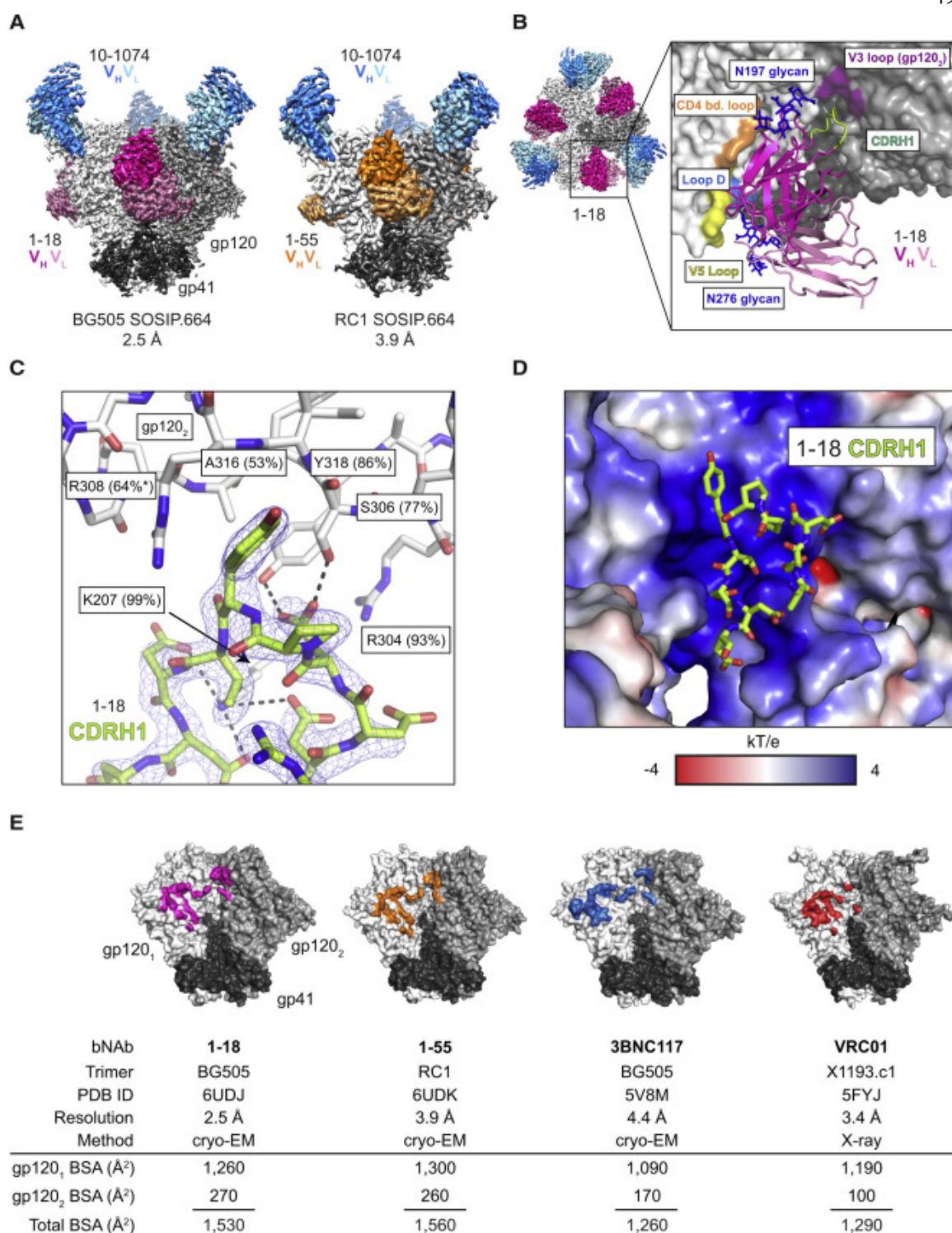


**Figure 3.** Cryo-EM Structures of 1-18 and 1-55 Fab Complexes with Env Trimers (A) EM densities for side views of Env trimers complexed with 1-18 or 1-55 Fabs and 10-1074 bNAb Fabs. 1-55 Fabs were based on sequence variants that contained primer-induced mutations

at the start and end of the V genes (total of 2 aa [V<sub>H</sub>] and 4 aa [V<sub>κ</sub>] mutations). (B) Top view of 1-18-BG505-10-1074 complex density. The inset shows a close up of the interactions between the 1-18 V<sub>H</sub>-V<sub>L</sub> domains (cartoon representation) and Env, with primary gp120 shown in light gray and secondary gp120 (gp120<sub>2</sub>) shown in dark gray. Protein regions that are contacted by 1-18 are shown as colored surfaces, and glycans are shown as sticks. (C) Close up of interactions of 1-18 CDRH1 residues with residues on secondary gp120. Hydrogen bonds and electrostatic contacts are shown as dotted lines. The percent conservation among Env sequences of gp120<sub>2</sub> residues contacted by CDRH1 is indicated in parentheses (West et al., 2013). \* denotes the conservation percentage in the 500 viruses that have residue 308. (D) Electrostatic surface representation of the Env region contacted by the 1-18 CDRH1. (E) Buried surface areas from CD4bs bNAb contacts on the primary (gp120<sub>1</sub>) and secondary (gp120<sub>2</sub>) protomers. Env trimer structures are SOSIP.664 versions of the indicated Env strains. See also Figures S3 and S4 and Table S6.

In addition to the canonical VH1-46 contacts, 1-18 contains a six-residue insertion in its CDRH1, resulting in a negatively charged <sup>25</sup>DDDPYTDDD<sup>33</sup> motif that interacts with the adjacent gp120 protomer (Figures 3B–3D). At the adjacent protomer, four Asp residues in the 1-18 CDRH1 (D25<sub>HC</sub>, D27<sub>HC</sub>, D31<sub>HC</sub>, and D32<sub>HC</sub>) plus T30<sub>HC</sub> form coordinated interactions around the highly conserved Env residue K207<sub>gp120</sub> (Figure 3C). In addition, the increased length of the 1-18 CDRH1 places Y29<sub>HC</sub> in a position to interact with residues in the V3 loop on the adjacent protomer (S306<sub>gp120</sub>, R308<sub>gp120</sub>, A316<sub>gp120</sub>, and Y318<sub>gp120</sub>) (Figure 3C). Although not all of the Asp residues in the 1-18 CDRH1 contact positively charged residues on gp120, the Asp-rich insertion may have been selected to carry an overall negative charge that is electrostatically attracted to the positively charged patch within the V3 loop on the adjacent protomer (Figure 3D), which could drive formation of an initial Env-antibody complex (Schreiber et al., 1996). Although other CD4bs bNAbs include Asp-containing insertions in either the CDRH1 or heavy-chain framework region 3 (FWRH3) that interact with the positively charged gp120 patch (Lee et al., 2017; Liu et al., 2019; Xu et al., 2018; Figure S4C), the number of Asp in the CDRH1 of 1-18 and the extent of their interaction to Env have not been described before. Notably, gp120 residues contacted by the 1-18 CDRH1 contribute to the CD4 and/or co-receptor binding sites (Liu et al., 2017; Rizzuto et al., 1998; Shaik et al., 2019), and most residues are highly conserved (Figure 3C). Demonstrating their importance for viral function, mutations in some of these residues have been shown to substantially reduce infectivity (de Taeye et al., 2015; Liu et al., 2017).

To evaluate the relevance of the CDRH1 insertion for the neutralizing activity of 1-18, we engineered 1-18Dins, a 1-18 variant lacking the insertion. When tested against the 12-strain global panel, 1-18 $\Delta$ ins showed significantly reduced potency compared with 1-18 (GeoMean IC<sub>50</sub> values of 0.114  $\mu$ g/mL [1-18 $\Delta$ ins] and 0.035  $\mu$ g/mL [1-18], respectively;  $p = 0.012$ ; Table S3B). In addition, we investigated antibody 561\_02\_12 (referred to as 2-12), a member of clone 4 that developed in individual IDC561 but does not have a CDRH1 insertion. Compared with 1-18, antibody 2-12 showed lower breadth on extended pseudovirus panels (119-strain multiclade panel: 1-18, 97% breadth; 2-12, 87% breadth; 100-strain clade C panel: 1-18, 90% breadth; 2-12, 74% breadth; Tables S5A and S5B). Analysis of the neutralization panel data (West et al., 2013) indicated reduced potency of 2-12 against viruses carrying H364<sub>gp120</sub> in the CD4 binding loop. In contrast, 1-18 is less affected by this variation, suggesting a higher tolerance for structural variations in this site.

Compared with the epitopes of the CD4bs bNAbs 3BNC117 and VRC01 (Lee et al., 2017; Stewart-Jones et al., 2016), 1-18 and 1-55 bury more surface area on both the primary gp120 epitope and the adjacent protomer, another potential mechanism for their increased breadth and potency (Chuang et al., 2019; Figure 3E). Finally, the slightly higher neutralizing activity of 1-18 compared with 1-55 might be explained by variations in glycan accommodation (Figure S4D). We conclude that 1-18 mediates exceptional HIV-1-neutralizing activity by an increase in buried surface on gp120, primarily through increased interprotomer contacts mediated by its unique CDRH1.

### **1-18 Is Not Affected by Typical VRC01-Class Escape Mutations**

To determine how known Env escape mutations affect the neutralizing activity of 1-18, we evaluated the sensitivity of HIV-1<sub>YU2</sub> pseudovirus variants. As expected, removal of potential N-linked glycosylation sites (PNGSs) in the V2 (N160<sub>gp120</sub>) and V3 (N301<sub>gp120</sub>, N332<sub>gp120</sub>) loops mediated resistance to the V1/V2-directed bNAbs PG16 and PDGM1400 and the V3-directed bNAbs 10-1074 and PGT128, respectively (Mouquet et al., 2012; Pejchal et al., 2011; Sok et al., 2014; Walker et al., 2009, 2011), but did not affect neutralization by 1-18 or other CD4bs bNAbs (Figure 4). Similarly, removal of a PNGS adjacent to the CD4bs

(N276<sub>gp120</sub>) reduced sensitivity to the gp120-gp41 interface bNAb 8ANC195 (Scharf et al., 2014) but had no effect on 1-18 (Figure 4).

		1-18	3BNC117	VRC01	N6	8ANC131	8ANC195	10-1074	PGT128	PGDM1400	PG16	
YU2 IC <sub>50</sub> (µg/ml)		0.019	0.029	0.107	0.047	0.256	0.491	0.232	0.080	0.387	0.125	
Site	Mutation	Fold-change IC <sub>50</sub> relative to YU2 wild type										
YU2 gp160 mutations	V2 loop	E102K	0.63	0.83	0.64	0.72	1.75	0.87	0.48	1.30	0.50	0.46
		N160K	0.47	0.38	0.54	0.36	0.54	0.41	0.39	0.75	>6.5	>20.0
		N160T	0.32	0.66	0.53	0.47	0.71	0.77	0.41	1.44	>6.5	>20.0
		T162I	0.84	0.62	0.50	0.72	0.93	0.97	0.38	0.64	>6.5	>20.0
		T162N	0.63	0.45	0.48	0.43	0.88	0.86	0.44	1.48	>6.5	>20.0
	Loop D	N276D	0.16	0.31	0.36	0.15	0.11	>5.1	0.40	1.80	0.67	1.67
		T278K	0.21	0.31	0.35	0.32	0.18	>5.1	1.45	1.43	1.03	1.29
		T278A	0.11	0.28	0.31	0.30	0.16	>5.1	0.83	1.45	1.12	1.39
		T278I	0.26	0.28	0.31	0.26	0.22	>5.1	1.34	1.29	1.31	1.42
		N279K	0.32	>86.2	>23.4	4.74	>9.8	1.86	0.53	0.38	0.59	0.73
		N279H	0.32	1.17	0.52	0.40	0.48	1.60	0.56	0.31	0.44	0.78
		N280Y	0.26	9.83	>23.4	0.32	>9.8	0.35	0.16	0.08	0.19	0.43
		A281T	2.21	>86.2	>23.4	15.17	>9.8	0.76	0.29	0.15	0.37	0.46
		T278I/A281T	1.84	>86.2	>23.4	>53.2	>9.8	>5.1	1.44	0.23	0.57	0.74
	V3 loop	N295S	0.68	0.62	0.61	0.77	0.73	0.97	0.38	1.35	0.57	1.18
		N301D	0.11	0.17	0.28	0.34	0.49	1.24	0.67	>31.3	0.76	2.05
		N332K	0.63	0.41	0.38	0.28	0.37	0.52	>10.8	>31.3	0.21	0.70
		N332S	0.53	0.52	0.41	0.60	1.14	0.88	9.89	>31.3	0.51	1.28
		N332Y	0.58	0.62	0.42	0.68	0.95	1.12	>10.8	>31.3	0.67	0.99
		S334D	0.58	0.79	1.32	0.81	1.25	0.74	>10.8	>31.3	0.41	1.10
		S334N	0.42	0.48	0.46	0.68	0.89	0.90	>10.8	>31.3	0.49	0.78
	CD4 bind. loop	G366E	0.37	0.41	0.41	0.34	0.27	0.75	0.45	0.14	0.55	0.54
		N365L	0.37	0.48	0.30	0.34	0.71	0.90	0.17	0.19	0.31	0.70
		I371M	0.58	0.62	0.63	0.64	0.68	0.94	0.75	0.34	0.60	0.73
	β23/ V5 loop /β24	E429K	0.47	1.10	1.02	0.83	0.62	0.98	0.72	0.50	1.48	1.00
		N448Q	1.58	0.83	0.65	1.00	1.41	1.92	0.67	1.26	1.21	1.26
		G458D	0.21	2.76	0.97	0.51	5.36	0.88	0.86	0.26	0.29	0.70
		G459D	0.32	0.72	0.70	0.19	0.59	0.64	0.41	0.28	0.40	0.54
		G471R	0.53	0.76	1.06	0.60	>9.8	0.82	0.44	0.14	0.74	0.60

**Figure 4.** 1-18 Overcomes Typical bNAb Escape Mutations *In Vitro*. The top row shows bNAb IC<sub>50</sub> values against the YU2 wild-type pseudovirus. The panels show the change in bNAb sensitivity (fold change of IC<sub>50</sub>) for YU2 pseudovirus mutants compared with the wild type.

VH-restricted CD4bs bNAbs typically interact with loop D residues N279<sub>gp120</sub> and/or N280<sub>gp120</sub>, and changes in these residues have been associated with viral rebound from CD4bs therapy (Diskin et al., 2013; Horwitz et al., 2013; Julg et al., 2017; Klein et al., 2012; Lynch et al., 2015a). When we tested HIV-1<sub>YU2</sub> variants with mutations at these residues, we observed reduced or abrogated sensitivity to VRC01-class bNAbs and to the VH1-46-

derived CD4bs bNAb 8ANC131 (Figure 4). In contrast, these mutations had no or only minimal effects on 1-18 (Figure 4). Maintained neutralizing activity against these variants might be mediated by increased contacts of 1-18's extended CDRH1 that formed compensatory interactions, alleviating the necessity for loop D contacts normally required by CD4bs antibodies. Additionally, the portion of 1-18's CDRL3 that contacts loop D utilizes a glycine-rich <sup>92</sup>GGT<sup>94</sup> motif rather than the <sup>92</sup>SST<sup>94</sup> motif in 8ANC131. This could accommodate mutations in loop D (N279K, N280Y) through increased flexibility. Finally, the 7 Å shift in CDRL2 location between 1-18 and 8ANC131 could allow greater accommodation of a glycan at N279<sub>gp120</sub> in two HIV-1<sub>YU2</sub> variants (A281T and T278I/A281T).

Mutations in the  $\beta$ 23 and  $\beta$ 24 strands surrounding the V5 loop (gp120 residues 451-471) were associated with viral resistance against 8ANC131 but were tolerated by 1-18 (Figure 4). V5 loop residue D457<sub>gp120</sub> interacts with 1-18 R64<sub>HC</sub>, a somatic mutation from the VH1-46 germline that is present in 1-18 but not in 8ANC131. We hypothesize that the R64<sub>HC</sub>-D457<sub>gp120</sub> salt bridge is a crucial interaction between 1-18 and gp120 that potentially allows it to tolerate common routes of Env escape within the V5 loop.

We conclude that 1-18 maintains full activity against viruses carrying mutations associated with viral resistance against other CD4bs bNAbs *in vitro*.

### **Mutational Antigenic Profiling of 1-18 Reveals Restricted HIV-1 Escape**

To identify potential pathways of viral escape from 1-18, we used mutational antigenic profiling with libraries of HIV-1<sub>BG505</sub> variants containing all single amino acid substitutions within the ecto and transmembrane domains of Env (Figure S5; Dingens et al., 2017; Haddox et al., 2018). In this assay, the effects of Env mutations on antibody resistance are quantitatively determined by deep sequencing of cells that become infected in the presence versus the absence of an antibody.

1-18 only selected escape mutants at a small number of residues, all of which were outside of the canonical CD4bs. In contrast to 3BNC117 and VRC01 (Dingens et al., 2019), we

observed no statistically significant escape from 1-18 in loop D and the CD4 binding loop (Figures 5A–5C and S5). Rather, 1-18-mediated selection was localized to the V3 loop and the stem of the V1/V2 loop of gp120 (Figure 5C). Among the four sites of significant escape, three residues (K207<sub>gp120</sub>, R304<sub>gp120</sub>, and Y318<sub>gp120</sub>) interact with the CDRH1 of 1-18 (Figure 5C). The fourth residue, C119<sub>gp120</sub>, generally forms a disulfide bond with C205<sub>gp120</sub> at the stem of the V1/V2 loop. Thus, mutations at residue C119<sub>gp120</sub> may reduce 1-18 accessibility to the highly conserved K207<sub>gp120</sub> by disordering the V1/V2 loop structure (Leonard et al., 1990; van Anken et al., 2008).

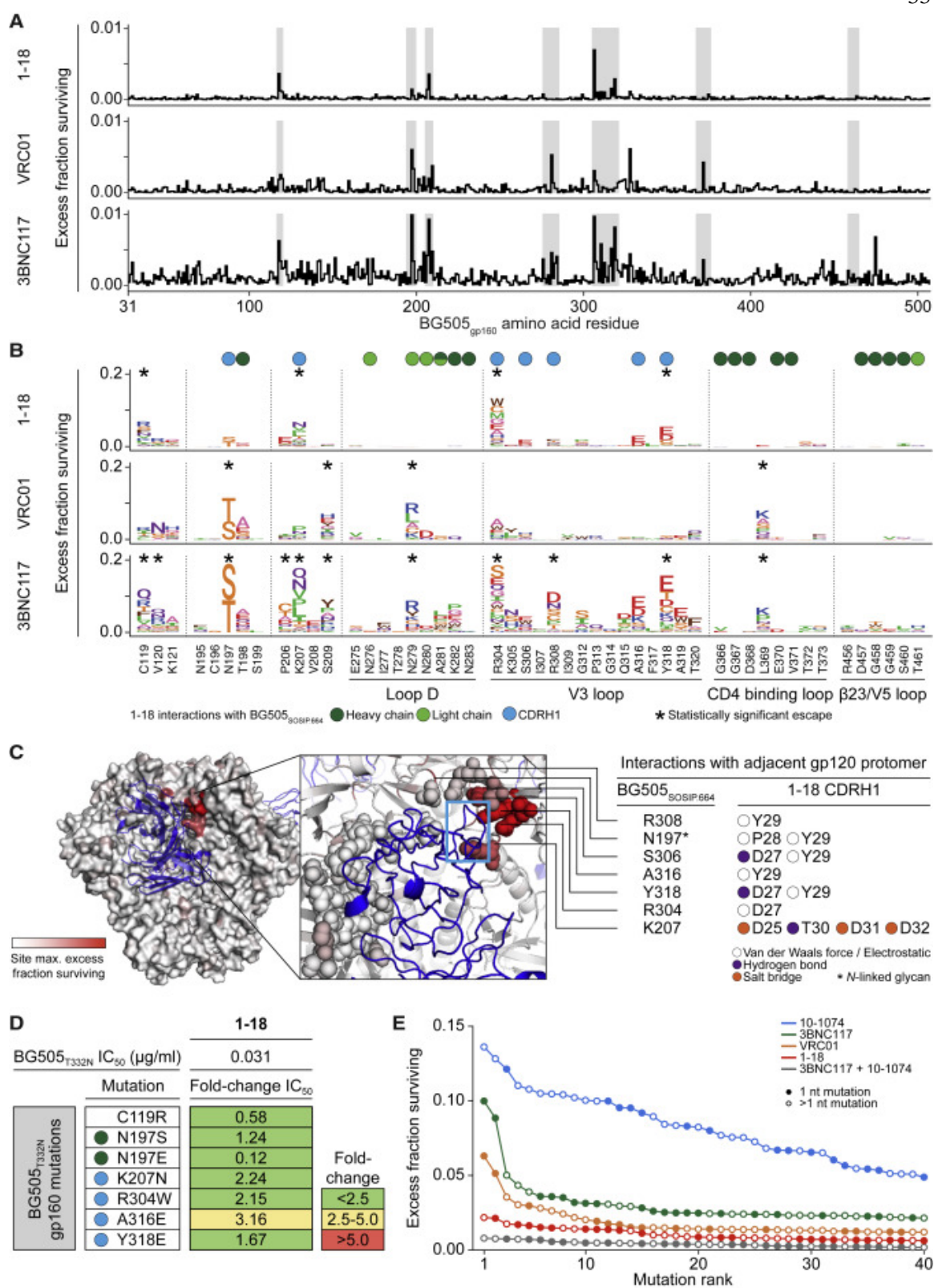


**Figure 5.** Restricted Pathways of Escape from 1-18 Identified by Mutational Antigenic Profiling (A) Line plots indicate the HIV-1<sub>BG505</sub> library excess fraction surviving antibody neutralization, averaged across all mutations at each site. Data for antibodies other than 1-18 in all panels are from Dingens et al. (2019). Regions in gray are detailed in (B). (B) HIV-1<sub>BG505</sub> escape profiles, with letter heights indicating the excess fraction surviving for each mutation. Circles indicate HIV-1<sub>BG505</sub> residues interacting with 1-18 (cryo-EM). Asterisks indicate residues with statistically significant antibody escape. (C) The BG505<sub>SOSIP.664</sub> trimer, colored according to the maximum excess fraction surviving 1-18 at each site, with 1-18 shown in blue. In the inset, structurally defined contacts are shown as spheres, and the CDRH1 is highlighted by the rectangle. Interactions of the CDRH1 with the adjacent gp120 protomer are indicated on the right. (D) The top row indicates IC<sub>50</sub> of 1-18 against the BG505<sub>T332N</sub> pseudovirus, and the panels show fold change in IC<sub>50</sub> for BG505<sub>T332N</sub> pseudovirus variants with mutations in the six residues showing the highest excess fraction surviving 1-18 neutralization. Circles indicate interactions as in (B). (E) Excess fraction surviving for the 40 mutations with the largest effect sizes for each antibody. Circles indicate the number of nucleotide changes required for the respective amino acid mutation. See also Figure S5.

Mutational antigenic profiling allows identification of the strongest escape mutations for each antibody (Figures 5A–5C and S5E). Importantly, although VRC01 escape mutations were associated with a 3- to more than 175-fold increase in the antibody IC<sub>50</sub> values for HIV-1<sub>BG505</sub> pseudovirus variants (Dingens et al., 2019), the effects were much less pronounced for potential 1-18 escape mutants (Figure 5D). When we evaluated HIV-1<sub>BG505</sub> pseudoviruses carrying single mutations at the six residues with the highest level of 1-18-mediated selection, the sensitivity to 1-18 was reduced by less than 2.3-fold for 5 of the 6 tested viruses (Figure 5D). The sixth virus, carrying an A316E mutation, showed a 3.2-fold decrease in sensitivity (IC<sub>50</sub> increased to 0.098 µg/mL) (Figure 5D). Therefore, all tested potential escape variants remained highly 1-18-sensitive when evaluated as pseudoviruses. To determine the ease of viral escape, we compared the effects of the 40 strongest mutations from antigenic profiling of 1-18 with those of VRC01, 3BNC117, 10-1074, or the combination of 3BNC117 and 10-1074 (Dingens et al., 2019). The levels of escape observed for 1-18 were lower than those for the single bNAbs and similar to the combination of 3BNC117 and 10-1074 (Figure 5E).

Overall, mutational antigenic profiling of 1-18 revealed a strong limitation of HIV-1<sub>BG505</sub> escape via single amino acid mutations, with no evidence of selection at the canonical CD4bs that is critical for resistance against VRC01-class bNAbs.

### **Full Suppression of Viremia by 1-18 Monotherapy *In Vivo***

To determine the antiviral activity of 1-18 *in vivo*, we used HIV-1<sub>YU2</sub>-infected humanized mice that can maintain stable viremia with a rate of HIV-1 diversification similar to what is observed in humans (Gruell and Klein, 2017; Ince et al., 2010; Klein et al., 2012; Zhang et al., 2002; Figure S6A).

Following a 1-mg loading dose of antibody administered subcutaneously (s.c.), we treated HIV-1<sub>YU2</sub>-infected mice (n = 6–10 per group) twice a week with s.c. injections of 0.5 mg per bNAb for 4–8 weeks (Figure 6A). Treatment with 3BNC117, VRC01, or the combination of both bNAbs resulted in mean viral load reductions of 0.5, 0.5, and 0.7 log<sub>10</sub> copies/mL, respectively. However, these effects were only transient, and viral rebound occurred within the first 2 weeks in most animals, indicating rapid viral escape (Figure 6A). Indeed, when plasma single genome sequencing (SGS) (Salazar-Gonzalez et al., 2008) was performed at week 4 after the start of treatment, 79 of 82 isolated viruses from 16 mice showed mutations in the VRC01 and 3BNC117 target sites in loop D and/or the  $\beta$ 23/ V5 loop regions of gp120 (Figures 6B and 7A; Tables S7A–S7C).

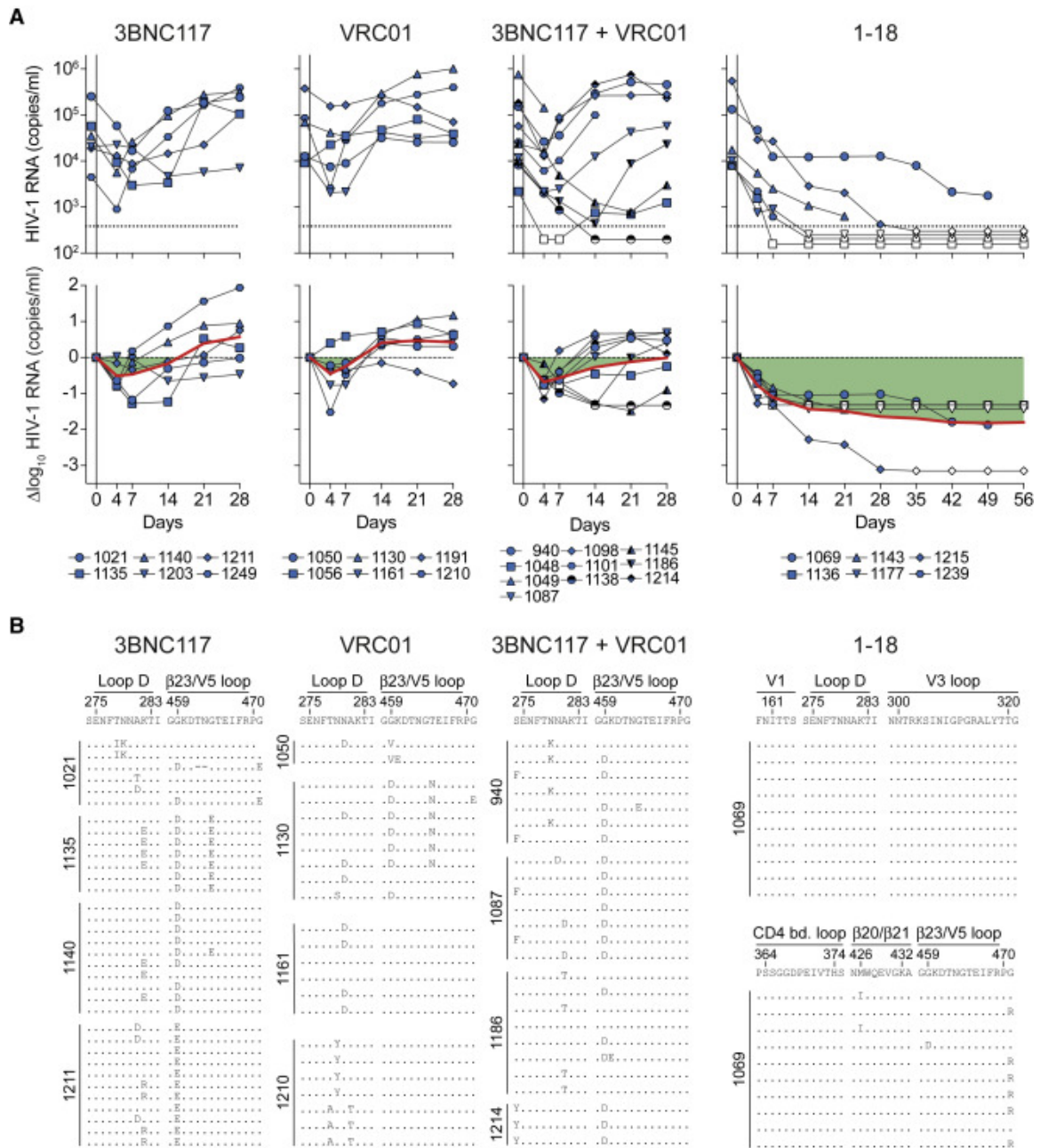


**Figure 6.** Full Suppression of Viremia by 1-18 Monotherapy *In Vivo* (A) HIV-1 RNA plasma copies (top) and  $\log_{10}$  viral load changes compared with baseline (day -1) (bottom). Dashed lines in the top panels indicate the quantitation limit of accuracy (384 copies/mL), and data points in white indicate viral loads of less than 384 copies/mL. Red lines show average  $\log_{10}$  viral load changes compared with baseline. (B) *Env* sequences obtained from day 28 plasma RNA of indicated mice by SGS. Letters indicate amino acid mutations compared with wild-type YU2 shown on top. Residues are numbered according to HIV-1<sub>HXB2</sub>. See also Figure S6 and Table S7.

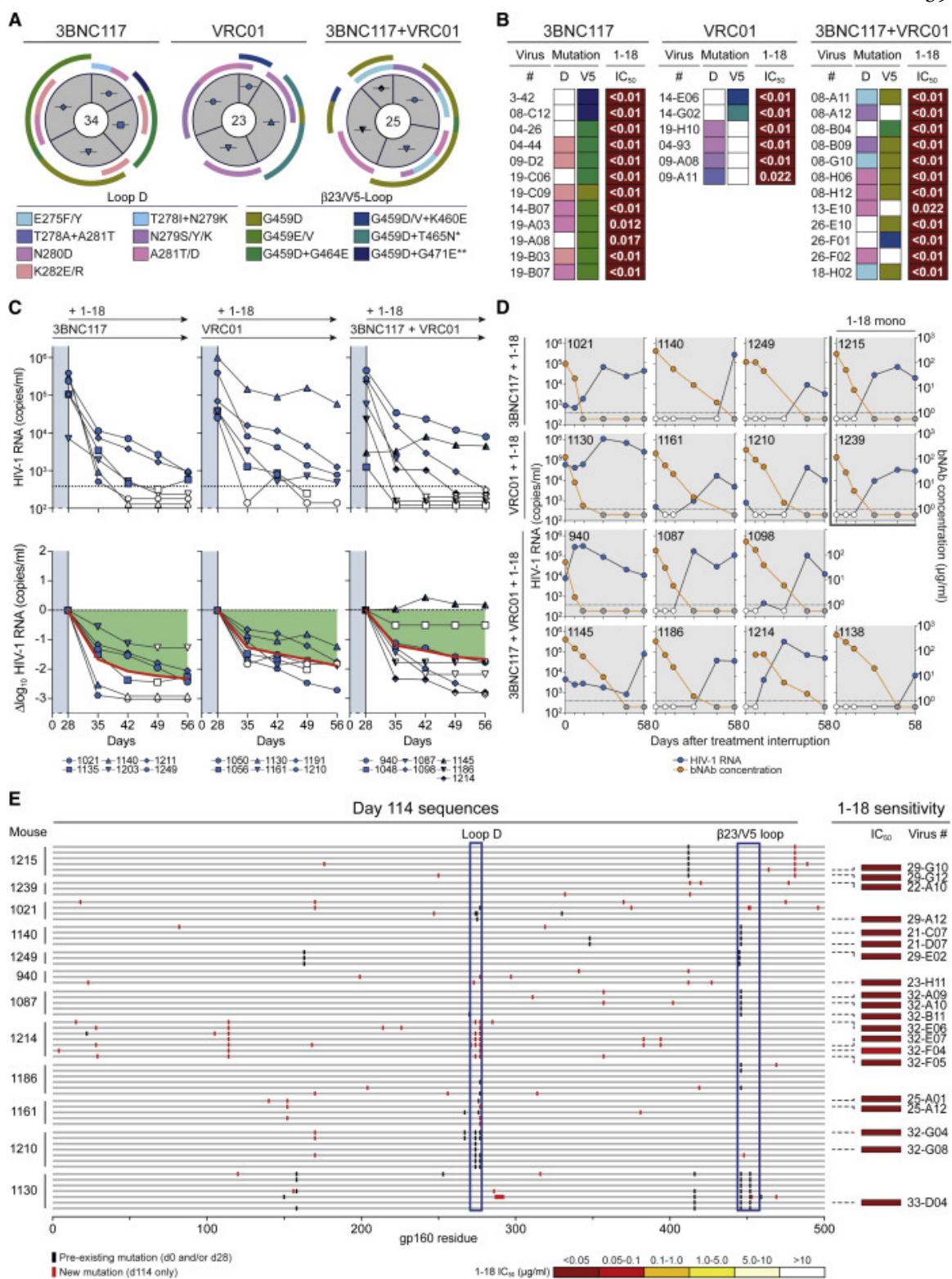


**Figure 7.** bNAb 1-18 Overcomes VRC01-Class Escape *In Vivo* (A) Pie charts indicate the number of plasma *env* sequences obtained from HIV-1<sub>YU2</sub>-infected humanized mice on day 28 of treatment with 3BNC117, VRC01, or 3BNC117+VRC01. Icons are as in Figure 6A. Outer bars indicate mutations in loop D and/or the  $\beta$ 23 strand/V5 loop. \*+ G471E mutation. \*\*+  $\Delta$ T462 &  $\Delta$ N463 mutations. (B) IC<sub>50</sub>s of 1-18 SGS-derived day 28 *env* sequence pseudoviruses with mutations as indicated in (A). (C) Addition of 1-18 treatment on day 28 to HIV-1<sub>YU2</sub>-infected humanized mice that showed viral rebound during 3BNC117, VRC01, or 3BNC117+VRC01 therapy (Figure 6A). The previous treatment regimen was continued. HIV-1 RNA plasma copies are shown at the top and log<sub>10</sub> viral load changes compared with baseline (day 28) at the bottom. Dashed lines in the top panels indicate the quantitation limit of accuracy (384 copies/mL), and data points in white indicate viral loads of less than 384 copies/mL. Red lines show average log<sub>10</sub> viral load changes compared with baseline (day 28). (D) HIV-1 RNA plasma copies (left y axis) and plasma bNAb levels determined by BG505<sub>SOSIP.664</sub>-ELISA (right y axis) after interruption of bNAb therapy on day 56 as indicated in (C). Only mice that could be followed for 58 days are included. Dashed lines indicate the HIV-1 RNA quantitation limit of accuracy (384 copies/mL). White circles show viral loads of less than 384 copies/mL, and gray circles indicate antibody levels of less than 1  $\mu$ g/mL. (E) Plasma SGS-derived *env* sequences obtained on day 114. Black bars indicate amino acid mutations compared with the YU2 wild-type found previously; red bars indicate mutations only found on day 114 within individual mice. Numbering is according to HIV-1<sub>YU2</sub>. Boxes indicate IC<sub>50</sub> values of 1-18 against the corresponding pseudoviruses (right). See also Table S7.

In contrast to the transient effects of 3BNC117 and VRC01, monotherapy of HIV-1<sub>YU2</sub>-infected humanized mice with 1-18 resulted in sustained viral suppression over a period of 8 weeks in all treated animals (average drop of 1.7 log<sub>10</sub> copies/mL; Figure 6A). Moreover, in all but one mouse, viremia dropped to levels below the level of quantitation (384 copies/mL) by day 35. From the one mouse (1069) that had quantifiable levels of viremia but was suppressed (drop of 1.9 log<sub>10</sub> copies/mL), we analyzed HIV-1 *env* sequences at week 4 (Figures 6A and 6B). We detected no recurrent mutations at contact residues of 1-18 or typical CD4bs bNAbs, and pseudoviruses derived from these sequences remained sensitive to 1-18 (Figure 6B; Table S7D). These results were confirmed in an independent repeat experiment for 1-18 as well as for 1-55, another member of clone 4.1 (Figure S6B). Although five of six 1-18-treated mice in this experiment were fully suppressed, one mouse (1730) continued to show high HIV-1 RNA copy numbers (Figure S6B). However, all *env* sequences obtained from this mouse carried large V4 loop deletions as well as early stop codons (Figure S6C). Thus, despite detectable rebound of viremia in 1 of 18 mice treated

with 1-18 or 1-55, no functional escape viruses were observed by SGS and evaluation of pseudoviruses.

Effective clinical application of bNAbs depends on favorable safety and pharmacokinetic profiles. Following a single injection of 1-18 or 1-55, their decline in serum of immunodeficient mice was slower compared with VRC01-class bNAbs and more similar to 10-1074, which has a longer half-life than 3BNC117 and VRC01 in humans (Bar-On et al., 2018; Caskey et al., 2015, 2017; Ledgerwood et al., 2015; Lynch et al., 2015a; Mendoza et al., 2018; Figure S6D). In addition, whereas some bNAbs demonstrate binding to self-antigens (Haynes et al., 2005), we found no indication for autoreactivity of 1-18 or 1-55 when tested against HEP-2 cells (Figure S6E).

In summary, we conclude that 1-18 has exceptional antiviral *in vivo* activity against HIV-1<sub>YU2</sub>. This activity is superior to the CD4bs antibodies 3BNC117 and VRC01, which are currently being evaluated in clinical trials. Importantly, single bNAb therapy with 1-18 is sufficient to effectively prevent development of viral escape variants that rapidly emerge during HIV-1<sub>YU2</sub> monotherapy with other bNAbs (Horwitz et al., 2013; Klein et al., 2012).

### **1-18 Overcomes VRC01-Class Escape Mutations *In Vivo***

To confirm that mutations occurring during 3BNC117 and/or VRC01 therapy conferred antibody resistance, we generated 30 pseudoviruses derived from day 28 *env* sequences of 11 VRC01-class-treated mice. We found 23 viral variants that were fully resistant to the administered antibodies ( $IC_{50} > 25 \mu\text{g/mL}$ ) or showed increased VRC01-class resistance ( $>5$ -fold increase in  $IC_{50}$  values). Notably, however, all of these pseudoviruses remained sensitive to 1-18 *in vitro* (Figure 7B; Table S7).

To determine whether 1-18 can overcome escape from VRC01-class bNAbs *in vivo*, we added bNAb 1-18 therapy (1-mg loading dose s.c. followed by 0.5 mg s.c. twice weekly) to 3BNC117- and/or VRC01-pretreated animals while continuing 3BNC117 and/or VRC01 administrations (Figure 7C). Despite circulating VRC01-class-resistant viral variants, 1-18 effectively reduced viremia and maintained viral suppression in 17 of 18 mice (Figure 7C).

Following interruption of bNAb therapy, viral rebound occurred in all fully suppressed mice when Env-reactive antibody plasma concentrations declined to a median of 0.1  $\mu\text{g/mL}$  (Figure 7D). To determine whether declining 1-18 levels resulted in selection of 1-18-resistant escape variants, we performed plasma SGS of rebound viruses 8 weeks after treatment interruption (day 114) (Figure 7E). Although we found novel mutations compared with day 0 and day 28 in 39 of 60 sequences from 12 mice, there was no recurrent pattern of mutations that developed after 1-18 therapy (Figure 7E). Indeed, all 20 sequences tested as pseudoviruses were demonstrated to be fully sensitive to 1-18 (Figure 7E; Table S7).

We conclude that bNAb 1-18 effectively overcomes VRC01-class resistance *in vivo* and maintains viral suppression without the development of 1-18-resistant HIV-1<sub>YU2</sub> variants.

## Discussion

Implementation of HIV-1-neutralizing antibodies for clinical practice requires antibodies with specific characteristics. These include safety, a favorable pharmacokinetic profile, and broad and highly potent neutralizing activity to effectively target the remarkable diversity of HIV-1 (Caskey et al., 2019). In addition, as for any drug against HIV-1, viral escape represents one of the biggest challenges for clinical application. This became evident when (1) single bNAbs were used for therapy and HIV-1 resistance developed within a few weeks (Bar et al., 2016; Caskey et al., 2015, 2017; Klein et al., 2012; Lynch et al., 2015a; Scheid et al., 2016), and (2) antibody combinations resulted in improved viral control by preventing early development of resistance (Bar-On et al., 2018; Klein et al., 2012; Mendoza et al., 2018). Therefore, restriction of HIV-1 escape will be an antibody-dependent feature of utmost importance for successful bNAb applications.

VRC01-class antibodies targeting the functionally critical CD4bs have broad and potent neutralizing activity but fail to prevent viral escape *in vivo* (Bar et al., 2016; Caskey et al., 2015; Horwitz et al., 2013; Klein et al., 2012; Lynch et al., 2015a; Scheid et al., 2016). Through a combination of functional *in vitro* mapping and *in vivo* therapy of HIV-1-infected humanized mice, we demonstrated that the VH1-46-derived CD4bs bNAb 1-18 effectively restricts development of HIV-1 resistance. Contrasting other CD4bs bNAbs, we did not

identify single amino acid mutations resulting in 1-18 resistance in two viral strains of different clades (BG505, clade A; YU2, clade B). Most importantly, in the setting of viral replication and diversification in HIV-1<sub>YU2</sub>-infected humanized mice, 1-18 monotherapy resulted in effective and sustained viral suppression. Notably, the *in vivo* activity of 1-18 was not affected by VRC01-class-resistant viral variants. Thus, despite mutations in up to two sites associated with escape from CD4bs antibodies, 1-18 effectively suppressed viremia and restricted the development of additional escape mutations.

In our cryo-EM analysis of a 1-18-BG505 complex, the highest-resolution HIV-1 Env trimer structure obtained to date (2.5 Å), the details of 1-18 recognition of Env were determined. The structure demonstrated that 1-18 combines favorable features found in potent VH1-2 bNAbs that likely contribute to its exceptional potency and breadth. These characteristics include (1) an aromatic residue that mimics residue Phe43 of CD4 to target the ‘Phe43<sub>gp120</sub> pocket’, as seen in bNAb N6 (Huang et al., 2016a); (2) contacts with the adjacent gp120 protomer, as seen for bNAb 3BNC117 (Lee et al., 2017; Lyumkis et al., 2013) but with increased buried surface area (via its six-residue insertion in CDRH1); and (3) a larger buried surface area on gp120 than other VH1-2 bNAbs: 1,530 Å<sup>2</sup> compared with 1,260 Å<sup>2</sup> (VRC01) and 1,290 Å<sup>2</sup> (3BNC117). Finally, 1-18’s unique mode of binding enables it to make additional contacts with conserved residues on gp120 not found in other CD4bs bNAbs, allowing 1-18 to rely less on classical CD4bs bNAb contacts and making viral escape more difficult. These characteristics may explain 1-18’s exceptional potency, breadth, and resistance to viral escape. Notably, functional antigenic mapping demonstrated that 1-18-mediated selection was focused on contact residues within the CDRH1. Moreover, the lack of the CDRH1 insertion in antibodies 1-18 $\Delta$ ins and 2-12 was associated with reduced neutralizing activity compared with 1-18.

Despite the remarkable neutralization breadth of 1-18 (covering 256 of 271 evaluated primary viruses and pseudoviruses), a small number of viruses was found to be 1-18 resistant. However, sequence analysis (West et al., 2013) did not identify single residues that were associated with 1-18 resistance. In addition, we analyzed viruses from individual IDC561,

from whom 1-18 was identified. Although viremia was controlled in the absence of ART for more than 15 years, it was detectable by the time of 1-18 isolation. Indeed, viruses obtained at this time showed resistance against 1-18 and clonal members (Figure S7). Remarkably, however, their CD4bs sequences presented with highly infrequent amino acid residues (Figure S7).

For example, among 2,351 clade B *env* sequences in the Los Alamos HIV Sequence Database, only 0.8% carried a glycine at the loop D residue 281<sub>gp120</sub>, and not a single virus had a glutamic acid at position 474<sub>gp120</sub> (Figure S7). Similarly, uncommon amino acids were found in other loop D (282<sub>gp120</sub>) and V5 loop (471<sub>gp120</sub>) positions as well as at residue 208<sub>gp120</sub>, which neighbors K207<sub>gp120</sub> that strongly interacts with the CDRH1 of 1-18 (Figure S7). Taking the results from profiling escape pathways *in vitro* together with the lack of viral escape in humanized mouse experiments, the occurrence of multiple uncommon amino acid residues in 1-18-resistant viruses suggests a restricted escape pathway from 1-18 that may require accumulation of multiple rare mutations.

Current strategies to combine bNAbs are based on the use of antibodies targeting non-overlapping epitopes (Bar-On et al., 2018; Barouch et al., 2013; Huang et al., 2016b; Klein et al., 2012; Mendoza et al., 2018; Shingai et al., 2013; Xu et al., 2017). To this end, the combination of 1-18 with bNAbs targeting other epitopes (e.g., the MPER antibody DH511.2\_K3, which neutralizes 100% of tested clade C viruses; Williams et al., 2017) may be a promising option. Because the most potent known CD4bs bNAbs are of the VRC01-class, synergistic effects by combinations of these antibodies are not expected. However, given their different binding, neutralization, and escape patterns, a combination of 1-18 with VRC01-class CD4bs bNAbs may be highly beneficial. The capacity of 1-18 to overcome VRC01-class escape mutations *in vivo* as well as a calculated breadth of more than 99% when 1-18 is combined with VRC01-class bNAbs (e.g., N6 or 3BNC117) offers new possibilities of bNAb combinations, such as a dual anti-CD4bs therapy. Finally, CD4bs bNAbs have been demonstrated to induce escape variants with reduced viral fitness (Lynch et al., 2015b; Otsuka et al., 2018; Sather et al., 2012). Applying double CD4bs-targeting

pressure may force the virus to more extensively mutate this functionally critical epitope and, therefore, result in impaired viral variants and prolonged viral control.

In summary, by combining outstanding neutralizing activity and a high barrier for viral escape, 1-18 provides a new option for highly effective treatment and prevention of HIV-1 infection.

## **Methods**

### Human Subjects

Blood and leukapheresis samples were obtained under protocols approved by the Institutional Review Board of the University of Cologne (protocols 13-364 and 16-054) and the local IRBs. All participants provided written informed consent. Participants of the neutralization screening cohort are recruited at hospitals and/or private practices in Germany (Cologne, Essen, and Frankfurt), Cameroon (Yaoundé), Nepal (Kathmandu), and Tanzania (Mbeya). At the time of leukapheresis, IDC561 was a 48-year-old male who was diagnosed with HIV-1 infection 21 years earlier. He was recruited at the University Hospital Cologne. PBMCs for bulk viral outgrowth cultures were obtained from individuals recruited in Germany (Cologne).

### Mouse Models

NOD.Cg-Rag1<sup>tm1mom</sup>Il2rg<sup>tm1Wjl</sup>/SzJ (NRG) mice were purchased at The Jackson Laboratory and bred and maintained at the Decentralized Animal Husbandry Network (Dezentrales Tierhaltungsnetzwerk) of the University of Cologne under specific pathogen-free (SPF) conditions with 12-hour light/dark cycles. For breeding purposes, mice were provided with ssniff 1124 breeding feed; for experimental purposes, mice were provided with ssniff 1543 maintenance feed. Humanized mice were generated as previously described with modifications (Klein et al., 2012). In brief, human CD34<sup>+</sup> hematopoietic stem cells were isolated from cord blood and perfused placental tissues using CD34 microbeads (Miltenyi Biotec). Collection of cord blood and placental tissues was conducted under a protocol approved by the Institutional Review Board of the University of Cologne (16-110), and all

donors provided written informed consent. NRG mice were sublethally irradiated within 5 days of birth and intrahepatically injected with purified human CD34<sup>+</sup> stem cells 4 to 6 hours later. Success of humanization was determined approximately 12 weeks later by FACS analysis of blood for human PBMCs. All mouse experiments were authorized by the State Agency for Nature, Environmental Protection, and Consumer Protection North Rhine-Westphalia (LANUV).

### Cell Lines

HEK293T cells (American Type Culture Collection) were maintained at 37°C and 5% CO<sub>2</sub> in Dulbecco's Modified Eagle Medium (DMEM, Thermo Fisher) supplemented with 10% fetal bovine serum (FBS, Sigma-Aldrich), 1 mM sodium pyruvate, 2 mM L-glutamine, and 1x antibiotic-antimycotic (all from Thermo Fisher). TZM-bl cells (Platt et al., 1998) were maintained at 37°C in 5% CO<sub>2</sub> in DMEM supplemented with 10% FBS, 1 mM sodium pyruvate, 2 mM L-glutamine, 50 µg/ml gentamicin (Merck), and 25 mM HEPES (Millipore). 293-6E cells (National Research Council of Canada) were maintained at 37°C and 6% CO<sub>2</sub> in FreeStyle Expression Medium (Thermo Fisher) and kept under constant shaking at 90-120 rpm. Expi293 cells (Thermo Fisher) were maintained at 37°C and 8% CO<sub>2</sub> in Expi293 Expression medium (Thermo Fisher) and kept under constant shaking at 130 rpm. CHO cells were maintained at 37°C and 5% CO<sub>2</sub> in ProCHO-5 media (Lonza) supplemented with 0.1 M HEPES, 1x GlutaMAX, 1x MEM NEAA, 1 mM sodium pyruvate, and 0.5 mg/ml hygromycin B (all from Thermo Fisher). SupT1-R5 cells (Didigu et al., 2014) were maintained at 37°C and 5% CO<sub>2</sub> in RPMI 1640 supplemented with 300 mg/l L-glutamine (Thermo Fisher), 10% FBS (Sigma-Aldrich), and 1% penicillin/streptomycin (Thermo Fisher). The sex of HEK293T, TZM-bl, 293-6E, Expi293, and CHO cell lines is female, and the sex of SupT1-R5 cells is male. Cell lines were not specifically authenticated.

### Clinical Samples

Peripheral blood mononuclear cells (PBMCs) were isolated by density-gradient centrifugation and stored at  $-150^{\circ}\text{C}$  in 90% FBS and 10% DMSO (Sigma-Aldrich) until further use. Plasma and serum samples were stored at  $-80^{\circ}\text{C}$  until further use.

### Serum and Plasma IgG Isolation

Serum and plasma samples were heat-inactivated ( $56^{\circ}\text{C}$  for 40 min) and incubated with Protein G Sepharose (GE Life Sciences) overnight at  $4^{\circ}\text{C}$ . IgGs were eluted from Protein G in chromatography columns using 0.1 M glycine (pH = 3.0) and buffered in 1 M Tris (pH = 8.0). Subsequently, buffer exchange to PBS and antibody concentration was performed using Amicon 30 kDa spin membranes (Millipore). Purified IgGs were stored at  $4^{\circ}\text{C}$  until further use.

### Single Cell Sort

B cells were isolated from PBMCs using the Pan B Cell Isolation Kit, B Cell Isolation Kit II, or IgG<sup>+</sup> Memory B Cell Isolation Kit (Miltenyi Biotec). Isolated cells were labeled with anti-human CD19-AF700 (BD), anti-human IgG-APC (BD), DAPI (Thermo Fisher), and the respective HIV-1 Env bait for 30 minutes on ice. BG505<sub>SOSIP.664</sub>-GFP or biotinylated YU2<sub>gp140</sub> that was labeled with Streptavidin-PE (BD) were used as HIV-1 Env baits. Env-reactive CD19<sup>+</sup>IgG<sup>+</sup>DAPI<sup>-</sup> single cells were sorted into 96-well plates containing 4  $\mu\text{l}$  of lysis buffer (0.5x PBS, 10 mM DTT (Thermo Fisher), 2 U/ $\mu\text{l}$  RNasin (Promega), and 1 U/ $\mu\text{l}$  RNaseOUT (Thermo Fisher)) per well using a BD FACSAria Fusion. Plates were stored at  $-80^{\circ}\text{C}$  until further use.

### Single Cell cDNA Synthesis and PCR

Sorted cells were incubated with 0.75  $\mu\text{l}$  Random Hexamer Primer (Thermo Fisher), 0.5  $\mu\text{l}$  NP-40 (Thermo Fisher), and 5.6  $\mu\text{l}$  RNase-free H<sub>2</sub>O for 1 min at  $65^{\circ}\text{C}$ . Subsequently, 3  $\mu\text{l}$  of 5x RT Buffer (Thermo Fisher), 0.5  $\mu\text{l}$  dNTPs mix (25 mM, Thermo Fisher), 1  $\mu\text{l}$  DTT (100 mM, Sigma Aldrich), 2.05  $\mu\text{l}$  of RNase-free H<sub>2</sub>O, 0.1  $\mu\text{l}$  RNasin (40 U/ $\mu\text{l}$ , Promega), 0.1  $\mu\text{l}$  RNaseOUT (40 U/ $\mu\text{l}$ , Promega), and 0.25  $\mu\text{l}$  Superscript IV (200 U/ $\mu\text{l}$ , Thermo Fisher)

were added and samples were incubated at 42°C for 10 min, 25°C for 10 min, 50°C for 10 min, and 94°C for 5 min. Antibody sequences for single cell analysis were amplified by semi-nested PCRs using Platinum Taq DNA Polymerase or Platinum Taq Green Hot Start DNA Polymerase (Thermo Fisher) and previously described primers, including the novel OPT5/oPR-primer set optimized for detection of highly mutated IgG sequences (Kreer et al., 2019), using the OPT5/oPR-primer mix and CG\_RT 5'-AGGTGTGCACGCCGCTGGTC (Ozawa et al., 2006) for the 1<sup>st</sup> PCR, and the OPT5/oPR-primer mix and IgG\_Internal RT 5'-GTTCGGGGAAGTAGTCCTTGAC (Tiller et al., 2008) for the 2<sup>nd</sup> PCR. First-round PCR was run at 94°C for 2 min; followed by 50 cycles of 94°C for 30 s, 55°C for 30 s, and 72°C for 55 s. Second-round PCR was run at 94°C for 2 min; followed by 50 cycles of 94°C for 30 s, 55°C for 30 s, and 72°C for 45 s. Second-round PCR products were sequenced by Sanger sequencing and used for further sequence analyses.

#### Antibody Sequence Analysis

Sequences with a mean Phred score  $\geq 28$  and a minimal length of 240 nucleotides were annotated with IgBLAST (Ye et al., 2013) and trimmed from framework region (FWR) 1 of the variable region to the end of the J gene. Base calls with a Phred score  $< 16$  were masked and sequences with  $> 15$  masked nucleotides, frameshifts, or stop codons were excluded from further analyses. To analyze the sequences for potential clonalities, all productive heavy chain sequences were grouped by identical V genes and the pairwise Levenshtein distance of their CDRH3s was determined. Individual sequences were grouped into clones when they shared the same V gene and had a minimal CDRH3 identity of 75%. After 10 rounds with a randomized input of sequences, the result that yielded the lowest number of unassigned (non-clonal) sequences was selected for further analyses. All clones were re-validated manually by the investigators in order to identify shared mutations. Sequences that were initially assigned to different clones but shared the same VDJ genes and amino acid and/or silent nucleotide mutations were subsequently grouped into subclones. Nucleotide sequence identity to germline was calculated using IgBLAST. The maximum-likelihood phylogenetic tree in Figure 1D was generated using nucleotide sequences of heavy-chain V genes (FWRH1-FWRH3) of subclones 4.1, 4.2, 4.3, and 4.4 ( $n = 86$  sequences) and of the IGHV1-

46\*01 *Homo sapiens* allele (GenBank X92343.1). All sequences were aligned using ClustalW (Geneious R10; cost matrix: IUB; gap open cost: 15; gap extend cost: 6.66) and the maximum-likelihood phylogenetic tree was calculated using PhyML with 1,000 bootstrap replicates (Guindon et al., 2010) (substitution model: general time reversible [GTR]; Geneious R10). The best-scoring tree was then rooted to IGHV1-46\*01.

### Antibody Cloning and Production

For cloning of single cell-derived antibodies, the 1<sup>st</sup> PCR product of single cell-PCR was used as template and amplified using Q5 Hot Start High Fidelity DNA Polymerase (New England Biolabs) and specific forward and reverse primers that resembled the respective nucleotide sequence of the V- and J-regions (Tiller et al., 2008) with expression vector overhangs for subsequent sequence and ligation independent cloning (SLIC). PCR was run at 98°C for 30 s; 35 cycles of 98°C for 10 s, 65°C for 30 s, and 72°C for 30 s; and 72°C for 2 min. 561\_01\_18\_ΔINS was generated by cloning a synthesized (Eurofins Genomics) heavy-chain variable region DNA fragment of 1-18 lacking the CDRH1 insertion (<sup>28</sup>PYTDDD<sup>33</sup>). PCR products or synthesized DNA fragments were cloned into human antibody expression vectors (IgG1, kappa, or lambda chain) by SLIC assembly as previously described (von Boehmer et al., 2016). Antibodies were produced in 293-6E cells (National Research Council Canada) by transfection using 25 kDa branched polyethylenimine (PEI) (Sigma-Aldrich). Cells were maintained at 37°C and 6% CO<sub>2</sub> in FreeStyle 293 Expression Medium (Thermo Fisher) and 0.2% penicillin/streptomycin (Thermo Fisher). 5-7 days after transfection, culture supernatants were harvested, filtered, and incubated with Protein G Sepharose (GE Life Sciences) overnight at 4°C. Antibodies were eluted from chromatography columns using 0.1 M glycine (pH = 3.0) and buffered in 1 M Tris (pH = 8.0). Subsequent buffer exchange to PBS and antibody concentration was performed using Amicon 30 kDa spin membranes (Millipore). Antibodies were filter-sterilized using Ultrafree-CL or Ultrafree-MC 0.22 μm membranes (Millipore) and stored at 4°C.

### Pseudovirus Production

Pseudoviruses for the 12-strain global screening panel and f61 finger printing panel were produced in HEK293T cells by co-transfection with pSG3ΔEnv plasmid as described previously (Doria-Rose et al., 2017, Hraber et al., 2017, Sarzotti-Kelsoe et al., 2014, Seaman et al., 2010). Single genome sequencing (SGS)-derived pseudoviruses were generated by co-transfection of SGS-derived CMV promoter-Env products and pSG3ΔEnv as previously described (Kirchherr et al., 2007). For sequences obtained from mice, *env/rev* cassettes were amplified from the first-round SGS PCR product using primers env1Atopo 5'-CACCGGCTTAGGCATCTCCTATGGCAGGAAGAA and envB3in 5'-CACCTTAGGCATCTCCTATGGCAGGAAGAAG. Pseudoviruses were only produced from sequences containing no ambiguities. For patient-derived sequences, *env/rev* cassettes were amplified from the first-round SGS product using primers env1Atopo and Rev19 5'-ACTTTTGGACCACTTGCCACCCAT. CMV promoter and *env/rev* overlap PCR was performed using primers CMVenv 5'-AGTAATCAATTACGGGGTCATTAGTTCAT and Rev19. Mouse-derived sequences were amplified using the Platinum Taq High Fidelity Polymerase (Thermo Fisher), patient-derived sequences using the Phusion Hot Start Flex Polymerase (New England Biolabs).

### Neutralization Assays

Neutralization assays were performed as previously described (Sarzotti-Kelsoe et al., 2014). In brief, pseudoviruses and dilution series of antibodies or purified IgG were mixed and co-incubated at 37°C for 1 h, followed by the addition of TZM-bl cells at a final concentration of 10<sup>4</sup> cells per well on a 96-well plate in 250 µl medium supplemented with DEAE-dextran at a final concentration of 10 µg/ml. Following a 2-day incubation at 37°C and 5% CO<sub>2</sub>, 150 µl of culture supernatant was removed and 100 µl luciferase assay reagent was added. After a 2 min incubation, 150 µl of lysate was transferred to a black microtiter assay plate and luminescence was determined using a luminometer. After subtracting background relative luminescence units (RLUs) of non-infected TZM-bl cells, 50% and 80% inhibitory concentrations (IC<sub>50</sub>s and IC<sub>80</sub>s) were determined as the antibody/IgG concentrations resulting in a 50%/80% RLU reduction compared to untreated virus control wells. Murine leukemia virus (MuLV)-pseudotyped virus was used to determine unspecific activity. Initial

screening of isolated antibody clonal members was performed using a single dilution series per antibody. Antibodies or purified serum IgG in all further neutralization assays were tested in duplicates. For screening assays, assays against culture-derived viruses, assays of pseudovirus mutant variants, and assays of IDC561-derived pseudoviruses, bioluminescence was determined after adding a luciferin/lysis-buffer (10 mM MgCl<sub>2</sub>, 0.3 mM ATP, 0.5 mM Coenzyme A, 17 mM IGEPAL (all Sigma-Aldrich), and 1 mM D-Luciferin (GoldBio) in Tris-HCL). For assays against the 119-pseudovirus panel, the 100-pseudovirus clade C panel, and the f61 panel, bioluminescence was determined after adding Bright-Glo reagent (Promega).

#### Neutralization Fingerprinting Panel-Based Antibody Epitope Prediction

Computational epitope prediction of serum IgG neutralizing activity was conducted as previously described (Doria-Rose et al., 2017). In brief, neutralizing serum IgG activity was determined against the 20 pseudoviruses included in the f61 fingerprinting panel by a TZM-bl cell neutralization assay as described above. The determined IgG neutralization fingerprint is compared to the fingerprint of 10 bNAbs picked as reference for their specific epitope, and the prevalence of these reference antibody epitope specificities is computationally predicted and assigned a delineation score between 0 (low) and 1 (high).

#### HIV-1 Envelope Protein Production and Purification

YU2<sub>gp120</sub>, YU2<sub>gp140</sub> (foldon trimer), and BaL<sub>gp140</sub> (foldon trimer) (Pietzsch et al., 2010) were produced in 293-6E cells after transfection with polyethylenimine. Proteins were purified from culture supernatants using Ni-NTA Agarose beads (Macherey-Nagel) according to the manufacturer's instructions and stored at -80°C until further use after buffer exchange to PBS. eOD-GT8 was produced as previously described (Dosenovic et al., 2019). 93THO527 (Anderson et al., 2000) was produced in 293-6E cells in the presence of kifunensine at a concentration of 1 mg/l.

#### HIV-1 Env ELISAs

High-binding ELISA plates (Corning) were coated with HIV-1 Env antigens at 2 µg/ml in PBS overnight at 4°C. Wells were blocked with 3% BSA (Sigma Aldrich) in PBS for 60 min at 37°C. HIV-1 antibodies were diluted in PBS and incubated for 60 min at RT, followed by horseradish peroxidase (HRP)-conjugated anti-human IgG (Jackson ImmunoResearch) diluted 1:1,000 in 3% BSA in PBS for 60 min at room temperature (RT). Absorbance was determined on a microplate reader (Tecan) after addition of ABTS solution (Thermo Fisher). Plates were washed with 0.05% Tween 20 (Carl Roth) in PBS between each step.

### Competition ELISAs

Antibodies of interest were biotinylated using the EZ Link Sulfo NHS Biotin and Labeling Kit (Thermo Fisher) according to the manufacturer's instructions, followed by a buffer exchange to PBS using Amicon 10 kDa centrifugation filter membranes (Millipore). High-binding ELISA plates (Corning) were coated with anti-6x His tag antibody (Abcam) at 2 µg/ml overnight at 4°C. Wells were blocked with 3% BSA in PBS for 60 min at 37°C, and incubated with BG505<sub>SOSIP.664</sub>-His at 2 µg/ml in PBS for 60 min at 37°C. Competing antibodies were incubated in a 1:3 dilution series starting at a concentration of 32 µg/ml in PBS for 60 min at RT. Biotinylated antibodies of interest were diluted to 0.5 µg/ml in 3% BSA in PBS and incubated for 60 min at RT, followed by peroxidase-streptavidin (Jackson ImmunoResearch) diluted 1:5,000 in 1% BSA/0.05% Tween 20 in PBS. Absorbance at 415 nm was determined on a microplate reader (Tecan) after addition of ABTS solution (Thermo Fisher). Plates were washed with 0.05% Tween 20 in PBS between each step.

### Generation of HIV-1<sub>YU2</sub> and HIV-1<sub>BG505</sub> Pseudovirus Mutants

Point mutations were introduced into HIV-1<sub>YU2</sub> and HIV-1<sub>BG505</sub> envelope expression plasmids using either the QuikChange II XL Site-Directed Mutagenesis Kit (Agilent) or the Q5 Site-Directed Mutagenesis Kit (New England Biolabs). Pseudoviruses were produced as described above.

### Recombinant HIV-1 Production

Replication-competent recombinant HIV-1 (YU2 *env* in NL4-3 backbone (Zhang et al., 2002)) was produced by transfection of HEK293T cells using FuGENE 6 Transfection Reagent (Promega). Harvested viral supernatants were stored at  $-80^{\circ}\text{C}$  to  $-150^{\circ}\text{C}$ .

#### HIV-1-Infected Humanized Mice and Viral Load Measurements

Humanized NRG mice were challenged with replication-competent HIV-1 intraperitoneally. HIV-1-infected mice were treated using 0.22  $\mu\text{m}$ -filtered monoclonal antibodies diluted in PBS, starting 25–26 days after viral challenge. Antibodies were injected subcutaneously. Following a 1-mg loading dose per antibody, doses of 0.5 mg per antibody were injected every 3–4 days. Plasma RNA was extracted from EDTA plasma samples using the MinElute Virus Mini Spin Kit (QIAGEN), including an on-column DNase I (QIAGEN) digestion step. Viral loads were determined by quantitative real-time PCR using *pol*-specific primers 5'-TAATGGCAGCAATTCACCA and 5'-GAATGCCAAATTCCTGCTTGA, and 5'-/56-FAM/CCCACCAACARGCRGCCTTAACTG/ZenDQ/ as probe, as previously described (Horwitz et al., 2013). qPCR was performed on a LightCycler 480 II (Roche) using the Taqman RNA-to-Ct 1-Step-Kit (Thermo Fisher). An HIV-1<sub>YU2</sub> standard produced by infection of SupT1-R5 cells was included for every PCR run, and HIV-1 copy number of the standard was determined using the quantitative cobas 6800 HIV-1 kit (Roche). The limit of accuracy of the qPCR was determined as 384 copies/ml.  $\text{Log}_{10}$  changes for viral loads  $< 384$  copies/ml were calculated by assigning a copy number of 383 copies/ml.

#### Humanized Mouse Plasma RNA-Derived Single Genome Sequencing

Single genome sequencing has been described previously (Salazar-Gonzalez et al., 2008). Plasma RNA was extracted using the MinElute Virus Spin Kit (QIAGEN), including a DNase I (QIAGEN) digestion step. cDNA was generated from plasma RNA using the antisense primer YB383 5'-TTTTTTTTTTTTTTTTTTTTTTTTTTTTRAAGCAC (Horwitz et al., 2017) and Superscript IV (Thermo Fisher) according to the manufacturer's protocol, followed by incubation with 0.25 U/ $\mu\text{l}$  RNase H (Thermo Fisher) at  $37^{\circ}\text{C}$  for 20 min. *Env* cDNA was subsequently amplified by nested PCR at dilutions that yield  $< 30\%$  positive PCR reactions so that  $> 80\%$  of positive reactions would be amplified from a single

virion (based on Poisson distribution). First-round PCR was conducted using primers YB383 5'-TTTTTTTTTTTTTTTTTTTTTTTTTTTTRAAGCAC and YB50 5'-GGCTTAGGCATCTCCTATGGCAGGAAGAA, and run at 94°C for 2 min; 35 cycles of 94°C for 30 s, 55°C for 30 s, and 72°C for 4 min; and 72°C for 15 min. 1 µL of first-round PCR product was used as template for the second-round PCR that was conducted using primers YB49 5'-TAGAAAGAGCAGAAGACAGTGGCAATGA and YB52 5'-GGTGTGTAGTTCTGCCAATCAGGGAAGWAGCCTTGTG, and run at 94°C for 2 min; 45 cycles of 94°C for 30 s, 55°C for 30 s, and 72°C for 4 min; and 72°C for 15 min. PCR was performed using the Platinum Taq Green Hot Start DNA Polymerase (Thermo Fisher) or Phusion Hot Start Flex DNA Polymerase (New England Biolabs).

#### Illumina Dye Sequencing of Humanized Mouse SGS-Derived *env* Amplicons

Libraries of purified PCR products were prepared for Illumina dye sequencing as described before with modifications (Kryazhimskiy et al., 2014, Schoofs et al., 2016). In brief, PCR products were cleaved by tagmentation using the Nextera DNA Library Prep Kit (Illumina). Indices (Nextera Index Kit, Illumina) were added by limited cycle PCR using the KAPA HiFi HotStart ReadyMix (Roche), followed by adaptor addition (P1, 5'-AATGATACGGCGACCACCGA; P2, 5'-CAAGCAGAAGACGGCATACGA) by limited cycle PCR using the KAPA HiFi HotStart ReadyMix. PCR products were purified using AMPure XP beads (Beckman Coulter), pooled, and sequenced using the MiSeq 300-cycle Nano Kit v2 (Illumina) spiked with approximately 10% PhiX. Paired-end reads were assembled as previously described (Gaebler et al., 2019). For further analyses, a consensus sequence was generated and nucleotides with < 75% identity across reads were defined as ambiguities. Only full-length envelope sequences with high base call quality, less than 10 ambiguities, and no early stop-codons (unless due to ambiguities) were analyzed. Otherwise acceptable sequences showing ambiguities resulting in stop-codons or a frameshift were corrected manually.

#### Human Plasma RNA-Derived Single Genome Sequencing

Plasma RNA was extracted using the MinElute Virus Spin Kit (QIAGEN), including a DNase I (QIAGEN) digestion step. cDNA was generated using the antisense primer envB3out 5'-TTGCTACTTGTGATTGCTCCATGT and SuperScript III Reverse Transcriptase (Thermo Fisher), followed by an RNase H digest (Thermo Fisher). *Env* cDNA was subsequently amplified as described previously with modifications (Mendoza et al., 2018, Salazar-Gonzalez et al., 2008). PCR was performed using the Phusion Hot Start Flex DNA Polymerase (New England Biolabs). First-round PCR was run at 98°C for 45 s; 35 cycles of 98°C for 15 s, 55°C for 30 s, and 72°C for 4 min; and 72°C for 15 min. 1 µL of first-round PCR product was used as template for the second-round PCR which was run at 98°C for 45 s; 45 cycles of 98°C for 15 s, 55°C for 30 s, and 72°C for 4 min; and 72°C for 15 min. Purified PCR products were sequenced using Sanger sequencing and analyzed using Geneious software (Geneious).

#### Bulk Viral Outgrowth Cultures

CD4<sup>+</sup> T cells were isolated from PBMCs of HIV-1-infected individuals using the CD4<sup>+</sup> T cell isolation MACS kit (Miltenyi Biotec) and stimulated by co-culture with irradiated (50 Gy) healthy donor PBMCs in T cell medium (RPMI 1640 supplemented with 300 mg/l L-glutamine (Thermo Fisher), 10% FBS (Sigma-Aldrich), and 1% penicillin/streptomycin (Thermo Fisher)) in the presence of 1 µg/ml PHA-M (Sigma-Aldrich) and 100 U/ml interleukin-2 (IL-2) (Miltenyi Biotec). One day later, medium was changed to T cell medium supplemented with 100 U/ml IL-2 and 5 µg/ml polybrene (Sigma-Aldrich). In addition, healthy donor PBMCs were added that had been stimulated for two days in T cell medium supplemented with 1 µg/ml PHA-M and 100 U/ml IL-2. Before addition, donor PBMCs were depleted of CD8<sup>+</sup> T cells using CD8 MACS microbeads (Miltenyi Biotec). Additional CD8<sup>+</sup> T cell-depleted donor PBMCs were added weekly. Culture supernatants were monitored for p24 production using the Architect HIV Ag/Ab combo assay (Abbott), and p24-positive culture supernatants were stored at -80°C to -150°C after harvesting.

#### *In vivo* Antibody Pharmacokinetic Analysis

NOD.Cg-*Rag1<sup>tm1mom</sup> Il2rg<sup>tm1Wjl</sup>*/SzJ mice (The Jackson Laboratory) aged 33-42 weeks were intravenously injected (tail vein) with 0.5 mg of purified antibody in PBS. Total serum concentrations of human IgG were determined by ELISA as previously described with minor modifications (Klein et al., 2012). In brief, high-binding ELISA plates (Corning) were coated with anti-human IgG (Jackson ImmunoResearch) at a concentration of 2.5 µg/ml overnight at RT. Subsequently, wells were blocked with blocking buffer (2% BSA (Carl Roth), 1 µM EDTA (Thermo Fisher), and 0.1% Tween 20 (Carl Roth) in PBS). To generate a standard curve, human IgG1 kappa purified from myeloma plasma (Sigma-Aldrich) was diluted in PBS. Serial dilutions of the IgG standard (in duplicates) and serum samples in PBS were incubated for 90 min at RT, followed by HRP-conjugated anti-human IgG (Jackson ImmunoResearch) diluted 1:1,000 in blocking buffer for 90 min at RT. Following the addition of ABTS (Thermo Fisher), optical density at 415 nm was determined using a microplate reader (Tecan). Plates were washed with 0.05% Tween 20 in PBS between each step. Serum samples obtained before the antibody injection confirmed baseline absence of human serum IgG.

For determination of bNAb-levels following treatment interruption in HIV-1-infected humanized mice, high-binding ELISA plates (Corning) were coated overnight with BG505<sub>SOSIP.664</sub> at a concentration of 2 µg/ml at 4°C. Subsequently, wells were blocked with 3% BSA in PBS for 5 h at RT. Plasma samples were inactivated in 1% Triton X-100 (Carl Roth) for 1 h at RT. Triton X-100-treated 1-18 diluted in PBS was used as standard in duplicates. Serial dilutions of plasma samples in PBS and standard were incubated for 90 min at RT, followed by HRP-conjugated anti-human IgG (Jackson ImmunoResearch) diluted 1:2,000 in 3% BSA in PBS for 90 min at RT. Following the addition of ABTS (Thermo Fisher), optical density at 415 nm was determined using a microplate reader (Tecan). Plates were washed with 0.05% Tween 20 in PBS between each step.

#### HEp-2 Cell Assay

HEp-2 cell autoreactivity analysis was performed using the NOVA Lite Hep-2 ANA Kit (Inova Diagnostics) according to the manufacturer's instructions using monoclonal

antibodies at a concentration of 100 µg/ml in PBS. Images were acquired using a DMI 6000 B fluorescence microscope (Leica) with 3 s exposure at 100% intensity and gain 10.

#### Unbiased B Cell Repertoire Analyses

B cells were isolated from PBMCs using CD19 microbeads (Miltenyi Biotec) and stained with DAPI (Thermo Fisher), CD20-AF 700, IgG-APC, IgD-Pe-Cy7, IgM-FITC, and CD27-PE (all BD Biosciences) for 30 min on ice. 200,000 CD20<sup>+</sup>IgG<sup>+</sup>IgM<sup>-</sup>IgD<sup>-</sup>CD27<sup>-</sup> B cells were sorted into FBS (Sigma-Aldrich) using a BD FACSAria Fusion, and RNA of sorted B cells was isolated with the RNeasy Micro Kit (QIAGEN). cDNA was generated by template-switch reverse transcription according to the SMARTer RACE 5'/3' manual using the SMARTScribe Reverse Transcriptase (Takara) with a template-switch oligo including an 18-nucleotide unique molecular identifier. Heavy-chain variable regions were amplified with an IgG-specific nested PCR and amplicons were used for library preparation and MiSeq 2x300 bp sequencing (Illumina). Raw NGS reads were pre-processed and assembled to final sequences as previously described (Ehrhardt et al., 2019).

#### Mutational Antigenic Profiling

Mutational antigenic profiling has been previously described (Dingens et al., 2017, Dingens et al., 2019). Briefly,  $5 \times 10^5$  infectious units of two independently generated HIV-1<sub>BG505</sub> mutant virus libraries (Haddox et al., 2018) were neutralized with both 4 µg/ml or 8 µg/ml of 1-18 for one hour. Neutralized libraries were then used to infect  $1 \times 10^6$  SupT1.CCR5 cells in R10 (RPMI (GE Life Sciences) supplemented with 10% FBS, 2 mM L-glutamine, and 100 U/ml of penicillin and streptomycin) containing 100 µg/ml DEAE-dextran. Three hours post infection, the cells were resuspended in 1 mL R10. At twelve hours post infection, the non-integrated viral cDNA was isolated from cells via a miniprep. Each mutant virus library was also subjected to a mock selection, and four 10-fold serial dilutions of each mutant virus library were infected into  $1 \times 10^6$  cells to serve as an infectivity standard curve from which the overall fraction of the library that survived antibody neutralization was quantified using qPCR (Dingens et al., 2019). Viral cDNA from antibody- and mock-selected samples was then sequenced on an Illumina MiSeq using the

previously described barcoded subamplicon sequencing approach (Haddox et al., 2016). Details on the analysis of the resulting data are provided in the Quantification and Statistical Analysis and Data and Code Availability subsections below.

#### Protein Expression and Purification for Cryo-EM Structures

1-18 IgG was expressed by transient transfection in Expi293 cells (Thermo Fisher) and purified from transfected cell supernatants using a HiTrap MabSelect Protein A column (GE Life Sciences). Fab fragments were isolated as described (Diskin et al., 2011) after papain cleavage of 1-18 IgG, removal of Fc by protein A chromatography, and then purification by size exclusion chromatography (SEC) on a Superdex-200 Increase 10/300 column (GE Life Sciences) equilibrated with TBS (20 mM Tris pH 8.0, 150 mM NaCl). 1-55 Fab was expressed as a light-chain C-terminal His<sub>6</sub>-tagged Fab by transient transfection in 293-6E cells (National Research Council of Canada) and purified from supernatants using Ni<sup>2+</sup>-NTA affinity chromatography (GE Life Sciences) followed by SEC purification with a Superdex-200 Increase 10/300 column equilibrated with TBS. All Fabs were stored at 4°C.

BG505<sub>SOSIP.664</sub> trimer was stably expressed in Chinese hamster ovary cells (kind gift of J.P. Moore and A. Cupo) as described (Chung et al., 2014) and purified from cell culture supernatant over a 2G12 immunoaffinity column followed by SEC purification on a Superdex-200 16/60 column (GE Life Sciences) equilibrated with TBS. RC1<sub>SOSIP.664</sub> was expressed by transient transfection in 293-6E cells and purified as described (Escolano et al., 2019). Individual SEC fractions of each SOSIP trimer were stored at 4°C.

#### Cryo-EM Sample Preparation

1-18 or 1-55 Fab and 10-1074 Fab were incubated with BG505<sub>SOSIP.664</sub> or RC1 in a 3:3:1 molar ratio per protomer overnight at room temperature and then purified by SEC on a Superdex-200 Increase 10/300 column. Fab-Env complexes were concentrated to 2.2 mg/ml (1-18 complex) or 0.75 mg/mL (1-55 complex) in TBS, and 3 µL was added to a Quantifoil grid (R2/2 Cu 400 mesh for the 1-18 complex and R1.2/1.3 Cu 300 mesh for 1-55 complex; Electron Microscopy Services) that had been freshly glow-discharged using a PELCO

easiGLOW (Ted Pella). Samples were vitrified in 100% liquid ethane using a Mark IV Vitrobot (Thermo Fisher) after blotting for 3-3.5 s with Whatman No. 1 filter paper at 22°C and 100% humidity.

#### Cryo-EM Data Collection and Processing

For the 1-18-BG505-10-1074 complex, micrographs were collected on a Titan Krios transmission electron microscope (Thermo Fisher) operating at 300 kV using EPU automated software (Thermo Fisher). Movies were obtained on a Gatan K2 Summit direct electron detector operating in counting mode at a nominal magnification of 130,000x (1.057 Å/pixel calibrated) using a defocus range of -1 to -2.6 μm. Movies were collected with an 8 s exposure time with a rate of 8 e<sup>-</sup>/pix/s, which resulted in a total dose of ~60 e<sup>-</sup>/Å<sup>2</sup> over 40 fractions. Movies were motion corrected including dose-weighting using Motioncor2 (Zheng et al., 2017) within Relion-3 (Zivanov et al., 2018). The non-dose-weighted images were used for CTF estimation using Gctf (Zhang, 2016), and micrographs with power spectra that showed poor CTF fits or signs of crystalline ice were discarded. Particles were then picked in a reference-free manner using the Laplacian-of-Gaussian auto-picking function in Relion-3. A total of 352,598 particles were extracted, binned 4x4 (4.23 Å/pixel), and subjected to reference-free 2D classification in Relion-3. Particles corresponding to good classes were re-extracted and un-binned (1.057 Å/pixel). An *ab initio* volume was generated in cryoSPARC (Punjani et al., 2017) from micrographs that were collected from the same grid in a Talos Arctica that was used as an initial model for homogeneous 3D-refinement in Relion 3 (assuming C1 symmetry). Particles were then subjected to 3D classification (C1 symmetry), and classes with low-resolution features were removed. Selected classes that appeared 3-fold symmetric were thus subjected to homogeneous 3D refinement assuming C3 symmetry with a soft mask applied that did not include the Fab C<sub>H</sub>C<sub>L</sub> domains. Per-particle motion correction and CTF refinement were performed in Relion-3, followed by a final homogeneous 3D refinement. A masked post-processed volume of 230,924 particles resulted in a gold-standard FSC (GSFSC) calculation of 2.5 Å (Scheres and Chen, 2012).

For the 1-55–RC1–10-1074 complex, data collection on a Thermo Fisher 200 kV Talos Arctica cryo-electron microscope equipped with a Falcon 3EC camera, and 10-1074 interactions with RC1 were previously described (Escolano et al., 2019). For analysis of the 1-55–RC1 interaction, we reprocessed the data using Relion-3, following a similar procedure as described above for the 1-18–BG505–10-1074 complex. Compared to the original reconstruction, per-particle motion correction and CTF refinement were done in Relion-3, followed by a final homogeneous 3D refinement. A masked post-processed volume of 110,126 particles resulted in a GSFSC calculation of 3.9 Å.

### Structure Modeling and Refinement

Initial coordinates were generated by docking individual chains from reference structures into cryo-EM density using UCSF Chimera (Goddard et al., 2007). The following PDB coordinates were used: gp120: 5T3Z; gp41: 6MTJ; 10-1074: 5T3Z; 1-18 and 1-55: 4RWY. These initial models were then refined into cryo-EM maps using one round of rigid body refinement followed by real space refinement. Sequence-updated models were built manually in Coot (Emsley et al., 2010) and then refined using iterative rounds of refinement in Coot and Phenix (Adams et al., 2010). Glycans were modeled at PNGSs in Coot using ‘blurred’ maps processed with a variety of B-factors (Terwilliger et al., 2018). Water molecules were added to the 1-18–BG505–10-1074 model based on local density and distance to hydrogen bonding partners. Validation of model coordinates was performed using MolProbity (Chen et al., 2010) and is reported in Table S6.

### Structural Analyses

Structural figures were made using PyMOL (Version 1.8.2.1 Schrodinger, LLC) or UCSF Chimera (Goddard et al., 2007). Electrostatic calculations were done using the APBS and PDB2PQR servers (Unni et al., 2011). Buried surface areas (BSAs) were calculated using the PDBePISA server (Krissinel and Henrick, 2007). Local resolution maps were calculated using the Local Res program embedded in Relion-3 (Kucukelbir et al., 2014).

### Quantification and Statistical Analysis

The mutational antigenic profiling data were analyzed with `dms_tools2` version 2.5.1 ([https://jbloomlab.github.io/dms\\_tools2/](https://jbloomlab.github.io/dms_tools2/); Bloom, 2015). The fraction surviving and excess fraction surviving statistics have been previously described (Dingens et al., 2019, Doud et al., 2018) and are documented at [https://jbloomlab.github.io/dms\\_tools2/fracsurvive.html](https://jbloomlab.github.io/dms_tools2/fracsurvive.html). Sequencing wild-type DNA plasmid served as the error control during the calculation of the fraction surviving. The HIV Antibody Database (West et al., 2013) was used for the calculation of Env conservation in 1-18 contact residues and for the analysis of neutralization panel data. Clade B reference sequences were obtained through the Los Alamos National Laboratory HIV Database (Filtered Web Alignment, <https://www-hiv-lanl-gov.caltech.idm.oclc.org/>). Median germline nucleotide identity and CDRH3 lengths of HIV-1 Env-reactive and total IgG<sup>+</sup> B cells of IDC561 were compared using the Mann-Whitney U-test in Python 3 using the “stats” module in the “scipy” package. For the correlation of the neutralizing activity of 1-18 and serum IgG of IDC561, spearman’s rank correlation coefficient was calculated in Prism (GraphPad). The neutralizing activity of 1-18 and 1-18Δins was compared using the Wilcoxon matched-pairs signed rank test in Prism (GraphPad).

### **Data and Code Availability**

Heavy and light chain sequences of tested monoclonal antibodies have been deposited at GenBank (accession numbers MN867951 - MN868062). SGS-derived HIV-1 *env* obtained from HIV-1<sub>YU2</sub>-infected humanized mice and from individual IDC561 have been deposited at GenBank (accession numbers MN870987 - MN871327 and MN871328 - MN871333, respectively). Density maps and atomic coordinates for the 1-18–BG505–10-1074 and 1-55–RC1–10-1074 complexes were deposited in the Electron Microscopy Data Bank (EMDB) and Protein Data Bank (PDB) with accession numbers EMD-20739 and PDB 6UDJ (1-18 complex) and EMD-20740 and PDB 6UDK (1-55 complex). The entire mutational antigenic profiling analysis is available at [https://github.com/jbloomlab/MAP\\_118](https://github.com/jbloomlab/MAP_118), and the accompanying Illumina sequencing data is on the NCBI SRA with accession numbers SRX6752366 - SRX6752371.

## Acknowledgments

We thank all study participants who devoted time to our research; members of the Klein and Bjorkman laboratories for helpful discussion; A.P. West, Jr. for sequence analysis; M.S. Ercanoglu and K. Jain for cell sorting; K. Jain, H. Janicki, C. Ruping, and J. Schmatz for antibody production and sample processing; S. Arzberger and F. Bach for generating humanized mice; A. Adhikari, R. Duerr, S. Esser, O. Geisenberger, C. Geldmacher, M. Hölscher, A. Kroidl, T. Kümmerle, K. Römer, S. Scholten, C. Stephan, H. Streeck, T. Wolf, C. Wyen, and S. Zolla-Pazner for contributing to the screening cohort; J.P. Moore and A. Cupo for the stable CHO cell line expressing BG505<sub>SOSIP.664</sub>; E. Heger for SupT1-R5 cells; T.Y. Oliveira for providing sequence assembly software; I.S. Georgiev for neutralizing fingerprint analysis; N.A. Doria-Rose for providing RSC3; L. Stamatatos for providing eOD-GT8; Z. Yang and A. Malyutin for assistance with cryo-EM data collection; the Cologne Center for Genomics for sequencing support; and the staff of the Animal Care Facility Weyertal at the University of Cologne. The panel of global HIV-1 clones was obtained through the NIH AIDS Reagent Program, Division of AIDS, NIAID, NIH (ARP) from David Montefiori (deCamp et al., 2014), and TZM-bl cells were obtained through the ARP from John C. Kappes and Xiaoyun Wu (Platt et al., 1998). Cryo-EM was done at the Beckman Institute Resource Center for Transmission Electron Microscopy at Caltech. Support was provided by fellowships from the German Center for Infection Research (DZIF) (to P.S. and H.G.), the Graduate Research Fellowship Program (GRFP) of the National Science Foundation (NSF) (to M.E.A), scholarships from the Hans-Böckler Foundation and the Köln Fortune Program of the Faculty of Medicine of the University of Cologne (to M.-K.T), the Ernst Jung Career Advancement Award for Medical Research (to T.S.), and the Federal Joint Committee (G-BA) (01VSF18036 to C.L.). J.D.B. is an Investigator of the Howard Hughes Medical Institute. This work was supported by Bill and Melinda Gates Foundation Collaboration for AIDS Vaccine Discovery (CAVD) grant OPP1146996 (to M.S.S.); National Institute of Allergy and Infectious Diseases (NIAID) of the National Institutes of Health (NIH) grants R01 AI140891 (to J.D.B.), HIVRAD P01 AI110657 (to R.W.S.), and HIVRAD P01 AI100148 (to P.J.B.); NIH grant P50 GM082545-06 (to P.J.B.); and grants from the German Center for Infection Research (DZIF; to F.K.), the German

Research Foundation (CRC 1279 and CRC 1310 to F.K.), the DFG Heisenberg Program (KL2389/2-1 to F.K.), and the European Research Council (ERC-StG639961 to F.K.).

## References

- Adams, P.D., Afonine, P.V., Bunko' czi, G., Chen, V.B., Davis, I.W., Echols, N., Headd, J.J., Hung, L.W., Kapral, G.J., Grosse-Kunstleve, R.W., et al. (2010). PHENIX: a comprehensive Python-based system for macromolecular structure solution. *Acta Crystallogr. D Biol. Crystallogr.* *66*, 213–221.
- Anderson, J.P., Rodrigo, A.G., Learn, G.H., Madan, A., Delahunty, C., Coon, M., Girard, M., Osmanov, S., Hood, L., and Mullins, J.I. (2000). Testing the hypothesis of a recombinant origin of human immunodeficiency virus type 1 subtype E. *J. Virol.* *74*, 10752–10765.
- Balazs, A.B., Chen, J., Hong, C.M., Rao, D.S., Yang, L., and Baltimore, D. (2011). Antibody-based protection against HIV infection by vectored immunoprophylaxis. *Nature* *481*, 81–84.
- Bar, K.J., Sneller, M.C., Harrison, L.J., Justement, J.S., Overton, E.T., Petrone, M.E., Salantes, D.B., Seamon, C.A., Scheinfeld, B., Kwan, R.W., et al. (2016). Effect of HIV Antibody VRC01 on Viral Rebound after Treatment Interruption. *N. Engl. J. Med.* *375*, 2037–2050.
- Bar-On, Y., Gruell, H., Schoofs, T., Pai, J.A., Nogueira, L., Butler, A.L., Millard, K., Lehmann, C., Sua' rez, I., Oliveira, T.Y., et al. (2018). Safety and antiviral activity of combination HIV-1 broadly neutralizing antibodies in viremic individuals. *Nat. Med.* *24*, 1701–1707.
- Barouch, D.H., Whitney, J.B., Moldt, B., Klein, F., Oliveira, T.Y., Liu, J., Stephenson, K.E., Chang, H.W., Shekhar, K., Gupta, S., et al. (2013). Therapeutic efficacy of potent neutralizing HIV-1-specific monoclonal antibodies in SHIV-infected rhesus monkeys. *Nature* *503*, 224–228.
- Bloom, J.D. (2015). Software for the analysis and visualization of deep mutational scanning data. *BMC Bioinformatics* *16*, 168.
- Bonsignori, M., Zhou, T., Sheng, Z., Chen, L., Gao, F., Joyce, M.G., Ozorowski, G., Chuang, G.Y., Schramm, C.A., Wiehe, K., et al.; NISC Comparative Sequencing Program (2016). Maturation Pathway from Germline to Broad HIV-1 Neutralizer of a CD4-Mimic Antibody. *Cell* *165*, 449–463.
- Caskey, M., Klein, F., Lorenzi, J.C., Seaman, M.S., West, A.P., Jr., Buckley, N., Kremer, G., Nogueira, L., Braunschweig, M., Scheid, J.F., et al. (2015). Viraemia suppressed in HIV-1-infected humans by broadly neutralizing antibody 3BNC117. *Nature* *522*, 487–491.
- Caskey, M., Schoofs, T., Gruell, H., Settler, A., Karagounis, T., Kreider, E.F., Murrell, B., Pfeifer, N., Nogueira, L., Oliveira, T.Y., et al. (2017). Antibody 10-1074 suppresses viremia in HIV-1-infected individuals. *Nat. Med.* *23*, 185–191.

Caskey, M., Klein, F., and Nussenzweig, M.C. (2019). Broadly neutralizing anti- HIV-1 monoclonal antibodies in the clinic. *Nat. Med.* 25, 547–553.

Chen, V.B., Arendall, W.B., 3rd, Headd, J.J., Keedy, D.A., Immormino, R.M., Kapral, G.J., Murray, L.W., Richardson, J.S., and Richardson, D.C. (2010). MolProbity: all-atom structure validation for macromolecular crystallography. *Acta Crystallogr. D Biol. Crystallogr.* 66, 12–21.

Chuang, G.Y., Zhou, J., Acharya, P., Rawi, R., Shen, C.H., Sheng, Z., Zhang, B., Zhou, T., Bailer, R.T., Dandey, V.P., et al. (2019). Structural Survey of Broadly Neutralizing Antibodies Targeting the HIV-1 Env Trimer Delineates Epitope Categories and Characteristics of Recognition. *Structure* 27, 196–206.e6.

Chung, N.P., Matthews, K., Kim, H.J., Ketas, T.J., Golabek, M., de Los Reyes, K., Korzun, J., Yasmeen, A., Sanders, R.W., Klasse, P.J., et al. (2014). Stable 293 T and CHO cell lines expressing cleaved, stable HIV-1 envelope glycoprotein trimers for structural and vaccine studies. *Retrovirology* 11, 33.

Cohen, Y.Z., Lorenzi, J.C.C., Krassnig, L., Barton, J.P., Burke, L., Pai, J., Lu, C.L., Mendoza, P., Oliveira, T.Y., Sleckman, C., et al. (2018a). Relationship between latent and rebound viruses in a clinical trial of anti-HIV-1 antibody 3BNC117. *J. Exp. Med.* 215, 2311–2324.

Cohen, Y.Z., Lorenzi, J.C.C., Seaman, M.S., Nogueira, L., Schoofs, T., Krassnig, L., Butler, A., Millard, K., Fitzsimons, T., Daniell, X., et al. (2018b). Neutralizing Activity of Broadly Neutralizing Anti-HIV-1 Antibodies against Clade B Clinical Isolates Produced in Peripheral Blood Mononuclear Cells. *J. Virol.* 92, e01883-17.

Crowell, T.A., Colby, D.J., Pinyakorn, S., Sacdalan, C., Pagliuzza, A., Intasan, J., Benjapornpong, K., Tangnaree, K., Chomchey, N., Kroon, E., et al.; RV397 Study Group (2019). Safety and efficacy of VRC01 broadly neutralising antibodies in adults with acutely treated HIV (RV397): a phase 2, randomised, double-blind, placebo-controlled trial. *Lancet HIV* 6, e297–e306.

de Taeye, S.W., Ozorowski, G., Torrents de la Peña, A., Guttman, M., Julien, J.P., van den Kerkhof, T.L., Burger, J.A., Pritchard, L.K., Pugach, P., Yasmeen, A., et al. (2015). Immunogenicity of Stabilized HIV-1 Envelope Trimers with Reduced Exposure of Non-neutralizing Epitopes. *Cell* 163, 1702–1715.

deCamp, A., Hraber, P., Bailer, R.T., Seaman, M.S., Ochsenbauer, C., Kappes, J., Gottardo, R., Edlefsen, P., Self, S., Tang, H., et al. (2014). Global panel of HIV-1 Env reference strains for standardized assessments of vaccine-elicited neutralizing antibodies. *J. Virol.* 88, 2489–2507.

Didigu, C.A., Wilen, C.B., Wang, J., Duong, J., Secreto, A.J., Danet-Desnoyers, G.A., Riley, J.L., Gregory, P.D., June, C.H., Holmes, M.C., and Doms, R.W. (2014). Simultaneous zinc-finger nuclease editing of the HIV coreceptors *ccr5* and *cxcr4* protects CD4+ T cells from HIV-1 infection. *Blood* *123*, 61–69.

Dingens, A.S., Haddox, H.K., Overbaugh, J., and Bloom, J.D. (2017). Comprehensive Mapping of HIV-1 Escape from a Broadly Neutralizing Antibody. *Cell Host Microbe* *21*, 777–787.e4.

Dingens, A.S., Arenz, D., Weight, H., Overbaugh, J., and Bloom, J.D. (2019). An Antigenic Atlas of HIV-1 Escape from Broadly Neutralizing Antibodies Distinguishes Functional and Structural Epitopes. *Immunity* *50*, 520–532.e3.

Diskin, R., Scheid, J.F., Marcovecchio, P.M., West, A.P., Jr., Klein, F., Gao, H., Gnanapragasam, P.N., Abadir, A., Seaman, M.S., Nussenzweig, M.C., and Bjorkman, P.J. (2011). Increasing the potency and breadth of an HIV antibody by using structure-based rational design. *Science* *334*, 1289–1293.

Diskin, R., Klein, F., Horwitz, J.A., Halper-Stromberg, A., Sather, D.N., Marcovecchio, P.M., Lee, T., West, A.P., Jr., Gao, H., Seaman, M.S., et al. (2013). Restricting HIV-1 pathways for escape using rationally designed anti-HIV-1 antibodies. *J. Exp. Med.* *210*, 1235–1249.

Doria-Rose, N.A., Altae-Tran, H.R., Roark, R.S., Schmidt, S.D., Sutton, M.S., Louder, M.K., Chuang, G.Y., Bailer, R.T., Cortez, V., Kong, R., et al. (2017). Mapping Polyclonal HIV-1 Antibody Responses via Next-Generation Neutralization Fingerprinting. *PLoS Pathog.* *13*, e1006148.

Dosenovic, P., Pettersson, A.K., Wall, A., Thientosapol, E.S., Feng, J., Weidle, C., Bhullar, K., Kara, E.E., Hartweger, H., Pai, J.A., et al. (2019). Anti-idiotypic antibodies elicit anti-HIV-1-specific B cell responses. *J. Exp. Med.* *216*, 2316–2330.

Doud, M.B., Lee, J.M., and Bloom, J.D. (2018). How single mutations affect viral escape from broad and narrow antibodies to H1 influenza hemagglutinin. *Nat. Commun.* *9*, 1386.

Ehrhardt, S.A., Zehner, M., Kraehling, V., Cohen-Dvashi, H., Kreer, C., Elad, N., Gruell, H., Ercanoglu, M.S., Schommers, P., Gieselmann, L., et al. (2019). Polyclonal and convergent antibody response to Ebola virus vaccine rVSV-ZEBOV. *Nat. Med.* *25*, 1589–1600.

Emsley, P., Lohkamp, B., Scott, W.G., and Cowtan, K. (2010). Features and development of Coot. *Acta Crystallogr. D Biol. Crystallogr.* *66*, 486–501.

Escolano, A., Gristick, H.B., Abernathy, M.E., Merckenschlager, J., Gautam, R., Oliveira, T.Y., Pai, J., West, A.P., Jr., Barnes, C.O., Cohen, A.A., et al. (2019). Immunization expands B cells specific to HIV-1 V3 glycan in mice and macaques. *Nature* 570, 468–473.

Gaebler, C., Lorenzi, J.C.C., Oliveira, T.Y., Nogueira, L., Ramos, V., Lu, C.L., Pai, J.A., Mendoza, P., Jankovic, M., Caskey, M., and Nussenzweig, M.C. (2019). Combination of quadruplex qPCR and next-generation sequencing for qualitative and quantitative analysis of the HIV-1 latent reservoir. *J. Exp. Med.* 216, 2253–2264.

Gama, L., and Koup, R.A. (2018). New-Generation High-Potency and Designer Antibodies: Role in HIV-1 Treatment. *Annu. Rev. Med.* 69, 409–419.

Gao, F., Bonsignori, M., Liao, H.X., Kumar, A., Xia, S.M., Lu, X., Cai, F., Hwang, K.K., Song, H., Zhou, T., et al. (2014). Cooperation of B cell lineages in induction of HIV-1-broadly neutralizing antibodies. *Cell* 158, 481–491.

Gaudinski, M.R., Coates, E.E., Houser, K.V., Chen, G.L., Yamshchikov, G., Saunders, J.G., Holman, L.A., Gordon, I., Plummer, S., Hendel, C.S., et al.; VRC 606 Study Team (2018). Safety and pharmacokinetics of the Fc-modified HIV-1 human monoclonal antibody VRC01LS: A Phase 1 open-label clinical trial in healthy adults. *PLoS Med.* 15, e1002493.

Gaudinski, M.R., Houser, K.V., Doria-Rose, N.A., Chen, G.L., Rothwell, R.S.S., Berkowitz, N., Costner, P., Holman, L.A., Gordon, I.J., Hendel, C.S., et al.; VRC 605 study team (2019). Safety and pharmacokinetics of broadly neutralising human monoclonal antibody VRC07-523LS in healthy adults: a phase 1 dose-escalation clinical trial. *Lancet HIV* 6, e667–e679.

Gautam, R., Nishimura, Y., Pegu, A., Nason, M.C., Klein, F., Gazumyan, A., Golijanin, J., Buckler-White, A., Sadjadpour, R., Wang, K., et al. (2016). A single injection of anti-HIV-1 antibodies protects against repeated SHIV challenges. *Nature* 533, 105–109.

Goddard, T.D., Huang, C.C., and Ferrin, T.E. (2007). Visualizing density maps with UCSF Chimera. *J. Struct. Biol.* 157, 281–287.

Gruell, H., and Klein, F. (2017). Progress in HIV-1 antibody research using humanized mice. *Curr. Opin. HIV AIDS* 12, 285–293.

Gruell, H., and Klein, F. (2018). Antibody-mediated prevention and treatment of HIV-1 infection. *Retrovirology* 15, 73.

Guindon, S., Dufayard, J.F., Lefort, V., Anisimova, M., Hordijk, W., and Gascuel, O. (2010). New algorithms and methods to estimate maximum-likelihood phylogenies: assessing the performance of PhyML 3.0. *Syst. Biol.* 59, 307–321.

Haddox, H.K., Dingens, A.S., and Bloom, J.D. (2016). Experimental Estimation of the Effects of All Amino-Acid Mutations to HIV's Envelope Protein on Viral Replication in Cell Culture. *PLoS Pathog.* *12*, e1006114.

Haddox, H.K., Dingens, A.S., Hilton, S.K., Overbaugh, J., and Bloom, J.D. (2018). Mapping mutational effects along the evolutionary landscape of HIV envelope. *eLife* *7*, e34420.

Haynes, B.F., Fleming, J., St Clair, E.W., Katinger, H., Stiegler, G., Kunert, R., Robinson, J., Scarce, R.M., Plonk, K., Staats, H.F., et al. (2005). Cardiolipin polyspecific autoreactivity in two broadly neutralizing HIV-1 antibodies. *Science* *308*, 1906–1908.

Horwitz, J.A., Halper-Stromberg, A., Mouquet, H., Gitlin, A.D., Tretiakova, A., Eisenreich, T.R., Malbec, M., Gravemann, S., Billerbeck, E., Dorner, M., et al. (2013). HIV-1 suppression and durable control by combining single broadly neutralizing antibodies and antiretroviral drugs in humanized mice. *Proc. Natl. Acad. Sci. USA* *110*, 16538–16543.

Horwitz, J.A., Bar-On, Y., Lu, C.L., Fera, D., Lockhart, A.A.K., Lorenzi, J.C.C., Nogueira, L., Golijanin, J., Scheid, J.F., Seaman, M.S., et al. (2017). Non-neutralizing Antibodies Alter the Course of HIV-1 Infection In Vivo. *Cell* *170*, 637–648.e10.

Hraber, P., Rademeyer, C., Williamson, C., Seaman, M.S., Gottardo, R., Tang, H., Greene, K., Gao, H., LaBranche, C., Mascola, J.R., et al. (2017). Panels of HIV-1 Subtype C Env Reference Strains for Standardized Neutralization Assessments. *J. Virol.* *91*, e00991-17.

Huang, J., Kang, B.H., Ishida, E., Zhou, T., Griesman, T., Sheng, Z., Wu, F., Doria-Rose, N.A., Zhang, B., McKee, K., et al. (2016a). Identification of a CD4- Binding-Site Antibody to HIV that Evolved Near-Pan Neutralization Breadth. *Immunity* *45*, 1108–1121.

Huang, Y., Yu, J., Lanzi, A., Yao, X., Andrews, C.D., Tsai, L., Gajjar, M.R., Sun, M., Seaman, M.S., Padte, N.N., and Ho, D.D. (2016b). Engineered Bispecific Antibodies with Exquisite HIV-1-Neutralizing Activity. *Cell* *165*, 1621–1631.

Ince, W.L., Zhang, L., Jiang, Q., Arrildt, K., Su, L., and Swanstrom, R. (2010). Evolution of the HIV-1 env gene in the Rag2<sup>-/-</sup> gammaC<sup>-/-</sup> humanized mouse model. *J. Virol.* *84*, 2740–2752.

Julg, B., and Barouch, D.H. (2019). Neutralizing antibodies for HIV-1 prevention. *Curr. Opin. HIV AIDS* *14*, 318–324.

Julg, B., Pegu, A., Abbink, P., Liu, J., Brinkman, A., Molloy, K., Mojta, S., Chandrashekar, A., Callow, K., Wang, K., et al. (2017). Virological Control by the CD4-Binding Site Antibody N6 in Simian-Human Immunodeficiency Virus-Infected Rhesus Monkeys. *J. Virol.* *91*, e00498-17.

- Kirchherr, J.L., Lu, X., Kasongo, W., Chalwe, V., Mwananyanda, L., Musonda, R.M., Xia, S.M., Scarce, R.M., Liao, H.X., Montefiori, D.C., et al. (2007). High throughput functional analysis of HIV-1 env genes without cloning. *J. Virol. Methods* *143*, 104–111.
- Klein, F., Halper-Stromberg, A., Horwitz, J.A., Gruell, H., Scheid, J.F., Bournazos, S., Mouquet, H., Spatz, L.A., Diskin, R., Abadir, A., et al. (2012). HIV therapy by a combination of broadly neutralizing antibodies in humanized mice. *Nature* *492*, 118–122.
- Kreer, C., Döring, M., Lehnen, N., Ercanoglu, M.S., Gieselmann, L., Luca, D., Jain, K., Schommers, P., Pfeifer, N., and Klein, F. (2019). openPrimeR for multiplex amplification of highly diverse templates. *bioRxiv*. <https://doi.org/10.1101/847574>.
- Krissinel, E., and Henrick, K. (2007). Inference of macromolecular assemblies from crystalline state. *J. Mol. Biol.* *372*, 774–797.
- Kryazhimskiy, S., Rice, D.P., Jerison, E.R., and Desai, M.M. (2014). Microbial evolution. Global epistasis makes adaptation predictable despite sequence-level stochasticity. *Science* *344*, 1519–1522.
- Kucukelbir, A., Sigworth, F.J., and Tagare, H.D. (2014). Quantifying the local resolution of cryo-EM density maps. *Nat. Methods* *11*, 63–65.
- Kwong, P.D., Wyatt, R., Robinson, J., Sweet, R.W., Sodroski, J., and Hendrickson, W.A. (1998). Structure of an HIV gp120 envelope glycoprotein in complex with the CD4 receptor and a neutralizing human antibody. *Nature* *393*, 648–659.
- Ledgerwood, J.E., Coates, E.E., Yamshechikov, G., Saunders, J.G., Holman, L., Enama, M.E., DeZure, A., Lynch, R.M., Gordon, I., Plummer, S., et al.; VRC 602 Study Team (2015). Safety, pharmacokinetics and neutralization of the broadly neutralizing HIV-1 human monoclonal antibody VRC01 in healthy adults. *Clin. Exp. Immunol.* *182*, 289–301.
- Lee, J.H., Andrabi, R., Su, C.Y., Yasmeeen, A., Julien, J.P., Kong, L., Wu, N.C., McBride, R., Sok, D., Pauthner, M., et al. (2017). A Broadly Neutralizing Antibody Targets the Dynamic HIV Envelope Trimer Apex via a Long, Rigidified, and Anionic b-Hairpin Structure. *Immunity* *46*, 690–702.
- Leonard, C.K., Spellman, M.W., Riddle, L., Harris, R.J., Thomas, J.N., and Gregory, T.J. (1990). Assignment of intrachain disulfide bonds and characterization of potential glycosylation sites of the type 1 recombinant human immunodeficiency virus envelope glycoprotein (gp120) expressed in Chinese hamster ovary cells. *J. Biol. Chem.* *265*, 10373–10382.
- Liu, Q., Acharya, P., Dolan, M.A., Zhang, P., Guzzo, C., Lu, J., Kwon, A., Gururani, D., Miao, H., Bylund, T., et al. (2017). Quaternary contact in the initial interaction of CD4 with the HIV-1 envelope trimer. *Nat. Struct. Mol. Biol.* *24*, 370–378.

Liu, Q., Lai, Y.T., Zhang, P., Louder, M.K., Pegu, A., Rawi, R., Asokan, M., Chen, X., Shen, C.H., Chuang, G.Y., et al. (2019). Improvement of antibody functionality by structure-guided paratope engraftment. *Nat. Commun.* *10*, 721.

Lynch, R.M., Boritz, E., Coates, E.E., DeZure, A., Madden, P., Costner, P., Enama, M.E., Plummer, S., Holman, L., Hendel, C.S., et al.; VRC 601 Study Team (2015a). Virologic effects of broadly neutralizing antibody VRC01 administration during chronic HIV-1 infection. *Sci. Transl. Med.* *7*, 319ra206.

Lynch, R.M., Wong, P., Tran, L., O'Dell, S., Nason, M.C., Li, Y., Wu, X., and Mascola, J.R. (2015b). HIV-1 fitness cost associated with escape from the VRC01 class of CD4 binding site neutralizing antibodies. *J. Virol.* *89*, 4201–4213.

Lyumkis, D., Julien, J.P., de Val, N., Cupo, A., Potter, C.S., Klasse, P.J., Burton, D.R., Sanders, R.W., Moore, J.P., Carragher, B., et al. (2013). Cryo-EM structure of a fully glycosylated soluble cleaved HIV-1 envelope trimer. *Science* *342*, 1484–1490.

Maddon, P.J., Dalglish, A.G., McDougal, J.S., Clapham, P.R., Weiss, R.A., and Axel, R. (1986). The T4 gene encodes the AIDS virus receptor and is expressed in the immune system and the brain. *Cell* *47*, 333–348.

Mayer, K.H., Seaton, K.E., Huang, Y., Grunenberg, N., Isaacs, A., Allen, M., Ledgerwood, J.E., Frank, I., Sobieszczyk, M.E., Baden, L.R., et al.; HVTN 104 Protocol Team; and the NIAID HIV Vaccine Trials Network (2017). Safety, pharmacokinetics, and immunological activities of multiple intravenous or subcutaneous doses of an anti-HIV monoclonal antibody, VRC01, administered to HIV-uninfected adults: Results of a phase 1 randomized trial. *PLoS Med.* *14*, e1002435.

Mendoza, P., Gruell, H., Nogueira, L., Pai, J.A., Butler, A.L., Millard, K., Lehmann, C., Suarez, I., Oliveira, T.Y., Lorenzi, J.C.C., et al. (2018). Combination therapy with anti-HIV-1 antibodies maintains viral suppression. *Nature* *561*, 479–484.

Moldt, B., Rakasz, E.G., Schultz, N., Chan-Hui, P.Y., Swiderek, K., Weisgrau, K.L., Piaskowski, S.M., Bergman, Z., Watkins, D.I., Poignard, P., and Burton, D.R. (2012). Highly potent HIV-specific antibody neutralization in vitro translates into effective protection against mucosal SHIV challenge in vivo. *Proc. Natl. Acad. Sci. USA* *109*, 18921–18925.

Mouquet, H., Scharf, L., Euler, Z., Liu, Y., Eden, C., Scheid, J.F., Halper-Stromberg, A., Gnanapragasam, P.N., Spencer, D.I., Seaman, M.S., et al. (2012). Complex-type N-glycan recognition by potent broadly neutralizing HIV antibodies. *Proc. Natl. Acad. Sci. USA* *109*, E3268–E3277.

- Otsuka, Y., Schmitt, K., Quinlan, B.D., Gardner, M.R., Alfant, B., Reich, A., Farzan, M., and Choe, H. (2018). Diverse pathways of escape from all well-characterized VRC01-class broadly neutralizing HIV-1 antibodies. *PLoS Pathog.* *14*, e1007238.
- Ozawa, T., Kishi, H., and Muraguchi, A. (2006). Amplification and analysis of cDNA generated from a single cell by 50'-RACE: application to isolation of antibody heavy and light chain variable gene sequences from single B cells. *Biotechniques* *40*, 469–470, 472, 474 passim.
- Pejchal, R., Doores, K.J., Walker, L.M., Khayat, R., Huang, P.S., Wang, S.K., Stanfield, R.L., Julien, J.P., Ramos, A., Crispin, M., et al. (2011). A potent and broad neutralizing antibody recognizes and penetrates the HIV glycan shield. *Science* *334*, 1097–1103.
- Pietzsch, J., Scheid, J.F., Mouquet, H., Klein, F., Seaman, M.S., Jankovic, M., Corti, D., Lanzavecchia, A., and Nussenzweig, M.C. (2010). Human anti-HIV-1 neutralizing antibodies frequently target a conserved epitope essential for viral fitness. *J. Exp. Med.* *207*, 1995–2002.
- Platt, E.J., Wehrly, K., Kuhmann, S.E., Chesebro, B., and Kabat, D. (1998). Effects of CCR5 and CD4 cell surface concentrations on infections by macrophagetropic isolates of human immunodeficiency virus type 1. *J. Virol.* *72*, 2855–2864.
- Punjani, A., Rubinstein, J.L., Fleet, D.J., and Brubaker, M.A. (2017). cryoSPARC: algorithms for rapid unsupervised cryo-EM structure determination. *Nat. Methods* *14*, 290–296.
- Riddler, S.A., Zheng, L., Durand, C.M., Ritz, J., Koup, R.A., Ledgerwood, J., Bailer, R.T., Koletar, S.L., Eron, J.J., Keefer, M.C., et al.; AIDS Clinical Trials Group A5342 Protocol Team (2018). Randomized Clinical Trial to Assess the Impact of the Broadly Neutralizing HIV-1 Monoclonal Antibody VRC01 on HIV-1 Persistence in Individuals on Effective ART. *Open Forum Infect. Dis.* *5*, ofy242.
- Rizzuto, C.D., Wyatt, R., Hernandez-Ramos, N., Sun, Y., Kwong, P.D., Hendrickson, W.A., and Sodroski, J. (1998). A conserved HIV gp120 glycoprotein structure involved in chemokine receptor binding. *Science* *280*, 1949–1953.
- Rudicell, R.S., Kwon, Y.D., Ko, S.Y., Pegu, A., Louder, M.K., Georgiev, I.S., Wu, X., Zhu, J., Boyington, J.C., Chen, X., et al.; NISC Comparative Sequencing Program (2014). Enhanced potency of a broadly neutralizing HIV-1 antibody in vitro improves protection against lentiviral infection in vivo. *J. Virol.* *88*, 12669–12682.
- Sajadi, M.M., Dashti, A., Rikhtegaran Tehrani, Z., Tolbert, W.D., Seaman, M.S., Ouyang, X., Gohain, N., Pazgier, M., Kim, D., Cavet, G., et al. (2018). Identification of Near-Pan-neutralizing Antibodies against HIV-1 by Deconvolution of Plasma Humoral Responses. *Cell* *173*, 1783–1795.e14.

Salazar-Gonzalez, J.F., Bailes, E., Pham, K.T., Salazar, M.G., Guffey, M.B., Keele, B.F., Derdeyn, C.A., Farmer, P., Hunter, E., Allen, S., et al. (2008). Deciphering human immunodeficiency virus type 1 transmission and early envelope diversification by single-genome amplification and sequencing. *J. Virol.* *82*, 3952–3970.

Sanders, R.W., Derking, R., Cupo, A., Julien, J.P., Yasmeen, A., de Val, N., Kim, H.J., Blattner, C., de la Peña, A.T., Korzun, J., et al. (2013). A next-generation cleaved, soluble HIV-1 Env trimer, BG505 SOSIP.664 gp140, expresses multiple epitopes for broadly neutralizing but not non-neutralizing antibodies. *PLoS Pathog.* *9*, e1003618.

Sarzotti-Kelsoe, M., Bailer, R.T., Turk, E., Lin, C.L., Bilska, M., Greene, K.M., Gao, H., Todd, C.A., Ozaki, D.A., Seaman, M.S., et al. (2014). Optimization and validation of the TZM-bl assay for standardized assessments of neutralizing antibodies against HIV-1. *J. Immunol. Methods* *409*, 131–146.

Sather, D.N., Carbonetti, S., Kehayia, J., Kraft, Z., Mikell, I., Scheid, J.F., Klein, F., and Stamatatos, L. (2012). Broadly neutralizing antibodies developed by an HIV-positive elite neutralizer exact a replication fitness cost on the contemporaneous virus. *J. Virol.* *86*, 12676–12685.

Scharf, L., Scheid, J.F., Lee, J.H., West, A.P., Jr., Chen, C., Gao, H., Gnanapragasam, P.N., Mares, R., Seaman, M.S., Ward, A.B., et al. (2014). Antibody 8ANC195 reveals a site of broad vulnerability on the HIV-1 envelope spike. *Cell Rep.* *7*, 785–795.

Scheid, J.F., Mouquet, H., Feldhahn, N., Walker, B.D., Pereyra, F., Cutrell, E., Seaman, M.S., Mascola, J.R., Wyatt, R.T., Wardemann, H., and Nussenzweig, M.C. (2009). A method for identification of HIV gp140 binding memory B cells in human blood. *J. Immunol. Methods* *343*, 65–67.

Scheid, J.F., Mouquet, H., Ueberheide, B., Diskin, R., Klein, F., Oliveira, T.Y., Pietzsch, J., Fenyo, D., Abadir, A., Velinzon, K., et al. (2011). Sequence and structural convergence of broad and potent HIV antibodies that mimic CD4 binding. *Science* *333*, 1633–1637.

Scheid, J.F., Horwitz, J.A., Bar-On, Y., Kreider, E.F., Lu, C.L., Lorenzi, J.C., Feldmann, A., Braunschweig, M., Nogueira, L., Oliveira, T., et al. (2016). HIV-1 antibody 3BNC117 suppresses viral rebound in humans during treatment interruption. *Nature* *535*, 556–560.

Scheres, S.H., and Chen, S. (2012). Prevention of overfitting in cryo-EM structure determination. *Nat. Methods* *9*, 853–854.

Schoofs, T., Klein, F., Braunschweig, M., Kreider, E.F., Feldmann, A., Nogueira, L., Oliveira, T., Lorenzi, J.C., Parrish, E.H., Learn, G.H., et al. (2016). HIV-1 therapy with monoclonal antibody 3BNC117 elicits host immune responses against HIV-1. *Science* *352*, 997–1001.

- Schreiber, M., Wachsmuth, C., Müller, H., Hagen, C., Schmitz, H., and van Lunzen, J. (1996). Loss of antibody reactivity directed against the V3 domain of certain human immunodeficiency virus type 1 variants during disease progression. *J. Gen. Virol.* *77*, 2403–2414.
- Seaman, M.S., Janes, H., Hawkins, N., Grandpre, L.E., Devoy, C., Giri, A., Coffey, R.T., Harris, L., Wood, B., Daniels, M.G., et al. (2010). Tiered categorization of a diverse panel of HIV-1 Env pseudoviruses for assessment of neutralizing antibodies. *J. Virol.* *84*, 1439–1452.
- Shaik, M.M., Peng, H., Lu, J., Rits-Volloch, S., Xu, C., Liao, M., and Chen, B. (2019). Structural basis of coreceptor recognition by HIV-1 envelope spike. *Nature* *565*, 318–323.
- Shingai, M., Nishimura, Y., Klein, F., Mouquet, H., Donau, O.K., Plishka, R., Buckler-White, A., Seaman, M., Piatak, M., Jr., Lifson, J.D., et al. (2013). Antibody-mediated immunotherapy of macaques chronically infected with SHIV suppresses viraemia. *Nature* *503*, 277–280.
- Shingai, M., Donau, O.K., Plishka, R.J., Buckler-White, A., Mascola, J.R., Nabel, G.J., Nason, M.C., Montefiori, D., Moldt, B., Poignard, P., et al. (2014). Passive transfer of modest titers of potent and broadly neutralizing anti-HIV monoclonal antibodies block SHIV infection in macaques. *J. Exp. Med.* *211*, 2061–2074.
- Slieden, K., van Montfort, T., Ozorowski, G., Pritchard, L.K., Crispin, M., Ward, A.B., and Sanders, R.W. (2015). Engineering and Characterization of a Fluorescent Native-Like HIV-1 Envelope Glycoprotein Trimer. *Biomolecules* *5*, 2919–2934.
- Sok, D., and Burton, D.R. (2018). Recent progress in broadly neutralizing antibodies to HIV. *Nat. Immunol.* *19*, 1179–1188.
- Sok, D., van Gils, M.J., Pauthner, M., Julien, J.P., Saye-Francisco, K.L., Hsueh, J., Briney, B., Lee, J.H., Le, K.M., Lee, P.S., et al. (2014). Recombinant HIV envelope trimer selects for quaternary-dependent antibodies targeting the trimer apex. *Proc. Natl. Acad. Sci. USA* *111*, 17624–17629.
- Stewart-Jones, G.B., Soto, C., Lemmin, T., Chuang, G.Y., Druz, A., Kong, R., Thomas, P.V., Wagh, K., Zhou, T., Behrens, A.J., et al. (2016). Trimeric HIV-1- Env Structures Define Glycan Shields from Clades A, B, and G. *Cell* *165*, 813–826.
- Terwilliger, T.C., Sobolev, O.V., Afonine, P.V., and Adams, P.D. (2018). Automated map sharpening by maximization of detail and connectivity. *Acta Crystallogr. D Struct. Biol.* *74*, 545–559.

- Tiller, T., Meffre, E., Yurasov, S., Tsuiji, M., Nussenzweig, M.C., and Wardemann, H. (2008). Efficient generation of monoclonal antibodies from single human B cells by single cell RT-PCR and expression vector cloning. *J. Immunol. Methods* 329, 112–124.
- Unni, S., Huang, Y., Hanson, R.M., Tobias, M., Krishnan, S., Li, W.W., Nielsen, J.E., and Baker, N.A. (2011). Web servers and services for electrostatics calculations with APBS and PDB2PQR. *J. Comput. Chem.* 32, 1488–1491.
- van Anken, E., Sanders, R.W., Liscaljet, I.M., Land, A., Bontjer, I., Tillemans, S., Nabatov, A.A., Paxton, W.A., Berkhout, B., and Braakman, I. (2008). Only five of 10 strictly conserved disulfide bonds are essential for folding and eight for function of the HIV-1 envelope glycoprotein. *Mol. Biol. Cell* 19, 4298–4309.
- von Boehmer, L., Liu, C., Ackerman, S., Gitlin, A.D., Wang, Q., Gazumyan, A., and Nussenzweig, M.C. (2016). Sequencing and cloning of antigen-specific antibodies from mouse memory B cells. *Nat. Protoc.* 11, 1908–1923.
- Walker, L.M., and Burton, D.R. (2018). Passive immunotherapy of viral infections: ‘super-antibodies’ enter the fray. *Nat. Rev. Immunol.* 18, 297–308.
- Walker, B.D., and Yu, X.G. (2013). Unravelling the mechanisms of durable control of HIV-1. *Nat. Rev. Immunol.* 13, 487–498.
- Walker, L.M., Phogat, S.K., Chan-Hui, P.Y., Wagner, D., Phung, P., Goss, J.L., Wrin, T., Simek, M.D., Fling, S., Mitcham, J.L., et al.; Protocol G Principal Investigators (2009). Broad and potent neutralizing antibodies from an African donor reveal a new HIV-1 vaccine target. *Science* 326, 285–289.
- Walker, L.M., Huber, M., Doores, K.J., Falkowska, E., Pejchal, R., Julien, J.P., Wang, S.K., Ramos, A., Chan-Hui, P.Y., Moyle, M., et al.; Protocol G Principal Investigators (2011). Broad neutralization coverage of HIV by multiple highly potent antibodies. *Nature* 477, 466–470.
- West, A.P., Jr., Diskin, R., Nussenzweig, M.C., and Bjorkman, P.J. (2012). Structural basis for germ-line gene usage of a potent class of antibodies targeting the CD4-binding site of HIV-1 gp120. *Proc. Natl. Acad. Sci. USA* 109, E2083–E2090.
- West, A.P., Jr., Scharf, L., Horwitz, J., Klein, F., Nussenzweig, M.C., and Bjorkman, P.J. (2013). Computational analysis of anti-HIV-1 antibody neutralization panel data to identify potential functional epitope residues. *Proc. Natl. Acad. Sci. USA* 110, 10598–10603.
- Williams, L.D., Ofek, G., Schaetzle, S., McDaniel, J.R., Lu, X., Nicely, N.I., Wu, L., Loughheed, C.S., Bradley, T., Louder, M.K., et al. (2017). Potent and broad HIV-neutralizing antibodies in memory B cells and plasma. *Sci. Immunol.* 2, eaal2200.

- Wu, X., Yang, Z.Y., Li, Y., Hogerkorp, C.M., Schief, W.R., Seaman, M.S., Zhou, T., Schmidt, S.D., Wu, L., Xu, L., et al. (2010). Rational design of envelope identifies broadly neutralizing human monoclonal antibodies to HIV-1. *Science* 329, 856–861.
- Xu, L., Pegu, A., Rao, E., Doria-Rose, N., Beninga, J., McKee, K., Lord, D.M., Wei, R.R., Deng, G., Louder, M., et al. (2017). Trispecific broadly neutralizing HIV antibodies mediate potent SHIV protection in macaques. *Science* 358, 85–90.
- Xu, K., Acharya, P., Kong, R., Cheng, C., Chuang, G.Y., Liu, K., Louder, M.K., O’Dell, S., Rawi, R., Sastry, M., et al. (2018). Epitope-based vaccine design yields fusion peptide-directed antibodies that neutralize diverse strains of HIV-1. *Nat. Med.* 24, 857–867.
- Yang, X., Farzan, M., Wyatt, R., and Sodroski, J. (2000). Characterization of stable, soluble trimers containing complete ectodomains of human immunodeficiency virus type 1 envelope glycoproteins. *J. Virol.* 74, 5716–5725.
- Ye, J., Ma, N., Madden, T.L., and Ostell, J.M. (2013). IgBLAST: an immunoglobulin variable domain sequence analysis tool. *Nucleic Acids Res.* 41, W34-40.
- Yoon, H., Macke, J., West, A.P., Jr., Foley, B., Bjorkman, P.J., Korber, B., and Yusim, K. (2015). CATNAP: a tool to compile, analyze and tally neutralizing antibody panels. *Nucleic Acids Res.* 43 (W1), W213-9.
- Zhang, K. (2016). Gctf: Real-time CTF determination and correction. *J. Struct. Biol.* 193, 1–12.
- Zhang, Y.J., Hatzioannou, T., Zang, T., Braaten, D., Luban, J., Goff, S.P., and Bieniasz, P.D. (2002). Envelope-dependent, cyclophilin-independent effects of glycosaminoglycans on human immunodeficiency virus type 1 attachment and infection. *J. Virol.* 76, 6332–6343.
- Zheng, S.Q., Palovcak, E., Armache, J.P., Verba, K.A., Cheng, Y., and Agard, D.A. (2017). MotionCor2: anisotropic correction of beam-induced motion for improved cryo-electron microscopy. *Nat. Methods* 14, 331–332.
- Zhou, T., Xu, L., Dey, B., Hessel, A.J., Van Ryk, D., Xiang, S.H., Yang, X., Zhang, M.Y., Zwick, M.B., Arthos, J., et al. (2007). Structural definition of a conserved neutralization epitope on HIV-1 gp120. *Nature* 445, 732–737.
- Zhou, T., Georgiev, I., Wu, X., Yang, Z.Y., Dai, K., Finzi, A., Kwon, Y.D., Scheid, J.F., Shi, W., Xu, L., et al. (2010). Structural basis for broad and potent neutralization of HIV-1 by antibody VRC01. *Science* 329, 811–817.
- Zhou, T., Zhu, J., Wu, X., Moquin, S., Zhang, B., Acharya, P., Georgiev, I.S., Altae-Tran, H.R., Chuang, G.Y., Joyce, M.G., et al.; NISC Comparative Sequencing Program (2013).

Multidonor analysis reveals structural elements, genetic determinants, and maturation pathway for HIV-1 neutralization by VRC01-class antibodies. *Immunity* 39, 245–258.

Zhou, T., Lynch, R.M., Chen, L., Acharya, P., Wu, X., Doria-Rose, N.A., Joyce, M.G., Lingwood, D., Soto, C., Bailer, R.T., et al.; NISC Comparative Sequencing Program (2015). Structural Repertoire of HIV-1-Neutralizing Antibodies Targeting the CD4 Supersite in 14 Donors. *Cell* 161, 1280–1292.

Zivanov, J., Nakane, T., Forsberg, B.O., Kimanius, D., Hagen, W.J.H., Lindahl, E., and Scheres, S.H.W. (2018). New tools for automated high-resolution cryo-EM structure determination in RELION-3. *eLife* 7, e42166.

**Supplemental Material**

Additional Supplementary Tables are available online at <https://doi.org/10.1016/j.cell.2020.01.010>.

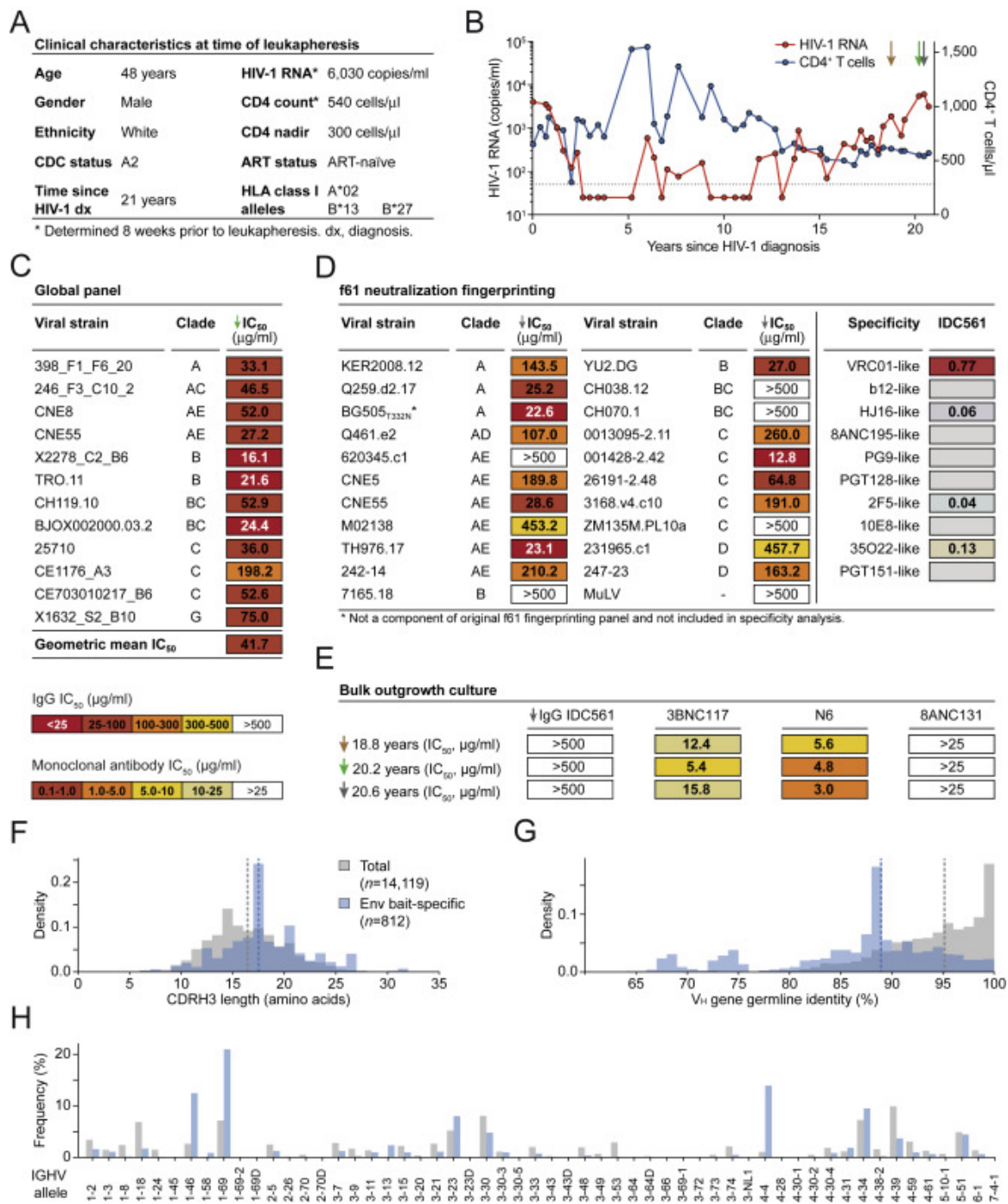


**Figure S1.** Clinical Characteristics, Neutralizing IgG Activity, and B Cell Repertoire of Individual IDC561, Related to Figure 1. (A) Clinical characteristics of IDC561 at the time of leukapheresis from which monoclonal antibodies were isolated. (B) Plasma HIV-1 RNA copies (left y axis) and CD4<sup>+</sup> T cell counts (right y axis). Arrows indicate sample collections. Monoclonal antibodies were isolated from the last indicated sampling time point. Dashed line indicates HIV-1 RNA quantification limit. (C) Neutralizing activity of IDC561 serum IgG against global panel. (D) Neutralizing activity of IDC561 serum IgG against f61 fingerprinting panel and BG505<sub>T332N</sub> (left, colors as in C). Right panels show delineation scores of f61 panel-based computational epitope mapping. (E) Neutralizing activity of IDC561 serum IgG and monoclonal bNAbs against outgrowth culture-derived viruses from bulk CD4<sup>+</sup> T cells obtained at indicated time points (colors as in C). (F–H) Comparison of total B cell repertoire of IDC561 and Env-reactive B cells, indicating (F) CDRH3 lengths, (G) V<sub>H</sub> gene germline identity, and (H) V<sub>H</sub> allele distribution. Dashed lines indicate medians.

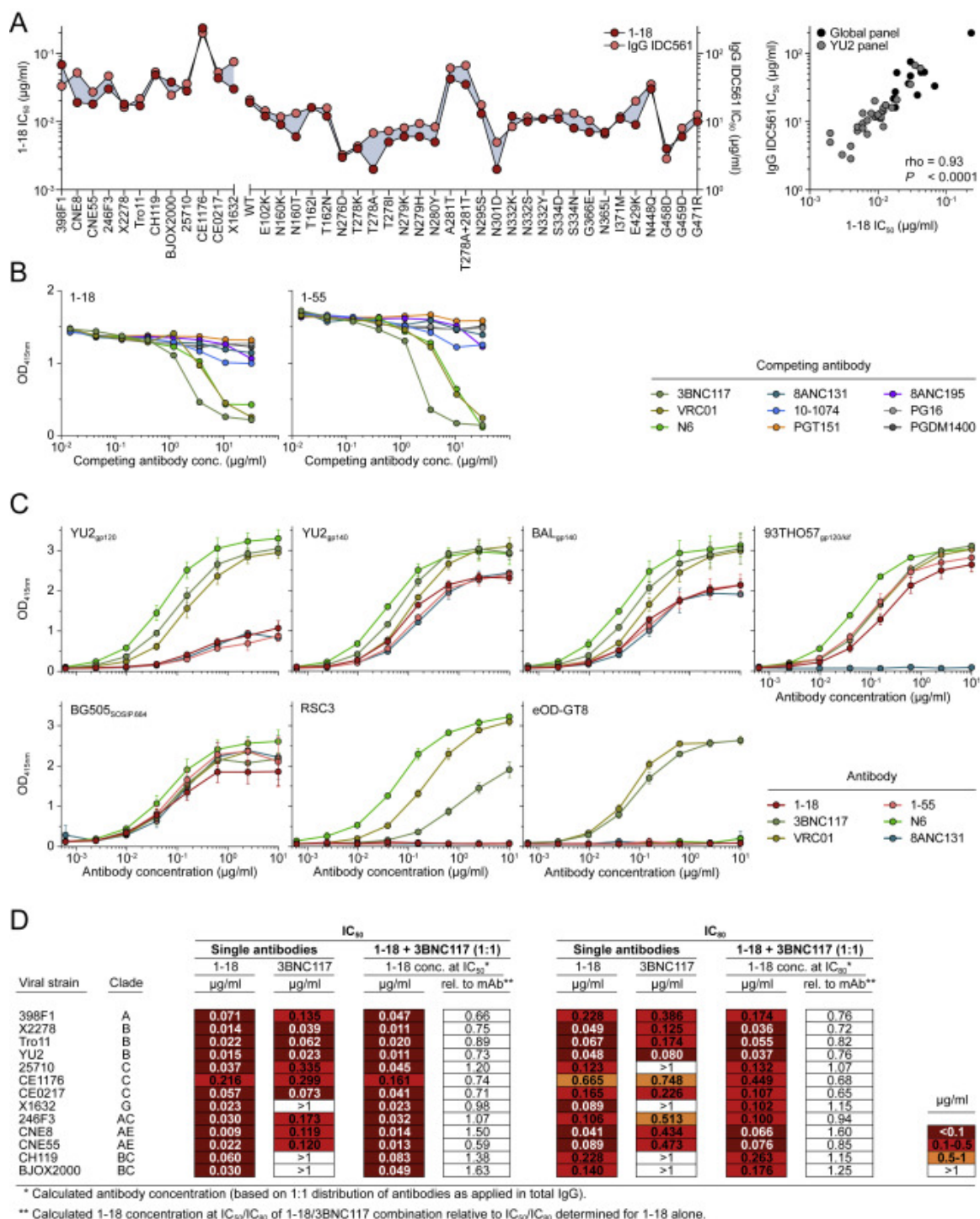


**Figure S2.** Neutralization and ELISA Binding Profiles, Related to Figures 1 and 2. (A) Left panel indicates neutralizing activity of 1-18 (left y axis) compared to serum IgG of donor IDC561 (right y axis) against the global pseudovirus panel (left x axis) and a 30-strain YU2

pseudovirus mutant panel (right x axis), with pseudoviruses indicated on the x axis. Right panel indicates correlation and calculated Spearman's rho. (B) Competition ELISAs indicating binding of 1-18 (left) and 1-55 (right) to BG505<sub>SOSIP.664</sub> following an incubation with increasing concentrations of the indicated competing antibodies. (C) ELISAs of 1-18, 1-55, and additional CD4bs antibodies against the indicated HIV-1 Env antigens. Circles show means and error bars indicate standard deviation. (D) Neutralizing activity of 1-18, 3BNC117, and the combination of both (mixed at a 1:1 ratio) against the global pseudovirus panel and YU2. Single antibodies were tested up to a concentration of 1 µg/ml, the combination up to a concentration of 2 µg/ml (total IgG amount).

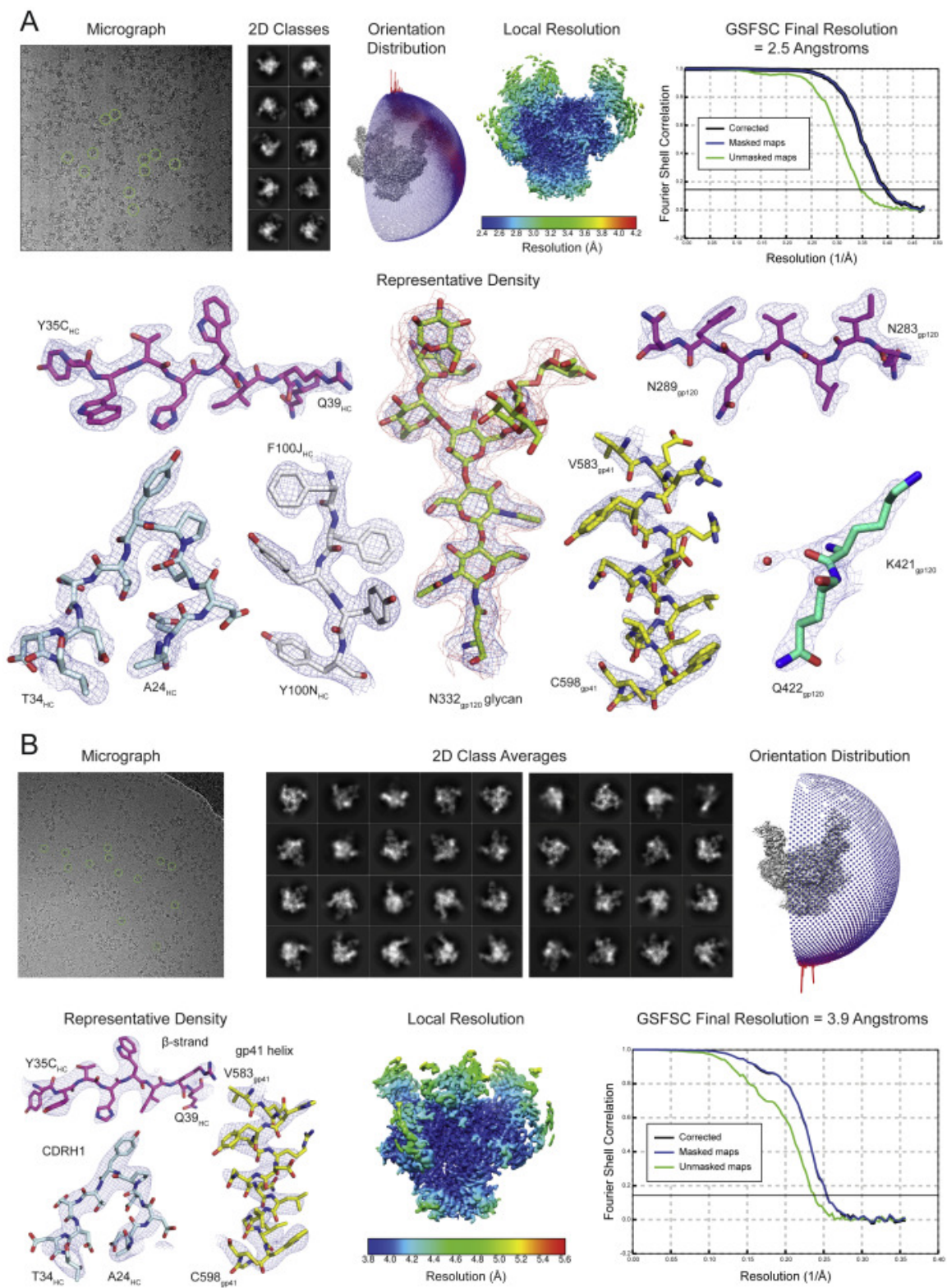
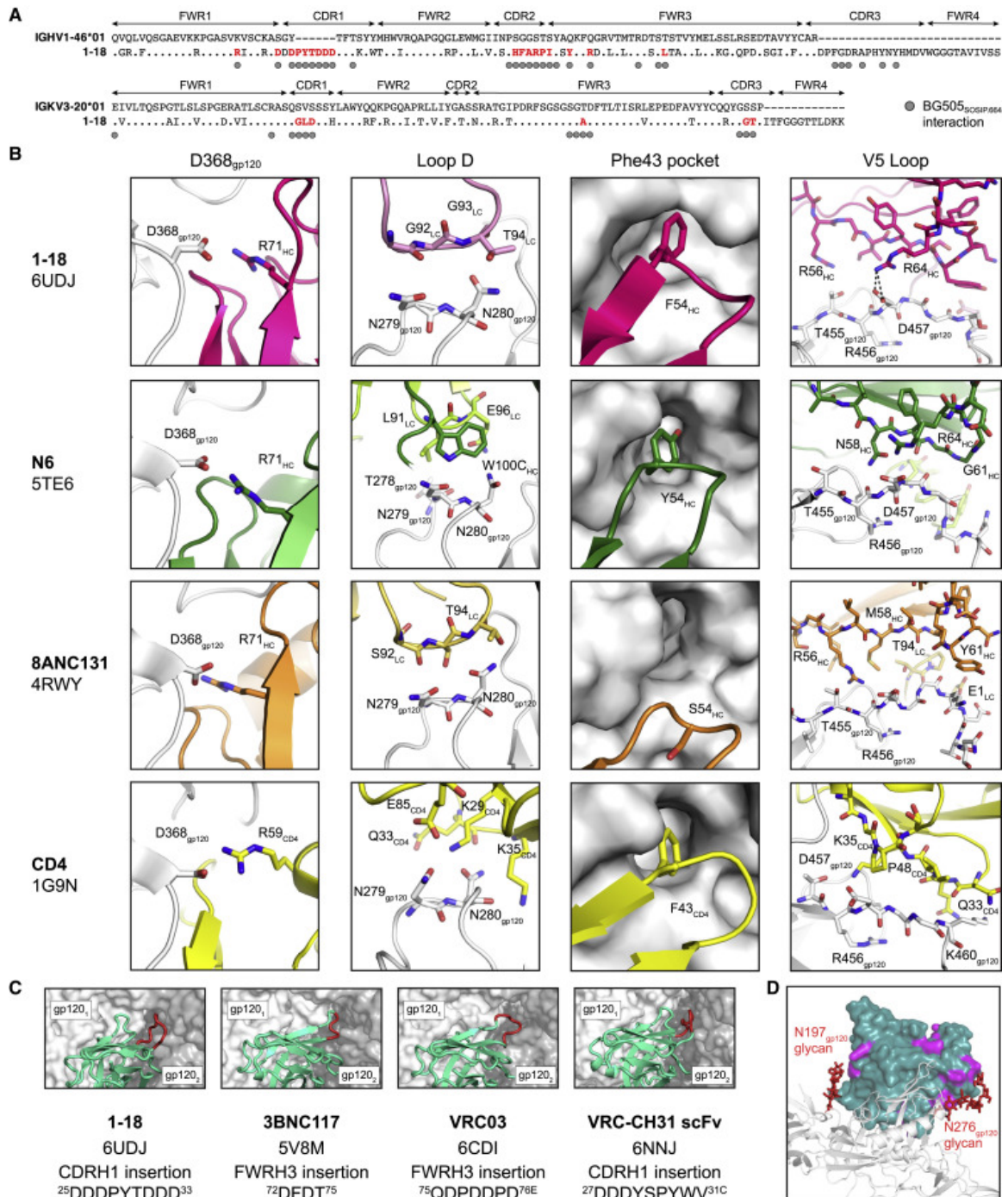


**Figure S3.** Cryo-EM Data Collection and Processing, Related to Figure 3. (A–B) A micrograph with examples of picked particles, selected two-dimensional class averages, an orientation distribution image, a local resolution graphic, a GSFSC resolution plot, and representative densities for protein and *N*-linked glycan regions are shown for the (A) 1-18–BG505–10-1074 and (B) 1-55–RC1–10-1074 complexes.



light chains. PDB codes are indicated on the left. (C) Comparison of Env-interactions of bNAbs with Asp-rich insertions in CDRH1 or FWRH3 contacting the adjacent gp120 protomer. Each SOSIP.664 trimer is shown as semi-transparent surface with the primary gp120 protomer in white and the adjacent gp120 in gray. V<sub>H</sub>V<sub>L</sub> regions are shown in teal with insertions in red. PDB code, insertion location, and insertion sequence are listed. (D) Differences between Fabs of 1-18 and 1-55. One 1-18 V<sub>H</sub>V<sub>L</sub> (dark green surface) is shown bound to one gp120 (gray cartoon). Locations of residues varying between 1-18 and 1-55 are highlighted in magenta. Glycans at positions N197<sub>gp120</sub> and N276<sub>gp120</sub> are shown as red sticks. 1-55 Fabs were based on earlier sequence variants and contained primer-induced mutations at the start and end of the V genes (for a total of 2 aa [V<sub>H</sub>] and 4 aa [V<sub>K</sub>] mutations).

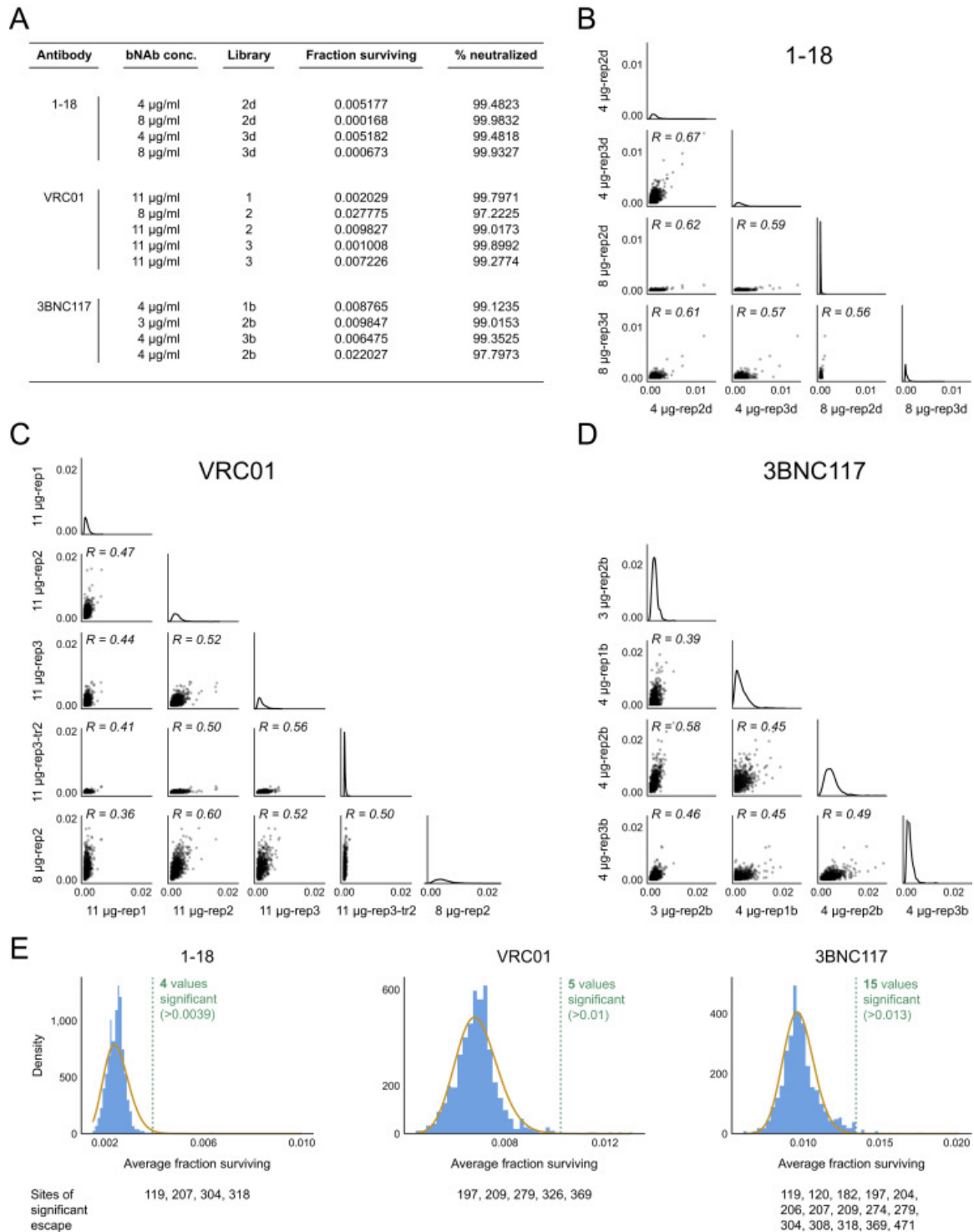


**Figure S5.** Mutational Antigenic Profiling: Fractions Surviving, Correlation between Replicates, and Determination of Sites of Significant Escape, Related to Figure 5. (A) Antibody concentration during selection, batch of mutant virus library, and fraction of

library surviving antibody selection for each biological replicate. (B–D) Correlation between biological replicate selections of average excess fraction surviving at each site in the presence of (B) 1-18, (C) VRC01, and (D) 3BNC117. (E) Distribution of average fraction surviving at each site for each antibody (blue bars). The yellow line overlays the gamma distribution fit using robust regression to site fraction surviving data. Dotted lines mark sites that fall beyond this distribution at a false discovery rate of 0.01. Number of sites beyond this cutoff is labeled in green and individual sites are listed at the bottom. Data for 3BNC117 and VRC01 are from Dingens et al. (2019).

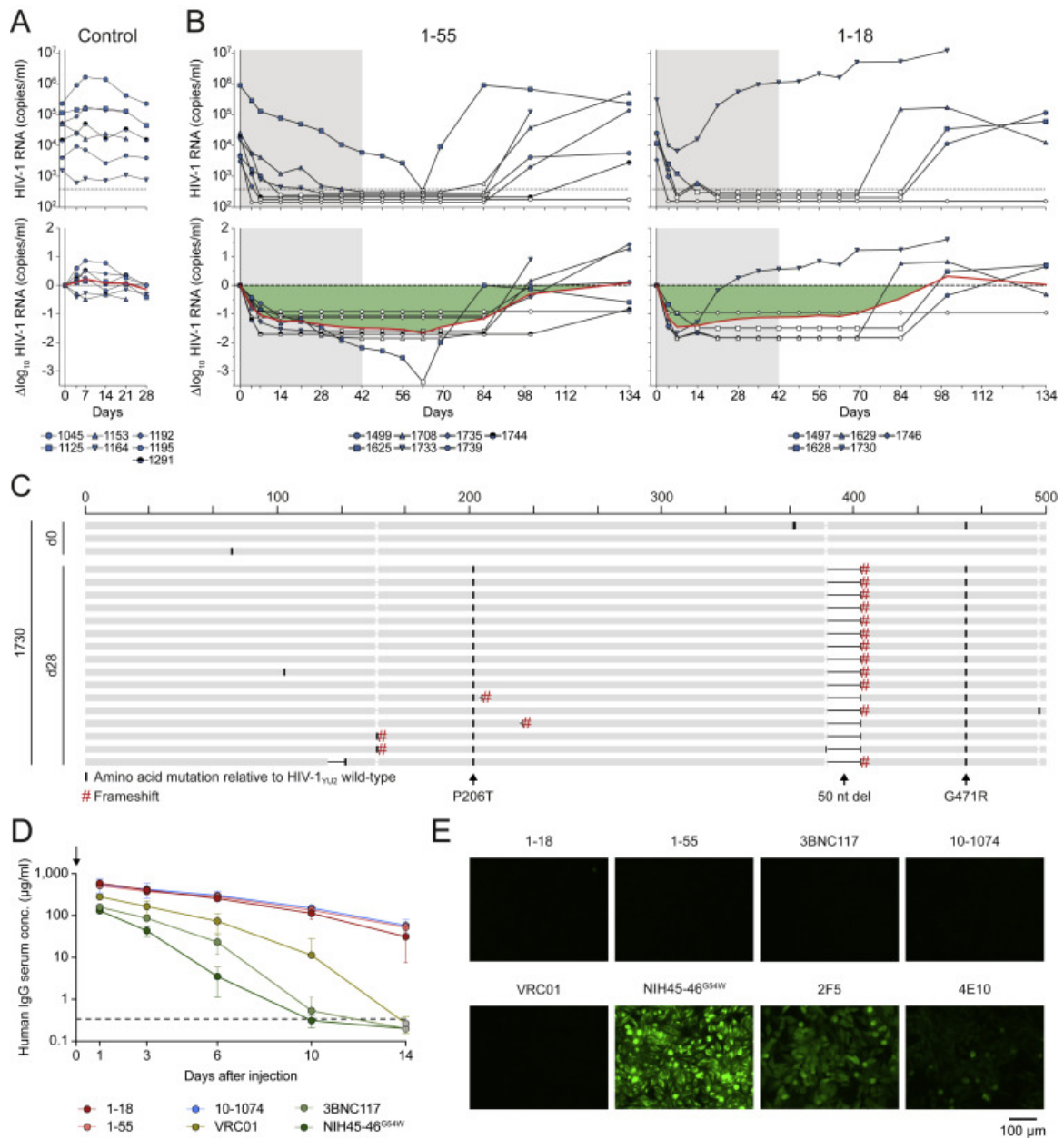


**Figure S6.** 1-18 and 1-55 Antiviral Activity in HIV-1<sub>YU2</sub>-Infected Humanized Mice, Pharmacokinetics, and Autoreactive Properties, Related to Figures 6 and 7. (A) Absolute HIV-1 RNA copies (top) and  $\log_{10}$  viral load changes (bottom) in untreated HIV-1<sub>YU2</sub>-infected humanized mice. Red line shows average  $\log_{10}$  viral load change compared to baseline. Dashed line in top panel indicates quantitation limit of accuracy (384 copies/ml). (B) Absolute HIV-1 RNA copies (top) and  $\log_{10}$  viral load changes (bottom) in HIV-1<sub>YU2</sub>-infected humanized mice treated with 1-55 (left) or 1-18 (right). Grey shading indicates duration of bNAb therapy. Dashed lines in top panels indicate quantitation limit of accuracy (384 copies/ml). Data points in white indicate viral loads < 384 copies/ml. Red lines show average  $\log_{10}$  viral load change compared to baseline. (C) Alignment of plasma SGS-

derived *env* sequences from mouse 1730 obtained on day 0 (top) and day 28 (bottom) based on nucleotide sequences. Indicated changes are amino acid mutations (black bars), mutations resulting in frameshifts (red hash), and nucleotide deletions (black horizontal lines) compared to YU2 wild-type sequence. Amino acid numbering on top is based on HIV-1<sub>YU2</sub>, and indicated mutations are numbered based on HIV-1<sub>HXB2</sub>. (D) Serum human IgG levels in NRG mice after intravenous injection of 0.5 mg of antibody on day 0 (left). Data are represented as mean  $\pm$  standard deviation, respectively. (E) HEp-2 cell reactivity using the indicated monoclonal antibodies at a concentration of 100  $\mu$ g/ml.

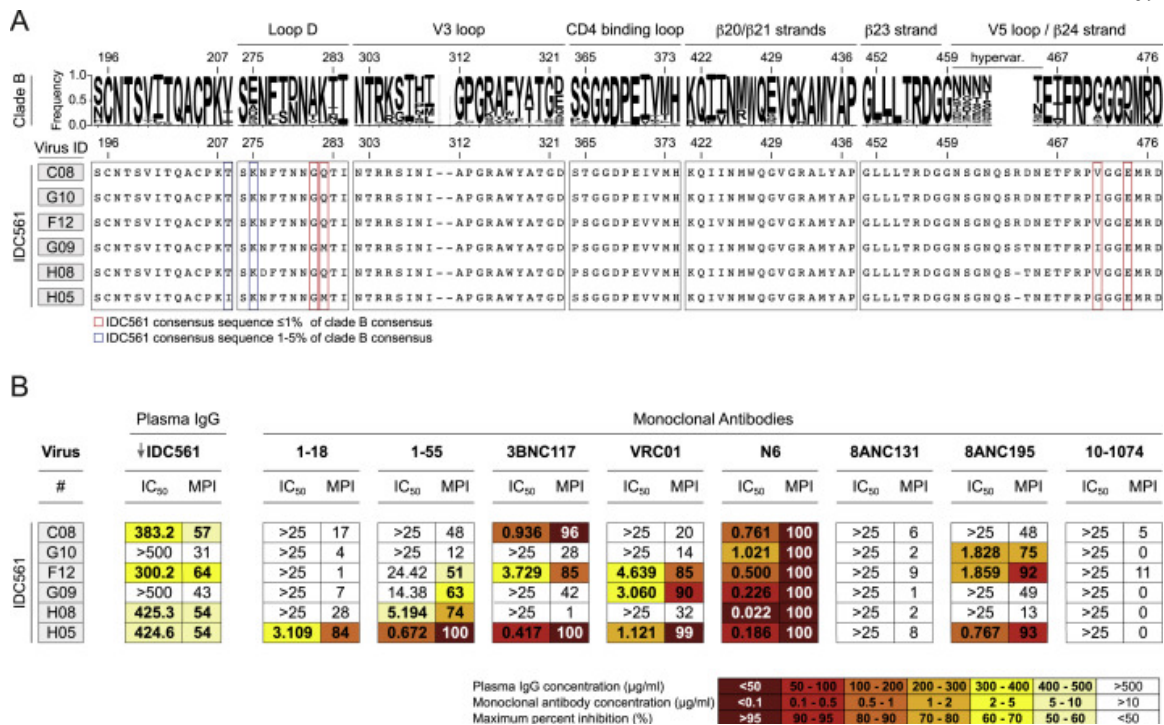


**Figure S7.** Plasma SGS-Derived *env* Sequences Obtained from Donor IDC561, Related to Figures 1 and S1. (A) Letter heights indicate amino acid frequency among 2,351 clade B sequences obtained from the Los Alamos National Laboratory (LANL) database (top). Bottom panels show selected sites of plasma SGS-derived *env* sequences obtained from IDC561 from the leukapheresis sample from which 1-18 and 1-55 were isolated. Boxes indicate amino acids for which IDC561 consensus sequence is represented in  $\leq 1\%$  (red) or 1%–5% (blue) of the LANL clade B sequences. Numbering relative to HIV-1<sub>HXB2</sub> reference strain. (B) Neutralization sensitivity of pseudoviruses based on IDC561 sequences indicated in (A). Maximum percent inhibition (MPI) determined when tested at maximum concentrations of 500 µg/ml (purified IgG) or 25 µg/ml (monoclonal antibodies). Plasma IgG was obtained at the time of leukapheresis from which 1-18 was isolated.

## IMMUNIZATION EXPANDS B CELLS SPECIFIC TO HIV-1 V3 GLYCAN IN MICE AND MACAQUES

Escolano, A.\*, Gristick, H.B.\*, **Abernathy, M.E.**, Merckenschlager, J., Gautam, R., Oliveira, T.Y., Pai, J., West, A.P., Barnes, C.O., Cohen, A.A., Wang, H., Golijanin, J., Yost, D., Keeffe, J.R., Wang, Z., Zhao, P., Yao, K-H., Bauer, J., Nogueira, L., Gao, H., Voll, A.V., Montefiori, D.C., Seaman, M.S., Gazumyan, A., Silva, M., McGuire, A.T., Stamatatos, L., Irvine, D.J., Wells, L., Martin, M.A., Bjorkman, P.J., Nussenzweig, M.C. Immunization expands HIV-1 glycan patch-specific B-cells in mice and macaques. *Nature*, **570**: 468-73 (2019). doi:10.1038/s41586-019-1250-z

\* *Equal Contributions*

### Summary

Broadly neutralizing monoclonal antibodies protect against infection with HIV-1 in animal models, suggesting that a vaccine that elicits these antibodies would be protective in humans. However, it has not yet been possible to induce adequate serological responses by vaccination. Here, to activate B cells that express precursors of broadly neutralizing antibodies within polyclonal repertoires, we developed an immunogen, RC1, that facilitates the recognition of the variable loop 3 (V3)-glycan patch on the envelope protein of HIV-1. RC1 conceals non-conserved immunodominant regions by the addition of glycans and/or multimerization on virus-like particles. Immunization of mice, rabbits and rhesus macaques with RC1 elicited serological responses that targeted the V3-glycan patch. Antibody cloning and cryo-electron microscopy structures of antibody–envelope complexes confirmed that immunization with RC1 expands clones of B cells that carry the anti-V3-glycan patch antibodies, which resemble precursors of human broadly neutralizing antibodies. Thus, RC1 may be a suitable priming immunogen for sequential vaccination strategies in the context of polyclonal repertoires.

## Introduction

Single-cell antibody cloning from human donors who are infected with HIV-1 revealed that broadly neutralizing antibodies (bNAbs) have undergone unusually extensive somatic mutations<sup>1-4</sup>. Moreover, the high degree of somatic mutations is essential for binding to the native HIV-1 envelope (Env) spike and for the neutralizing activity of bNAbs<sup>5</sup>. The accumulation of large numbers of mutations suggests that bNAbs evolve in response to iterative rounds of somatic hypermutation and selection in germinal centres<sup>6</sup>. Studies in humans revealed that this occurs in response to viral escape variants that arise from antibody pressure<sup>4</sup>. Together, these observations suggest that vaccination to elicit bNAbs requires a series of sequential immunogens starting with an immunogen that induces the expansion<sup>7</sup> of B lymphocytes expressing appropriate germline precursors<sup>8</sup>.

Sequential immunization to guide bNAb development was demonstrated in genetically modified mice that carry inferred-germline precursors of human bNAbs<sup>8,9</sup>. However, the priming immunogens that were used to initiate the response failed to activate and expand B cells that expressed inferred bNAb precursors in animals with polyclonal antibody repertoires. Thus, a goal of HIV-1 vaccine development has been to design immunogens that recruit B cells that express bNAb precursors into germinal centre reactions in animals with polyclonal repertoires.

The germline-targeting approach to immunogen design focuses on producing immunogens that bind with high affinity to specific bNAb precursors, the rationale being that the recruitment of B cells to germinal centres is in part dependent on receptor affinity for antigen<sup>10-14</sup>. However, this methodology effectively limits the repertoire of recruited B cells qualitatively and quantitatively. Moreover, it fails to account for the findings that each germinal centre accommodates different founder B cells with a wide range of affinities and that entry into the germinal centre is limited by competition and not absolute affinity<sup>7,10</sup>.

Here we describe RC1, an immunogen designed to recruit and expand diverse V3-glycan-specific B cells by improving accessibility of the V3-glycan patch epitope, which includes a group of high-mannose and complex-type N-glycans that surround V3 (gp120 residues

N133, N137, N156, N295, N301, N332, N339, N385 and N392)<sup>15</sup>. bNAbs that target this site, including PGT121<sup>16</sup>, 10-1074<sup>17</sup> and BG18<sup>18</sup>, reach through these glycans using elongated heavy chain complementarity-determining region (CDR) 3 (CDRH3) loops and portions of light chain CDRs 1 and 3 (CDRL1 and CDRL3) to contact the highly conserved GDIR (G324-D325-I326-R327) motif at the base of V3<sup>19</sup>. Here we show that RC1 activates and expands a diverse group of B cells expressing antibodies that resemble human V3-glycan patch bNAb precursors in mice, rabbits and rhesus macaques.

## **Results & Discussion**

### **RC1 facilitates antibody binding to the V3-glycan patch**

RC1 was designed using 11MUTB<sup>20</sup>, a modified native-like Env trimer (SOSIP.664) derived from the clade A/E BG505 Env<sup>21</sup>, as a template. Compared to BG505, 11MUTB includes substitutions in V1 and lacks potential N-linked glycosylation sites (PNGSs) at N133 and N137<sup>20</sup> (Fig. 1a). We reasoned that removal of the N156 PNGS (N156Q) to create RC1 would facilitate recognition of the V3-glycan patch by increasing accessibility of V1 residues that interact with V3-glycan bNAbs<sup>22,23</sup>. Consistent with this idea, the absence of the N156 PNGS enhances neutralization by PGT121 and 10-1074, whereas the absence of other glycans, such as N301 or N137, reduces neutralization (Extended Data Fig. 1a). In addition, we hypothesized that removal of the N156 glycan, which includes negatively charged terminal sialic acids<sup>22,24</sup>, would produce a more electrostatically neutral Env surface that could facilitate the binding of the largely neutral precursor of PGT121 and 10-1074 (inferred germline PGT121/10-1074)<sup>25</sup>.

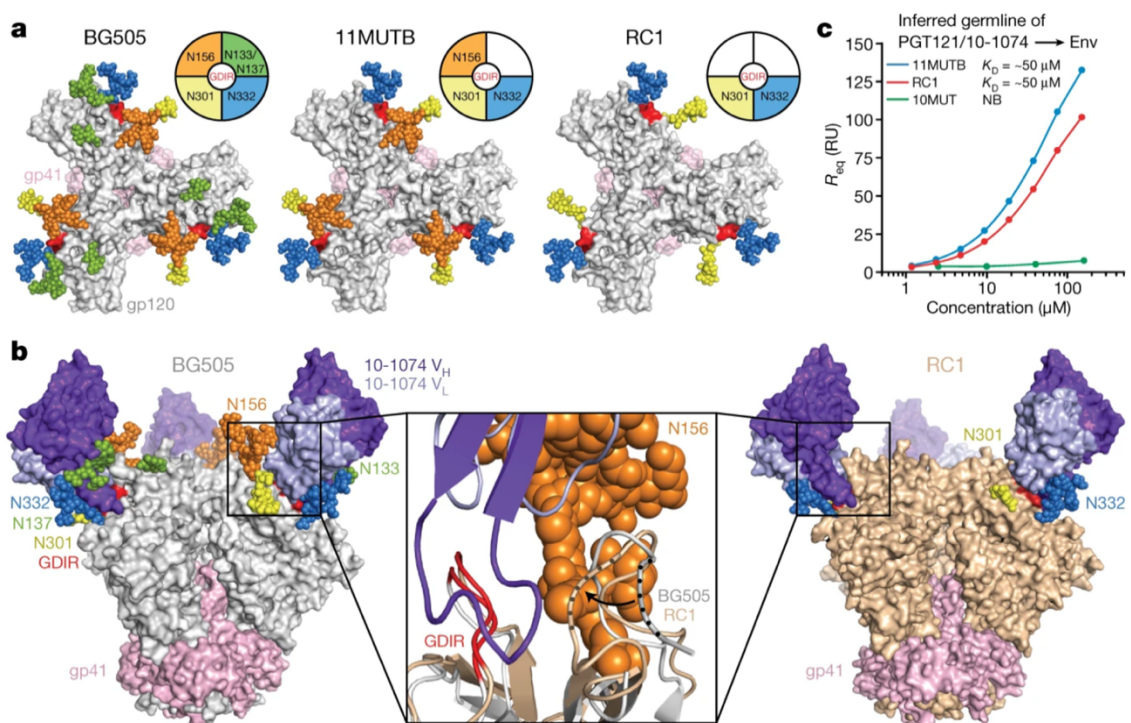


**Figure 1.** Characterization of the RC1 immunogen. **a**, *N*-glycans (coloured spheres) and GDIR motifs (red surfaces) mapped onto BG505 (Protein Data Bank (PDB) code 5T3Z) (N137 glycan from PDB 5FYL) in the top-down orientation. **b**, Left and right, side views of structures of BG505 and RC1 complexed with 10-1074 (glycan atoms are coloured spheres). Middle, superimposition of the boxed regions with protein in cartoon representations. Dark and light purple, 10-1074 V<sub>H</sub> and V<sub>L</sub>, respectively; red, GDIR; wheat, other portions of RC1; grey, BG505; orange spheres, N156 glycan. Regions of V1 showing displacement (gp120 residues 139–140) are indicated by dots and an arrow. **c**, Surface plasmon resonance (SPR) data for PGT121/10-1074 binding to Env trimers. NB, no binding above background; RU, response units. Representative plot from three independent experiments.

To characterize RC1, we compared its antigenic properties to BG505 (Extended Data Fig. 1b) and solved a 4.0 Å single-particle cryo-electron microscopy (cryo-EM) structure of RC1 complexed with 10-1074, comparing it to a BG505-10-1074 structure<sup>22</sup> (Fig. 1b, Extended Data Fig. 2 and Extended Data Table 1). Both structures showed three 10-1074 antigen-binding fragments (Fabs) bound to the V3-glycan patch epitopes of a closed Env trimer (Fig. 1b). Compared with BG505, the V1 loop in RC1 included more ordered residues and was shifted towards the 10-1074 CDRH3, allowing for increased interactions between RC1 and 10-1074 (Fig. 1b).

Despite structural changes in V1—which resulted from deletion of the N156 glycan (Fig. 1b)—the inferred germline PGT121/10-1074<sup>17</sup> bound to RC1 and 11MUTB with similar affinities (dissociation constant ( $K_D$ ) values of approximately 50  $\mu$ M; Fig. 1c), and priming immunizations with RC1 and 11MUTB elicited comparable V3-glycan-specific serological responses in knock-in (KI) mice that carried genes encoding the inferred germline of PGT121/10-1074<sup>9</sup> (Fig. 2a–c). Thus, RC1 exhibited structural changes resulting from N156 glycan deletion that did not affect its affinity for the inferred germline PGT121/10-1074.

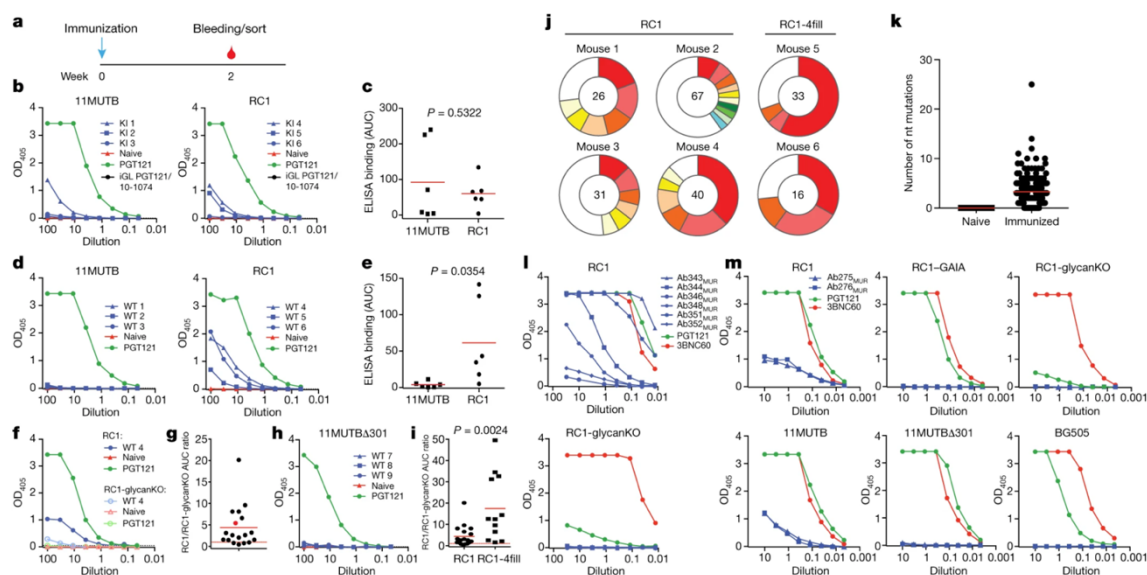


**Figure 2.** Wild-type mouse immunization with RC1 elicits V3-glycan patch antibodies. **a**, Immunization protocol. **b**, **d**, **f**, **h**, Representative ELISAs showing serum binding to indicated immunogens. Controls include naive serum (red), purified PGT121 (green) and inferred germline (iGL) of PGT121/10-1074 (black). OD<sub>405</sub>, optical density at 405 nm. **b**, The inferred germline of PGT121 knock-in (KI) mice<sup>9</sup>. **d**, **f**, **h**, Wild-type (WT) mice. **c**, **e**, Area under the curve (AUC) for ELISAs in **b** and **d**, respectively, but combined results from two experiments using three or four mice each. Each dot represents serum from one mouse. **f**, Binding to RC1 and RC1-glycanKO. **g**, Ratio of the AUC for RC1 and RC1-glycanKO ELISAs from seven experiments with two or three mice immunized with RC1. Red dot corresponds to mouse WT 4 in **f**. **i**, Ratio of the AUC for RC1 and RC1-glycanKO ELISAs for wild-type mice immunized with RC1 (seven experiments) or RC1-4fill (five experiments). **j**, Pie charts show clonal expansion of RC1-binding B cells in the germinal centre. Coloured slices are proportional to the number of clonal relatives. White indicates single IgV<sub>H</sub> sequences. The number of heavy chains analysed is indicated in the centre. **k**, IgH nucleotide (nt) mutations from naive and RC1 immunized mice in **j**. **l**, ELISA binding

of representative monoclonal antibodies from RC1-immunized mice to RC1 and RC1-glycanKO. **m**, ELISA binding of Ab275<sub>MUR</sub> and Ab276<sub>MUR</sub> to indicated Env proteins. **c, e, i**, Unpaired *t*-tests. **c, e, g, i, k**, Data are mean and each dot is an individual mouse (**c, e, g, i**) or an individual sequence (**k**).

### **RC1 elicits V3-glycan antibodies in wild-type mice**

To determine whether RC1 can activate B cells carrying antibodies that are specific to the V3-glycan patch in wild-type mice, we immunized C57BL/6J mice once with RC1 or 11MUTB (Fig. 2a). 11MUTB did not produce a measurable serological response, but RC1-immunized mice showed reproducible anti-V3-glycan-patch-specific serological responses as shown by enzyme-linked immunosorbent assays (ELISAs), in which we compared binding to RC1 and a mutant variant of RC1 (RC1-glycanKO) that lacks two V3 PNGSs (N301 and N332) that are critical for human V3-glycan patch bNAbs (Fig. 2d–g and Extended Data Table 2). Moreover, serum from the RC1-immunized mice cross-reacted with 11MUTB but not with the more native-like Env 10MUT<sup>20</sup> or with BG505 (Extended Data Fig. 3a). The improved immunogenicity of the V3-glycan patch epitope of RC1 results from specific removal of the N156 glycan from 11MUTB, because removal of a nearby glycan at N301 that is also part of the glycan patch (11MUTB $\Delta$ 301) (Extended Data Table 2) failed to induce detectable serological responses (Fig. 2h). We conclude that, in contrast to 11MUTB and 11MUTB $\Delta$ 301, RC1 elicits V3-glycan-specific serological responses in wild-type mice.

To reduce antibody responses to off-target epitopes<sup>26–29</sup> and further focus responses on the V3-glycan patch, we produced an RC1 variant, RC1-4fill, by introducing PNGSs to add glycans to gp120 positions 230, 241, 289 and 344 (Extended Data Fig. 4). Compared with RC1, RC1-4fill elicited serological responses that were more focused on the V3-glycan patch in wild-type mice (Fig. 2i). We conclude that RC1-4fill focuses antibody responses to the V3-glycan patch.

### **Expansion of V3-glycan-specific B cells in mice**

To further characterize the humoral responses elicited by RC1 and RC1-4fill, we sequenced antibody genes from single B cells from the germinal centre that bound to RC1 but not RC1-glycanKO (Extended Data Fig. 3b). All analysed RC1- and RC1-4fill-immunized mice

showed expansion of B cell clones in the germinal centre (Fig. 2a, j). The expanded clones predominantly expressed heavy-chain V genes  $V_{H5-6}$ ,  $V_{H9-3}$  and  $V_{H2-9}$ , and light chain genes  $V_{K3-4}$  and  $V_{K14-111}$  (Fig. 2j, Extended Data Table 4 and Supplementary Tables 1, 2). The CDRH3 sequences in expanded clones showed similarities to human V3-glycan patch bNAbs, such as Tyr-rich or RXY motifs and longer-than-average CDRH3 sequences (Extended Data Table 4 and Supplementary Table 1). Consistent with a single immunization, the  $V_H$  genes of the expanded clones had an average of 3.2 nucleotide mutations (Fig. 2k and Supplementary Table 1).

We mapped the target sites of these antibodies by ELISA against RC1 and RC1 mutant proteins. A diverse group of monoclonal antibodies showed V3-glycan-patch-specific binding (Fig. 2l). Further characterization of two mouse (MUR) antibodies, Ab275<sub>MUR</sub> and Ab276<sub>MUR</sub>, showed that they bind to the V3-glycan patch of RC1 (Ab275<sub>MUR</sub>,  $K_D \sim 30$  nM) in a GDIR- and N301-glycan-dependent manner, and both retained binding to 11MUTB (Ab275<sub>MUR</sub>,  $K_D \sim 230$  nM), demonstrating accommodation of the N156 glycan, whereas neither antibody bound to BG505 or a peptide that covers the crown of the V3 loop (Fig. 2m, Extended Data Table 2 and Extended Data Fig. 3c, d). Acquired mutations were essential for binding, because RC1 did not bind to the Ab276<sub>MUR</sub>-reverted inferred germline (Extended Data Fig. 3e). Consistent with a single immunization, neither Ab275<sub>MUR</sub> nor Ab276<sub>MUR</sub> showed detectable neutralizing activity against a panel of tier 1B and tier 2 HIV-1 isolates in assays using the TZM-bl reporter cell line. We conclude that RC1 and RC1-4fill expand mouse B cell clones expressing antibodies that target the V3-glycan patch.

### **V3-glycan antibody responses in rabbits and macaques**

To enhance potential avidity effects and limit exposure of off-target epitopes at the Env base, we multimerized RC1-4fill on virus-like particles (VLPs) using the SpyTag–SpyCatcher system<sup>30,31</sup> (Fig. 3a, b). VLPs were used to prime rabbits and rhesus macaques. Single immunizations of 4 rabbits and 16 macaques with VLP-RC1-4fill elicited serological responses that were partially specific for the V3-glycan patch in all animals (Fig. 3c–f and Extended Data Fig. 5a). Serum from macaques primed with VLP-RC1-4fill showed

sequentially reduced binding to the more native-like immunogens 11MUTB and 10MUT<sup>20</sup> (Extended Data Fig. 5b) and no neutralizing activity against a small panel of HIV-1 isolates that included fully glycosylated tier 2 and glycan-deleted viruses (Extended Data Table 3). Thus, VLP-RC1-4fill elicited robust serological responses that mapped in part to the V3-glycan patch in rabbits and rhesus macaques.

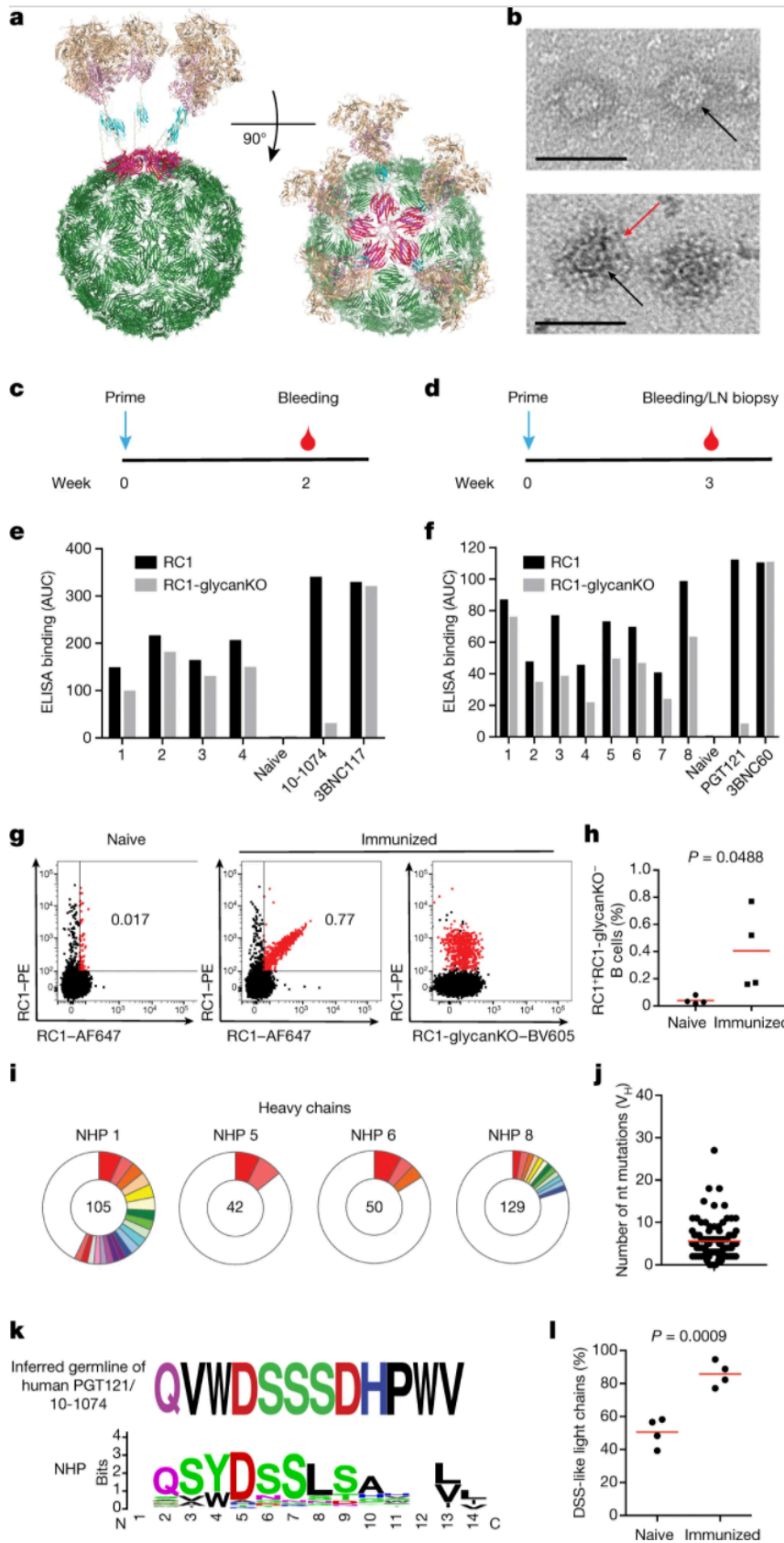


**Figure 3.** Macaque immunization with RC1-4fill VLPs elicits anti-V3-glycan patch antibodies that resemble inferred germlines of bNAbs. **a**, Model of VLP-RC1-4fill: RC1-4fill (wheat and pink), SpyTag (gold), SpyCatcher (cyan) and bacteriophage AP205 (green). **b**, Negative-stain electron microscopy images comparing VLPs (top) and VLP-RC1 (bottom). Arrows indicate the VLP surface (black) and RC1 (red). Scale bars, 50 nm. Representative image from three independent experiments. **c**, **d**, Immunization protocols for rabbits (**c**) and non-human primates (**d**). LN, lymph node. **e**, **f**, AUC for ELISAs with serum from four rabbits (**e**) and eight non-human primates (**f**) primed with VLP-RC1-4fill against RC1 (black) and RC1-glycanKO (grey). **g**, **h**, Flow cytometry plots showing frequency of B cells in the germinal centre that bind to RC1 but not to RC1-glycanKO. **g**, Representative flow cytometry plots. **h**, Quantification.  $n = 4$  naive and  $n = 4$  immunized non-human primates. **i**, Pie charts showing clonal expansion of RC1-binding B cells in the germinal centre (see legend in Fig. 2j). **j**, IgV<sub>H</sub> mutations for the sequences of clones shown in **i** (Supplementary Table 3). **k**, Logo plots comparing CDRL3 of inferred germline of PGT121/10-1074 and all IgL from B cells in the germinal centre shown in **i**. **l**, Fraction of CDRL3 sequences from **i** that show a DSS-like motif. **h**, **l**, Unpaired *t*-test. **h**, **j**, **l**, Data are mean and individual values.

To further characterize responses elicited by VLP-RC1-4fill in macaques, we purified germinal centre B cells from the draining lymph nodes that bound to RC1 but not to RC1-glycanKO by flow cytometry (RC1<sup>+</sup>RC1-glycanKO<sup>−</sup>). Whereas RC1<sup>+</sup> cells were absent from germinal centres of naive macaques, RC1<sup>+</sup>RC1-glycanKO<sup>−</sup> germinal centre B cells were found at an average frequency of 0.4% of germinal centre B cells in the lymph nodes in the four macaques analysed (Fig. 3g, h).

Antibody cloning from four immunized macaques revealed expanded B cell clones that used a variety of V<sub>H</sub> genes, as found for human V3-glycan patch bNAbs<sup>32</sup>, with an average of 5.6 nucleotide somatic mutations (Fig. 3i, j and Supplementary Table 3). Most characterized human V3-glycan patch bNAbs contain a lambda light chain<sup>18,33</sup>. Analysis of lambda genes revealed that macaque RC1-binding cells preferentially used gene segments V<sub>L</sub>132 (91% nucleotide sequence identity to V<sub>L</sub>2-8 germline gene segments in PGT125–128 and PGT130–131) and V<sub>L</sub>124 (94% nucleotide sequence identity to the V<sub>L</sub>3-21 germline in PGT121–123/10-1074) (Fig. 3k). In addition, 86% of the lambda light chains had CDRL3 sequences that included a Asp-Ser-Ser (DSS) motif present in the inferred germlines of PGT121–123 and 10-1074/PGT124<sup>17</sup> (Fig. 3l and Supplementary Table 4). This motif mutates to Asp-Ser-Arg (DSR) in the mature bNAbs, which is critical for the neutralization

activity of PGT121<sup>34</sup>. Thus, there is congruence between the sequence of precursors of human V3-glycan patch bNAbs and the antibodies expressed by macaque B cell clones that are elicited by priming with VLP-RC1-4fill.

We expressed 38 macaque germinal centre antibodies with CDRL3 sequences that resembled the CDRL3 sequences of inferred-germline V3-glycan patch bNAbs (Supplementary Table 5). The CDRL3 sequences of 33 out of 38 antibodies contained a DSS motif and a Gln at position 89 (QXXDSS motif), which was also found in the CDRL3 sequence of the inferred germlines of PGT121-123, 10-1074, PGT124 and BG18<sup>17,18</sup> (Extended Data Table 5). In addition, 5 out of 38 antibodies contained a Ser-Tyr-Ala-Gly (SYAG) motif, which is present in the CDRL3 sequences of the inferred germlines of PGT125-128, PGT130 and PGT131 (Extended Data Table 5). In total, 30 out of 33 QXXDSS motif-containing antibodies and 2 out of 5 SYAG motif-containing antibodies bound to the V3-glycan patch epitope, as determined by ELISA using RC1 and RC1-glycanKO with additional mutations in the GDIR sequence (RC1-glycanKO-GAIA) (Fig. 4a and Supplementary Table 5). In addition, the CDRL1 of all 38 macaque antibodies contained an Asn-Ile-Gly (NIG)-like motif present in the PGT121/10-1074 antibody (33 NIG, 4 DIG and 1 NLG) (Supplementary Table 5). The CDRH3 lengths of the 38 antibodies were relatively long (11–21 residues; average = 15.5 residues) (Fig. 4b). Longer CDRH3 sequences were enriched in Tyr and/or Phe residues, similar to the long CDRH3 sequences found in human V3-glycan patch bNAbs<sup>16–18</sup> (Supplementary Table 5). The antibody V<sub>H</sub> and V<sub>L</sub> genes included an average of 4.9 and 3.3 nucleotide mutations, respectively (Fig. 4c). Consistent with recruitment of antibodies with a range of affinities to germinal centres and their subsequent affinity maturation<sup>7,10</sup>, the inferred germline versions of the macaque antibodies showed lower affinities for RC1 than their mutated counterparts, ranging from levels that were below quantification to  $K_D$  values in the micromolar range (Extended Data Fig. 5c). Similarity between the macaque antibodies and PGT121/10-1074 was corroborated by ELISAs using an anti-idiotypic antibody specific for the PGT121/10-1074 inferred germline antibody (Extended Data Fig. 5d). The inferred germline-reverted versions of 5 out of 11 macaque antibodies were recognized by the anti-PGT121/10-1074 antibody (Extended Data Fig. 5d).

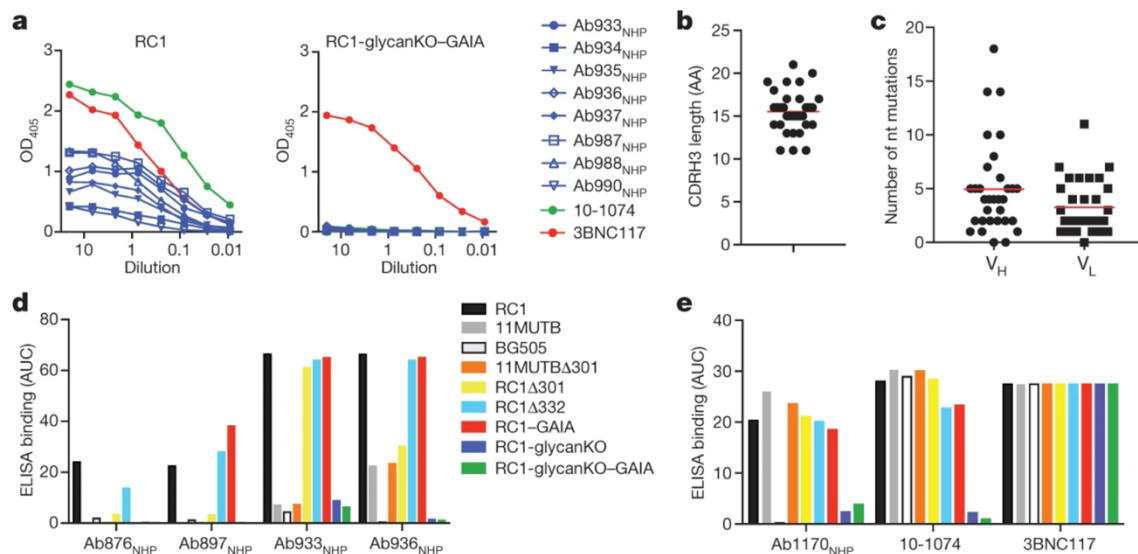


**Figure 4.** Monoclonal antibodies from macaques bind to the V3-glycan patch. **a**, ELISA binding of representative macaque monoclonal antibodies to RC1 and RC1-glycanKO-GAIA. **b**, CDRH3 length of 32 V3-glycan-patch-specific monoclonal antibodies. AA, amino acids. **c**, Nucleotide mutations in IgV<sub>H</sub> and IgV<sub>L</sub> of 32 V3-glycan-patch-specific monoclonal antibodies. **d**, **e**, AUCs for ELISA binding of monoclonal antibodies to indicated proteins. Each AUC value corresponds to one ELISA curve. **b**, **c**, Data are mean and each dot is an individual sequence.

To further characterize the target site of the macaque antibodies, we performed ELISAs against additional proteins: RC1-glycanKO, RC1-GAIA, RC1-glycanKO-GAIA, 11MUTBΔ301, RC1Δ301, RC1Δ332, 11MUTB<sup>20</sup> and BG505 (Fig. 4d, e and Extended Data Table 2). The ELISAs suggested four distinct RC1-binding patterns among antibodies that contained a CDRL3 QXXDSS motif (Fig. 4d) and another pattern among antibodies that contained a SYAG motif (Fig. 4e). Whereas all antibodies were glycan dependent as determined by no binding to RC1-glycanKO, they differed in binding to 11MUTB or 10MUT and dependence on GDIR and N301, N332, and N156 glycans (Fig. 4a, d, e). Although none of the antibodies recognized BG505, Ab933<sub>NHP</sub> (where NHP denotes antibodies elicited in non-human primates), Ab936<sub>NHP</sub> and Ab1170<sub>NHP</sub> bound to 11MUTB, indicating that they can accommodate the N156 glycan (Fig. 4d, e). Consistent with no binding to BG505, none of the antibodies exhibited neutralizing activity, and removal of the N133, N137 and N156 glycans did not render the BG505/T332N and JRCSF.JB viruses

sensitive to neutralization (Extended Data Table 3b, c), suggesting that the lack of neutralization is not due to clashes with those glycans. We conclude that macaque immunization with VLP-RC1-4fill elicits V3-glycan-patch-specific antibodies that resemble precursors of human bNAbs that target this site.

### Cryo-EM structures of antibodies bound to RC1

We determined structures of one mouse and two macaque Fabs complexed with RC1 using single-particle cryo-EM. Ab275<sub>MUR</sub> (4.4 Å resolution) and Ab874<sub>NHP</sub> (3.9 Å) (derived from the same clone as Ab876<sub>NHP</sub>) bound RC1 similarly to each other, consistent with their 69% V<sub>H</sub> domain amino acid sequence identity, whereas Ab897<sub>NHP</sub> (4.4 Å) (related by 48% and 54% V<sub>H</sub> sequence identity to Ab275<sub>MUR</sub> and Ab874<sub>NHP</sub>, respectively) adopted a distinct angle of approach (Fig. 5a and Extended Data Fig. 5e).

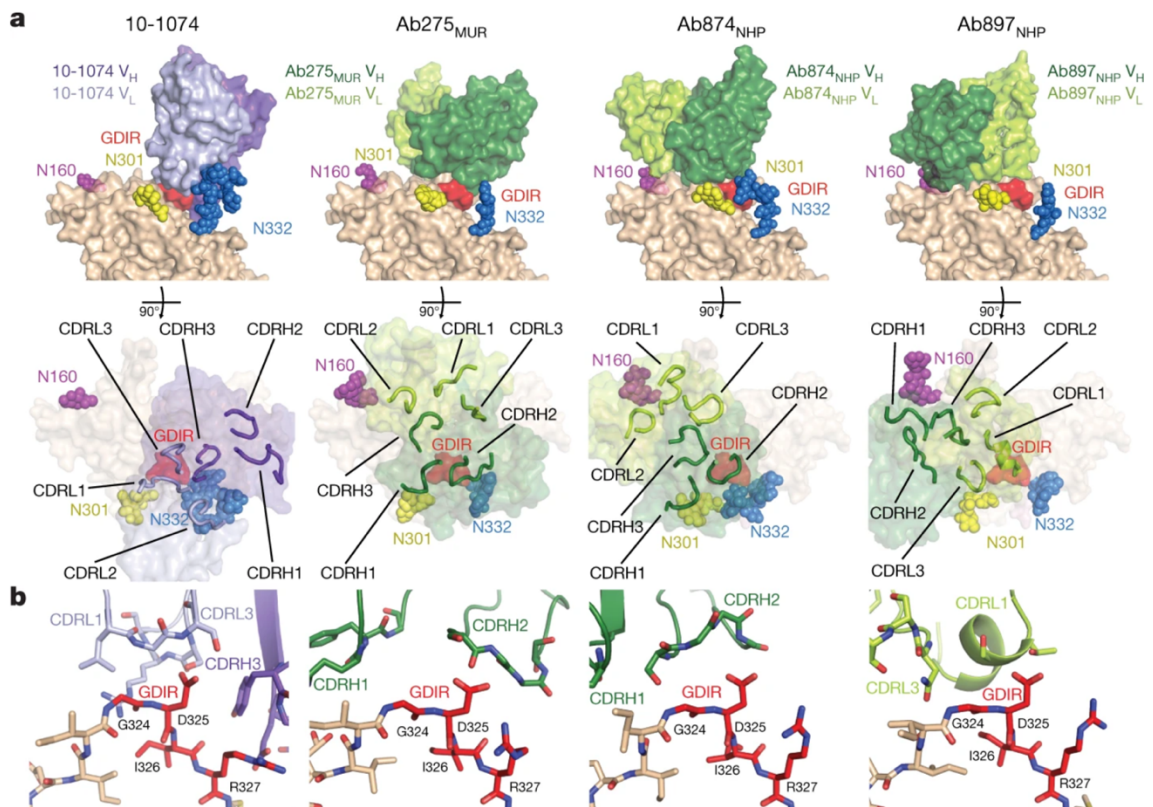


**Figure 5.** Structures of 10-1074 and elicited antibodies bound to RC1. **a**, Top, V<sub>H</sub>-V<sub>L</sub> domains of 10-1074 and elicited antibodies bound to one protomer of RC1 (GDIR

residues are red; glycans are coloured spheres). Bottom, antibody combining sites (CDRs shown as loops) mapped onto gp120 (glycans as coloured spheres; GDIR in red). **b**, Comparisons of interactions of the GDIR motif with 10-1074 and elicited antibodies (colours as in **a**).

All three Fabs in the RC1 complexes bound to the V3-glycan patch epitope and contacted the GDIR motif, but with different orientations and footprints from each other and from V3-glycan patch bNAbs (Fig. 5a and Extended Data Fig. 5e). 10-1074 contacts the conserved GDIR motif using CDRH3, CDRL1 and CDRL3<sup>22</sup> (Figs. 1c, 5a), Ab874<sub>NHP</sub> and Ab275<sub>MUR</sub> made GDIR contacts using their CDRH2s, whereas Ab897<sub>NHP</sub> used CDRL1 and CDRL3 (Fig. 5a, b). In addition, Ab874<sub>NHP</sub> and Ab897<sub>NHP</sub> contain the conserved CDRL3 QXXDSS motif, which make contacts with conserved regions of the V3-glycan epitope in mature bNAbs<sup>22,35</sup>. Similar to mature V3-glycan patch bNAbs, Ab897<sub>NHP</sub> contains a substitution (Ser93Asn) within the QXXDSS motif that enables contacts with gp120<sub>GDIR</sub> and also uses its conserved CDRL1 NIG motif to contact the V1 loop (Extended Data Fig. 5f).

Ab275<sub>MUR</sub> and Ab874<sub>NHP</sub> also interacted with the N332 glycan, consistent with mature V3-glycan bNAbs (Fig. 5a and Extended Data Fig. 5e). However, in contrast to 10-1074, which interacts with the N332 glycan via its CDRL1, light chain framework region 3 (FRWL3), CDRH2 and CDRH3<sup>22</sup>, Ab275<sub>MUR</sub> made contacts using CDRH2, whereas Ab874<sub>NHP</sub> engaged the N332 glycan with CDRH2 and heavy chain framework region 3 (FRWH3). We did not observe N332 glycan interactions in the Ab897<sub>NHP</sub>-RC1 structure. Despite reduced binding of Ab275<sub>MUR</sub>, Ab876<sub>NHP</sub> (same clone as Ab874<sub>NHP</sub>) and Ab897<sub>NHP</sub> to RC1Δ301 (Fig. 2l), none of these Fabs showed interactions with the N301 glycan in our structures, suggesting that glycan heterogeneity obscures this interaction and/or conformational heterogeneity in a V3-glycan patch that lacks this glycan diminishes binding<sup>36</sup>. We conclude that RC1 elicits V3-glycan-patch-targeting antibodies with distinct binding modes in animals with polyclonal antibody repertoires.

## Conclusions

HIV-1 bNAbs develop in infected humans by sequential rounds of somatic mutation in response to a rapidly evolving pathogen<sup>4</sup>. Vaccination with a series of related antigens can reproduce this progression of events in genetically engineered mice that carry supraphysiological numbers of B lymphocytes that express the inferred-germline precursors of bNAbs<sup>9</sup>. An important goal of HIV-1 vaccine design is to develop immunogens that initiate this response in organisms with polyclonal immune systems and then reproduce these responses in humans.

HIV-1 immunogen design has focused on increasing the affinity of candidate immunogens for specific inferred-germline precursors of bNAbs with the objective of recruiting a specific group of rare precursors into the germinal centre<sup>1</sup>. This approach typically fails to account for increases in apparent affinity produced by interactions between multimerized antigen and clusters of bivalent antigen receptors on the surface of a B cell. Moreover, entry into the germinal centre is primarily limited by competition<sup>7,10,11,14</sup>. Thus, the importance of affinity is relative, as shown by the observation that B cells bearing low affinity receptors are frequently found in germinal centres under physiological conditions<sup>10,37</sup>, and by our finding that inferred germline precursors of macaque antibodies elicited by RC1 showed relatively low affinity for the immunogen.

The principles used to produce RC1 did not take affinity for a germline B cell receptor into account. Instead, RC1 was designed to increase the number of bNAb progenitors that compete for entry into germinal centres by making the antigenic target site more available and facilitating binding to electrostatically neutral inferred-germline precursors<sup>25</sup>. In addition, VLP-RC1-4fill incorporates the idea that masking competing off-target epitopes<sup>26,29</sup> by addition of glycans<sup>27</sup> and tethering the bottom of the trimer to a VLP minimizes competition for entry into the germinal centre.

RC1 differs from other HIV-1 vaccine candidates in that it induces B cells that express antibodies against a targeted epitope to undergo clonal expansion in germinal centres in animals with a fully polyclonal B cell repertoire. In macaques, these B cells express

antibodies that show sequence and structural similarities to inferred-germline precursors of bNAbs that target the V3-glycan patch. Like the precursors of human bNAbs, they do not bind to wild-type Env or neutralize HIV-1<sup>5</sup>. Notably, biochemical and structural results showed that antibodies with distinct mechanisms of targeting the V3-glycan patch were elicited by RC1, increasing the probability that one or more might develop breadth and potency after boosting<sup>9</sup>. Thus, VLP-RC1-4fill is a suitable candidate immunogen for further evaluation in sequential vaccination strategies to elicit bNAbs.

## Methods

### Data reporting

No statistical methods were used to predetermine sample size. The experiments were not randomized and the investigators were not blinded to allocation during experiments and outcome assessment.

### Envelope proteins

Env trimers were expressed as soluble native-like gp140 trimers<sup>21</sup>. The newly engineered Env SOSIP trimers, RC1, RC1-4fill, RC1-Avitag, RC1-SpyTag, RC1-glycanKO, RC1-glycanKO-Avitag, RC1-glycanKO-GAIA and RC1-GAIA, BG505<sup>21</sup> and the BG505 variants 11MUTB, 10MUT, 7MUT and 5MUT<sup>20</sup> were cloned in the pPPPI4 expression vector using synthetic gene fragments (Integrated DNA Technologies (IDT)). The glycan variants RC1 $\Delta$ 301, RC1 $\Delta$ 332 and 11MUTB $\Delta$ 301 were produced by site-directed mutagenesis (QuikChange Lightning Multi-site directed mutagenesis kit, Agilent Technologies). Specific modifications of each protein are listed in Extended Data Table 2.

Soluble Env trimers were expressed by transient transfection in HEK293-6E cells (National Research Council of Canada) or Expi293 cells (Life Technologies) and purified from cell supernatants by 2G12 or NIH45-46 immunoaffinity chromatography and size-exclusion chromatography (SEC) as previously described<sup>38</sup>. Proteins were stored at 4 °C in 20 mM Tris pH 8.0 and 150 mM sodium chloride (TBS buffer). SpyTagged immunogens were buffer-

exchanged into 20 mM sodium phosphate pH 7.5, 150 mM NaCl. Cell lines were not tested for mycoplasma contamination.

#### VLP production and conjugation

A C-terminal SpyTag sequence (13 residues) was added to RC1-4fill to form an irreversible isopeptide bond to SpyCatcher protein<sup>31</sup>. We produced and purified SpyCatcher–AP205<sup>39</sup> VLPs as described<sup>30</sup> and separated conjugated VLPs from free Env trimers by SEC on a Superdex 200 column. Conjugation of Env trimers was verified by negative-stain electron microscopy and/or SDS–PAGE (Fig. 3, Extended Data Fig. 4), and immunogen concentrations were estimated by comparing to known amounts of free immunogen run on the same SDS–PAGE gel. Conjugated and unconjugated VLPs were compared by negative-stain electron microscopy on a FEI Tecnai T12 transmission electron microscope at 120 keV using a Gatan Ultrascan 2k × 2k CCD detector.

#### Mass spectrometry

The glycosylation profiles of RC1 and RC1-4fill were determined as previously described<sup>40</sup>. In brief, samples were denatured with Lys-C (Promega), Arg-C (Promega), Glu-C (Promega) and chymotrypsin (Promega). Following digestion, the samples were deglycosylated by Endo H (Promega) and PNGase F (Glyko, Prozyme) in the presence of <sup>18</sup>O water (Cambridge Isotope Laboratories). The resulting peptides were separated on an Acclaim PepMap RSLC C18 column (75 μm × 15 cm) and analysed using an Orbitrap Fusion Lumos Tribrid mass spectrometer (Thermo Fisher Scientific) with a 240-min linear gradient consisting of 1–100% solvent B over 180 min at a flow rate of 200 nl min<sup>-1</sup>. Full mass spectrometry scans were acquired using the Fusion instrument software (v.2.0, Thermo Fisher Scientific), and the resulting spectra were analysed and filtered using SEQUEST (Proteome Discoverer 1.4, Thermo Fisher Scientific) and ProteoIQ (v.2.7, Premier Biosoft). Site occupancy was calculated using spectral counts assigned to the <sup>18</sup>O-Asp-containing (PNGase-F-cleaved) and/or HexNAc-modified (Endo-H-cleaved) peptides and their unmodified counterparts.

## Animals

Mice carrying the inferred germline IgH and IgL human PGT121 and 10-1074 bNAbs (GL<sub>HL</sub>121 knock-in mice) were previously described<sup>9</sup>. Six-to-eight-week-old C57BL/6J male mice from The Jackson Laboratory were used for immunizations. All animal procedures were performed in accordance to protocols approved by the Rockefeller University Institutional Animal Care and Use Committee (IACUC). Male and female GL<sub>HL</sub>121 knock-in mice or C57BL/6J wild-type mice were equally distributed in groups and immunized intraperitoneally with 10 µg of soluble SOSIP Env trimer in Ribi adjuvant (Sigma-Aldrich) (1:1).

Six-month-old New Zealand white rabbits (Covance) were used for immunizations. Rabbits were immunized subcutaneously with approximately 22 µg of RC1-4fill SOSIP Env trimer conjugated to VLP (VLP-RC1-4fill) in an ISCOMs-like saponin adjuvant (see below). Serum samples were collected from mice and rabbits on weeks 0 and 2 after immunization. All procedures in rabbits were approved by the Denver PA IACUC.

Sixteen rhesus macaques (*Macaca mulatta*) of Indian genetic origin, two-to-four years of age, were housed and cared for in accordance with Guide for Care and Use of Laboratory Animals Report number NIH 82-53 (Department of Health and Human Services, Bethesda, 1985) in a biosafety level 2 NIH facility. All animal procedures and experiments were performed according to protocols approved by the IACUC of NIAID, NIH.

Macaques were immunized subcutaneously in the medial inner forelegs and hind legs (total of four sites per animal) with approximately 200 µg (experiment 1; Fig. 3f) or 100 µg (experiment 2; Extended Data Fig. 5a) of RC1-4fill SOSIP trimer conjugated to VLP (RC1-4fill VLP) adjuvated in IscoMPLA. Blood and lymph node biopsies were obtained from naive macaques and from the immunized macaques three weeks after immunization.

### Adjuvant synthesis

ISCOM-like saponin adjuvant was prepared as described<sup>41</sup>. Final adjuvant concentrations were determined by cholesterol quantification (Sigma-Aldrich, MAK043).

### ELISA

ELISAs with SOSIP Env trimers 11MUTB, RC1, 11MUTB $\Delta$ 301, RC1 $\Delta$ 301, RC1-GAIA, RC1-glycanKO, RC1-glycanKO-GAIA, RC1 $\Delta$ 332, BG505, 10MUT, 7MUT, 5MUT or the V3 loop-consensus C peptide (KGKGGKGGKGGCTRPNNNTRKSIRIGPGQTFYATGDIIGDIRQAHC) were performed as described<sup>9</sup>. Serum samples were assayed at a 1:100 or 1:30 starting dilution and seven additional threefold serial dilutions. Mouse and human IgGs or human Fabs were evaluated at concentrations specified in the main text.

Alternatively, 96-well plates were directly coated with 50  $\mu$ l of a solution of Fab at 20  $\mu$ g ml<sup>-1</sup> in 1 $\times$  PBS overnight at 4 °C, washed and blocked as above and incubated in 50  $\mu$ l of a solution of RC1 or RC1-glycanKO-GAIA at 2  $\mu$ g ml<sup>-1</sup> in blocking buffer for 1 h at room temperature. Plates were washed as above and developed using a chimeric version (human Fabs and mouse crystallizable fragment (Fc)) of the CD4-binding site bNAbs 3BNC60<sup>42</sup> at threefold serial dilutions starting at 5  $\mu$ g ml<sup>-1</sup> followed by anti-mouse IgG secondary antibody conjugated to HRP (Jackson ImmunoResearch, 115-035-071).

For anti-idiotypic ELISAs, 96-well plates were coated with 50  $\mu$ l of a solution of IgG at 10  $\mu$ g ml<sup>-1</sup> in 1 $\times$  PBS overnight at 4 °C, washed and blocked as above and incubated with biotinylated anti-inferred germline PGT121 idiotypic antibody. Plates were developed with streptavidin conjugated to HRP.

### Flow cytometry and single B cell sorting

Single-cell suspensions were obtained from the draining lymph nodes and spleens of immunized mice, and mature B cells were isolated by negative selection using anti-CD43 magnetic beads (MACS) following the manufacturer's instructions.

Frozen peripheral blood mononuclear cells or cells from lymph node biopsies obtained from the naive and immunized macaques were thawed and washed in RPMI 1640 medium (1×) (Gibco, 11875-093). Mouse or macaque cells were incubated with 100 µl of FACS buffer (1× PBS with 2% fetal bovine serum and 1 mM EDTA) with mouse (BD Biosciences, 553142) or human (BD Biosciences, 564219) Fc Block, respectively, at a 1:500 dilution for 30 min on ice.

RC1 and RC1-glycanKO (RC1<sup>+</sup>RC1-glycanKO<sup>-</sup>) tetramers were prepared by incubating 5 µg of Avitagged and biotinylated RC1 (RC1–AviBio) or Avitagged and biotinylated RC1-glycanKO (RC1-glycanKO–AviBio) with fluorophore-conjugated streptavidin at a 1:200 dilution in 1× PBS for 30 min on ice.

RC1<sup>+</sup>RC1-glycanKO<sup>-</sup> mouse B cells were isolated using RC1–AviBio conjugated to streptavidin BV711 (BD Biosciences, 563262) and RC1-glycanKO–AviBio conjugated to streptavidin–PE (BD Biosciences, 554061) as baits. RC1<sup>+</sup>RC1-glycanKO<sup>-</sup> macaque B cells were isolated using RC1–AviBio conjugated with streptavidin–PE and streptavidin–AF647 and RC1-glycanKO–AviBio conjugated with streptavidin–BV605 (BD Biosciences, 563260). Tetramers were mixed with the human or mouse antibody cocktails indicated below to a final concentration of 5 µg ml<sup>-1</sup> each.

Mouse cells were stained with anti-CD4–APC-eFluor780 (Invitrogen, 47-0042-82), anti-CD8–APC-eFluor780 (Invitrogen, 47-0081-82), anti-F4/80–APC-eFluor780 (Invitrogen, 47-4801-82), anti-NK1.1–APC-eFluor780 (Invitrogen, 47-5941-82), anti-CD11b–APC-eFluor780 (eBioscience, 47-0112-82), anti-CD11c–APC-eFluor780 (eBioscience, 47-0114-82), anti-Gr-1–APC-eFluor780 (Invitrogen, 47-5931-82), anti-B220–APC (Biolegend, 103212), anti-GL7–FITC (BD Biosciences, 553666) and anti-CD95–BV421 (BD Biosciences, 562633) antibodies at 1:200 dilution and the live/dead marker Zombie NIR (Biolegend, 77184) at a 1:400 dilution in FACS buffer. Macaque cells were stained with anti-CD16–APC-eFluor780 (Invitrogen, 47-0168-41), anti-CD8a–APC-eFluor780 (Invitrogen,

47-0086-42), anti-CD3–APC–eFluor780 (Invitrogen, 47-0037-41), anti-CD14–APC–eFluor780 (eBiosciences, 47-0149-41), anti-CD20–PE–Cy7 (BD, 335793), anti-CD38–FITC (Stem Cell Technologies, 60131FI), anti-IgG–BV421 (BD Biosciences, 562581) and anti-IgM–PerCP–Cy5.5 (BD Biosciences, 561285) antibodies at a 1:200 dilution and the live/dead marker Zombie NIR at a 1:400 dilution in FACS buffer.

Zombie NIR<sup>−</sup>CD4<sup>−</sup>CD8<sup>−</sup>F4/80<sup>−</sup>NK1.1<sup>−</sup>CD11b<sup>−</sup>CD11c<sup>−</sup>B220<sup>+</sup>GL7<sup>+</sup>CD95<sup>+</sup>RC1<sup>+</sup>RC1-glycanKO<sup>−</sup> single cells were isolated from the mouse cell homogenates and Zombie NIR<sup>−</sup>CD16<sup>−</sup>CD8a<sup>−</sup>CD3<sup>−</sup>CD14<sup>−</sup>CD20<sup>+</sup>CD38<sup>+</sup>IgG<sup>+/-</sup>double RC1<sup>+</sup>RC1-glycanKO<sup>−</sup> single cells were isolated from the macaque cell homogenates using a FACS Aria III (Becton Dickinson).

Single cells were sorted into individual wells of a 96-well plate containing 5  $\mu$ l of lysis buffer (TCL buffer (Qiagen, 1031576) with 1% of 2- $\beta$ -mercaptoethanol). Plates were immediately frozen on dry ice and stored at  $-80^{\circ}\text{C}$ .

#### Antibody sequencing and cloning

Single-cell RNA was purified using magnetic beads (RNAClean XP, A63987, Beckman Coulter). RNA was eluted from the magnetic beads with 11  $\mu$ l of a solution containing 14.5 ng  $\mu\text{l}^{-1}$  of random primers (Invitrogen, 48190-011), 0.5% of tergitol (type NP-40, 70% in H<sub>2</sub>O, Sigma-Aldrich, NP40S-100ML) and 0.6 U  $\mu\text{l}^{-1}$  of RNase inhibitor (Promega, N2615) in nuclease-free water (Qiagen), and incubated at 65  $^{\circ}\text{C}$  for 3 min. cDNA was synthesized by reverse transcription (SuperScript III Reverse Transcriptase, Invitrogen, 18080-044, 10,000 U)<sup>43</sup>. cDNA was stored at  $-80^{\circ}\text{C}$  or used for antibody gene amplification by nested polymerase chain reaction (PCR) after addition of 10  $\mu$ l of nuclease-free water.

Mouse and macaque antibody genes were cloned<sup>43</sup> using the primers in Supplementary Table 6. PCR protocols were as follows for annealing ( $^{\circ}\text{C}$ )/elongation (s)/number of cycles: first PCR (IgG IgH and Ig $\lambda$ ): 46/55/50; second PCR (IgG IgH and Ig $\lambda$ ): 50/55/50.

Inferred germline macaque IgGs and Fabs were produced by reverting all nucleotide mutations in the V(D)J antibody genes to their corresponding inferred germline sequences

while conserving the N nucleotides from the V(D)J junctions found in the mutated antibodies.

#### Antibody production and purification

Immunoglobulins were purified from 200  $\mu$ l of mouse or macaque serum using Ab Spin Trap Protein G Sepharose columns (GE Healthcare, 28-4083-47). Immunoglobulin-containing fractions were buffer-exchanged with PBS by overnight dialysis at 4 °C (dialysis cassettes 20000 MWCO, Thermo Fisher Scientific, 66005).

For structural studies, mouse IgGs and macaque His<sub>6</sub>-tagged Fabs were expressed by transient transfection in HEK293-6E or Expi293 cells and purified from cell supernatants using protein A or G (GE Healthcare) (for IgGs) or Ni-NTA (GE Healthcare) or Ni Sepharose 6 Fast Flow (GE Healthcare) (for Fabs) chromatography and SEC<sup>44</sup>. Mouse Fab was obtained by digesting IgG at 1–5 mg ml<sup>-1</sup> with ficin (Sigma-Aldrich). Fab was purified by protein G (GE Healthcare) and SEC chromatography<sup>45</sup>, followed by monoQ 5/50 (GE Healthcare) ion-exchange chromatography. The common inferred germline of the PGT121 and 10-1074 bNAbs<sup>17</sup> was expressed as a His<sub>6</sub>-tagged Fab.

#### In vitro neutralization assays

TZM-bl assays were performed as previously described<sup>46</sup>. In brief, neutralization activity was calculated as a function of the reduction in Tat-induced luciferase expression in the TZM-bl reporter cell line after a single round of virus infection with Env pseudoviruses.

#### SPR and OCTET binding studies

SPR experiments were performed using a T200 (Biacore). For measuring the affinity for PGT121/10-1074 inferred germline Fab, protein A was immobilized on a CM5 chip by primary amine chemistry (Biacore manual) and 200 nM 8ANC195<sub>G52K5</sub> IgG or a non-HIV Env-binding IgG (mG053) was injected as previously described<sup>44</sup>. Then, 1  $\mu$ M human Fc was injected to block remaining protein A sites. After capturing 10  $\mu$ M RC1, 11MUTB or 10MUT, a concentration series of PGT121/10-1074 inferred germline Fab (fourfold dilutions

from a top concentration of 160  $\mu\text{M}$  for 10MUT, and twofold dilutions from a top concentration of 150  $\mu\text{M}$  for 11MUTB and RC1) was injected, and binding reactions were allowed to reach equilibrium.  $K_D$  values were derived by nonlinear regression analysis of plots of  $R_{\text{eq}}$  (equilibrium binding response) versus the log of the injected protein concentration and the data were fitted to a 1:1 binding model<sup>47</sup>. To measure the affinity of Ab275<sub>MUR</sub>, a concentration series of Fab was injected over immobilized RC1 or 11MUTB (fourfold dilutions from a top concentration of 50  $\mu\text{M}$ ).  $K_D$  values were calculated from the on/off rates ( $k_a/k_d$ ), which were derived using a 1:1 binding model from seven concentrations of Ab275<sub>MUR</sub> Fab (3.125  $\mu\text{M}$  to 0.763 nM). Flow cells were regenerated as previously described<sup>44</sup> with 1 M guanidine HCl and/or 10 mM glycine pH 2.0 at a flow rate of 90  $\mu\text{l min}^{-1}$ .

OCTET experiments were performed using the OCTET Red96 system to determine affinities of inferred germline and mutated macaque Fabs for RC1. Biotinylated RC1–Avitag was immobilized on high-precision streptavidin (SAX) biosensors (FORTÉBIO) using a solution of biotinylated RC1–Avitag at 400 nM in dilution buffer (FORTÉBIO). Four serial dilutions of each macaque Fab, one irrelevant Fab and 3BNC60 Fab were prepared in dilution buffer (FORTÉBIO). The binding experiment was performed at 30 °C using the following protocol: baseline 1 (60 s), load RC1 (300 s), baseline 2 (200 s), Fab association (300 s) and Fab dissociation (600 s). Analysis was performed using OCTET software Data Analysis HT 10.0 (FORTÉBIO).

#### Cryo-EM sample and grid preparation

RC1 complexed with 10-1074 was prepared by incubating purified RC1 with 10-1074 Fab and a CD4-binding site (CD4bs) Fab at a 1:3:3 molar ratio (gp140 protomer:10-1074 Fab:CD4bs Fab) overnight at room temperature. The RC1–Fab complex was isolated by SEC in TBS (20 mM Tris pH 8.0, 100 mM NaCl) using a Superdex-200 Increase 10/300 column (GE Healthcare). RC1–mouse/macaque Fab complexes were prepared by incubating purified RC1 with a mouse or macaque Fab and with 8ANC195 Fab<sup>42</sup> at a 1:1.3:1.3 molar ratio as above and used without SEC purification. RC1–Fab complexes were diluted to 0.75–

1.4 mg ml<sup>-1</sup> in TBS, and 3  $\mu$ l was added to Quantifoil R1.2/1.3 300 mesh copper grids (Electron Microscopy Services) that had been freshly glow-discharged using a PELCO easiGlow (Ted Pella). Samples were vitrified in 100% liquid ethane using a Mark IV Vitrobot (Thermo Fisher Scientific). Sample preparation conditions are summarized in Extended Data Table 1.

#### Cryo-EM data collection

RC1–Fab complexes were collected on a 200 kV Thermo Fisher Talos Arctica electron microscope using EPU automated image acquisition software<sup>48</sup>. Movies were collected on a Falcon 3EC direct electron detector (Thermo Fisher Scientific) operating in counting mode at a nominal magnification of 73,000 $\times$  (1.436  $\text{\AA}$  per pixel) using a defocus range of  $-1.4 \mu\text{m}$  to  $-3.0 \mu\text{m}$  or  $-0.8 \mu\text{m}$  to  $-2.5 \mu\text{m}$ . Data for the RC1–10-1074 complex were collected across two separate sessions and combined during data processing. Microscope conditions are summarized in Extended Data Table 1.

#### Cryo-EM data processing

Movies were motion-corrected and dose-weighted using the MotionCor2<sup>49</sup> frame alignment program in RELION-3<sup>50</sup>. Dose-weighted summed images were used for CTF determination using Gctf<sup>51</sup>, and reference-free particle picking from each micrograph was achieved using Laplacian-of-Gaussian filtering in RELION-3<sup>50</sup>. Unbinned extracted particles were imported into cryoSPARC v.2<sup>52</sup> and subjected to reference-free two-dimensional classification using a 240- $\text{\AA}$  circular mask. Particles from the best two-dimensional classes were selected for heterogeneous ab initio model generation (two models). The best model exhibited C3 symmetry and was used as an initial model for homogenous three-dimensional auto-refinement in cryoSPARC v.2<sup>52</sup>. Resolutions were estimated using the gold standard Fourier shell correlation (FSC = 0.143)<sup>53</sup>, and maps were auto-sharpened in cryoSPARC<sup>52</sup>. For interpreting *N*-linked glycans, maps were generated with overall *B*-factors ranging from  $-150$  to  $-400 \text{\AA}^2$  to improve local features and map connectivity<sup>54</sup>. See Extended Data Fig. 2 and Extended Data Table 1.

## Model building

Initial coordinates were generated by docking reference models into the maps using UCSF Chimera<sup>55</sup>. For the RC1–10-1074 complex, BG505 Env and 10-1074 Fab (PDB code 53TZ) were docked into the density maps. For RC1 complexes with mouse or macaque Fabs, BG505 Env and PGT121/10-1074 inferred germline (PDB codes 5CEZ and 4FQQ) coordinates were docked into density maps. Initial models were refined into electron microscopy maps using rigid body refinement<sup>55</sup>. Models were built using Fab and RC1 sequences following iterative rounds of real-space refinement in Coot and PHENIX<sup>56,57</sup>. Coordinates for glycans were added as Man<sub>9</sub> and then trimmed to fit the maps at  $\sigma = 5$ . Model validation was done using MolProbity<sup>58</sup> and Privateer<sup>59</sup>. Superposition calculations and molecular representations were generated with PyMOL (v.1.5.0.4 Schrodinger), UCSF Chimera<sup>55</sup> and ResMap<sup>60</sup>.

## Analysis

MacVector v.15.5.3 was used for sequence analysis and graphs were created using R language. Flow cytometry data were processed using FlowJo v.10.5.0. GraphPad Prism 7 was used for data analysis. Immunoglobulin gene sequence AB1 files were converted to FASTQ format using the Biopython package. FASTQ files were trimmed by quality using cutadapt v.1.18 software. Igbblast v.1.9.0 was used for VDJ assignment and clone analysis was performed using Change-O software v.0.3.7. For macaques, a custom VDJ database was created using previously reported immunoglobulin gene sequences<sup>61</sup>.

## Quantification and statistical analysis

Statistical information, including  $n$ , mean and statistical significance values, is indicated in the text or the figure legends. GraphPad Prism 7 was used for statistical analysis by unpaired Student's  $t$ -test. Data were considered statistically significant at  $*P \leq 0.05$ ,  $**P \leq 0.01$ ,  $***P \leq 0.001$  and  $****P \leq 0.0001$ .

**Data availability**

The atomic models and cryo-EM density maps generated during the current study have been deposited in the Protein Data Bank and Electron Microscopy Data Bank with accession numbers 6ORN and EMD-20175 (RC1–10-1074), 6ORQ and EMD-20178 (RC1–Ab275<sub>MUR</sub>), 6ORO and EMD-20176 (RC1–Ab874<sub>NHP</sub>), and 6ORP and EMD-20177 (RC1–Ab897<sub>NHP</sub>). Sequence datasets generated and analysed during the current study are available from the corresponding authors upon reasonable request.

**Acknowledgements**

We thank members of the Bjorkman, Martin and Nussenzweig laboratories for discussions, T. Eisenreich and S. Tittley for animal husbandry, K. Gordon for flow cytometry, S. Zolla-Pazner for providing the V3-consensus C peptide and anti-V3 monoclonal antibodies, M. Howarth for providing plasmids and advice for VLP expression and purification and A. Malyutin for help with cryo-EM data collection. Cryo-EM was done in the Beckman Institute Resource Center for Transmission Electron Microscopy at Caltech. This work was supported by the National Institute of Allergy and Infectious Diseases (NIAID) of the National Institutes of Health (NIH) Grant HIVRAD P01 AI100148 (to P.J.B. and M.C.N.), NIH Grant P50 GM082545-06 (to P.J.B.), NIH Center for HIV/AIDS Vaccine Immunology and Immunogen Discovery (CHAVI-ID) 1UM1 AI100663-01 (to M.C.N.), the Intramural Research Program of the NIAID (to M.A.M.), the National Center for Biomedical Glycomics P41GM103490 and NIGMS R01GM130915 (to L.W.), Gates CAVD grant OPP1146996 (to M.S.S. and D.C.M.), NIH/NIAID P01 AI138212 (to L.S., A.T.M. and M.C.N.) and the Robertson Fund of the Rockefeller University (M.C.N.). Additional support included an NSF GRFP (to M.E.A.), an EMBO fellowship (to J.M.), the HHMI Hanna Gray Fellowship and the Postdoctoral Enrichment Program from the Burroughs Wellcome Fund (to C.O.B.). M.C.N. and D.J.I. are HHMI investigators.

## References

1. McCoy, L. E. & Burton, D. R. Identification and specificity of broadly neutralizing antibodies against HIV. *Immunol. Rev.* **275**, 11–20 (2017).
2. West, A. P. Jr et al. Structural insights on the role of antibodies in HIV-1 vaccine and therapy. *Cell* **156**, 633–648 (2014).
3. Kwong, P. D. & Mascola, J. R. HIV-1 vaccines based on antibody identification, B cell ontogeny, and epitope structure. *Immunity* **48**, 855–871 (2018).
4. Bonsignori, M. et al. Antibody-virus co-evolution in HIV infection: paths for HIV vaccine development. *Immunol. Rev.* **275**, 145–160 (2017).
5. Klein, F. et al. Somatic mutations of the immunoglobulin framework are generally required for broad and potent HIV-1 neutralization. *Cell* **153**, 126–138 (2013).
6. Victora, G. D. & Nussenzweig, M. C. Germinal centers. *Annu. Rev. Immunol.* **30**, 429–457 (2012).
7. Schwickert, T. A. et al. A dynamic T cell-limited checkpoint regulates affinity-dependent B cell entry into the germinal center. *J. Exp. Med.* **208**, 1243–1252 (2011).
8. Escolano, A., Dosenovic, P. & Nussenzweig, M. C. Progress toward active or passive HIV-1 vaccination. *J. Exp. Med.* **214**, 3–16 (2017).
9. Escolano, A. et al. Sequential immunization elicits broadly neutralizing anti-HIV-1 Antibodies in Ig knockin mice. *Cell* **166**, 1445–1458 (2016).
10. Tas, J.M. et al. Visualizing antibody affinity maturation in germinal centers. *Science* **351**, 1048–1054 (2016).
11. DalPorto, J.M., Haberman, A.M., Shlomchik, M.J. & Kelsoe, G. Antigen drives very low affinity B cells to become plasmacytes and enter germinal centers. *J. Immunol.* **161**, 5373–5381 (1998).
12. Abbott, R.K. et al. Precursor frequency and affinity determine B cell competitive fitness in germinal centers, tested with germline-targeting HIV vaccine immunogens. *Immunity* **48**, 133–146 (2018).
13. Dosenovic, P. et al. Anti-HIV-1 B cell responses are dependent on B cell precursor frequency and antigen-binding affinity. *Proc. Natl Acad. Sci. USA* **115**, 4743–4748 (2018).

14. Shih, T.-A. Y., Meffre, E., Roederer, M. & Nussenzweig, M. C. Role of BCR affinity in T cell dependent antibody responses in vivo. *Nat. Immunol.* **3**, 570–575 (2002).
15. Kong, L. et al. Supersite of immune vulnerability on the glycosylated face of HIV-1 envelope glycoprotein gp120. *Nat. Struct. Mol. Biol.* **20**, 796–803 (2013).
16. Walker, L. M. et al. Broad neutralization coverage of HIV by multiple highly potent antibodies. *Nature* **477**, 466–470 (2011).
17. Mouquet, H. et al. Complex-type N-glycan recognition by potent broadly neutralizing HIV antibodies. *Proc. Natl Acad. Sci. USA* **109**, E3268–E3277 (2012).
18. Freund, N. T. et al. Coexistence of potent HIV-1 broadly neutralizing antibodies and antibody-sensitive viruses in a viremic controller. *Sci. Transl. Med.* **9**, eaal2144 (2017).
19. Sok, D. et al. A prominent site of antibody vulnerability on HIV envelope incorporates a motif associated with CCR5 binding and its camouflaging glycans. *Immunity* **45**, 31–45 (2016).
20. Steichen, J. M. et al. HIV vaccine design to target germline precursors of glycan-dependent broadly neutralizing antibodies. *Immunity* **45**, 483–496 (2016).
21. Sanders, R. W. et al. A next-generation cleaved, soluble HIV-1 Env trimer, BG505 SOSIP.664 gp140, expresses multiple epitopes for broadly neutralizing but not non-neutralizing antibodies. *PLoS Pathog.* **9**, e1003618 (2013).
22. Gristick, H. B. et al. Natively glycosylated HIV-1 Env structure reveals new mode for antibody recognition of the CD4-binding site. *Nat. Struct. Mol. Biol.* **23**, 906–915 (2016).
23. Garces, F. et al. Structural evolution of glycan recognition by a family of potent HIV antibodies. *Cell* **159**, 69–79 (2014).
24. Andrabi, R. et al. Glycans function as anchors for antibodies and help drive HIV broadly neutralizing antibody development. *Immunity* **47**, 524–537 (2017).
25. Scharf, L. et al. Structural basis for germline antibody recognition of HIV-1 immunogens. *eLife* **5**, e13783 (2016).
26. McCoy, L. E. et al. Holes in the glycan shield of the native HIV envelope are a target of trimer-elicited neutralizing antibodies. *Cell Rep.* **16**, 2327–2338 (2016).

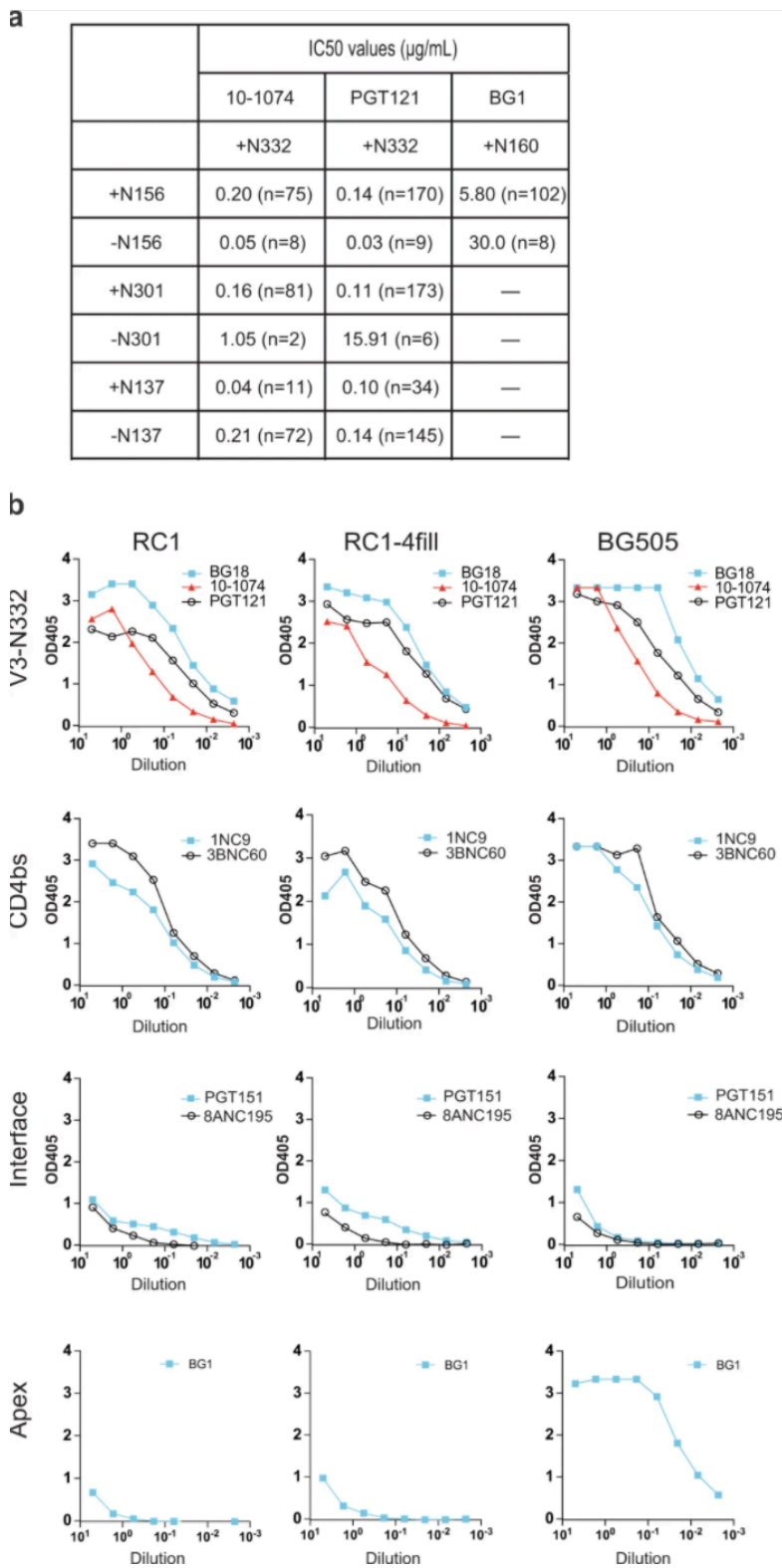
27. Duan, H. et al. Glycan masking focuses immune responses to the HIV-1 CD4-binding site and enhances elicitation of VRC01-class precursor antibodies. *Immunity* **49**, 301–311 (2018).
28. Garrity, R. R. et al. Refocusing neutralizing antibody response by targeted dampening of an immunodominant epitope. *J. Immunol.* **159**, 279–289 (1997).
29. Klasse, P. J. et al. Epitopes for neutralizing antibodies induced by HIV-1 envelope glycoprotein BG505 SOSIP trimers in rabbits and macaques. *PLoS Pathog.* **14**, e1006913 (2018).
30. Brune, K. D. et al. Plug-and-Display: decoration of virus-like particles via isopeptide bonds for modular immunization. *Sci. Rep.* **6**, 19234 (2016).
31. Zakeri, B. et al. Peptide tag forming a rapid covalent bond to a protein, through engineering a bacterial adhesin. *Proc. Natl Acad. Sci. USA* **109**, E690–E697 (2012).
32. Longo, N. S. et al. Multiple antibody lineages in one donor target the glycan-V3 supersite of the HIV-1 envelope glycoprotein and display a preference for quaternary binding. *J. Virol.* **90**, 10574–10586 (2016).
33. Burton, D. R. & Hangartner, L. Broadly neutralizing antibodies to HIV and their role in vaccine design. *Annu. Rev. Immunol.* **34**, 635–659 (2016).
34. Sok, D. et al. The effects of somatic hypermutation on neutralization and binding in the PGT121 family of broadly neutralizing HIV antibodies. *PLoS Pathog.* **9**, e1003754 (2013).
35. Lee, J. H., de Val, N., Lyumkis, D. & Ward, A. B. Model building and refinement of a natively glycosylated HIV-1 Env protein by high-resolution cryoelectron microscopy. *Structure* **23**, 1943–1951 (2015).
36. Zolla-Pazner, S. et al. Structure/function studies involving the V3 region of the HIV-1 envelope delineate multiple factors that affect neutralization sensitivity. *J. Virol.* **90**, 636–649 (2015).
37. Murugan, R. et al. Clonal selection drives protective memory B cell responses in controlled human malaria infection. *Sci. Immunol.* **3**, eaap8029 (2018).
38. Wang, H. et al. Asymmetric recognition of HIV-1 envelope trimer by V1V2 loop-targeting antibodies. *eLife* **6**, e27389 (2017).

39. Tissot, A. C. et al. Versatile virus-like particle carrier for epitope based vaccines. *PLoS ONE* **5**, e9809 (2010).
40. Duan, H. et al. Glycan masking focuses immune responses to the HIV-1 CD4-binding site and enhances elicitation of VRC01-class precursor antibodies. *Immunity* **49**, 301–311 (2018).
41. Lövgren-Bengtsson, K. & Morein, B. in *Vaccine Adjuvants: Preparation Methods and Research Protocols* (ed. O'Hagan, D.) 239–258 (Humana, 2000).
42. Scheid, J. F. et al. Sequence and structural convergence of broad and potent HIV antibodies that mimic CD4 binding. *Science* **333**, 1633–1637 (2011).
43. von Boehmer, L. et al. Sequencing and cloning of antigen-specific antibodies from mouse memory B cells. *Nat. Protocols* **11**, 1908–1923 (2016).
44. Scharf, L. et al. Broadly neutralizing antibody 8ANC195 recognizes closed and open states of HIV-1 Env. *Cell* **162**, 1379–1390 (2015).
45. Diskin, R., Marcovecchio, P. M. & Bjorkman, P. J. Structure of a clade C HIV-1 gp120 bound to CD4 and CD4-induced antibody reveals anti-CD4 polyreactivity. *Nat. Struct. Mol. Biol.* **17**, 608–613 (2010).
46. Montefiori, D. C. Measuring HIV neutralization in a luciferase reporter gene assay. *Methods Mol. Biol.* **485**, 395–405 (2009).
47. Vaughn, D. E. & Bjorkman, P. J. High-affinity binding of the neonatal Fc receptor to its IgG ligand requires receptor immobilization. *Biochemistry* **36**, 9374–9380 (1997).
48. Tan, Y. Z., Cheng, A., Potter, C. S. & Carragher, B. Automated data collection in single particle electron microscopy. *Microscopy* **65**, 43–56 (2016).
49. Zheng, S. Q. et al. MotionCor2: anisotropic correction of beam-induced motion for improved cryo-electron microscopy. *Nat. Methods* **14**, 331–332 (2017).
50. Zivanov, J. et al. New tools for automated high-resolution cryo-EM structure determination in RELION-3. *eLife* **7**, e42166 (2018).
51. Zhang, K. Gctf: real-time CTF determination and correction. *J. Struct. Biol.* **193**, 1–12 (2016).
52. Punjani, A., Rubinstein, J. L., Fleet, D. J. & Brubaker, M. A. cryoSPARC: algorithms for rapid unsupervised cryo-EM structure determination. *Nat. Methods* **14**, 290–296 (2017).

53. Scheres, S. H. & Chen, S. Prevention of overfitting in cryo-EM structure determination. *Nat. Methods* **9**, 853–854 (2012).
54. Terwilliger, T. C., Sobolev, O. V., Afonine, P. V. & Adams, P. D. Automated map sharpening by maximization of detail and connectivity. *Acta Crystallogr.* **74**, 545–559 (2018).
55. Goddard, T. D., Huang, C. C. & Ferrin, T. E. Visualizing density maps with UCSF Chimera. *J. Struct. Biol.* **157**, 281–287 (2007).
56. Adams, P. D. et al. PHENIX: a comprehensive Python-based system for macromolecular structure solution. *Acta Crystallogr. D* **66**, 213–221 (2010).
57. Emsley, P., Lohkamp, B., Scott, W. G. & Cowtan, K. Features and development of Coot. *Acta Crystallogr. D* **66**, 486–501 (2010).
58. Chen, V. B. et al. MolProbity: all-atom structure validation for macromolecular crystallography. *Acta Crystallogr. D* **66**, 12–21 (2010).
59. Agirre, J. et al. Privateer: software for the conformational validation of carbohydrate structures. *Nat. Struct. Mol. Biol.* **22**, 833–834 (2015).
60. Kucukelbir, A., Sigworth, F. J. & Tagare, H. D. Quantifying the local resolution of cryo-EM density maps. *Nat. Methods* **11**, 63–65 (2014).
61. Corcoran, M. M. et al. Production of individualized V gene databases reveals high levels of immunoglobulin genetic diversity. *Nat. Commun.* **7**, 13642 (2016).

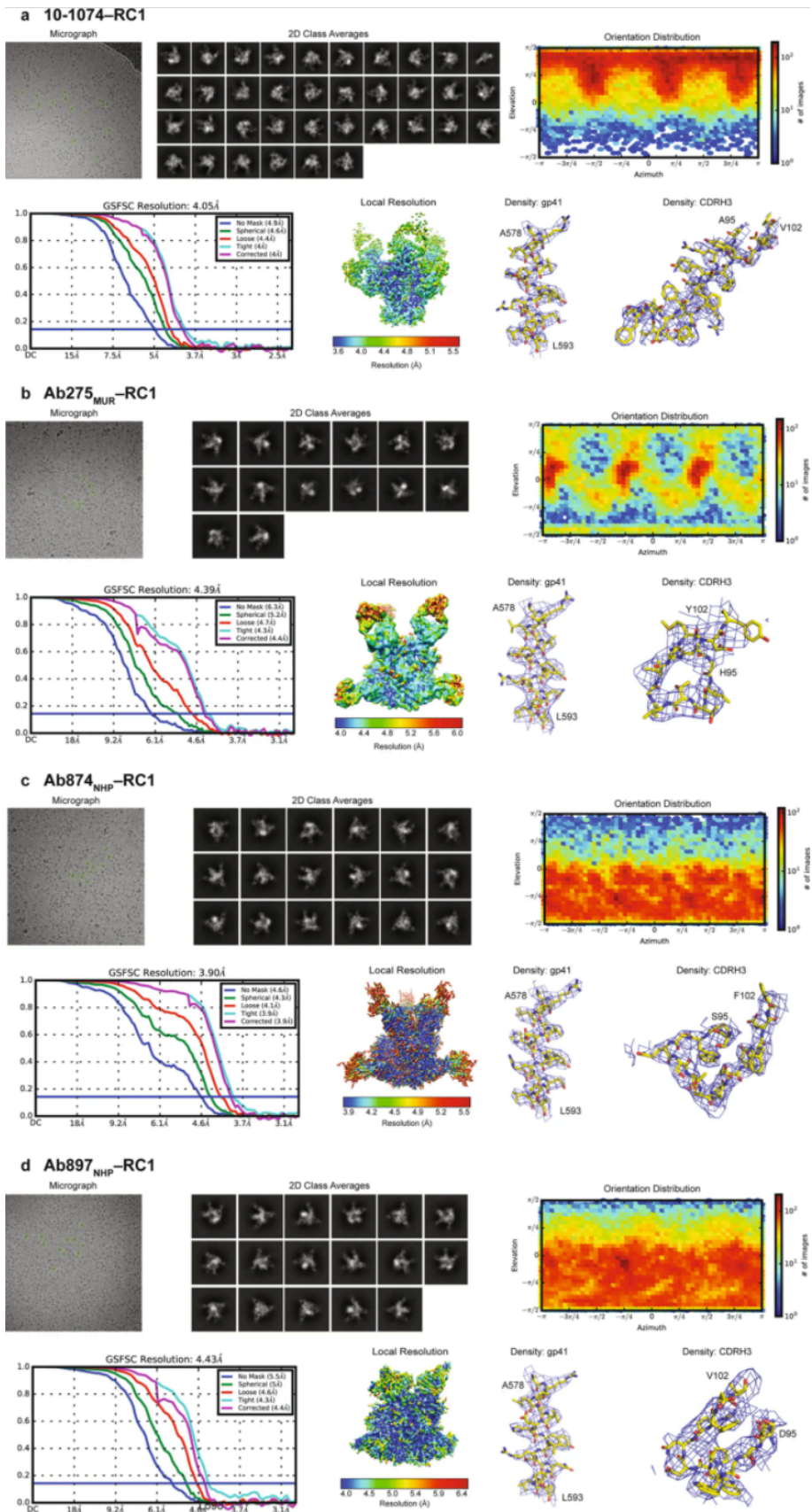
**Extended Data Figures and Tables**

Additional Extended Data and Supplementary Tables available online at  
<https://doi.org/10.1038/s41586-019-1250-z>.

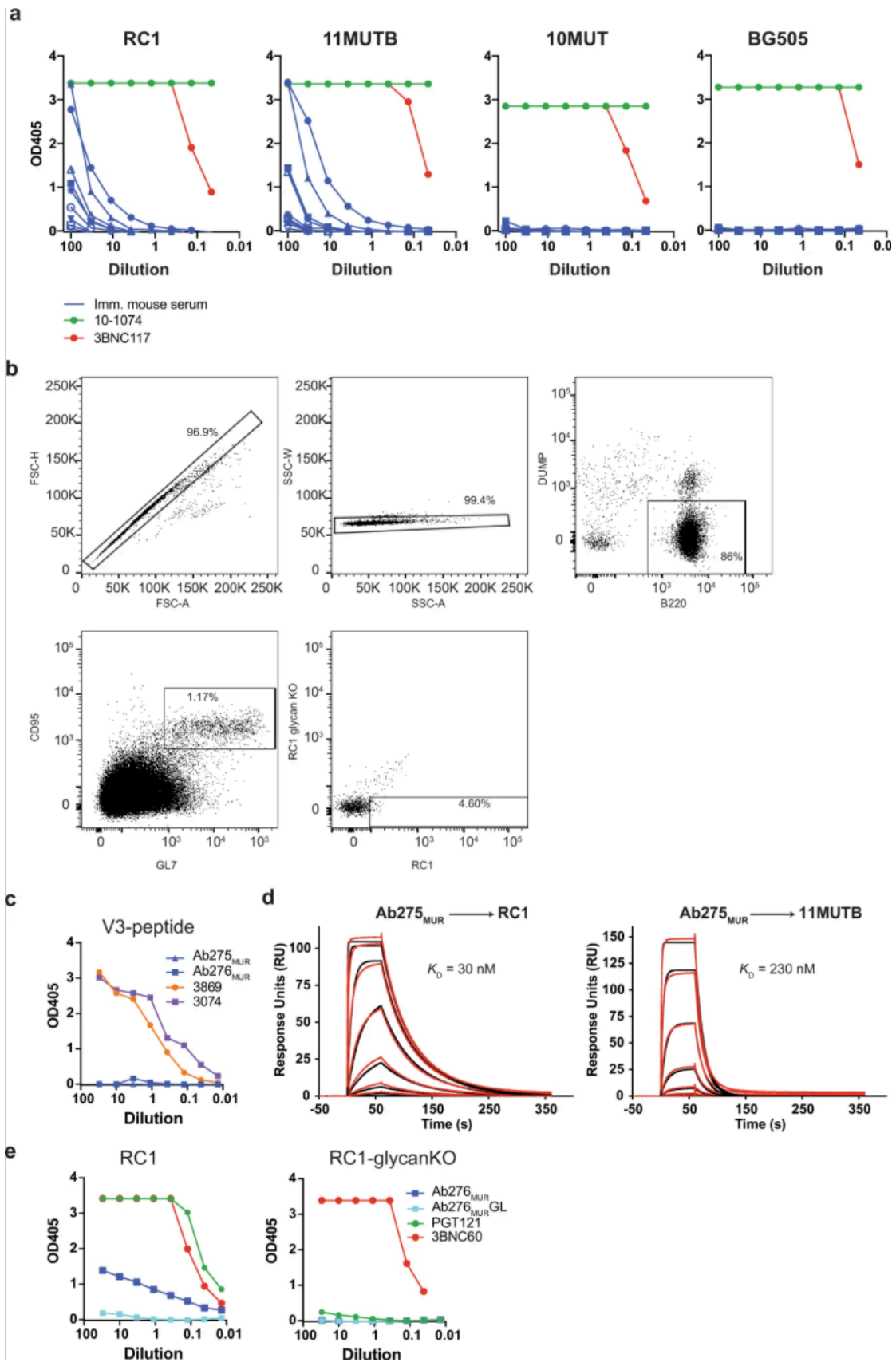


**Extended Data Fig. 1 RC1 characterization.** **a**, Comparison of geometric mean half-maximum inhibitory concentrations ( $\text{IC}_{50}$ ) for V3-glycan patch bNAbs (10-1074 and

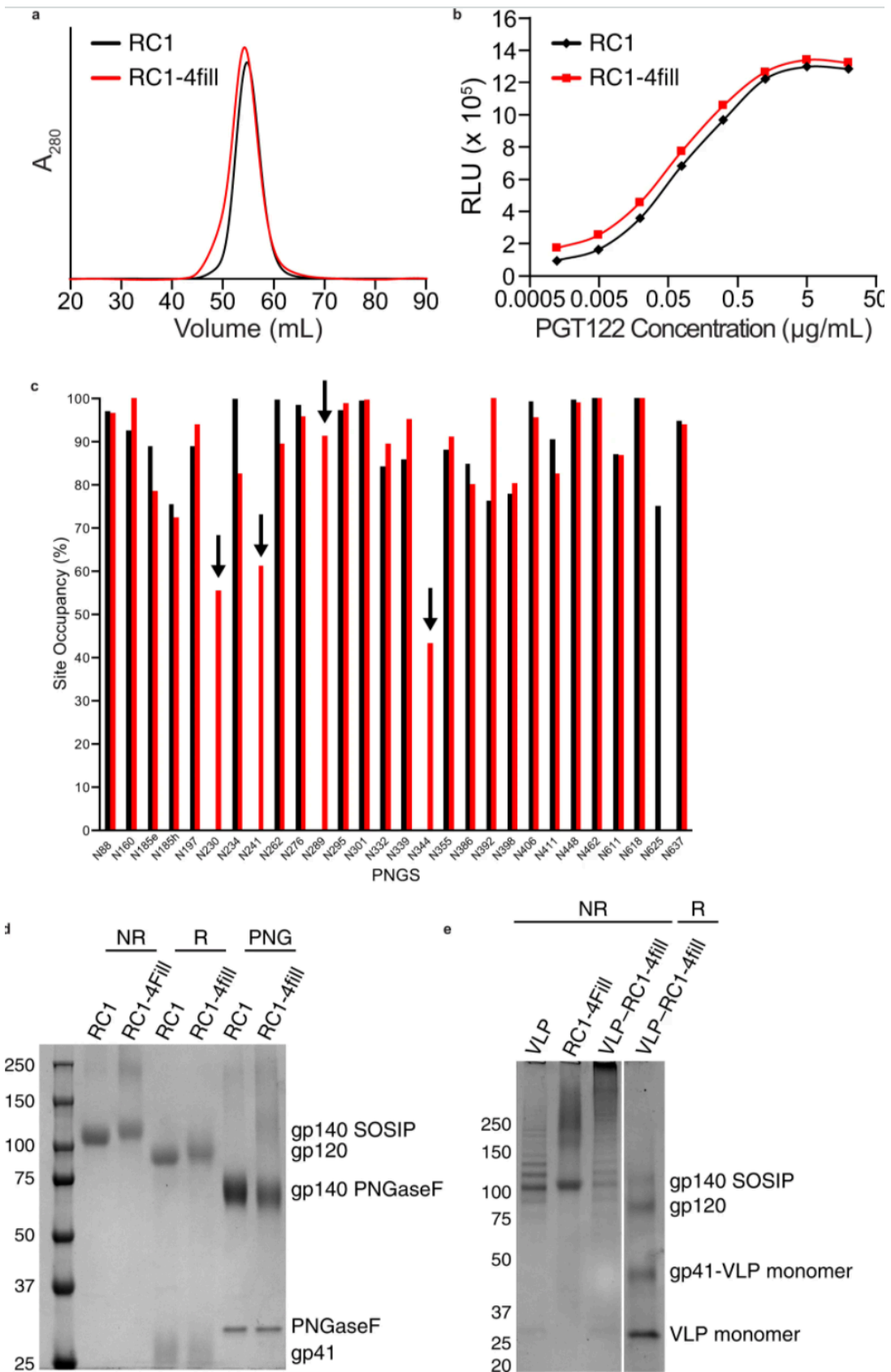
PGT121) and an N156 glycan-dependent V1V2 bNAb (BG1) evaluated against HIV-1 strains that either contained or did not contain a PNGS at the indicated positions (the number of HIV-1 strains is indicated in the parentheses). Values of  $IC_{50}$  greater than  $50 \mu\text{g ml}^{-1}$  were set to  $50 \mu\text{g ml}^{-1}$  for geometric mean calculations. Whereas V3-glycan patch bNAbs showed enhanced neutralization upon removal of the N156 glycan, removal of nearby glycans (N137 or N301) diminished or had little effect on neutralization. **b**, ELISA data showing the binding of different classes of bNAbs to RC1, RC1-4fill and BG505. bNAbs were evaluated at  $5 \mu\text{g ml}^{-1}$  and seven additional threefold dilutions.  $n = 2$ . RC1 and RC1-4fill show similar binding patterns for V3-glycan patch bNAbs, CD4-binding site bNAbs (CD4bs) and gp120–gp41 interface bNAbs, but reduced binding to BG1, a V1V2 bNAb that interacts with the N156 glycan (see **a**).



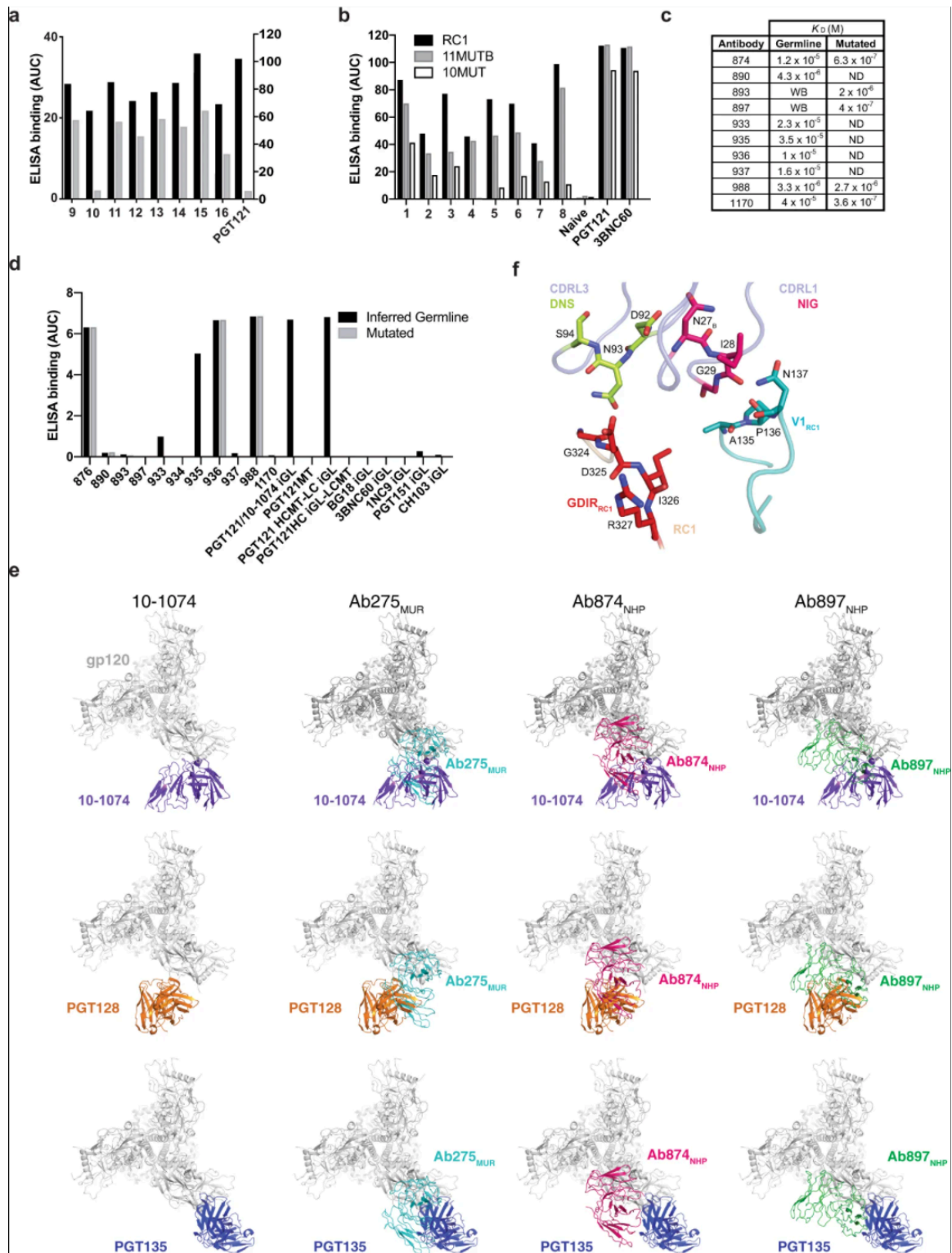
**Extended Data Fig. 2** Cryo-EM data collection and processing for RC1 complexes. **a–d**, A representative micrograph, selected two-dimensional class averages, orientation distribution summary, GSFSC resolution plot, local resolution (calculated using ResMap) and representative density maps contoured at  $7\sigma$  for a gp41 helix and antibody CDRH3 are shown. **a**, The 10-1074–RC1 complex. **b**, The Ab275<sub>MUR</sub>–RC1 complex. **c**, The Ab874<sub>NHP</sub>–RC1 complex. **d**, The Ab897<sub>NHP</sub>–RC1 complex.



**Extended Data Fig. 3** Antibody responses in wild-type mice. **a**, ELISA cross-reactivity of serum from RC1-immunized wild-type mice to 11MUTB. Binding of the serum from wild-type mice primed with RC1 to RC1, 11MUTB, 10MUT and BG505 is shown in blue. Binding of the human bNAbs 10-1074 (green) and 3BNC117 (red) was evaluated at  $5 \mu\text{g ml}^{-1}$  as a control.  $n = 2$ . **b**, FACS plots showing the gating strategy to isolate single RC1<sup>+</sup>RC1-glycanKO<sup>-</sup> germinal centre B cells (DUMP<sup>-</sup> (CD4<sup>-</sup>, CD8<sup>-</sup>, F4/80<sup>-</sup>, NK1.1<sup>-</sup>, CD11b<sup>-</sup>, CD11c<sup>-</sup> and Gr-1<sup>-</sup>) B220<sup>+</sup>CD95<sup>+</sup>GL7<sup>+</sup>RC1-glycanKO<sup>-</sup>RC1<sup>+</sup>) from the spleen and draining lymph nodes of wild-type mice primed with RC1 or RC1-4fill. **c**, Binding of the mouse antibodies Ab275<sub>MUR</sub> and Ab276<sub>MUR</sub> to a V3 loop-consensus C peptide (see Methods). Human antibodies 3869 and 3074 were used as positive controls. Antibodies were evaluated at  $30 \mu\text{g ml}^{-1}$ .  $n = 2$ . **d**, Representative sensograms from two independent SPR-binding experiments of Ab275<sub>MUR</sub> Fab injected over immobilized RC1 (left) or 11MUTB (right). Experimental binding curves (red) are overlaid with predicted curves (black) derived from a 1:1 binding model. Representative of 3 independent experiments. **e**, Binding of Ab276<sub>MUR</sub> and its inferred germline version (Ab276<sub>MUR</sub>GL) to RC1 (left) and RC1-glycanKO (right) at  $30 \mu\text{g ml}^{-1}$ . The human monoclonal antibodies PGT121 (green) and 3BNC60 (red) were used as controls at  $5 \mu\text{g ml}^{-1}$ .



**Extended Data Fig. 4** Characterization of RC1, RC1-4fill and VLPs. **a**, SEC profiles of RC1 and RC1-4fill showing a larger apparent hydrodynamic radius for RC1-4fill compared with RC1, consistent with addition of extra glycans at the introduced PNGSs. **b**, ELISAs showing comparable binding of PGT122 Fab to RC1 and RC1-4fill. RLU, relative luminescence unit. **c**, Glycan site occupancy for each PNGS in RC1 and RC1-4fill determined by mass spectrometry. **d**, SDS-PAGE analysis for RC1 and RC1-4fill under non-reducing (NR), reducing (R) and PNGaseF-treated (PNG) conditions. **e**, SDS-PAGE analysis for VLP, SpyTagged RC1-4fill and VLP-RC1-4fill under non-reducing and reducing conditions.



**Extended Data Fig. 5** Characterization of antibody responses in macaques. **a**, Binding of serum from macaques primed with RC1-4fill VLPs. ELISAs of the serum from eight macaques primed with RC1-4fill VLPs and PGT121 to RC1 (black) and RC1-glycanKO (grey) are shown. **b**, Binding of serum from macaques primed with RC1-4fill VLPs. ELISA of the serum from eight macaques primed with RC1-4fill VLP and one naive macaque to RC1 (black) and the sequentially less modified Env proteins 11MUTB (grey) and 10MUT (white). The human bNAbs PGT121 and 3BNC60 were used as controls at  $5 \mu\text{g ml}^{-1}$ , and the serum was evaluated at a 1:100 dilution and seven additional threefold serial dilutions. **c**, The affinities ( $K_D$ ) for RC1 of different macaque antibodies isolated after a prime with VLP-RC1-4fill and the corresponding inferred germline-reverted antibodies as determined by bio-layer interferometry (OCTET). **d**, Binding of an anti-idiotypic antibody that recognizes the inferred germline of PGT121/10-1074 to monoclonal antibodies isolated from macaques primed with VLP-RC1-4fill. The inferred germline (iGL) of PGT121/10-1074, two chimeric antibodies comprising the mutated (MT) heavy chain (HC) and inferred germline light chain (LC) of PGT121 (PGT121 HCMT-LC iGL) or the inferred germline HC and the mutated LC of PGT121 (PGT121HC iGL-LCMT) and different inferred germline bNAbs were used as controls. **a, b, d**, Results are shown as the area under the ELISA curve (AUC). **e**, Comparison of binding mode between the vaccine-elicited antibodies (Ab275<sub>MUR</sub>, Ab874<sub>NHP</sub> and Ab897<sub>NHP</sub>) and the V3-glycan patch bNAbs 10-1074, PGT128 and PGT135. RC1 trimer is shown in grey from above and all Fabs are modelled onto the same trimer. For clarity, only one Fab per trimer is shown. **f**, Interactions between Ab897<sub>NHP</sub> conserved light chain motifs and RC1 gp120. Lime, DNS motif in CDRL3; red, gp120 GDIR; pink, NIG motif in CDRL1; teal, gp120 V1 loop. Each AUC value corresponds to one ELISA curve.

	RC1-10-1074 (EMDB-20175) (PDB 6ORN)	RC1-Ab275 <sub>MUR</sub> (EMDB-20178) (PDB 6ORQ)	RC1-Ab874 <sub>NHP</sub> (EMDB-20176) (PDB 6ORO)	RC1-Ab897 <sub>NHP</sub> (EMDB-20177) (PDB 6ORP)
<b>Data collection and processing</b>				
Magnification	73,000x	73,000x	73,000x	73,000x
Voltage (kV)	200	200	200	200
Electron exposure (e-/Å <sup>2</sup> )	39.1	40	40	40
Defocus range (μm)	1 - 3.4	0.8 - 2.5	0.8 - 2.5	0.8 - 2.5
Pixel size (Å)	1.436	1.436	1.436	1.436
Symmetry imposed	C3	C3	C3	C3
Initial particle images (no.)	145,907	172,558	188,004	314,471
Final particle images (no.)	122,013	49,308	86,564	158,954
Map resolution (Å)	4.05	4.39	3.90	4.43
FSC threshold - 0.143				
Map resolution range (Å)	3.6 - 6	4.2 - 7	3.5 - 6.5	4.2 - 7
<b>Refinement</b>				
Initial model used (PDB code)	ab initio	ab initio	ab initio	ab initio
Model resolution (Å)	4.0	4.4	3.9	4.4
FSC threshold	0.143	0.143	0.143	0.143
Model resolution range (Å)	3.8 - 4.2	3.8 - 4.4	3.6 - 4.0	4.0 - 4.5
Map sharpening <i>B</i> factor (Å <sup>2</sup> )	-192.6	-252.4	-230.0	-322.1
<b>Model composition</b>				
Non-hydrogen atoms	20,475	19,932	20,010	19,590
Protein residues	2,418	2,430	2,421	2,397
Ligands	BMA:9 NAG:81 MAN:21	BMA:6 NAG:54 MAN:6	BMA:9 NAG:66 MAN:12	BMA:6 NAG:48 MAN:18
<b><i>B</i> factors (Å<sup>2</sup>)</b>				
Protein	52.4	162.6	74.6	135.0
Ligand	73.5	199.3	100.2	188.2
<b>R.m.s. deviations</b>				
Bond lengths (Å)	0.007	0.007	0.007	0.008
Bond angles (°)	0.884	1.108	1.091	1.084
<b>Validation</b>				
MolProbity score	2.07	2.19	1.92	2.43
Clashscore	10.87	8.12	4.67	7.61
Poor rotamers (%)	0.95	1.28	1.29	2.87
<b>Ramachandran plot</b>				
Favored (%)	91.0	84.8	88.0	84.9
Allowed (%)	8.9	15.0	12.0	15.1
Disallowed (%)	0.1	0.1	0	0

**Extended Data Table 1 Cryo-EM data collection, refinement and validation statistics.**

*Chapter 4***ANTIBODY ELICITED BY HIV-1 IMMUNOGEN VACCINATION IN MACAQUES DISPLACES ENV FUSION PEPTIDE AND DESTROYS A NEUTRALIZING EPITOPE**

**Abernathy, M.E.**, Gristick, H.B, Vielmetter, J., Keeffe, J.R., Gnanapragasam, P.N.P, Lee, Y.E., Escolano, A., Gautam, R., Seaman, M.S., Martin, M.A., Nussenzweig, M.C., Bjorkman, P.J. Antibody elicited by HIV-1 immunogen vaccination in macaques displaces Env fusion peptide and destroys a neutralizing epitope. *npj Vaccines*, **6**, 126 (2021). <https://doi.org/10.1038/s41541-021-00387-4>

**Summary**

HIV-1 vaccine design aims to develop an immunogen that elicits broadly neutralizing antibodies against a desired epitope, while eliminating responses to off-target regions of HIV-1 Env. We report characterization of Ab1245, an off-target antibody against the Env gp120-gp41 interface, from V3-glycan patch immunogen-primed and boosted macaques. A 3.7 Å cryo-EM structure of an Ab1245-Env complex reveals one Ab1245 Fab binding asymmetrically to Env trimer at the gp120-gp41 interface using its long CDRH3 to mimic regions of gp41. The mimicry includes positioning of a CDRH3 methionine into the gp41 tryptophan clasp, resulting in displacement of the fusion peptide and fusion peptide-proximal region. Despite fusion peptide displacement, Ab1245 is non-neutralizing even at high concentrations, raising the possibility that only two fusion peptides per trimer are required for viral–host membrane fusion. These structural analyses facilitate immunogen design to prevent elicitation of Ab1245-like antibodies that block neutralizing antibodies against the fusion peptide.

**Introduction**

Recent efforts in vaccine design for the HIV-1 virus have focused on developing neutralizing adaptive immune responses to the HIV-1 Env glycoprotein via sequential immunization<sup>1-3</sup>.

Studies of broadly neutralizing antibodies (bNAbs) isolated from HIV+ human donors have informed immunogen design efforts for various epitopes on the Env trimer, including the V3-glycan patch<sup>4,5</sup>, the fusion peptide (FP)<sup>6,7</sup>, and the CD4-binding site<sup>8,9</sup>. In some cases, on-target antibody responses are accompanied by off-target responses in which antibodies are made against undesired epitopes on the Env trimer including the ‘bottom’ or ‘base’ epitope<sup>10</sup> and/or a minimally-glycosylated region (glycan ‘hole’)<sup>11</sup>. These antibodies target immunodominant but non-neutralizing epitopes and therefore do not contribute meaningfully to a neutralizing antibody response.

We previously described the design and characterization of RC1, a BG505 SOSIP.664<sup>12</sup>-based engineered immunogen targeting the V3-glycan patch on the gp120 subunit of Env trimer<sup>4</sup>. We showed that RC1 and/or RC1-4fill (modified from RC1 to include additional potential N-linked glycosylation sites; PNGSs) that had been multimerized on virus-like particles (VLPs) elicited antibodies that recognized the V3-glycan patch in wild-type mice, rabbits, and non-human primates (NHPs)<sup>4</sup>. We subsequently boosted a subset of RC1-4fill-primed NHPs, isolated single Env-specific B cells, and derived antibody sequences from which monoclonal antibodies (mAbs) were produced<sup>13</sup>. Here, we describe a single-particle cryo-EM structure of a BG505 Env trimer bound to a monoclonal antibody (Ab1245) isolated from a rhesus macaque after a sequential immunization protocol that included multimerized HIV-1 SOSIP Envs derived from different clades. Ab1245 binds to an epitope overlapping with the FP-targeting bNAb VRC34<sup>6</sup> at the interface of the Env gp41 and gp120 subunits, but unlike VRC34, Ab1245 displaces the FP and fusion peptide-proximal region (FPPR). In addition, Ab1245 contains a methionine residue that structurally mimics Met530<sub>gp41</sub>, a key residue for the stability of the Env trimer, by engaging the “tryptophan clasp” formed by three gp41 tryptophan residues<sup>14,15</sup>. Despite inducing FP rearrangement and overlap with the neutralizing VRC34 epitope, Ab1245 did not neutralize BG505 or other viral strains, perhaps because of its sub-stoichiometric binding to Env trimer. These previously-unseen features of gp120-gp41 interface antibodies demonstrate that HIV-1 Env can elicit non-neutralizing antibodies that block a neutralizing epitope, inform immunogen design protocols to prevent

elicitation of similar antibodies, and provide potential mechanistic insight into HIV-1 Env-mediated fusion of the host and viral membranes.

## **Results & Discussion**

### **Sequential immunization after RC1-4-fill priming elicited Ab1245, a non-V3-targeting antibody**

We previously described a V3-glycan patch targeting immunogen, RC1, which was modified from a designed V3 immunogen, 11MUTB<sup>16</sup>, by removing the N-linked glycan attached to gp120 residue N156<sub>gp120</sub><sup>4</sup>. Both RC1 and 11MUTB were derived from clade A BG505 SOSIP.664 native-like Env trimers<sup>12</sup>. RC1-4fill and 11MUTB-4fill were modified from RC1 and 11MUTB, respectively, to reduce antibody responses to off-target epitopes<sup>11,17-19</sup> by inserting PNGSs to add glycans to residues 230<sub>gp120</sub>, 241<sub>gp120</sub>, 289<sub>gp120</sub>, and 344<sub>gp120</sub><sup>4</sup>. In addition, to enhance avidity effects and limit antibody access to the Env trimer base, we multimerized immunogens on VLPs using the SpyTag-SpyCatcher system<sup>20,21</sup>. Four NHPs primed with RC1-4fill-VLPs<sup>4</sup> were boosted sequentially with (i) VLPS coupled with 11MUTB-4fill<sup>16</sup> (clade A), (ii) VLPs coupled with B41 SOSIP (clade B), and (iii) VLPs coupled with a mixture of AMC011 and DU422 SOSIPs (clades B and C) over the course of 9 months<sup>22</sup> (Fig. 1a).

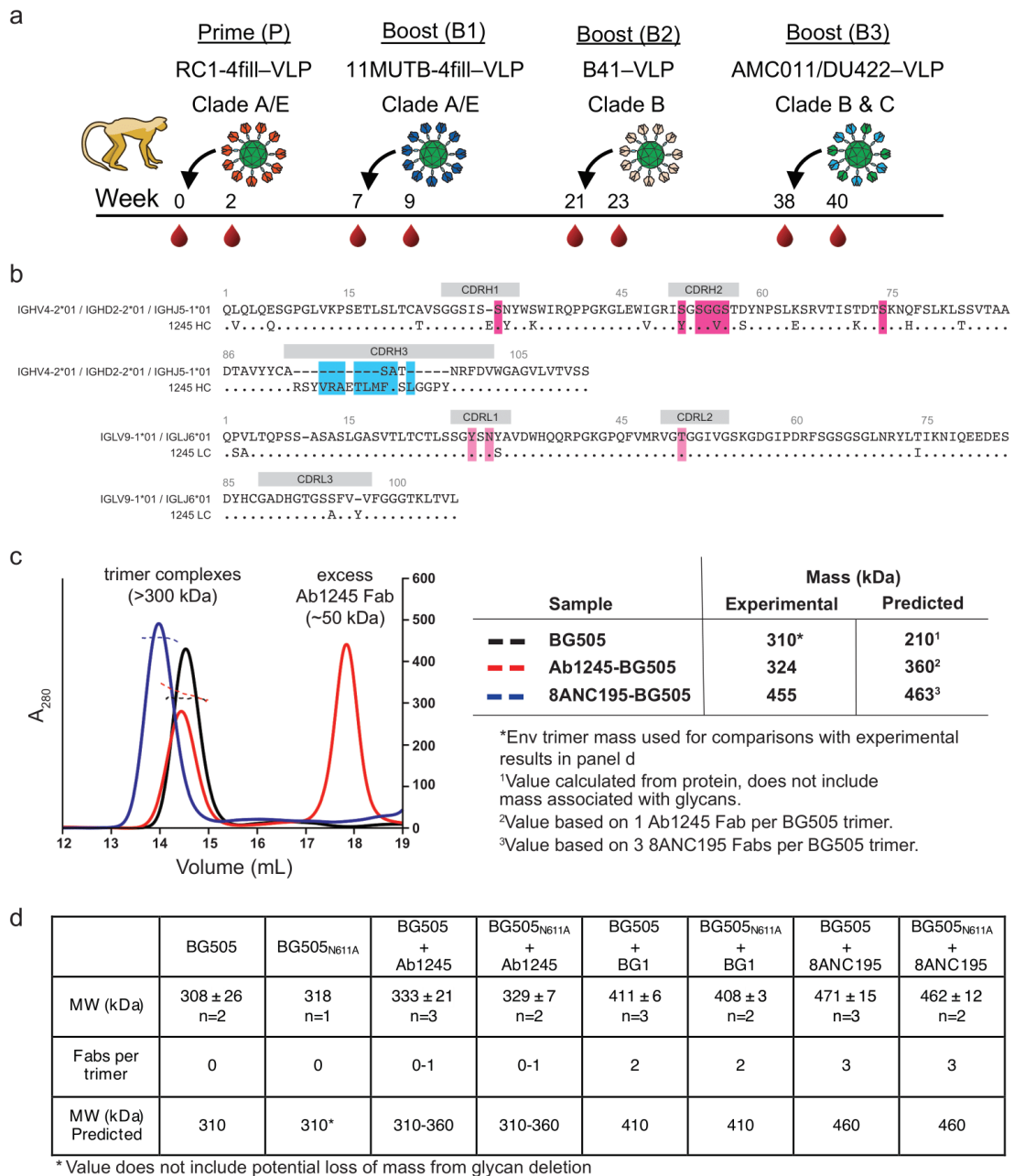


**Figure 1.** Characterization of Ab1245 elicited in macaques by sequential immunization. **a** Sequential immunization protocol for the macaque that produced Ab1245 over the course of 40 weeks. **b** Sequence alignment of Ab1245 heavy and light chains with their germline precursors. Contacts with BG505 Env are indicated by a colored box around the residue (cyan box of CDRH3 contact residues; dark pink and light pink boxes for heavy chain and light chain contact residues, respectively). Residues within CDRs are indicated; residues between CDRs are within framework regions (FWRs). CDRH3 residues derived from VDJ joining are shown as dashes in the top germline sequence, and changes from the germline

precursors are denoted a different residue in the mature Ab1245 sequence. Residues are numbered using the Kabat convention. **c** SEC-MALS profiles for BG505 SOSIP.664 Env trimer alone and complexed with a threefold molar excess of Ab1245 and 8ANC195 Fabs. Left: absorbance at 280 nm (left *y*-axis) plotted against elution volume from a Superdex 200 10/300 GL gel filtration column overlaid with the molar mass determined for each peak (right *y*-axis). Right: Table showing predicted and calculated molecular masses. **d** Mass photometry results. Derived molecular masses (MW) are listed for Env trimers (either BG505 or BG505<sub>N611A</sub>) incubated without an added Fab or with the indicated Fab (Ab1245, BG1, or 8ANC195) as mean and standard deviation for the indicated number of independent measurements. The Fabs/trimer row shows the expected number of Fabs for each Fab/Env trimer complex. The predicted mass row shows the mass calculated assuming 310 kDa for BG505 trimer (derived by SEC-MALS, (c)) plus 50 kDa per bound Fab.

The sequences of the heavy and light chains of Ab1245 were generated by single cell cloning from B cells isolated from one of the boosted NHPs that were captured using BG505 and B41 SOSIPs as baits as described<sup>13,22</sup> (Fig. 1b). The heavy and light chains were derived from the macaque V gene segments IGHV4-2\*01 and IGLV9-1\*01, respectively, and exhibited 14% (heavy chain) and 5% (light chain) amino acid changes due to somatic hypermutation. Of note, the third complementarity region (CDR) of the heavy chain (CDRH3) was longer than typical macaque CDRH3s (24 residues compared with an average of 13-15 residues<sup>23</sup>).

### **One Ab1245 Fab binds to each BG505 SOSIP trimer**

To determine the binding stoichiometry for the Ab1245 Fab interaction with BG505 SOSIP trimer, we derived the absolute molecular mass of BG505-Ab1245 Fab complexes using size-exclusion chromatography combined with multi-angle light scattering (SEC-MALS). When BG505 was incubated overnight with a 3-fold molar excess of Ab1245 Fab (three Fabs per gp120-gp41 protomer), we observed a heterogeneous mixture corresponding to zero to one Ab1245 Fabs bound per trimer, whereas incubation with 8ANC195 Fab resulted in a homogeneous complex corresponding to three Fabs per trimer (Fig. 1c), as expected from previous stoichiometry measurements and structures<sup>24-26</sup>. To verify that one or more Ab1245 Fabs per trimer did not dissociate during the chromatography procedure required for SEC-MALS, we used mass photometry, a technique that derives approximate masses for individual proteins and complexes in solution<sup>27</sup>, to measure the molecular masses of BG505

alone and complexed with Ab1245 or with control Fabs: 8ANC195 (three Fabs per BG505 trimer)<sup>24-26</sup> and BG1 (two Fabs per BG505 trimer)<sup>24</sup>. Consistent with the SEC-MALS results, mass photometry experiments suggested zero to one Ab1245 Fabs bound to each wild-type BG505 trimer and to a N611A mutant BG505 trimer (Fig. 1d). We conclude that Ab1245 Fab binds asymmetrically to Env with one or zero Fabs per trimer.

### **Ab1245 binds at the gp120-gp41 interface**

To further characterize the Ab1245 epitope on HIV-1 Env, we solved a single-particle cryo-EM structure of Ab1245 Fab bound to a BG505 Env trimer. To form complexes, we incubated a 3-fold molar excess of Ab1245 Fab with BG505, followed by an incubation with a 3-fold excess of 8ANC195<sup>28</sup> Fab to add mass to the complex and prevent problems associated with preferred orientation bias (Table 1, Supplementary Fig. 1c). This resulted in complex formation with three 8ANC195 Fabs and one Ab1245 Fab bound per BG505 trimer (Fig. 2a), consistent with the stoichiometry experiments (Fig. 1c,d). The complex with one Ab1245 Fab per BG505 trimer was resolved at 3.7 Å resolution and showed generally well-defined side chain density throughout the complex (Fig. 2b; Supplementary Fig. 1f). An additional 3D class of BG505 trimers was observed with three bound 8ANC195 Fabs and no Ab1245 Fabs (Supplementary Fig. 1e).

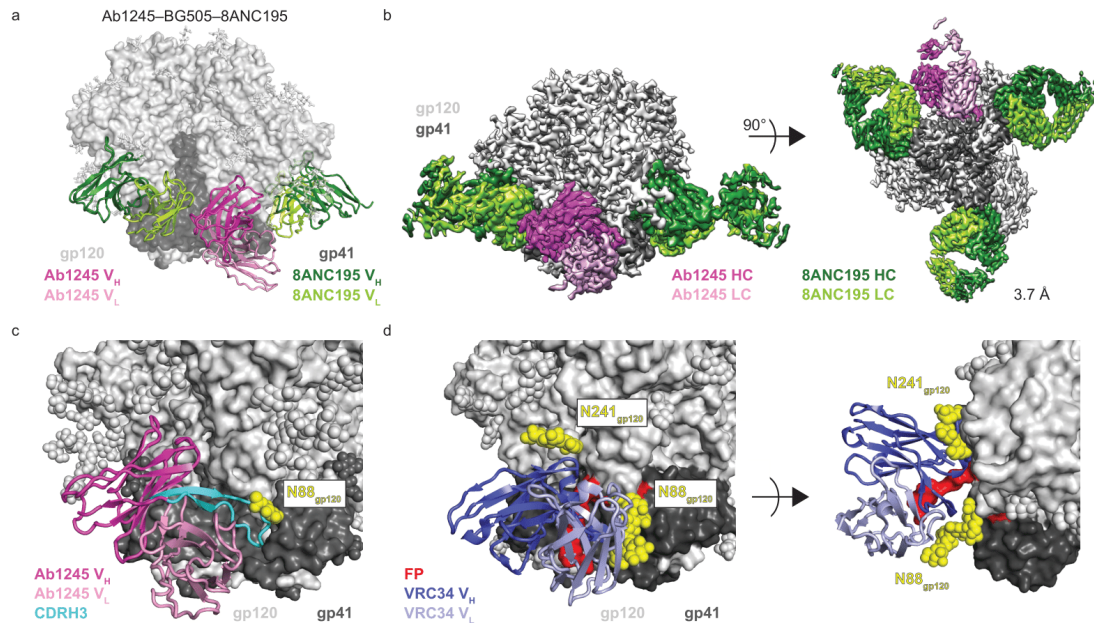


**Figure 2.** Ab1245 binds the gp120-gp41 interface. **a** Representation of Ab1245-BG505-8ANC195 structure. Fabs are shown in cartoon, BG505 is shown as surface, and glycans are shown as sticks. Within BG505, gp120 is light gray and gp41 is dark gray. The Ab1245 V<sub>H</sub>-V<sub>L</sub> is dark pink (heavy chain) and light pink (light chain); 8ANC195 Fabs are dark green (heavy chain) and light green (light chain). **b** Side view (left) and view looking up from the trimer base (right) of density map for 3.7 Å Ab1245-BG505-8ANC195 complex. Colors as in (a). **c** Close-up view of Ab1245 V<sub>H</sub>-V<sub>L</sub> domains (cartoon) interacting with gp120-gp41 interface with highlighted CDRH3 (cyan). N-linked glycans are light gray (gp120), dark gray (gp41), or yellow (N88<sub>gp120</sub> and N241<sub>gp120</sub> glycans) spheres. **d** Cartoon representation of VRC34-AMC011 SOSIP structure (PDB 6NC3) from the same view as c (left) and a different view from above the trimer (right). VRC34 heavy and light chains (PDB 6NC3) are dark and light purple, respectively.

The Ab1245-BG505-8ANC195 complex structure revealed non-overlapping epitopes at the gp120-gp41 interface for Ab1245 and 8ANC195 (Fig. 2a,b). The Ab1245 Fab was located at the interface between the gp120 and gp41 of its primary Env protomer and the gp41 of a neighboring protomer (Fig. 2c, Fig. 3a). By contrast, 8ANC195 recognized the gp120-gp41 interface of a single protomer with no contacts to neighboring protomers (Fig. 2a, Fig. 3a), and equivalent interactions with the three BG505 protomers<sup>26</sup>. The Ab1245 epitope overlaps with that of VRC34, a FP-directed bNAb that binds with a three Fab per Env trimer stoichiometry at a site that is located closer to the trimer base<sup>6</sup> than the Ab1245 epitope (Fig. 2d; Supplementary Fig. 2a). The Ab1245 heavy chain made the majority of contacts with

BG505 (only three light chain residues contact BG505), and all but one of the 19 heavy and light chain contact residues were located within CDRs rather than antibody framework regions (FWRs) (Fig. 1b, Fig. 3b). The Ab1245 CDRH1 and CDRH2 loops formed extensive interactions with a portion of gp120 between residues Pro79<sub>gp120</sub> and Glu87<sub>gp120</sub> (Fig. 3c), while the long (24-amino acid) CDRH3 loop contacted gp41 residues as well as residues at the termini of gp120 that fit inside the previously-defined membrane-proximal collar<sup>14</sup> (Fig. 3d). The Ab1245 light chain made contacts with the terminal helix of an adjacent gp41 subunit, which had undergone a change in conformation from a helix to a unstructured region that was partially disordered, suggesting the possibility that the gp41 helix conformation sterically interferes with binding, as was also proposed for the interaction of the human bNAb 3BC315 with BG505 Env trimer<sup>29</sup> (Fig. 3a,e). The majority of the Ab1245 Fab contacts with BG505 were contacts to protein residues, with the only glycan contact involving the third framework region of the antibody heavy chain (FRWH3) with a terminal sugar on the Asn448<sub>gp120</sub> glycan (Fig. 3a). By contrast, the 8ANC195 epitope includes required contacts with glycans attached to residues Asn276<sub>gp120</sub> and Asn234<sub>gp120</sub><sup>26,30</sup>, and the VRC34 epitope includes contacts with glycans at residues Asn88<sub>gp120</sub> and Asn241<sub>gp120</sub><sup>6</sup> (Fig. 3a, Fig. 2d). The possibility that an N-glycan attached to Asn611<sub>gp41</sub> could occlude Ab1245 Fab binding was suggested by a lack of density for this glycan on the primary Ab1245-binding protomer compared with density for one GlcNAc attached to the Asn611<sub>gp41</sub> residues on the other two protomers (Supplementary Fig. 2b). However, only one Ab1245 Fab bound to a soluble BG505<sub>N611A</sub> trimer (Fig. 1d), implying that the presence of the Asn611<sub>gp41</sub> glycan does not account for sub-stoichiometric binding of Ab1245 to Env trimers.

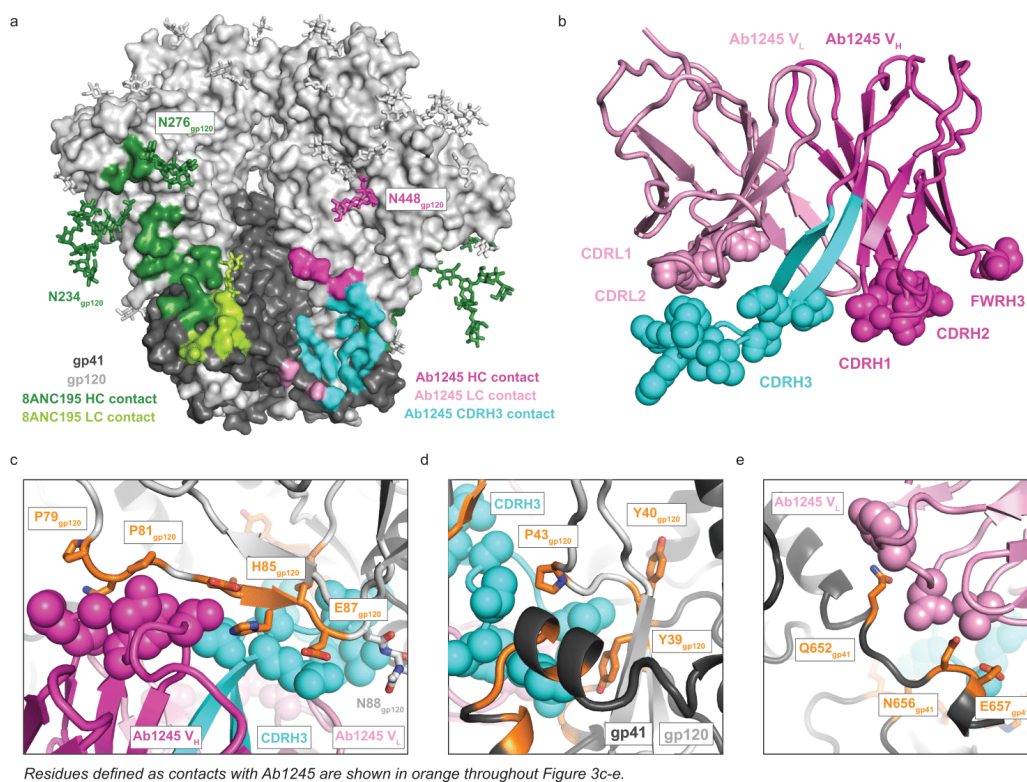
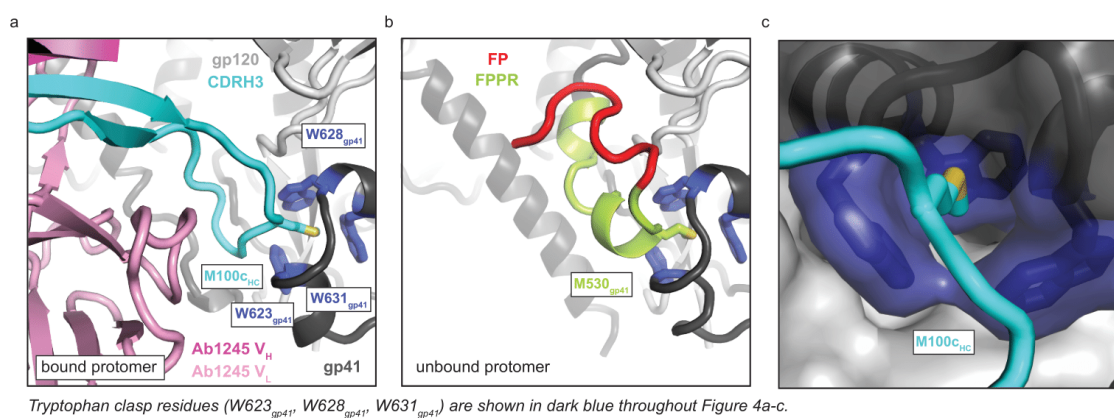


**Figure 3.** Ab1245 CDRH3 makes the majority of contacts to BG505 Env. **a** Surface representation of BG505 trimer with colored highlights showing the epitopes of Ab1245 (light and dark pink with CDRH3 contacts highlighted in cyan and pink sticks for glycan contacts) and 8ANC195 (green, with green sticks representing glycans within the epitope). Glycans represented that are not part of an epitope are shown as gray sticks. **b** Cartoon representation of Ab1245 with paratope residue atoms shown as colored spheres. **c** gp120 interactions with Ab1245 CDRH1 and CDRH2 loops (dark pink spheres). gp120 is gray with contacts to Ab1245 highlighted in orange. Sidechains of gp120 contacts are shown as sticks. The Ab1245 paratope is represented as in (b). **d** Interactions of Ab1245 CDRH3 (cyan spheres) with gp120 (light gray) and gp41 (dark gray). Contacting residues are orange, and side chains discussed in the text are shown. **e** Ab1245 light chain (light pink spheres) contacts with the terminal helix of an adjacent gp41. Contacting residues are orange with side chains shown.

### The Ab1245 CDRH3 contains a gp41 mimicry motif

Unlike binding of the FP-specific bNAb VRC34<sup>6</sup> or any other reported HIV-1 antibody, Ab1245 binding to BG505 Env trimer resulted in displacement of the FP (residues 512<sub>gp41</sub>-527<sub>gp41</sub>) and FPPR (residues 528<sub>gp41</sub>-540<sub>gp41</sub>) of the gp41 subunit within the primary protomer to which Ab1245 was bound (Fig. 4a,b). The FP/FPPR displacement resulted from

intercalation of the Ab1245 CDRH3 (Fig. 4a). Although the gp41 residues of HR1N (547<sub>gp41</sub>-568<sub>gp41</sub>) are usually disordered in structures of Env trimer (except when an interface antibody is bound), residues N-terminal to this region, 520<sub>gp41</sub>-546<sub>gp41</sub>, are ordered whether or not the Env was complexed with a gp120-gp41 interface antibody (e.g.,<sup>31,32</sup>). In the Ab1245-BG505 complex structure, there was no observed density for residues spanning 512<sub>gp41</sub>-565<sub>gp41</sub> on the primary gp41 to which Ab1245 was bound, thus both regions of gp41 were disordered. The disorder resulted from Ab1245 binding because residues 520<sub>gp41</sub> to 546<sub>gp41</sub> were resolved in the two adjacent gp41 subunits (Fig. 4b, Supplementary Fig. 2c).



**d**

Virus ID	Ab1245	N6
	IC <sub>50</sub> (μg/mL)	IC <sub>50</sub> (μg/mL)
6545.v3.c13	>250	-
X1100_c7	>250	-
BB1012-11.TC21	>250	-
Ce704809221_1B3	>250	-
21283649	>250	-
CNE56	>250	-
CAP269.2.00_F11_1	>250	-
JRCSF_N611D	>250	-
MuLV (Neg. Control)	>250	-
BG505	>500	0.47
BG505 <sub>N611A</sub>	>500	0.033

**Figure 4.** Ab1245 CDRH3 mimics gp41 interactions with the tryptophan clasp. **a** Cartoon representation of the interactions between Ab1245 V<sub>H</sub>-V<sub>L</sub> domains (pink with CDRH3 in cyan) and the tryptophan clasp of gp41 (gp41 in dark gray with Trp residues 623<sub>gp41</sub>, 628<sub>gp41</sub>, and 631<sub>gp41</sub> in dark blue) with gp120 in light gray. Interacting residues between M100<sub>c<sub>HC</sub></sub> and the tryptophan clasp shown as sticks. **b** Cartoon representation of the same view of an unbound protomer of gp41 with the portion of gp41 containing the fusion peptide (red) and fusion peptide proximal region (FPPR, green) interacting with the gp41 tryptophan clasp (same coloring as in **a**). Interactions between M530<sub>gp41</sub> and the tryptophan clasp are shown as sticks. **c** Surface representation of gp41 (dark gray) and gp120 (light gray) with tryptophan clasp residues in dark blue. Ab1245 CDRH3 is cyan with a stick representation for the Met100<sub>c<sub>HC</sub></sub> sidechain. **d** In vitro neutralization assays using IgGs Ab1245 or N6<sup>66</sup> (positive

control for neutralization) against the indicated viral strains. In addition to those listed, Ab1245 was tested in-house against pseudoviruses from strains CE0217, CNE55, JRCSF, Du422, T250-4, Tro, X1632, 246F3, CH119, CE1176, BJOX002000\_03\_02, 25710, X2278, CNE8, and 398F1 at a top concentration of 500  $\mu\text{g}/\text{mL}$  or 1000  $\mu\text{g}/\text{mL}$  along with IgG N6 (positive control at a top concentration of 10  $\mu\text{g}/\text{mL}$ ). N6 was not evaluated in against the strains indicated by a dash because its neutralization potencies were previously published<sup>66</sup>. Whereas N6 exhibited expected neutralization potencies against evaluated strains<sup>66</sup>, Ab1245 exhibited no neutralization activity.

One of the disordered gp41 residues in the Ab1245-BG505-8ANC195 structure, Met530<sub>gp41</sub>, normally inserts into the gp41 ‘tryptophan clasp’ formed by residues Trp623<sub>gp41</sub>, Trp628<sub>gp41</sub>, and Trp631<sub>gp41</sub><sup>14,15</sup> (Fig. 4b). The tryptophan clasp has been hypothesized to be a key interaction that stabilizes the Env trimer in both its closed, prefusion conformation and its CD4-bound open conformation, and it has been speculated that the disengagement of Met530<sub>gp41</sub> from the tryptophan clasp triggers elongation of HR1 into a full-length helix and the large rearrangement of the FP required for insertion into the host membrane<sup>14,15</sup>. However, the primary protomer to which Ab1245 is bound contained a disengaged Met530<sub>gp41</sub>, but adopted most structural characteristics of a closed, prefusion Env trimer (Fig. 2a,b). The limited structural changes in Ab1245-bound BG505 from other closed Env trimer structures included disorder of the gp41 FP and FPPR regions, a transition to an unstructured secondary structure in a gp41 terminal helix, a shift in the N88<sub>gp120</sub> glycan, and absence of density for the N611<sub>gp41</sub> glycan (Fig. 4a; Supplementary Fig. 2b,c). The stability of the Ab1245-bound BG505 trimer in the closed conformation despite displacement of Met530<sub>gp41</sub> from the tryptophan clasp is rationalized by the insertion of an Ab1245 CDRH3 residue, Met100c<sub>1245 HC</sub>, into the gp41 tryptophan clasp to mimic Env residue Met530<sub>gp41</sub> (Fig. 4a,c).

Some HIV-1 gp120-gp41 interface-binding antibodies induce dissociation of Env trimers into protomers after incubation for 30 minutes to several hours<sup>29,33</sup>. Disruption of residue(s) within the gp41 tryptophan clasp was hypothesized to be the mechanism by which these antibodies induce trimer dissociation<sup>29,34,35</sup>. Indeed, Met530<sub>gp41</sub>, which is part of the disordered gp41 region that is displaced by Ab1245 binding, has been implicated as an important anchoring residue that mediates gp41 dynamics<sup>36</sup>. However, we found no dissociation of Env trimers into protomers in the cryo-EM structure of the Ab1245-BG505-

8ANC195 complex that was derived after an overnight incubation of BG505 with Fabs or indication of dissociated protomers by SEC-MALS (Fig. 1c). We hypothesize that disruption of the tryptophan clasp by Ab1245 does not induce trimer dissociation because insertion of its CDRH3 residue Met100<sub>C1245 HC</sub> mimics gp41 Met530<sub>gp41</sub> to stabilize the tryptophan clasp conformation (Fig. 4a-c).

### **Ab1245 IgG is non-neutralizing**

Although Ab1245 Fab bound to BG505 SOSIP Env (Fig. 1c,d), we observed no neutralization of a BG505 pseudovirus at Ab1245 IgG concentrations up to 1 mg/mL (Fig. 4d). Additionally, we observed no neutralization by Ab1245 Fab at concentrations up to 100 µg/mL for eight strains of pseudovirus. The location of the Ab1245 epitope and its angle of approach for binding to BG505 SOSIP predicts no steric occlusion with the membrane of a virion (Fig. 2a,b). Since the conformations of membrane-bound and SOSIP Env trimers are similar<sup>37-39</sup>, the lack of neutralization of Ab1245 cannot be ascribed to Ab1245 failing to bind to Env trimers on virions.

A recent report described RM20E1, an antibody isolated from BG505-immunized NHPs, which neutralized an N611A<sub>gp41</sub> mutant strain of BG505, but not the wild-type version of BG505<sup>40</sup>. In common with Ab1245, RM20E1 binds BG505 SOSIP sub-stoichiometrically at an epitope that overlaps with the Ab1245 epitope, but it does not displace the FP or FPPR. To determine whether the Asn611<sub>gp41</sub> glycan interferes with Ab1245 neutralization of BG505 or viral strains containing a glycan at this position, we also evaluated neutralization of Ab1245 against a BG505<sub>N611A</sub> strain and eight other HIV-1 strains that lack a PNGS at position 611<sub>gp41</sub>. We observed no neutralization by Ab1245 IgG against any of the viral strains under conditions in which a positive control IgG exhibited neutralization (Fig. 4d).

The fact that the Ab1245 was elicited by a SOSIP immunogen implies that non-neutralizing gp41-mimicking antibodies could be raised during other vaccination experiments. Important features of Ab1245 that allow its gp41 mimicry include a long CDRH3 with a methionine roughly in the middle (Met100<sub>C1245 HC</sub> is the 11<sup>th</sup> residue of the 24 amino acid CDRH3). A

search of the Protein Data Bank<sup>41</sup> for Fab structures with features of the Ab1245 CDRH3 (22-26 residue length and a methionine at position 7-13) revealed three of 1657 Fabs with these features (PDBs 5CEZ, 6E4X, and 2XTJ). However, the conformations of the CDRH3s of these Fabs did not resemble the Ab1245 CDRH3 conformation. Given that the features required for Ab1245 mimicry of gp41 are apparently rare (i.e., not found in a survey of other antibody structures), Ab1245 CDRH3 characteristics (~24 residue CDRH3 with a methionine at position ~11) could be used to screen elicited antibody sequences to identify Ab1245-like antibodies that are likely to be non-neutralizing. In addition, the Ab1245-BG505 complex structure could inform the engineering of SOSIP immunogens to prevent displacement of the FP and FPPR residues surrounding Met530<sub>gp41</sub>.

Our results suggest that Ab1245 binds to at least some strains of Env trimer (e.g., BG505) on virions, but does not affect entry into target cells. Since only one Ab1245 Fab binds per Env trimer at a site that would not disrupt CD4 binding, Env trimers should still be able to undergo CD4-induced conformational changes<sup>42-45</sup> allowing coreceptor binding and subsequent insertion of one or two of the trimer FPs into the host cell membrane. This prompts the speculation that fusion requires only up to two of three FPs to be inserted into the target membrane. However, it is also possible that the third FP, which was displaced by Ab1245 binding and is disordered in the Ab1245-BG505 structure (Fig. 4a), could access the host cell membrane and insert itself despite Ab1245 binding, thus enabling all three FPs per Ab1245-bound Env trimer to function in membrane fusion. Alternatively, Ab1245 may dissociate from a virion-bound Env trimer upon its interaction with CD4, providing another potential mechanism rationalizing its lack of neutralizing activity.

The characterization of Ab1245 reported here raises the possibility that a neutralizing antibody against the FP epitope must directly bind the FP in order to prevent it from inserting into the host cell membrane. Thus displacement of the FP and FPPR by an antibody such as Ab1245 through gp41 mimicry may not result in neutralization. However, by blocking neutralizing antibodies such as VRC34, an antibody that directly interacts with the FP<sup>6</sup>, from

binding HIV-1 Envs, Ab1245 and similar antibodies might serve as decoys that protect a conserved epitope on Env from binding neutralizing antibodies.

## Methods

### Single B cell sorting and antibody sequencing

Cells from lymph node biopsies obtained from immunized macaques were thawed and washed in RPMI medium 1640 (1x) (Gibco #11875-093). Macaque cells were incubated with 100  $\mu$ l of FACS buffer (PBS 1x with 2% fetal bovine serum and 1mM EDTA) with human Fc Block (BD Biosciences #564219) at a 1:500 dilution for 30 min on ice.

BG505 and B41 tetrameric baits were prepared by incubating 5  $\mu$ g of AviTagged and biotinylated BG505 and B41 SOSIP trimers with fluorophore-conjugated streptavidin at a 1:200 dilution in 1xPBS for 30 min on ice<sup>4,46</sup>. Tetramers were mixed with the following anti-human antibody cocktail: anti-CD16 APC-eFluor780 (Invitrogen, #47-0168-41), anti-CD8 $\alpha$  APC-eFluor780 (Invitrogen, #47-0086-42), anti-CD3 APC-eFluor780 (Invitrogen, #47-0037-41), anti-CD14 APC-eFluor780 (eBiosciences, #47-0149-41), anti-CD20 PeCy7 (BD, #335793), anti-CD38 FITC (Stem Cell technologies, #60131FI) at a 1:200 dilution and the live/dead marker Zombie NIR at a 1:400 dilution in FACS buffer.

Zombie NIR-/CD16-/CD8 $\alpha$ -/CD3-/CD14-/CD20+/CD38+/double BG505<sup>+</sup> and B41<sup>+</sup> single cells were isolated from the macaque cell homogenates using a FACS Aria III (Becton Dickinson). Single cells were sorted into individual wells of a 96-well plate containing 5  $\mu$ l of lysis buffer (TCL buffer (Qiagen #1031576) with 1% of 2-b-mercaptoethanol). Plates were immediately frozen on dry ice and stored at -80°C.

Antibody sequencing and cloning were performed<sup>4</sup>. Assignments of V, D, and J genes, percent mutated from germline sequences, and identification of CDR loops for Fig. 1b were done using IMGT/V-QUEST analysis using genes from the species *macaca mulatta*<sup>47-49</sup>.

Percent change from germline does not include a one-amino acid insertion in the Ab1245 heavy chain. Antibody residues were numbered according to the Kabat convention<sup>50</sup>.

### **Protein Expression**

Fabs (Ab1245, 8ANC195, BG1) and IgGs (Ab1245, N6) were expressed and purified<sup>51</sup>. IgGs and 6xHis-tagged Fabs were expressed by transient transfection of paired heavy chain and light chain expression plasmids into HEK293-6E (National Research Council of Canada) or Expi293F cells (GIBCO; Cat#A14527). Fabs and IgGs were purified from transfected cell supernatants using Ni-NTA (GE Healthcare) (for Fabs) or protein A (GE Healthcare) (for IgG) affinity chromatography followed by SEC on a Superdex 200 16/60 column (GE Healthcare). Proteins were stored in 20 mM Tris, pH 8.0, and 150 mM sodium chloride (TBS buffer).

BG505 SOSIP.664, a soluble clade A gp140 trimer that includes ‘SOS’ substitutions (A501C<sub>gp120</sub>, T605C<sub>gp41</sub>), the ‘IP’ substitution (I559P<sub>gp41</sub>), the N-linked glycan sequence at residue 332<sub>gp120</sub> (T332N<sub>gp120</sub>), an enhanced gp120-gp41 cleavage site (REKR to RRRRRR), and a stop codon after residue 664<sub>gp41</sub> (Env numbering according to HX nomenclature)<sup>12</sup> was expressed in a stable CHO cell line (kind gift of John Moore, Weill Cornell Medical College)<sup>52</sup>. BG505<sub>N611A</sub> SOSIP was expressed by transient transfection in Expi-293 cells<sup>26</sup>. SOSIP proteins were isolated from cell supernatants using a 2G12 immunoaffinity column made by covalently coupling 2G12 IgG monomer to an NHS-activated Sepharose column (GE Healthcare). Protein was eluted with 3M MgCl<sub>2</sub> followed by buffer exchange into TBS, and trimers were purified using Superdex 200 16/60 SEC (GE Healthcare), and then stored in TBS.

### **SEC-MALS**

Purified BG505 SOSIP and BG505-Fab complexes were characterized by SEC-MALS to determine absolute molecular masses<sup>53</sup>. For complexes, BG505 SOSIP.664 was mixed with a 3-fold molar excess of Ab1245 Fab or 8ANC195 Fab relative to BG505 trimer in TBS. Complexes were incubated overnight at room temperature and injected onto a Superdex 200

10/300 GL gel-filtration chromatography column equilibrated with TBS. The chromatography column was connected with an 18-angle light-scattering detector (DAWN HELEOS II; Wyatt Technology), a dynamic light-scattering detector (DynaPro Nanostar; Wyatt Technology), and a refractive index detector (Optilab t-rEX; Wyatt Technology). Data were collected every second at 25°C at a flow rate of 0.5 mL/min. Calculated molecular masses were obtained by data analysis using the program ASTRA 6 (Wyatt Technology).

### **Mass photometry**

Microscope coverslips (No. 1.5, 24 × 50 mm, VWR) were cleaned by sequential rinsing with Milli-Q H<sub>2</sub>O followed by isopropanol and again Milli-Q H<sub>2</sub>O followed by drying using a filtered pressured air stream. Clean coverslips were assembled using CultureWell™ reusable silicon gaskets (Grace Bio-Labs, # 103250). Measurements were performed using a OneMP mass photometer (Refeyn Ltd, Oxford, UK). Immediately before each measurement, wells were filled with 15 µl TBS buffer. The focal position was identified and secured in place with an autofocus system based on total internal reflection for the entire measurement. Immediately following the focusing procedure, 1 µl of protein solution was added and gently mixed by pipetting up and down 3 times at a 5 µl mixing volume. Calibration standards (1 µM Bovine Serum Albumin (BSA) SIGMA #23209, 500 nM apoferritin SIGMA #A3360, and Thyroglobulin SIGMA #T9145) were measured first. SOSIP-Fab complexes (incubated at 7 µM SOSIP and ~7.7 µM Fab for either 2-5 days or for 1-2 hours and subsequently diluted 1:6 in TBS) was added to the 15 µl PBS buffer in the well resulting in an ~114 nM concentration with respect to the SOSIP unless indicated otherwise. Recording of a mass photometry movie was started immediately. Data acquisition was performed using AcquireMP 2.2.0 software (Refeyn Ltd.), and data analysis was carried out using DiscoverMP 2.2.0 software (Refeyn Ltd.). Resulting mass photometry graphs were evaluated and protein complex masses were determined against the BSA/apoferritin calibration measurements carried out on the same day.

### **Complex formation and cryo-EM data collection**

Ab1245-BG505 complex was prepared by adding a 3-fold molar excess of Ab1245 Fab (Fab to BG505 protomer) to CHO-expressed BG505 SOSIP.664 isolated from the second half of a monodisperse SEC peak. This mixture was incubated at room temperature for three hours, after which a 3-fold molar excess of 8ANC195 Fab to BG505 protomer was added and the complex was incubated at room temperature overnight. The Ab1245-BG505-8ANC195 complex was then purified using size-exclusion chromatography (Superdex 200) and concentrated to 4.7 mg/mL before vitrification on a freshly-glow discharged (15 mA for 1 min, Ted Pella PELCO easiGLOW) Quantifoil R 2/2 300 mesh Cu grid (Electron Microscopy Services). Samples were vitrified using a Mark IV Vitrobot (Thermo Fisher) in 100% liquid ethane after a 3 second blot with Whatman No. 1 filter paper at 22°C and 100% humidity. Micrograph movies were collected on a Titan Krios using SerialEM<sup>54</sup> automated collection software with a K3 camera (Gatan) operating in super resolution mode at a nominal magnification of 105,000x (0.433 Å/pixel) using a defocus range of -0.8 to -2.5 μm. The dose was 1.5 e-/Å<sup>2</sup> over 40 frames, resulting in a total dose of 60 e-/Å<sup>2</sup>. Data collection conditions are summarized in Supplementary Table 1.

### **Cryo-EM data processing**

Processing was carried out entirely within Relion-3<sup>55,56</sup>. First, micrograph movies were motion corrected, dose-weighted, and binned to 0.866 Å/pixel using Motioncor2<sup>57</sup>, and then the non-dose-weighted micrographs were used for CTF estimation using Gctf<sup>58</sup>. Micrographs with poor CTF fits or signs of crystalline ice were discarded. Selected micrographs then underwent auto-picking after which 4x4 binned particles were extracted (3.46 Å/pixel). These particles were then subjected to reference-free 2D classification after which selected particles underwent three rounds of iterative 3D classification, wherein only the final particles representing Ab1245-BG505-8ANC195 were selected and unbinned (0.866 Å/pixel) and classes representing BG505-8ANC195 were discarded (one is shown in Supplementary Fig. 1e). After the first round of 3D classification, 69% of particles belonged to classes that resembled a trimer with one bound Ab1245 Fab and three bound 8ANC195 Fabs, 29% of particles belonged to a class that resembled a trimer with three bound 8ANC195

Fabs but no bound Ab1245 Fabs, and 2% of particles belonged to a class that did not resemble a trimer. In the second and third rounds of 3D classification, some classes appeared to show density for a second 1245 Fab at less than full occupancy, but these classes did not contain a large proportion of particles and were not readily interpretable. Finally, the unbinned particles underwent 3D refinement (C1 symmetry imposed) and were post-processed into a map with a gold-standard FSC calculation<sup>59</sup> of 3.7 Å. A ‘blurred’ map was also created using a higher B-factor to uncover N-linked glycan densities.

### **Model building**

Coordinates of BG505-8ANC195 Fab V<sub>H</sub>-V<sub>L</sub> domains (PDB 5CJX) and VRC34 Fab V<sub>H</sub>-V<sub>L</sub> domains (PDB 6NC3) were fitted into map density using UCSF Chimera<sup>60</sup>. Coordinates were then built into densities using iterative rounds of refinement in Phenix<sup>61</sup> (rigid body and real-space refinement) and Coot<sup>62</sup>. Antibody numbering was done in the Kabat convention using the online ANARCI server<sup>63</sup>.

### **Structural analysis**

Structure figures were made using UCSF Chimera<sup>60</sup> or PyMol<sup>64</sup>. Contact residues were assigned as residues with any atom located <4.0 Å from an atom in a residue on the partner molecule. Hydrogen bond interactions were not assigned due to limited resolution.

### **In vitro neutralization assays**

Pseudovirus neutralization assays were conducted<sup>65</sup> either in-house (for strains BG505, BG505<sub>N611A</sub>, CE0217, CNE55, JRCSF, Du422, T250-4, Tro, X1632, 246F3, CH119, CE1176, BJOX002000\_03\_02, 25710, X2278, CNE8, and 398F1) or by the Collaboration for AIDS Vaccine Discovery (CAVD) core neutralization facility (for the remaining strains in Fig. 4d). IgGs (Ab1245 and an N6<sup>66</sup> positive control) were evaluated in duplicate with an 8-point, 4-fold dilution series starting at a top concentration of 500 or 1000 µg/mL for in-house neutralizations or an 8-point, 5-fold dilution series starting at a top concentration of 250 µg/mL at the CAVD facility.

**Data Availability**

The atomic model and cryo-EM maps have been deposited in the Protein Data Bank (PDB) accession code 7MXE and Electron Microscopy Data Bank (EMDB) entry EMD-24072.

**Acknowledgements**

We thank Anthony P. West for help with analysis of antibody CDRH3 sequence analyses. Cryo-EM was performed in the Beckman Institute Resource Center for Transmission Electron Microscopy at Caltech with assistance from directors A. Malyutin and S. Chen. We thank the Beckman Institute Protein Expression Center at Caltech for protein production, John Moore (Weill Cornell Medical College) for the BG505 stable cell line, Gabriella Kiss, Sofia Ferreira, and Brenda Watt at Refeyn Ltd. for providing a demonstration model OneMP mass photometer, training, and materials to Caltech, Kristie M. Gordon (The Rockefeller University) for assistance with flow cytometry, and Rogier W. Sanders and Marit J. van Gils (Academisch Medisch Centrum Universiteit van Amsterdam) for providing AviTagged and biotinylated BG505 and B41 SOSIP trimers. This work was supported by the National Institute of Allergy and Infectious Diseases (NIAID) HIVRAD P01 AI100148 (to P.J.B. and M.C.N.), Gates CAVD grant INV-002143 (to P.J.B., M.C.N., and M.A.M.), NIH P50 AI150464 (P.J.B.), an NSF Graduate Research Fellowship (to M.E.A.), and a Bill and Melinda Gates Foundation grant (#OPP1146996 to M.S.S.). M.C.N. is an HHMI Investigator. Under the grant conditions of the Gates Foundation, a Creative Commons Attribution 4.0 Generic License has already been assigned to the Author Accepted Manuscript version that might arise from this submission.

## References

1. Andrabi, R., Bhiman, J.N. & Burton, D.R. Strategies for a multi-stage neutralizing antibody-based HIV vaccine. *Curr Opin Immunol* **53**, 143-151 (2018).
2. Escolano, A., Dosenovic, P. & Nussenzweig, M.C. Progress toward active or passive HIV-1 vaccination. *J Exp Med* **214**, 3-16 (2017).
3. Kwong, P.D. & Mascola, J.R. HIV-1 Vaccines Based on Antibody Identification, B Cell Ontogeny, and Epitope Structure. *Immunity* **48**, 855-871 (2018).
4. Escolano, A. et al. Immunization expands B cells specific to HIV-1 V3 glycan in mice and macaques. *Nature* **570**, 468-473 (2019).
5. Steichen, J.M. et al. A generalized HIV vaccine design strategy for priming of broadly neutralizing antibody responses. *Science* **366**(2019).
6. Kong, R. et al. Fusion peptide of HIV-1 as a site of vulnerability to neutralizing antibody. *Science* **352**, 828-33 (2016).
7. Xu, K. et al. Epitope-based vaccine design yields fusion peptide-directed antibodies that neutralize diverse strains of HIV-1. *Nat Med* **24**, 857-867 (2018).
8. Jardine, J. et al. Rational HIV immunogen design to target specific germline B cell receptors. *Science* **340**, 711-6 (2013).
9. McGuire, A.T. et al. Specifically designed immunogens select and activate B cells expressing precursors of broadly neutralizing human antibodies to HIV-1 in knock-in mice. *Nature Comm* **7**, 10618 (2016).
10. Bianchi, M. et al. Electron-Microscopy-Based Epitope Mapping Defines Specificities of Polyclonal Antibodies Elicited during HIV-1 BG505 Envelope Trimer Immunization. *Immunity* **49**, 288-300 e8 (2018).
11. McCoy, L.E. et al. Holes in the Glycan Shield of the Native HIV Envelope Are a Target of Trimer-Elicited Neutralizing Antibodies. *Cell Rep* **16**, 2327-38 (2016).
12. Sanders, R.W. et al. A next-generation cleaved, soluble HIV-1 Env Trimer, BG505 SOSIP.664 gp140, expresses multiple epitopes for broadly neutralizing but not non-neutralizing antibodies. *PLoS Pathog* **9**, e1003618 (2013).
13. Wang, Z. et al. Isolation of single HIV-1 Envelope specific B cells and antibody cloning from immunized rhesus macaques. *J Immunol Methods* **478**, 112734 (2020).

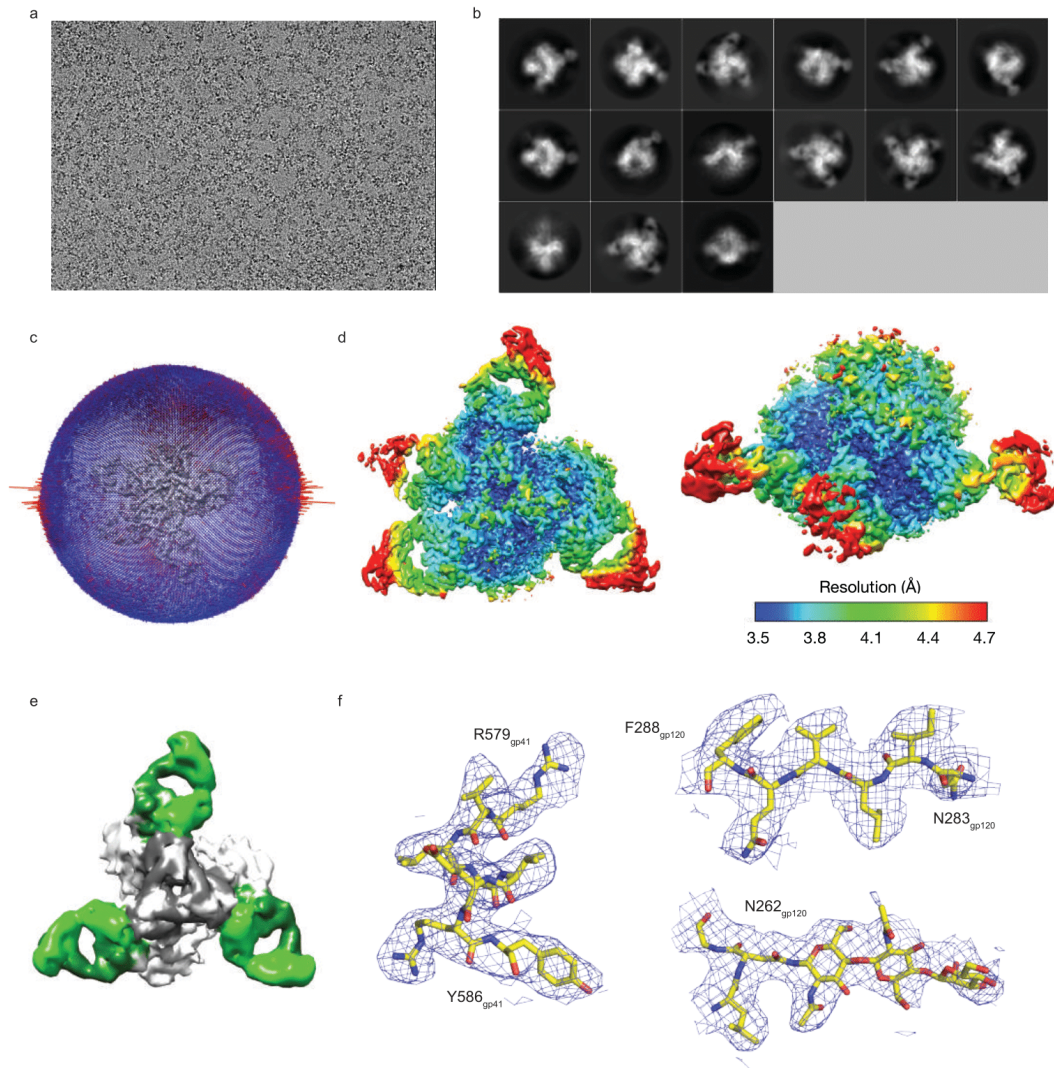
14. Pancera, M. et al. Structure and immune recognition of trimeric pre-fusion HIV-1 Env. *Nature* **514**, 455-61 (2014).
15. Burton, D.R. & Hangartner, L. Broadly Neutralizing Antibodies to HIV and Their Role in Vaccine Design. *Annu Rev Immunol* **34**, 635-59 (2016).
16. Steichen, J.M. et al. HIV Vaccine Design to Target Germline Precursors of Glycan-Dependent Broadly Neutralizing Antibodies. *Immunity* **45**, 483-96 (2016).
17. Duan, H. et al. Glycan Masking Focuses Immune Responses to the HIV-1 CD4-Binding Site and Enhances Elicitation of VRC01-Class Precursor Antibodies. *Immunity* **49**, 301-311 e5 (2018).
18. Garrity, R.R. et al. Refocusing neutralizing antibody response by targeted dampening of an immunodominant epitope. *J Immunol* **159**, 279-89 (1997).
19. Klasse, P.J. et al. Epitopes for neutralizing antibodies induced by HIV-1 envelope glycoprotein BG505 SOSIP trimers in rabbits and macaques. *PLoS Pathog* **14**, e1006913 (2018).
20. Brune, K.D. et al. Plug-and-Display: decoration of Virus-Like Particles via isopeptide bonds for modular immunization. *Sci Rep* **6**, 19234 (2016).
21. Zakeri, B. et al. Peptide tag forming a rapid covalent bond to a protein, through engineering a bacterial adhesin. *Proc Natl Acad Sci U S A* **109**, E690-7 (2012).
22. Escolano, A. et al. Sequential immunization elicits broad, but weakly neutralizing, anti-HIV-1 antibodies to the viral envelope V3-glycan patch and CD4bs in rhesus macaques. Submitted (2021).
23. Vigdorovich, V. et al. Repertoire comparison of the B-cell receptor-encoding loci in humans and rhesus macaques by next-generation sequencing. *Clin Transl Immunology* **5**, e93 (2016).
24. Wang, H. et al. Asymmetric recognition of HIV-1 Envelope trimer by V1V2 loop-targeting antibodies. *Elife* **6**(2017).
25. Scharf, L. et al. Antibody 8ANC195 reveals a site of broad vulnerability on the HIV-1 envelope spike. *Cell Rep* **7**, 785-95 (2014).
26. Scharf, L. et al. Broadly Neutralizing Antibody 8ANC195 Recognizes Closed and Open States of HIV-1 Env. *Cell* **162**, 1379-90 (2015).

27. Sonn-Segev, A. et al. Quantifying the heterogeneity of macromolecular machines by mass photometry. *Nat Commun* **11**, 1772 (2020).
28. Scheid, J.F. et al. Sequence and Structural Convergence of Broad and Potent HIV Antibodies That Mimic CD4 Binding. *Science* **333**, 1633-1637 (2011).
29. Lee, J.H. et al. Antibodies to a conformational epitope on gp41 neutralize HIV-1 by destabilizing the Env spike. *Nat Commun* **6**, 8167 (2015).
30. West, A.P., Jr. et al. Computational analysis of anti-HIV-1 antibody neutralization panel data to identify potential functional epitope residues. *Proc Natl Acad Sci U S A* **110**, 10598-603 (2013).
31. Gristick, H.B. et al. Natively glycosylated HIV-1 Env structure reveals new mode for antibody recognition of the CD4-binding site. *Nat Struct Mol Biol* **23**, 906-915 (2016).
32. Schommers, P. et al. Restriction of HIV-1 Escape by a Highly Broad and Potent Neutralizing Antibody. *Cell* **180**, 471-489 e22 (2020).
33. Dubrovskaya, V. et al. Targeted N-glycan deletion at the receptor-binding site retains HIV Env NFL trimer integrity and accelerates the elicited antibody response. *PLoS Pathog* **13**, e1006614 (2017).
34. Dubrovskaya, V. et al. Vaccination with Glycan-Modified HIV NFL Envelope Trimer-Liposomes Elicits Broadly Neutralizing Antibodies to Multiple Sites of Vulnerability. *Immunity* **51**, 915-929 e7 (2019).
35. Turner, H.L. et al. Disassembly of HIV envelope glycoprotein trimer immunogens is driven by antibodies elicited via immunization. *Sci Adv* **7**(2021).
36. Kumar, S. et al. Capturing the inherent structural dynamics of the HIV-1 envelope glycoprotein fusion peptide. *Nat Commun* **10**, 763 (2019).
37. Liu, J., Bartesaghi, A., Borgnia, M.J., Sapiro, G. & Subramaniam, S. Molecular architecture of native HIV-1 gp120 trimers. *Nature* **455**, 109-13 (2008).
38. Stadtmueller, B.M. et al. DEER spectroscopy measurements reveal multiple conformations of HIV-1 SOSIP Envelopes that show similarities with Envelopes on native virions. *Immunity* (2018).
39. Li, Z. et al. Subnanometer structures of HIV-1 envelope trimers on aldrithiol-2-inactivated virus particles. *Nature Structural & Molecular Biology* **27**, 726-734 (2020).

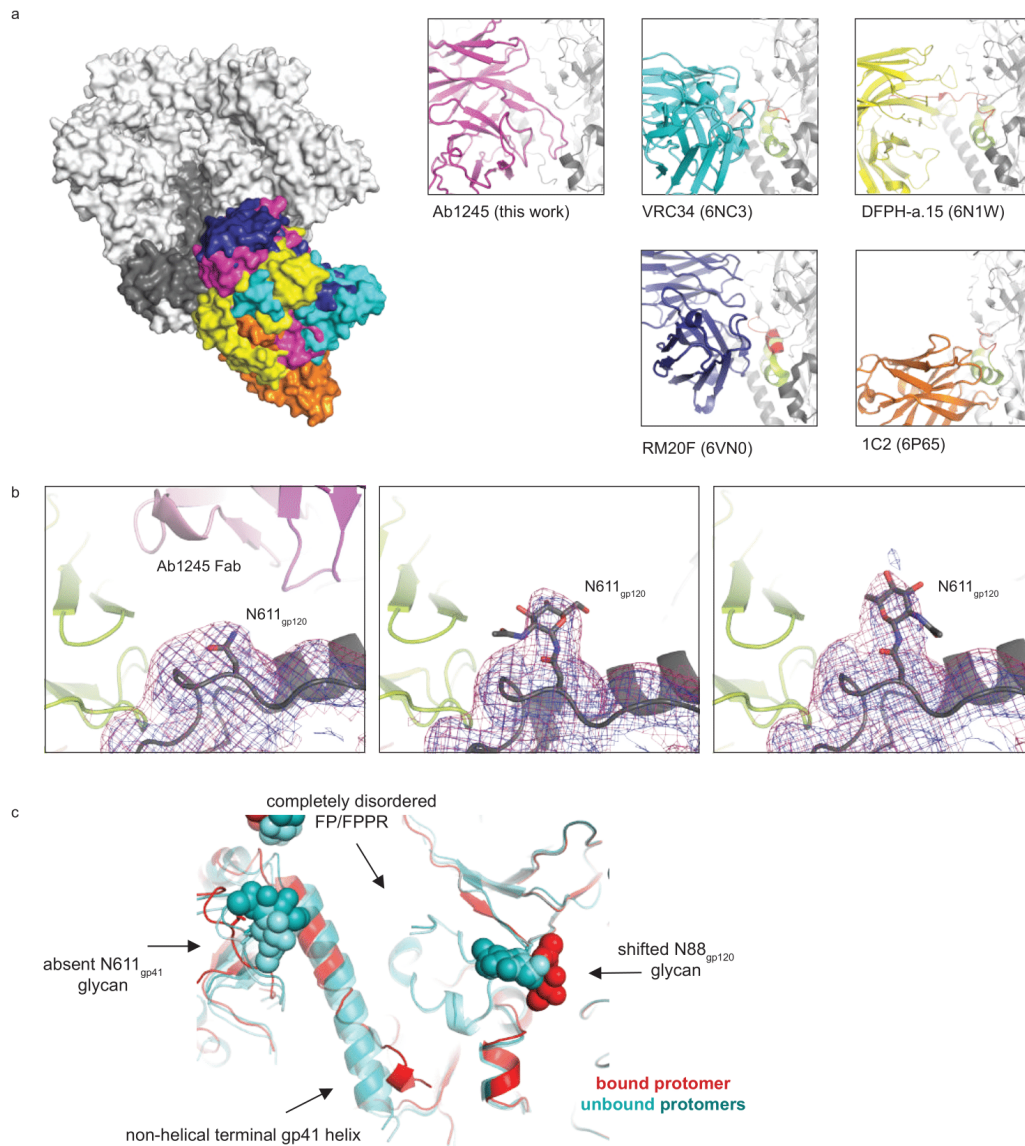
40. Desrosiers, R.C. et al. Mapping the immunogenic landscape of near-native HIV-1 envelope trimers in non-human primates. *PLOS Pathogens* **16**, e1008753 (2020).
41. Berman, H.M. et al. The Protein Data Bank. *Nucleic Acids Research* **28**, 235-242 (2000).
42. Wang, H. et al. Cryo-EM structure of a CD4-bound open HIV-1 envelope trimer reveals structural rearrangements of the gp120 V1V2 loop. *Proc Natl Acad Sci U S A* **113**, E7151-E7158 (2016).
43. Ozorowski, G. et al. Open and closed structures reveal allostery and pliability in the HIV-1 envelope spike. *Nature* **547**, 360-363 (2017).
44. Wang, H., Barnes, C.O., Yang, Z., Nussenzweig, M.C. & Bjorkman, P.J. Partially Open HIV-1 Envelope Structures Exhibit Conformational Changes Relevant for Coreceptor Binding and Fusion. *Cell Host Microbe* **24**, 579-592 e4 (2018).
45. Yang, Z., Wang, H., Liu, A.Z., Gristick, H.B. & Bjorkman, P.J. Asymmetric opening of HIV-1 Env bound to CD4 and a coreceptor-mimicking antibody. *Nat Struct Mol Biol* **26**, 1167-1175 (2019).
46. Wang, Z. et al. A broadly neutralizing macaque monoclonal antibody against the HIV-1 V3-Glycan patch. *eLife* **9**(2020).
47. Giudicelli, V. & Lefranc, M.P. IMGT/junctionanalysis: IMGT standardized analysis of the V-J and V-D-J junctions of the rearranged immunoglobulins (IG) and T cell receptors (TR). *Cold Spring Harb Protoc* **2011**, 716-25 (2011).
48. Giudicelli, V., Brochet, X. & Lefranc, M.P. IMGT/V-QUEST: IMGT standardized analysis of the immunoglobulin (IG) and T cell receptor (TR) nucleotide sequences. *Cold Spring Harb Protoc* **2011**, 695-715 (2011).
49. Brochet, X., Lefranc, M.P. & Giudicelli, V. IMGT/V-QUEST: the highly customized and integrated system for IG and TR standardized V-J and V-D-J sequence analysis. *Nucleic Acids Res* **36**, W503-8 (2008).
50. Kabat, E.A., Wu, T.T., Perry, H.M., Gottesman, K.S. & Foeller, C. Sequences of proteins of immunological interest. *Department of Health and Human Services, Washington, D.C.* (1991).
51. Scharf, L. et al. Structural basis for germline antibody recognition of HIV-1 immunogens. *Elife* **5**(2016).

52. Dey, A.K. et al. cGMP production and analysis of BG505 SOSIP.664, an extensively glycosylated, trimeric HIV-1 envelope glycoprotein vaccine candidate. *Biotechnol Bioeng* 10.1002/bit.26498(2017).
53. Wyatt, P.J. Light scattering and the absolute characterization of macromolecules. *Analytica Chimica Acta* **272**, 1-40 (1993).
54. Mastronarde, D.N. Automated electron microscope tomography using robust prediction of specimen movements. *J Struct Biol* **152**, 36-51 (2005).
55. Scheres, S.H. RELION: implementation of a Bayesian approach to cryo-EM structure determination. *J Struct Biol* **180**, 519-30 (2012).
56. Zivanov, J. et al. New tools for automated high-resolution cryo-EM structure determination in RELION-3. *Elife* **7**(2018).
57. Zheng, S.Q. et al. MotionCor2: anisotropic correction of beam-induced motion for improved cryo-electron microscopy. *Nat Methods* **14**, 331-332 (2017).
58. Zhang, K. Gctf: Real-time CTF determination and correction. *J Struct Biol* **193**, 1-12 (2016).
59. Scheres, S.H. & Chen, S. Prevention of overfitting in cryo-EM structure determination. *Nat Methods* **9**, 853-4 (2012).
60. Goddard, T.D., Huang, C.C. & Ferrin, T.E. Visualizing density maps with UCSF Chimera. *J Struct Biol* **157**, 281-7 (2007).
61. Liebschner, D. et al. Macromolecular structure determination using X-rays, neutrons and electrons: recent developments in Phenix. *Acta Crystallogr D Struct Biol* **75**, 861-877 (2019).
62. Emsley, P., Lohkamp, B., Scott, W.G. & Cowtan, K. Features and development of Coot. *Acta Crystallogr D Biol Crystallogr* **66**, 486-501 (2010).
63. Dunbar, J. & Deane, C.M. ANARCI: antigen receptor numbering and receptor classification. *Bioinformatics* **32**, 298-300 (2015).
64. Schrödinger, L. The PyMOL Molecular Graphics System. 1.2r3pre edn (The PyMOL Molecular Graphics System, 2011).
65. Montefiori, D.C. Evaluating neutralizing antibodies against HIV, SIV, and SHIV in luciferase reporter gene assays. *Curr Protoc Immunol* **Chapter 12**, Unit 12 11 (2005).

66.Huang, J. et al. Identification of a CD4-Binding-Site Antibody to HIV that Evolved Near-Pan Neutralization Breadth. *Immunity* **45**, 1108-1121 (2016).



**Supplementary Fig. 1. Cryo-EM Data Processing.** **a**, Representative motion-corrected micrograph. **b**, 4x-binned selected 2D classes. **c**, Orientation distribution analysis. **d**, Local resolution map from two angles. **e**, Map of 3D class that contained 3 8ANC195 Fabs and no Ab1245 Fabs (colors as in Fig. 2b). **f**, Representative images of map quality at indicated sites for the 3.7 Å Ab1245–BG505–8ANC195 cryo-EM structure.



**Supplementary Fig. 2. Ab1245 Structural Analysis.** **a**, Comparison of binding of gp120-gp41 interface or fusion peptide-directed antibodies. Left: BG505 trimer (gray surface) and Fab V<sub>H</sub>-V<sub>L</sub> domains (colored surfaces). Insets: individual antibodies bound to Env trimer (gray) are shown as cartoon with the FP in red and the FPPR in orange. **b**, Comparison of density for the N611<sub>gp120</sub> glycan on gp120 (gray cartoon), with 8ANC195 (green cartoon), and Ab1245 (pink cartoon with non-blurred (blue) and blurred (red) maps shown as mesh). **c**, Comparison of secondary structure between protomers of gp120-gp41 with Ab1245 bound (red cartoon) and not bound (shades of teal, cartoon). Glycans are shown as spheres, and differences between bound and unbound protomers are highlighted with arrows and descriptions.

*Chapter 5***HOW ANTIBODIES RECOGNIZE PATHOGENIC VIRUSES:  
STRUCTURAL CORRELATES OF ANTIBODY NEUTRALIZATION OF  
HIV-1, SARS-COV-2, AND ZIKA**

**Abernathy, M.E.\***, Dam, K.A.\*, Esswein, S.R.\*, Jette, C.A.\*, Bjorkman, P.J. How Antibodies Recognize Pathogenic Viruses: Structural Correlates of Antibody Neutralization of HIV-1, SARS-CoV-2, and Zika. *Viruses*, **13**, 2106 (2021). <https://doi.org/10.3390/v13102106>

*\* Equal Contributions*

**Summary**

The H1N1 pandemic of 2009-2010, MERS epidemic of 2012, Ebola epidemics of 2013-2016 and 2018-2020, Zika epidemic of 2015-2016, and COVID-19 pandemic of 2019-2021, are recent examples in the long history of epidemics that demonstrate the enormous global impact of viral infection. The rapid development of safe and effective vaccines and therapeutics has proven vital to reducing morbidity and mortality from newly emerging viruses. Structural biology methods can be used to determine how antibodies elicited during infection or vaccination target viral proteins and identify viral epitopes that correlate with potent neutralization. Here we review how structural and molecular biology approaches have contributed to our understanding of antibody recognition of pathogenic viruses, specifically HIV-1, SARS-CoV-2, and Zika. Determining structural correlates of neutralization of viruses has guided the design of vaccines, monoclonal antibodies, and small molecule inhibitors in response to the global threat of viral epidemics.

**1. Introduction**

Advances in structural biology in recent decades have played a key role in the determination of disease-relevant protein complexes and guided the design of new therapeutics and vaccines. An early pioneer in structural biology was the X-ray crystallographer Rosalind

Franklin. While she is best known for her role in collecting the X-ray fiber diffraction patterns that revealed the 3D structure of DNA, her contributions in biologically-related fields also included insights into the structures of protein encapsulated viruses such as tobacco mosaic virus (TMV), poliovirus, and turnip yellow mosaic virus. During Franklin's studies of viruses in the 1950s, a central question was how viruses managed to build a protein shell to shield their genetic material given that only a limited number of viral capsid proteins could be encoded within a viral genome based on capsid size constraints. Franklin's X-ray analysis revealed the arrangement of the protein subunits in TMV, allowing her to create the first three-dimensional model of a virus [1–4]. Following this work, she used X-ray data to determine the position and orientation of RNA packaged inside of the rod-shaped TMV [5]. Unlike prior speculation that placed the RNA at the center of the rod, her work revealed the virus was hollow, which led to the discovery that the RNA spiraled with the helical protein capsid. This work was fundamental in understanding principles of virus structure. Franklin's contributions to the field of virology are summarized on her tombstone, which reads, "Her research and discoveries on viruses remain of lasting benefit to mankind." Together, her remarkable contributions to structural studies in three separate areas, DNA, coal, and viruses, before her death at the age of 37 make her an inspiration to future generations of structural biologists, particularly women. We are proud to follow in her footsteps to use structural biology to gain insight into viruses with the goal of providing benefits to human health.

The severe acute respiratory syndrome coronavirus (SARS-CoV) epidemic of 2002, Middle East Respiratory Syndrome (MERS) epidemic of 2012, acquired immune deficiency syndrome (AIDS) pandemic starting in 1981, the Zika virus (ZIKV) epidemic of 2015-2016, and the ongoing SARS-CoV-2/COVID-19 pandemic are examples of the enormous global burden of viruses and the urgent need for vaccine and therapeutic development. Building on the prior contributions of early pioneers such as Rosalind Franklin, structural biologists continue to advance techniques in X-ray crystallography and cryo-electron microscopy (cryo-EM) to investigate viruses and viral proteins. We are interested in investigating antibody (Ab) recognition of viruses, which we do by solving 3D structures of viral proteins bound to Abs elicited by infection or vaccination. Understanding the structural correlates of

Ab recognition of viruses is key for the development of effective monoclonal Ab therapies and vaccines (**Figure 1**).

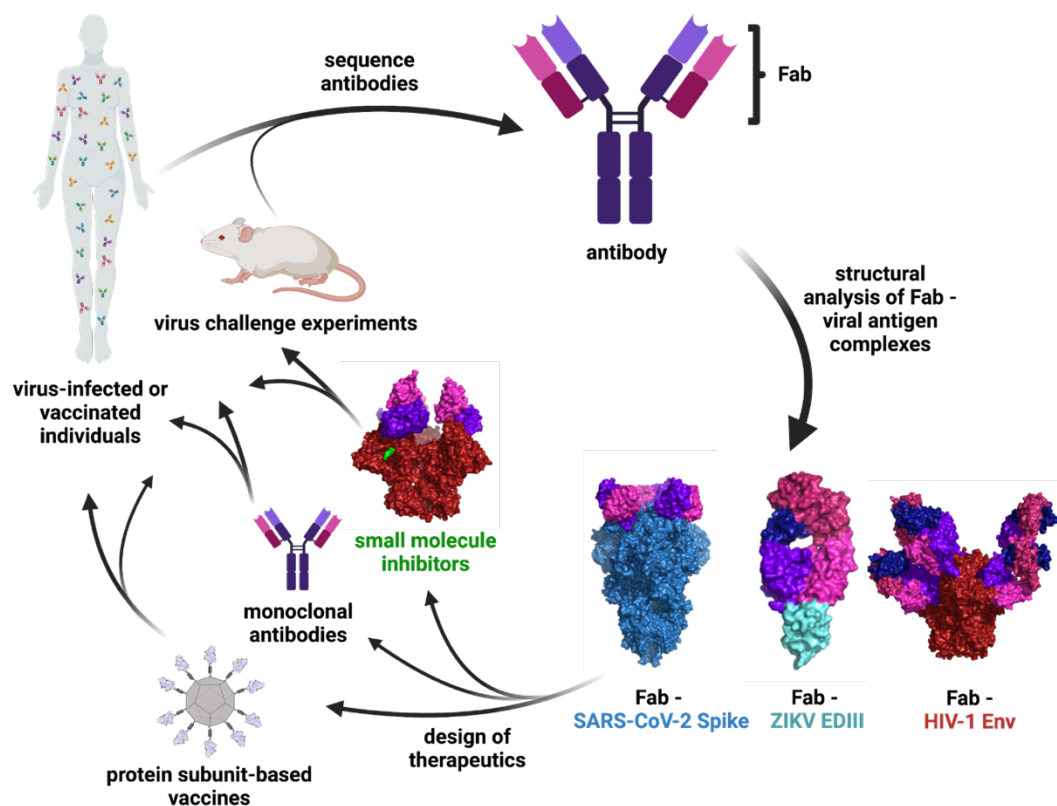


**Figure 1.** Schematic of Ab characterization and therapeutic development. The binding epitopes of Abs isolated from infected or vaccinated individuals or animal studies are determined through structural analysis of Fab - viral antigen complexes. These structures inform the design of vaccines, monoclonal Abs, and small molecule therapeutics that can be tested in clinical trials and animal models. Surface representations are shown for the following structures: Fab - SARS-CoV-2 S (PDB 7K90), Fab - ZIKV EDIII (PDB 5VIG), Fab - HIV-1 Env (PDB 5T3Z), and small molecule inhibitor - HIV-1 Env (PDB 7LO6).

Human immunodeficiency virus 1 (HIV-1) is responsible for the AIDS pandemic and 36 million deaths to date [6] and has long posed a challenge for vaccine development due to its remarkable ability to evade the host immune response and establish latent reservoirs. HIV-1 contains a single viral protein on its surface that facilitates infection of immune cells. This protein, named Envelope or Env, is a trimer of gp120/gp41 heterodimers (Figure 2A). The gp120 portion of Env interacts with host CD4 receptors, which stimulates conformational changes that allow binding to the co-receptor, usually a host chemokine receptor called

CCR5 [7]. These events trigger rearrangements in gp41 that allow fusion of the viral and host cell membranes, which is required for entry of the HIV-1 genome into the host cell [7]. In addition to small molecule anti-retroviral drug treatments to treat infected individuals, current strategies to prevent HIV-1 infection include vaccine design. Vaccine efforts seek to stimulate the evolution of broadly neutralizing Abs (bNAbs) that have been isolated in rare cases of human HIV-1 infection and are capable of broad and potent protection [8–10]. Advances in X-ray crystallography and cryo-EM have given us the invaluable opportunity to structurally characterize bNAb interactions with Env and Env conformational changes which have informed vaccine design efforts.

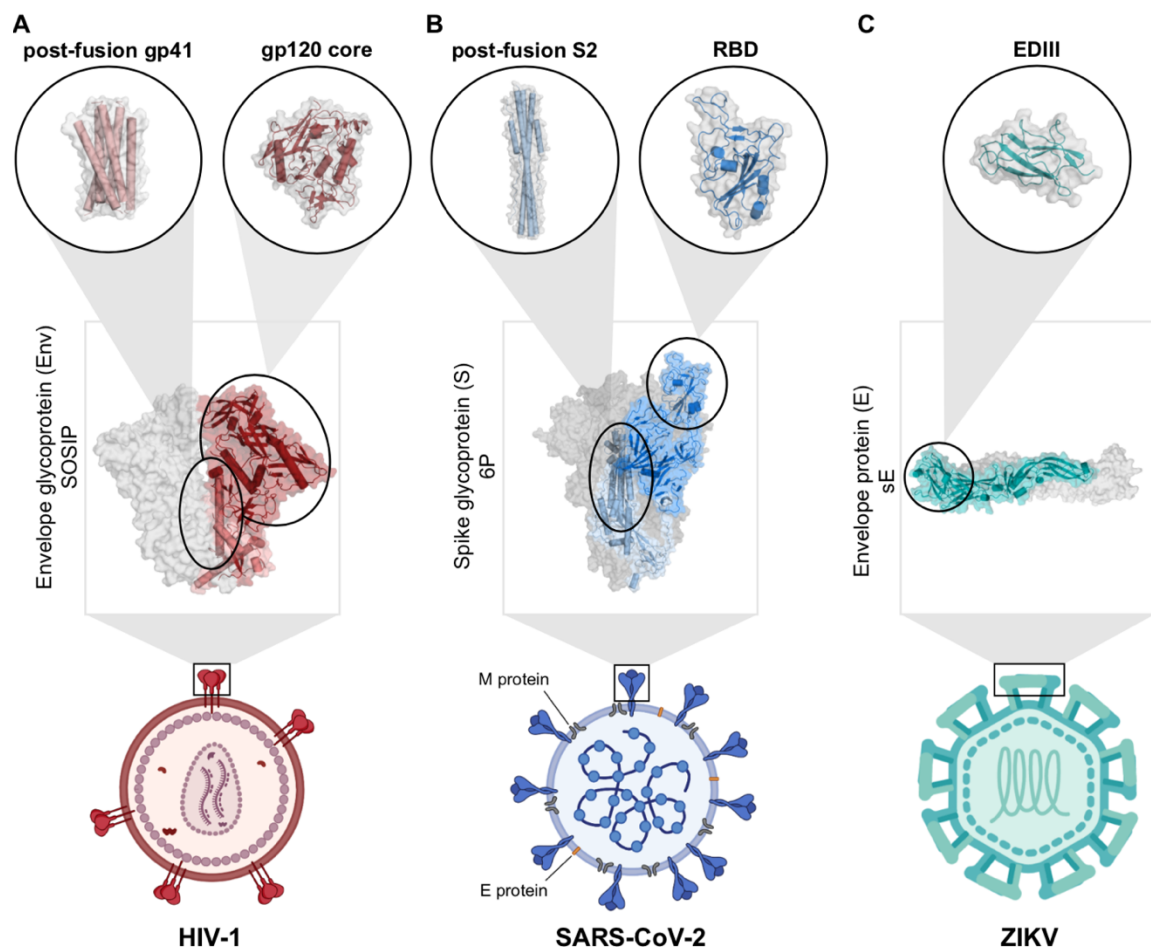


**Figure 2.** Structural targets of HIV-1, SARS-CoV-2, and ZIKV. (A) Cartoon HIV-1 virion with a closed, pre-fusion Env protein structure highlighted (PDB: 6UDJ). Circles show crystal structures of the postfusion gp41 bundle (left, PDB: 1A1K) and gp120 core (right,

PDB: 5F4P). (B) Cartoon SARS-CoV-2 virion with S protein (blue), M protein (grey), and E protein (orange). The closed, pre-fusion S protein structure with one 'up' RBD (blue subunit) and two 'down' RBDs (grey subunits) is shown in the box (PDB: 7K8V). Circles show postfusion S2 helices (left, PDB: 6LXT) and RBD (right, PDB: 7K8M) structures. (C) Cartoon ZIKV virion with E protein (teal). The soluble E (sE) protein dimer structure is shown in the box with one E protein highlighted (PDB: 5JHM). The EDIII structure is shown in the circle (PDB: 6UTA).

SARS-CoV-2, the virus responsible for the COVID-19 pandemic, has caused 4.5 million deaths and an estimated 225 million infections as of September 2021 [11]. The spike (S) proteins on the surface of SARS-CoV-2 allow it to infect host cells by binding the host cellular angiotensin-converting enzyme 2 (ACE2) receptor [12,13]. Each of the three protomers on an S protein includes two subunits, S1 and S2. The receptor binding domain (RBD) on S1 is the component that recognizes ACE2 during cell entry (Figure 2B) [13–16]. While the RBD can adopt both 'up' and 'down' conformations, it can only bind ACE2 when it is an 'up' conformation [14–20]. Due to the critical role of the RBD in facilitating infection, neutralizing Abs that target the RBD are an important component of the immune response against SARS-CoV-2 [21–31]. Structural biology has been instrumental in the rapid characterization and evaluation of the S protein and Abs produced in natural infection [15,21,21–33]. This work has contributed to the development of COVID-19 vaccines and monoclonal Ab (mAb) therapeutics, which have saved countless lives.

ZIKV is a mosquito-borne virus that can cause microcephaly and neurodevelopmental abnormalities in the newborns of infected mothers [34–37]. As part of the *flavivirus* genus, ZIKV shares similar features as other widespread flaviviruses such as dengue (DENV), West Nile virus (WNV), and yellow fever virus (YFV) [38–41]. Mature ZIKV has seven non-structural proteins (NS1, NS2A, NS2B, NS3, NS4A, NS4B and NS5) and three structural proteins: envelope (E), membrane (M), and capsid (C) [42–44]. The surface of ZIKV is coated by 180 copies of the E protein arranged as 90 dimers, and each E protein includes three ectodomains, EDI, EDII, and EDIII (Figure 2C) [38,42,43]. The flexible regions between the domains allows dynamic conformational changes to occur during viral entry and fusion [38,45–48]. EDII contains a conserved fusion loop (FL) peptide that becomes exposed

after viral entry into cells and initiates endosomal fusion [42,43,49,50]. EDIII is thought to be important for receptor binding during infection, and consequently, is an important target for neutralizing Abs [51–56]. There is not yet a safe and effective vaccine against ZIKV that is universally available.

Here we review how approaches in structural and molecular biology have increased our understanding of Ab recognition of HIV-1, SARS-CoV-2, and ZIKV. We discuss how the design of stable and soluble viral antigens amenable for structural approaches has enabled our ability to analyze complexes of viral antigens bound by the antigen binding fragment (Fab) of Abs. Use of both cryo-EM and X-ray crystallography has increased our understanding of key viral epitopes targeted by Abs and conformational changes of viral proteins necessary for infection. These structural insights, combined with analyses of the levels of somatic hypermutation found in potently neutralizing Abs, provide valuable information for the development of effective vaccines and monoclonal Ab therapies to reduce global morbidity and mortality from epidemic/pandemic-causing viruses.

## **2. Main Body**

### *2.1. Engineering viral surface proteins for structural studies*

Structural biology techniques such as X-ray crystallography and single particle cryo-EM require samples that are stable enough to be isolated and manipulated in the laboratory. For some viruses, especially those that are symmetric, it is feasible to structurally characterize intact viruses using cryo-EM. For example, cryo-EM structures of intact, whole ZIKV have been solved with and without Fabs of Abs bound [42,43,57–62]. Viruses with pleomorphic structures (e.g., most enveloped viruses) can also be investigated structurally using cryo-electron tomography [63–65]. In order to prepare surface viral proteins of enveloped viruses for structural studies and therapeutic development, it has been necessary to produce soluble, native-like versions that are stabilized in a pre-fusion conformation that is targeted by neutralizing Abs.

Classically, the simplest way to solubilize a surface viral protein is to remove the transmembrane and cytoplasmic domains by truncation [66,67]. Truncation has also been used to produce smaller components such as single domains. Examples of truncated domains include gp120 cores of HIV-1 Env, which have the  $\beta$ 4 and  $\beta$ 26 strands and all flexible loops removed [68,69], coronavirus RBDs truncated at the base where the flexible hinge connects them to the rest of the S1 subunit [70,71], and the individual EDIII truncated from the rest of the ZIKV E protein [52–54,72,73]. Truncation of individual domains has been especially powerful for X-ray crystallography as crystallization is hindered by flexible regions such as loops or inter-domain linkers and hinges. Single domains are useful for solving high resolution structures of Fab-domain complexes that provide detail about the Ab interactions that may not be possible using single particle cryo-EM due to flexibility or heterogeneity of larger protein complex structures [32,52–54,72–74].

While truncated proteins have been useful in the field of structural biology, they do not necessarily reflect all aspects of the whole antigen and cannot always recapitulate the properties of a native viral protein. An extra layer of complexity exists since many viral proteins adopt distinct conformations depending on the step in the viral life cycle, requiring engineering and stabilization of the desired conformation for larger, multi-subunit complexes [43,46,47,57]. Fusion proteins such as Env and S include folded helical bundles that must extend for fusion of the viral and host cell membrane bilayers. These proteins are metastable in their pre-fusion conformation, which is usually the target of neutralizing Abs [75]. The introduction of stabilizing mutations can be helpful for preparing soluble constructs of larger, multi-subunit complexes. For example, helix-breaking proline mutations have been introduced into the central helices of fusion proteins, preventing the extension of helices required for membrane fusion [76]. In combination with an inter-subunit disulfide bond and truncation after residue 664, these mutations were introduced into HIV-1 Env to produce the pre-fusion stabilized SOSIP.664 trimers [77]. The proline helix-breaking stabilizing mutations have been successfully adapted to other viral fusion proteins including those on coronaviruses, RSV, Ebola virus, human metapneumovirus, and Lassa virus [75]. For SARS-CoV-2 S, additional prolines were introduced that further stabilize the trimer in the 6P, or

‘HexaPro’ version [67]. For studies of the ZIKV E protein soluble constructs of both monomeric E protein [56,78–80] and engineered disulfide-linked E protein dimers [55,81] have been designed.

Most regions of proteins have a purpose that is important to their function, particularly transmembrane regions and cytoplasmic tails [82]. Consequently, truncated and stabilized proteins used as substitutes for full-length equivalents are only useful to the extent that they are able to approximate the native state of the protein. It is essential for the engineered forms used for structural studies to be characterized with non-structural methods to confirm that they behave in a similar fashion to the native form in the context they are being studied.

## *2.2. Dominant Ab Epitopes on Viral Fusion Proteins*

Structural analysis has facilitated identification of neutralizing epitopes on HIV-1, SARS-CoV-2 and ZIKV. Both X-ray crystallography and cryo-EM analyses of viral antigens in complex with neutralizing Ab Fabs have provided insights into mechanisms of neutralization by Abs and identified new therapeutic targets [7,32]. Neutralizing epitopes tend to be in structurally functional regions, and in many cases facilitate or hinder a structural change. In addition to neutralizing Abs, an immune response to a pathogen or vaccine can produce weakly neutralizing or non-neutralizing antibodies. which can be protective through various mechanisms such as antibody dependent cell cytotoxicity (ADCC) [83–86]. For viral fusion, there is typically a dramatic conformational change that occurs in the fusion protein to expose receptor binding sites for attachment and to insert the fusion machinery into the target membrane to undergo fusion [87]. Requiring a large conformational change is a strategy that allows viruses to hide vulnerable regions that are necessary for interactions important for viral function, such as target receptor binding. Many Abs bind in ways that can hinder or trigger fusion-necessitated conformational changes, resulting in various neutralization mechanisms [7].

### 2.2.1. HIV-1 Env Epitopes

HIV-1 Env is present on the surfaces of virions in a closed pre-fusion conformation that includes centrally located gp120 subunits and the V1/V2 and V3 variable loops interacting about the apex of the trimer, hiding the co-receptor binding site on V3 [88]. Upon binding to the host cell receptor CD4 at the CD4 binding site (CD4bs) in the gp120 subunit, the Env protein rearranges to an open state in which the gp120s are rotated outwards, the V1/V2 loop is displaced to the sides of the Env trimer, and the V3 loop is exposed, allowing access to the co-receptor binding site on V3 [89–93] (**Figure 3A**). In the CD4-bound open conformation, a 4-stranded antiparallel bridging sheet is formed by the gp120  $\beta$ -strands  $\beta$ 20,  $\beta$ 21,  $\beta$ 2, and  $\beta$ 3, the gp120 subunits swing away from the central axis and rotate slightly counter-clockwise, and the gp41 HR1 helices become more ordered and extended [90–92]. In this conformation, the V3 loop is exposed and can then bind to the co-receptor, which is required for entry [93]. HIV-1 Env epitopes target some of these intermediate fusion conformations, in addition to the closed, pre-fusion structure.

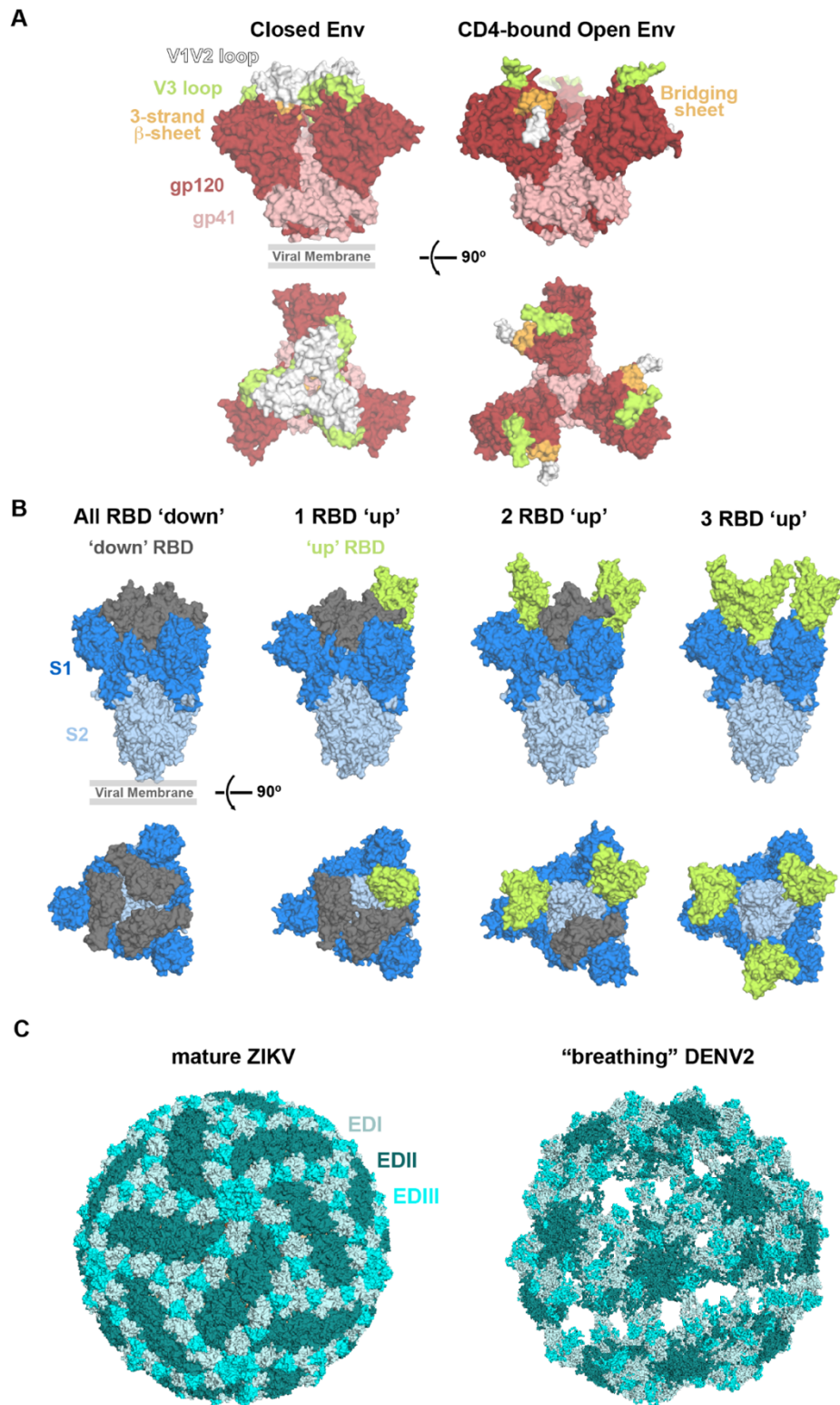


**Figure 3.** Conformational changes of HIV-1 Env, SARS-CoV-2 S, and ZIKV E. (A) Surface depictions of top down and side views of (left) closed, pre-fusion Env (PDB: 6UDJ) and (right) CD4-bound open conformation Env (PDB: 5VN3) highlighting the V1V2 loop (white), V3 loop (green), and 3-strand beta sheet (bright orange). Gp120 = dark red, gp41 = salmon. (B) Surface depictions of side and top down views of closed, pre-fusion S with three ‘down’ RBDs (grey, PDB: 7K90), 1 ‘up’ RBD (green, PDB: 7K8V), 2 ‘up’ RBDs (7K8Y), and 3 ‘up’ RBDs (6XCN). The location of the viral membrane is indicated in side views of viral proteins. (C) Surface depictions comparing the smooth mature ZIKV (PDB: 6CO8) and spiky “breathing” DENV2 (PDB: 3ZKO) structures. In the “breathing” DENV2 structure, EDI and EDIII of the E protein are protruding, giving the virus a “spiky” appearance, and holes are found in the surface.

The epitopes of bNAbs often include conserved functional regions that are conformationally masked in the closed, pre-fusion structure or sterically restricted by N-linked glycans [7]. In fact, in many cases, N-glycans that occlude the protein surface of Env actually become part of the Ab epitope. HIV-1 epitope targets of bNAbs can be divided into the following categories: (1) bNAbs that bind at the apex of the trimer, specifically to the V1/V2 loops that undergo a dramatic rearrangement during host receptor engagement [94–96], (2) bNAbs against the V3-glycan patch, which includes the highly conserved GDIR motif and several N-linked glycans on and around the V3 loop [97,98], (3) CD4bs bNAbs that target the host receptor binding domain [7,74,99], (4) bNAbs that only bind to Envs in a CD4-induced open state [68,89,91], (5) “silent face” bNAbs that target a glycan-rich patch on the opposite face from the CD4bs on gp120 [98,100,101], (6) bNAbs that target the gp120/gp41 interface, including those that interact with the fusion peptide [102,103], and (7) bNAbs that bind to the membrane proximal external region (MPER) on gp41 [104] (**Figure 4A**).

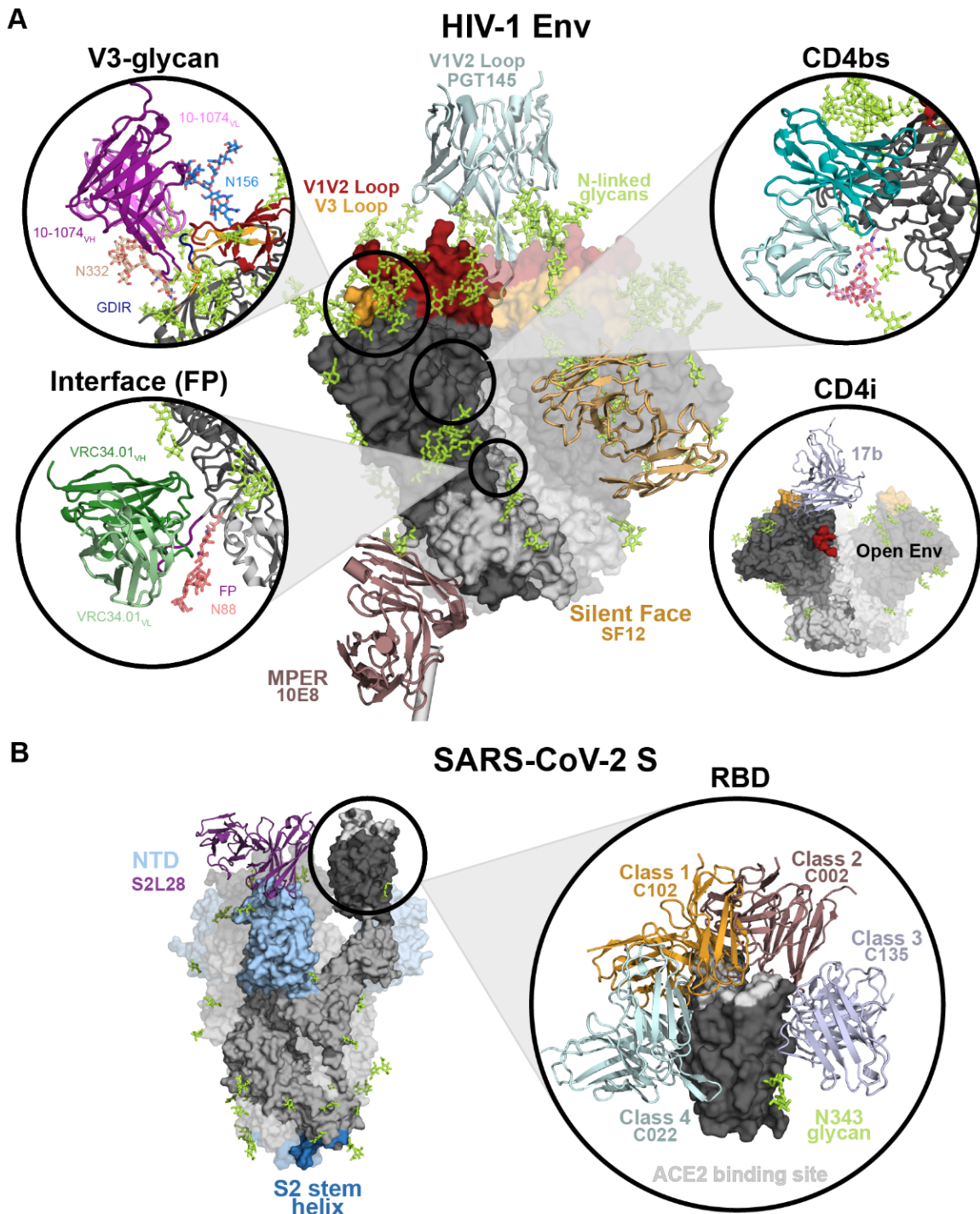


**Figure 4.** Neutralizing epitopes on HIV-1 Env and SARS-CoV-2 S. (A) HIV-1 Env structure (left) highlighting epitopes of representative bNAbs for each bNAb class. Env (PDB: 5T3Z) is shown as a surface with green N-linked glycans shown as sticks. Gp41 is light grey and gp120 is dark grey except for the V1V2 loop (dark red) and V3 loop (light orange). V<sub>H</sub>V<sub>L</sub> domains of Abs binding the epitopes MPER (mauve, 10E8, PDB: 6VPX), V1V2 loop (pale

cyan, PGT145, PDB: 5V8L) or Silent Face (sand, SF12, PDB: 6OKP) are shown as cartoons. Circles show details for Ab binding to the V3-glycan (10-1074, PDB: 5T3Z), interface (VRC34.01, PDB: 5I8H), CD4bs (3BNC117, PDB: 5V8L), and CD4i (17b, PDB: 7LO6). (B) SARS-CoV-2 S protein structure (left) highlighting the RBD (dark grey), S2 (blue), and NTD (light blue) Ab binding regions.  $V_HV_L$  domains of Ab binding to an NTD (S2L28, PDB: 7LXX) epitope is shown as a cartoon representation. The circle (right) shows an enlarged view of the RBD surface with  $V_HV_L$  domains for RBD-binding Abs shown as cartoons: Class 1 (light orange, C102, PDB: 7K8M), Class 2 (mauve, C002, PDB: 7K8S), Class 3 (pale purple, C135, PDB: 7K8Z), and Class 4 (pale cyan, C022, PDB: 7RKU). The ACE2 binding site is highlighted on the RBD in white.

Each epitope presents a distinct landscape for bNAbs binding and poses different challenges for Abs to overcome. For most epitopes, N-linked glycans on the heavily-glycosylated Env trimer sterically restrict access to conserved protein regions, and therefore bNAbs tend to include conserved N-linked glycans in the epitope and/or develop long complementary determining region (CDR) loops to penetrate through the glycan shield [7]. This is the case for V1/V2, V3, and silent face epitopes. For example, the V3-glycan patch epitope is defined by the V3 loop that is essential for co-receptor binding and several N-linked glycans. bNAbs that target this region, including 10-1074, PGT121, and BG18, have long, 20+ amino acid CDRH3 loops that reach through the glycan patch to bind a conserved V3 motif from gp120 residues 324-327 with the sequence GDIR [97]. These bNAbs also make important contacts with conserved glycans Asn156<sub>gp120</sub> and Asn332<sub>gp120</sub>. In contrast, some bNAbs against the CD4bs require short CDR loops to accommodate an N-linked glycan in that region. CD4bs bNAb 3BNC117 has a 5-residue deletion in CDRL1 that is necessary to prevent steric clashes with the Asn276<sub>gp120</sub> glycan and a short, 5-amino acid CDRL3 that is essential to avoid clashes with gp120 [105]. The gp120-gp41 interface epitope is composed of protein and glycan residues in both subunits. This category includes bNAbs that target the fusion peptide (FP), which are the highly conserved N terminal residues of gp41 responsible for burying into the host cell membrane during the fusion process of viral entry. FP bNAb VRC34.01 binds primarily to the N-terminal 8 residues of gp41 with the remainder of interactions made with Asn88<sub>gp120</sub> [102]. Together, these examples demonstrate the diverse epitope landscape of the HIV-1 Env trimer and how Abs develop particular features to overcome challenges posed by the dense glycan shield.

The mode of binding for bNAbs at all epitopes has been greatly illuminated by structural biology. In particular, X-ray crystallographic and cryo-EM structures of Ab:Env complexes have been essential tools to characterize which epitope newly isolated bNAbs bind, the mode of binding implemented, and to understand the context of atypical features in the sequence such as CDR lengths. The wealth of structural data has enabled structure-based design of gp120 and SOSIP-based immunogens that seek to elicit responses to particular epitopes and design small molecule drugs.

### 2.2.2. SARS-CoV-2 S Epitopes

The SARS-CoV-2 fusion machinery is the surface protein S, which is composed of three identical subunits each containing an RBD that sits at the apex of S and is attached to the rest of the subunits with a flexible hinge [14]. The RBDs are able to sample a ‘down’ conformation that hides the ACE2 binding site by packing it against a neighboring RBD, or an ‘up’ conformation, which exposes the ACE2 binding site at the tip of the RBD and is required for host receptor binding [15,32,106] (**Figure 3B**).

Abs that recognize the RBD of the SARS-CoV-2 S protein are a vital part of the neutralizing Ab response to infection and vaccination because the RBD contains the binding site for ACE2. Effective neutralization by many anti-RBD Abs is due to their ability to block the RBD from binding the host ACE2 receptor. The epitopes targeted by Abs against the RBD can be organized into four simplified classes [32]. Class 1, *VH3-53/VH3-63*-derived Abs, target epitopes overlapping with the ACE2 binding site and only bind ‘up’ conformation RBDs. Class 2 Abs target epitopes overlapping with the ACE2 binding site and can bind both ‘up’ and ‘down’ RBDs. Class 3 Abs target epitopes that do not overlap with the ACE2 binding site and bind both ‘up’ and ‘down’ RBDs. Finally, class 4 Abs target a cryptic surface facing the S trimer interior and only bind ‘up’ RBDs [32] (**Figure 4B**).

While the anti-SARS-CoV-2 Ab landscape has primarily focused on the RBD, a growing number of neutralizing Abs that target other regions of the S protein are being found.

Neutralizing Abs that bind to the N terminal domain (NTD) [107–109] and the S2 domain [107,110–113] have been reported, indicating that the RBD is not the only site of neutralization. In addition, some of these Abs are also broadly cross-reactive to other betacoronaviruses as they target highly conserved regions of S such as the class 4 cryptic epitope on the RBD [24,114–116] or the stem helix of S2 [111–113].

### 2.2.3. ZIKV Epitopes

The E protein of ZIKV and other flaviviruses is key for facilitating cellular entry and fusion [48]. The mature structure of ZIKV displays smooth virus particles with 180 copies of the E protein arranged as 90 dimers with icosahedral symmetry, and EDIII is thought to be responsible for binding cellular receptors [43,48,117–120]. After cellular entry through receptor-mediated endocytosis, the acidic pH triggers a conformational change by which the E proteins form trimers and expose the FL on EDII for membrane fusion [121–123].

Given its role in fusion, the E protein is an important target of neutralizing Abs that effectively clear ZIKV, inhibit ZIKV infection *in vitro*, decrease vertical transmission, and are protective in ZIKV challenge in animal models [53–56,72,79,124,125] (**Figure 2C**). Structural characterization of Abs that bind the ZIKV E protein have revealed multiple epitopes on the three domains: (1) the conserved FL found on EDII [56,126], (2) EDIII [52–54,72,73,127], (3) multiple domains of single E protein [79,80], (4) multiple domains spanning an E protein dimer [55,60,79,125,128,129], and (5) multiple domains spanning neighboring E dimer pairs [61,62,79,129]. Abs against the FL in EDII compose a large portion of the response to infection, and because the FL is conserved among flaviviruses, these Abs can cross-react with different flaviviruses [56,79,124–126,130]. However, many potentially-neutralizing Abs target EDIII and these Abs tend to be more specific for ZIKV than other flaviviruses [51–56,61,72,124,125,131–137] (**Figure 2C**).

Notably, some Ab epitopes characterized by crystallography are not accessible on the known cryo-EM structures of mature ZIKV [43,54,56,126] (**Figure 3C**). While cryo-EM structures show a static envelope, evidence suggests the E proteins are dynamic and sample different

conformations. The phenomenon of flavivirus “breathing” may result from conformational changes of the E protein during the viral life cycle, such as during fusion. The flavivirus DENV serotype 2 (DENV2) structure showed E protein rearrangements when heated to 37°C, providing further evidence for flavivirus breathing [47,138] (**Figure 3C**). However, ZIKV maintains a smooth structure at 40°C and its breathing conformation has not yet been determined [42].

### *2.3. Somatic Hypermutation of Neutralizing Abs*

Abs evolve to neutralize antigen targets through the process of affinity maturation. This process begins when germline-encoded B cell receptors interact with an antigen and receive signals from T cells. This activation stimulates iterative rounds of somatic hypermutation (SHM), whereby a cellular mechanism orchestrates single base pair mutations, insertions, and deletions (indels) primarily in the CDRs of Abs [139]. These mutations are random, although favorable mutations that enhance recognition of antigen are selected for in further rounds of SHM [139]. Affinity maturation can rapidly diversify the Ab repertoire, allowing for the recognition of innumerable antigens that can mutate to evade Ab recognition [140]. This arms race between distinct Abs and antigens has been monitored through structural biology, which can illuminate how SHM impacts the antigen:Ab interface. For different viral antigens, SHM plays different roles in overcoming infection.

In HIV-1 infection, SHM plays a major role in the creation of bNAbs. Human Abs that have undergone affinity maturation on average carry 15-20 nucleotide mutations in the variable heavy ( $V_H$ ) gene; however, HIV-1 bNAbs include 40-100  $V_H$  gene mutations [141]. High levels of bNAb SHM are necessary to combat a rapidly evolving antigen target in which Env mutations are selected to evade bNAb recognition. In fact, these mutations have been deemed critical for recognition and neutralization of native viral envelopes, as unmutated germline precursors of bNAbs do not usually interact with viral Envs [142]. X-ray crystallography and cryo-EM have allowed for the characterization of bNAb SHM to understand how mutated residues interact with HIV-1 Env and confer broadly neutralizing activity and potency [7,143,144]. Structures of Env:bNAb complexes have identified individual SHMs that are

critical for neutralization activity at different epitopes and have set forth criteria for predicting the capability of newly isolated bNAbs.

Furthermore, structural biology has given context to unusual bNAb characteristics brought on by SHM; namely, framework region (FWR) mutations and indels. The FWRs of an Ab variable domain are the relatively constant sequences that provide a scaffold for the more diverse CDR loops. SHMs in FWRs are often poorly tolerated as they impair the structural integrity of the Ab [145–147]. However, HIV-1 bNAbs FWR SHM has been found to be critical for breadth and potency [145]. Analysis of crystal structures of bNAbs bound to gp120s revealed that regions of FWR SHM can directly interact with the antigen to increase the binding affinity or contribute to the structural rigidity and flexibility of a Fab for optimal binding [99,145]. HIV-1 bNAbs also contain unusually high levels of SHM indels [76, 73]. Prior studies reporting sequences of Ab genes from memory B cells found between 1-3% of Ab genes contained indels [148]. For HIV-1 bNAbs, approximately 40% of bNAbs include indel mutations that range from 3-33 nucleotides in length [76, 73]. Analysis of crystal structures of bNAb:gp120 complexes found that these indels are preferentially found within 10Å of the Ab:antigen interface [149]. Indels are therefore important to optimize interactions with Env, specifically to penetrate the dense glycan shield. Thus, structural biology has aided in elucidating how unusual SHM features in HIV-1 bNAbs contribute to breadth and potency.

Unlike HIV-1 bNAbs, Abs against SARS-CoV-2 S and ZIKV E protein have much lower levels of SHM and, in fact, affinity maturation via SHM is not always required to interact with their viral antigen targets [23,54,150]. Longitudinal studies tracking Ab evolution after SARS-CoV-2 infection found 1.3 months post-infection averages of 4.2  $V_H$  and 2.8  $V_L$  nucleotide mutations [151]. However, after 12 months past infection, SHM increased to approximately 15  $V_H$  and 8  $V_L$  nucleotide mutations [152]. Low levels of SHM have also been reported in longitudinal studies tracking ZIKV infection and comparisons of mature and germline versions of anti-ZIKV Abs [52,54,56,150,153,154]. Inferred germline Abs

have been shown to be able to bind and even weakly neutralize ZIKV [52,54,153,155]. Structural analysis of Ab:antigen complexes for SARS-CoV-2 and ZIKV suggests most SHMs are found in CDR loops and contribute to the complex interface to create optimal contacts for antigen recognition [25,32,52,54]. For both of these viruses, the relatively low levels of SHM indicate near-germline and germline Abs are readily capable of recognizing viral antigens and maturing into potently neutralizing Abs.

#### *2.4. Structure-guided design of vaccines, small molecules inhibitors, and Ab therapeutics*

Structural biology has played a pivotal role in characterizing the optimal human Ab response which vaccines and therapeutics can be designed to mimic (**Figure 1**). For many viruses, the ability to produce a cross reactive response either to many strains of the same virus or to different viruses in the same group is necessary for complete protection from disease, presenting a challenge for vaccine design [156]. Therefore, the structure-guided development of small molecules, peptides, and protein decoys as therapeutics is a complementary strategy for treating viral infection [157].

Structural biology has allowed for the advancement of structure-based vaccine design, which is considered to be one of the current avenues most likely to eventually lead to an HIV-1 vaccine after the failure of subunit vaccines [158]. bNAbs are only elicited by a small subset of the population infected with HIV-1; even so these ‘elite controllers’ still never clear the virus [159]. In fact, arguably the biggest hurdle in creating an HIV-1 vaccine is eliciting an immune response that is far better than what is observed in infected people. The vast number of HIV-1 strains means a vaccine must protect against initial infection of countless distinct viral species rather than a single, or only a few, strains. Due to the inherent difficulty of eliciting bNAbs against HIV-1, some current structure-based efforts for HIV-1 vaccine design rely on structurally characterizing bNAbs in an effort to reverse engineer an immunogen that can elicit them, rather than the commonly-observed strain-specific, autologous neutralizing responses [158]. Structures of antigen:Ab complexes have allowed for the classification of Abs by their epitopes, which is necessary for the design of effective therapeutic monoclonal Ab cocktails [7]. In many cases, the dosing of single monoclonals is

often suboptimal due to the ability of viruses to rapidly mutate. For example, in the case of HIV-1, the viral swarm inside a patient can evolve resistance mutations that make a therapy either less or not effective within days to weeks [160]. Therapeutics have also been designed to mimic an existing interaction by binding directly, such as CD4 mimetic drugs that bind into the CD4 pocket on gp120 [161,162]. As an alternative therapeutic approach, binding targets separate from canonical interaction sites can be used to inhibit function by preventing conformational changes, such as inhibitors directed at the HIV-1 Env fusion peptide [163].

In the case of SARS-CoV-2, which mutates at a lower frequency than HIV-1 but whose variants of concern are posing current problems, future efforts will need to focus on producing vaccines that are effective in the face of new variants [164,165]. Key regions of the S protein are highly conserved across the subgenus of sarbecovirus coronaviruses, of which at least three others can infect human cells: SARS-CoV, SHC014, and RaTG13 [166]. Neutralizing Abs that target the S of SARS-CoV-2 and also bind and neutralize other sarbecoviruses including SARS-CoV-2 variants of concern have been identified by several groups and have been structurally characterized [24,112–116,167,168], suggesting that an immunogen could be designed to produce a pan-sarbecovirus vaccine. Additionally, therapeutic mAb cocktails have successfully been developed for the treatment of SARS-CoV-2 [169]. Therapeutics have also been designed to mimic an existing interaction by binding directly, such as ACE2-S small protein decoys [170].

For ZIKV, design of a safe vaccine is complicated due to the similarities in structures between ZIKV and other flaviviruses. Since the structure of ZIKV is similar to that of DENV, WENV and YFV [38–41], there is concern that Abs elicited during infection with one flavivirus may cross-react with, but not neutralize, other flaviviruses during a later infection. This cross-reactive Ab recognition may worsen symptoms due to a phenomenon termed Ab-dependent enhancement (ADE), by which Ab-bound viruses can infect cells through interactions of the Fc regions of the bound Abs with the host Fc $\gamma$  receptor, resulting in infection of cells after endocytosis of the Ab-virus complex [38,130,154,171–178]. This is

of particular concern for the mosquito-borne virus DENV, since it has been shown that prior DENV or ZIKV infection that results in low or intermediate Ab titers increases the risk of worsened disease severity from a subsequent DENV infection with a different serotype [38,179–187]. However, potent neutralizing Abs against ZIKV EDIII have been identified that appear to be more specific for ZIKV than other flaviviruses, suggesting ZIKV EDIII is a potential candidate for the design of a safe vaccine [51–56,61,72,124,125,131–136]. No vaccine is yet universally available for ZIKV, although both the full E protein and individual EDIII have been investigated as potential immunogens [78,135,188–194].

### **3. Conclusions**

Structural biology has allowed for a deeper understanding of the immune responses to many viruses, including HIV-1, SARS-CoV-2, and ZIKV discussed here. Mutations have been engineered that stabilize surface proteins in their pre-fusion conformations for use as starting immunogens for structure-based vaccine design and as laboratory reagents that can be used to study other aspects of the elicited humoral immune response. Structures of Abs bound to these stabilized proteins have allowed for the elucidation of neutralizing epitopes on the viral surface proteins. Additionally, such structures have increased our understanding of the role of features that Abs develop in response to antigens, such as somatic hypermutation, insertions, and deletions. For targets where whole inactivated or subunit vaccines have failed, structures of viral antigens bound to elicited Abs have facilitated alternative routes for structure-based design of vaccines, small molecules therapeutics, and Ab cocktails. It is through structural biology, inspired by advancements by Rosalind Franklin, that we are able to make progress toward vaccines and Ab treatments for the viruses we study, including HIV-1, SARS-CoV-2, and ZIKV.

### **Methods**

Biorender.com was used to produce portions of Figure 1 and Figure 2. All structure renderings were made using PyMOL ver. 2.5.0. or 1.7.6.4.

Figure 4 was produced in PyMOL by aligning the HIV-1 Env or SARS-CoV-2 S proteins of each Fab-bound structure with the structure of the viral protein depicted in the figure (Env PDB: 5T3Z, S PDB: 7K8V). Only  $V_{H}V_{L}$  domains are shown for each Ab.

**Acknowledgments:** We would like to thank members of the Bjorkman laboratory for helpful discussions; the Caltech Merkin Institute for Translational Research for resources that enable our work; the Caltech Beckman Institute Resource Center for Transmission Electron Microscopy for support in cryo-EM projects; the Gordon and Betty Moore and Beckman Foundations for gifts to support the Molecular Observatory at Caltech, which provides aid for protein crystallization; and the Stanford Synchrotron Radiation Lightsource (SSRL), which provides data collection capabilities for X-ray crystallography. This research was supported by the National Institute of Allergy and Infectious Diseases (NIAID) Grant HIVRAD P01 AI100148, a George Mason University Fast Grant GMU.SARSCOV2, an NSF GRFP (to M.E.A.), a NIH National Research Service Award Fellowship F30AI147579 (S.R.E.), NIH National Institute of General Medical Sciences Training Grant T32-GM008042 (to S.R.E.) through the University of California, Los Angeles–California Institute of Technology Medical Scientist Training Program, and the National Institutes of Health (NIH) Grant AI138938. This work was supported, in whole or in part, by the Bill & Melinda Gates Foundation (grant INV-002143). Under the grant conditions of the Foundation, a Creative Commons Attribution 4.0 Generic License has already been assigned to the Author Accepted Manuscript version that might arise from this submission. Finally, we are grateful for Rosalind Franklin’s contributions to structural biology and for her brazen career as a female scientist that continues to embolden researchers, especially women.

## References

1. Creager, A.N.H.; Morgan, G.J. After the Double Helix: Rosalind Franklin's Research on Tobacco Mosaic Virus. *Isis* **2008**, *99*, 239–272, doi:<https://doi.org/10.1086/588626>.
2. Franklin, R.E.; Klug, A. The Nature of the Helical Groove on the Tobacco Mosaic Virus Particle X-Ray Diffraction Studies. *Biochim. Biophys. Acta* **1956**, *19*, 403–416, doi:[https://doi.org/10.1016/0006-3002\(56\)90463-2](https://doi.org/10.1016/0006-3002(56)90463-2).
3. Franklin, R.E.; Holmes, K.C. The Helical Arrangement of the Protein Sub-Units in Tobacco Mosaic Virus. *Biochim. Biophys. Acta* **1956**, *21*, 405–406, doi:[https://doi.org/10.1016/0006-3002\(56\)90043-9](https://doi.org/10.1016/0006-3002(56)90043-9).
4. Franklin, R.E. X-Ray Diffraction Studies of Cucumber Virus 4 and Three Strains of Tobacco Mosaic Virus. *Biochim. Biophys. Acta* **1956**, *19*, 203–211, doi:[10.1016/0006-3002\(56\)90421-8](https://doi.org/10.1016/0006-3002(56)90421-8).
5. FRANKLIN, R.E. Structure of Tobacco Mosaic Virus: Location of the Ribonucleic Acid in the Tobacco Mosaic Virus Particle. *Nature* **1956**, *177*, 928–930, doi:[10.1038/177928b0](https://doi.org/10.1038/177928b0).
6. *Global HIV & AIDS Statistics Available Online: <https://www.unaids.org/en/resources/fact-sheet> (Accessed on 13 September 2021).*
7. West Jr, A.P.; Scharf, L.; Scheid, J.F.; Klein, F.; Bjorkman, P.J.; Nussenzweig, M.C. Structural Insights on the Role of Antibodies in HIV-1 Vaccine and Therapy. *Cell* **2014**, *156*, 633–648, doi:[10.1016/j.cell.2014.01.052](https://doi.org/10.1016/j.cell.2014.01.052).
8. Gray, E.S.; Madiga, M.C.; Hermanus, T.; Moore, P.L.; Wibmer, C.K.; Tumba, N.L.; Werner, L.; Mlisana, K.; Sibeko, S.; Williamson, C.; et al. The Neutralization Breadth of HIV-1 Develops Incrementally over Four Years and Is Associated with CD4+ T Cell Decline and High Viral Load during Acute Infection. *J. Virol.* **2011**, *85*, 4828–4840, doi:[10.1128/JVI.00198-11](https://doi.org/10.1128/JVI.00198-11).
9. Sather, D.N.; Armann, J.; Ching, L.K.; Mavrantoni, A.; Sellhorn, G.; Caldwell, Z.; Yu, X.; Wood, B.; Self, S.; Kalams, S.; et al. Factors Associated with the Development of Cross-Reactive Neutralizing Antibodies during Human Immunodeficiency Virus Type 1 Infection. *J. Virol.* **2009**, *83*, 757–769, doi:[10.1128/JVI.02036-08](https://doi.org/10.1128/JVI.02036-08).
10. Doria-Rose, N.A.; Klein, R.M.; Manion, M.M.; O'Dell, S.; Phogat, A.; Chakrabarti, B.; Hallahan, C.W.; Migueles, S.A.; Wrammert, J.; Ahmed, R.; et al. Frequency and Phenotype

of Human Immunodeficiency Virus Envelope-Specific B Cells from Patients with Broadly Cross-Neutralizing Antibodies. *J. Virol.* **2009**, *83*, 188–199, doi:10.1128/JVI.01583-08.

11. COVID-19 Map Available online: <https://coronavirus.jhu.edu/map.html> (13 September 2021).

12. Hoffmann, M.; Kleine-Weber, H.; Schroeder, S.; Krüger, N.; Herrler, T.; Erichsen, S.; Schiergens, T.S.; Herrler, G.; Wu, N.-H.; Nitsche, A.; et al. SARS-CoV-2 Cell Entry Depends on ACE2 and TMPRSS2 and Is Blocked by a Clinically Proven Protease Inhibitor. *Cell* **2020**, *181*, 271–280.e8, doi:10.1016/j.cell.2020.02.052.

13. Lan, J.; Ge, J.; Yu, J.; Shan, S.; Zhou, H.; Fan, S.; Zhang, Q.; Shi, X.; Wang, Q.; Zhang, L.; et al. Structure of the SARS-CoV-2 Spike Receptor-Binding Domain Bound to the ACE2 Receptor. *Nature* **2020**, *581*, 215–220, doi:10.1038/s41586-020-2180-5.

14. Wrapp, D.; Wang, N.; Corbett, K.S.; Goldsmith, J.A.; Hsieh, C.-L.; Abiona, O.; Graham, B.S.; McLellan, J.S. Cryo-EM Structure of the 2019-NCoV Spike in the Prefusion Conformation. *Science* **2020**, *367*, 1260–1263, doi:10.1126/science.abb2507.

15. Walls, A.C.; Park, Y.-J.; Tortorici, M.A.; Wall, A.; McGuire, A.T.; Velesler, D. Structure, Function, and Antigenicity of the SARS-CoV-2 Spike Glycoprotein. *Cell* **2020**, *181*, 281–292.e6, doi:10.1016/j.cell.2020.02.058.

16. Kirchdoerfer, R.N.; Cottrell, C.A.; Wang, N.; Pallesen, J.; Yassine, H.M.; Turner, H.L.; Corbett, K.S.; Graham, B.S.; McLellan, J.S.; Ward, A.B. Pre-Fusion Structure of a Human Coronavirus Spike Protein. *Nature* **2016**, *531*, 118–121, doi:10.1038/nature17200.

17. Yuan, Y.; Cao, D.; Zhang, Y.; Ma, J.; Qi, J.; Wang, Q.; Lu, G.; Wu, Y.; Yan, J.; Shi, Y.; et al. Cryo-EM Structures of MERS-CoV and SARS-CoV Spike Glycoproteins Reveal the Dynamic Receptor Binding Domains. *Nat. Commun.* **2017**, *8*, 15092, doi:10.1038/ncomms15092.

18. Li, Z.; Tomlinson, A.C.; Wong, A.H.; Zhou, D.; Desforjes, M.; Talbot, P.J.; Benlekbir, S.; Rubinstein, J.L.; Rini, J.M. The Human Coronavirus HCoV-229E S-Protein Structure and Receptor Binding. *eLife* **2019**, *8*, e51230, doi:10.7554/eLife.51230.

19. Walls, A.C.; Tortorici, M.A.; Bosch, B.-J.; Frenz, B.; Rottier, P.J.M.; DiMaio, F.; Rey, F.A.; Velesler, D. Cryo-Electron Microscopy Structure of a Coronavirus Spike Glycoprotein Trimer. *Nature* **2016**, *531*, 114–117, doi:10.1038/nature16988.
20. Roy, S.; Jaiswar, A.; Sarkar, R. Dynamic Asymmetry Exposes 2019-NCoV Prefusion Spike. *J. Phys. Chem. Lett.* **2020**, *11*, 7021–7027, doi:10.1021/acs.jpcllett.0c01431.
21. Brouwer, P.J.M.; Caniels, T.G.; Straten, K. van der; Snitselaar, J.L.; Aldon, Y.; Bangaru, S.; Torres, J.L.; Okba, N.M.A.; Claireaux, M.; Kerster, G.; et al. Potent Neutralizing Antibodies from COVID-19 Patients Define Multiple Targets of Vulnerability. *Science* **2020**, *369*, 643–650, doi:10.1126/science.abc5902.
22. Cao, Y.; Su, B.; Guo, X.; Sun, W.; Deng, Y.; Bao, L.; Zhu, Q.; Zhang, X.; Zheng, Y.; Geng, C.; et al. Potent Neutralizing Antibodies against SARS-CoV-2 Identified by High-Throughput Single-Cell Sequencing of Convalescent Patients' B Cells. *Cell* **2020**, *182*, 73–84.e16, doi:10.1016/j.cell.2020.05.025.
23. Kreer, C.; Zehner, M.; Weber, T.; Ercanoglu, M.S.; Giesemann, L.; Rohde, C.; Halwe, S.; Korenkov, M.; Schommers, P.; Vanshylla, K.; et al. Longitudinal Isolation of Potent Near-Germline SARS-CoV-2-Neutralizing Antibodies from COVID-19 Patients. *Cell* **2020**, *182*, 843–854.e12, doi:10.1016/j.cell.2020.06.044.
24. Liu, H.; Wu, N.C.; Yuan, M.; Bangaru, S.; Torres, J.L.; Caniels, T.G.; van Schooten, J.; Zhu, X.; Lee, C.-C.D.; Brouwer, P.J.M.; et al. Cross-Neutralization of a SARS-CoV-2 Antibody to a Functionally Conserved Site Is Mediated by Avidity. *Immunity* **2020**, *53*, 1272–1280.e5, doi:10.1016/j.immuni.2020.10.023.
25. Robbiani, D.F.; Gaebler, C.; Muecksch, F.; Lorenzi, J.C.C.; Wang, Z.; Cho, A.; Agudelo, M.; Barnes, C.O.; Gazumyan, A.; Finkin, S.; et al. Convergent Antibody Responses to SARS-CoV-2 in Convalescent Individuals. *Nature* **2020**, *584*, 437–442, doi:10.1038/s41586-020-2456-9.
26. Rogers, T.F.; Zhao, F.; Huang, D.; Beutler, N.; Burns, A.; He, W.; Limbo, O.; Smith, C.; Song, G.; Woehl, J.; et al. Isolation of Potent SARS-CoV-2 Neutralizing Antibodies and Protection from Disease in a Small Animal Model. *Science* **2020**, *369*, 956–963, doi:10.1126/science.abc7520.

27. Seydoux, E.; Homad, L.J.; MacCamy, A.J.; Parks, K.R.; Hurlburt, N.K.; Jennewein, M.F.; Akins, N.R.; Stuart, A.B.; Wan, Y.-H.; Feng, J.; et al. Analysis of a SARS-CoV-2-Infected Individual Reveals Development of Potent Neutralizing Antibodies with Limited Somatic Mutation. *Immunity* **2020**, *53*, 98-105.e5, doi:10.1016/j.immuni.2020.06.001.
28. Shi, R.; Shan, C.; Duan, X.; Chen, Z.; Liu, P.; Song, J.; Song, T.; Bi, X.; Han, C.; Wu, L.; et al. A Human Neutralizing Antibody Targets the Receptor-Binding Site of SARS-CoV-2. *Nature* **2020**, *584*, 120–124, doi:10.1038/s41586-020-2381-y.
29. Zost, S.J.; Gilchuk, P.; Case, J.B.; Binshtein, E.; Chen, R.E.; Nkolola, J.P.; Schäfer, A.; Reidy, J.X.; Trivette, A.; Nargi, R.S.; et al. Potently Neutralizing and Protective Human Antibodies against SARS-CoV-2. *Nature* **2020**, *584*, 443–449, doi:10.1038/s41586-020-2548-6.
30. Zost, S.J.; Gilchuk, P.; Chen, R.E.; Case, J.B.; Reidy, J.X.; Trivette, A.; Nargi, R.S.; Sutton, R.E.; Suryadevara, N.; Chen, E.C.; et al. Rapid Isolation and Profiling of a Diverse Panel of Human Monoclonal Antibodies Targeting the SARS-CoV-2 Spike Protein. *Nat. Med.* **2020**, *26*, 1422–1427, doi:10.1038/s41591-020-0998-x.
31. Pinto, D.; Park, Y.-J.; Beltramello, M.; Walls, A.C.; Tortorici, M.A.; Bianchi, S.; Jaconi, S.; Culap, K.; Zatta, F.; De Marco, A.; et al. Cross-Neutralization of SARS-CoV-2 by a Human Monoclonal SARS-CoV Antibody. *Nature* **2020**, *583*, 290–295, doi:10.1038/s41586-020-2349-y.
32. Barnes, C.O.; Jette, C.A.; Abernathy, M.E.; Dam, K.-M.A.; Esswein, S.R.; Gristick, H.B.; Malyutin, A.G.; Sharaf, N.G.; Huey-Tubman, K.E.; Lee, Y.E.; et al. SARS-CoV-2 Neutralizing Antibody Structures Inform Therapeutic Strategies. *Nature* **2020**, *588*, 682–687, doi:10.1038/s41586-020-2852-1.
33. Barnes, C.O.; West, A.P.; Huey-Tubman, K.E.; Hoffmann, M.A.G.; Sharaf, N.G.; Hoffman, P.R.; Koranda, N.; Gristick, H.B.; Gaebler, C.; Muecksch, F.; et al. Structures of Human Antibodies Bound to SARS-CoV-2 Spike Reveal Common Epitopes and Recurrent Features of Antibodies. *Cell* **2020**, *182*, 828-842.e16, doi:10.1016/j.cell.2020.06.025.
34. Suy, A.; Sulleiro, E.; Rodo, C.; Vazquez, E.; Bocanegra, C.; Molina, I.; Esperalba, J.; Sanchez-Seco, M.P.; Boix, H.; Pumarola, T.; et al. Prolonged Zika Virus Viremia during Pregnancy. *N Engl J Med* **2016**, *375*, 2611–2613, doi:10.1056/NEJMc1607580.

35. Brasil, P.; Pereira, J.P.; Moreira, M.E.; Ribeiro Nogueira, R.M.; Damasceno, L.; Wakimoto, M.; Rabello, R.S.; Valderramos, S.G.; Halai, U.A.; Salles, T.S.; et al. Zika Virus Infection in Pregnant Women in Rio de Janeiro. *N Engl J Med* **2016**, *375*, 2321–2334, doi:10.1056/NEJMoa1602412.
36. Coyne, C.B.; Lazear, H.M. Zika Virus - Reigniting the TORCH. *Nat Rev Microbiol* **2016**, *14*, 707–715, doi:10.1038/nrmicro.2016.125.
37. Mlakar, J.; Korva, M.; Tul, N.; Popović, M.; Poljšak-Prijatelj, M.; Mraz, J.; Kolenc, M.; Resman Rus, K.; Vesnaver Vipotnik, T.; Fabjan Vodusek, V.; et al. Zika Virus Associated with Microcephaly Available online: <https://www.nejm.org/doi/10.1056/NEJMoa1600651> (accessed on 18 June 2021).
38. Heinz, F.X.; Stiasny, K. The Antigenic Structure of Zika Virus and Its Relation to Other Flaviviruses: Implications for Infection and Immunoprophylaxis. *Microbiol Mol Biol Rev* **2017**, *81*, doi:10.1128/MMBR.00055-16.
39. Chang, H.-H.; Huber, R.G.; Bond, P.J.; Grad, Y.H.; Camerini, D.; Maurer-Stroh, S.; Lipsitch, M. Systematic Analysis of Protein Identity between Zika Virus and Other Arthropod-Borne Viruses. *Bull. World Health Organ.* **2017**, *95*, 517-525I, doi:10.2471/BLT.16.182105.
40. da Fonseca, N.J.; Lima Afonso, M.Q.; Pedersolli, N.G.; de Oliveira, L.C.; Andrade, D.S.; Bleicher, L. Sequence, Structure and Function Relationships in Flaviviruses as Assessed by Evolutive Aspects of Its Conserved Non-Structural Protein Domains. *Biochem. Biophys. Res. Commun.* **2017**, *492*, 565–571, doi:10.1016/j.bbrc.2017.01.041.
41. Ye, Q.; Liu, Z.-Y.; Han, J.-F.; Jiang, T.; Li, X.-F.; Qin, C.-F. Genomic Characterization and Phylogenetic Analysis of Zika Virus Circulating in the Americas. *Infect. Genet. Evol.* **2016**, *43*, 43–49, doi:10.1016/j.meegid.2016.05.004.
42. Kostyuchenko, V.A.; Lim, E.X.; Zhang, S.; Fibriansah, G.; Ng, T.S.; Ooi, J.S.; Shi, J.; Lok, S.M. Structure of the Thermally Stable Zika Virus. *Nature* **2016**, *533*, 425–8, doi:10.1038/nature17994.
43. Sirohi, D.; Chen, Z.; Sun, L.; Klose, T.; Pierson, T.C.; Rossmann, M.G.; Kuhn, R.J. The 3.8 Å Resolution Cryo-EM Structure of Zika Virus. *Science* **2016**, *352*, 467–70, doi:10.1126/science.aaf5316.

44. Pierson, T.C.; Diamond, M.S. The Emergence of Zika Virus and Its New Clinical Syndromes. *Nature* **2018**, *560*, 573–581, doi:10.1038/s41586-018-0446-y.
45. Kuhn, R.J.; Dowd, K.A.; Beth Post, C.; Pierson, T.C. Shake, Rattle, and Roll: Impact of the Dynamics of Flavivirus Particles on Their Interactions with the Host. *Virology* **2015**, *479–480*, 508–17, doi:10.1016/j.virol.2015.03.025.
46. Dowd, K.A.; DeMaso, C.R.; Pierson, T.C. Genotypic Differences in Dengue Virus Neutralization Are Explained by a Single Amino Acid Mutation That Modulates Virus Breathing. *MBio* **2015**, *6*, e01559-15, doi:10.1128/mBio.01559-15.
47. Fibriansah, G.; Ng, T.-S.; Kostyuchenko, V.A.; Lee, J.; Lee, S.; Wang, J.; Lok, S.-M. Structural Changes in Dengue Virus When Exposed to a Temperature of 37°C. *J. Virol.* **2013**, *87*, 7585–7592, doi:10.1128/JVI.00757-13.
48. Mukhopadhyay, S.; Kuhn, R.J.; Rossmann, M.G. A Structural Perspective of the Flavivirus Life Cycle. *Nat. Rev. Microbiol.* **2005**, *3*, 13–22, doi:10.1038/nrmicro1067.
49. Yu, I.M.; Zhang, W.; Holdaway, H.A.; Li, L.; Kostyuchenko, V.A.; Chipman, P.R.; Kuhn, R.J.; Rossmann, M.G.; Chen, J. Structure of the Immature Dengue Virus at Low PH Primes Proteolytic Maturation. *Science* **2008**, *319*, 1834–7, doi:10.1126/science.1153264.
50. Kuhn, R.J.; Zhang, W.; Rossmann, M.G.; Pletnev, S.V.; Corver, J.; Lenches, E.; Jones, C.T.; Mukhopadhyay, S.; Chipman, P.R.; Strauss, E.G.; et al. Structure of Dengue Virus: Implications for Flavivirus Organization, Maturation, and Fusion. *Cell* **2002**, *108*, 717–725, doi:10.1016/S0092-8674(02)00660-8.
51. Pierson, T.C.; Fremont, D.H.; Kuhn, R.J.; Diamond, M.S. Structural Insights into the Mechanisms of Antibody-Mediated Neutralization of Flavivirus Infection: Implications for Vaccine Development. *Cell Host Microbe* **2008**, *4*, 229–38, doi:10.1016/j.chom.2008.08.004.
52. Esswein, S.R.; Gristick, H.B.; Jurado, A.; Peace, A.; Keeffe, J.R.; Lee, Y.E.; Voll, A.V.; Saeed, M.; Nussenzweig, M.C.; Rice, C.M.; et al. Structural Basis for Zika Envelope Domain III Recognition by a Germline Version of a Recurrent Neutralizing Antibody. *Proc. Natl. Acad. Sci.* **2020**, doi:10.1073/pnas.1919269117.
53. Keeffe, J.R.; Van Rompay, K.K.A.; Olsen, P.C.; Wang, Q.; Gazumyan, A.; Azzopardi, S.A.; Schaefer-Babajew, D.; Lee, Y.E.; Stuart, J.B.; Singapuri, A.; et al. A Combination of

- Two Human Monoclonal Antibodies Prevents Zika Virus Escape Mutations in Non-Human Primates. *Cell Rep.* **2018**, *25*, 1385-1394.e7, doi:10.1016/j.celrep.2018.10.031.
54. Robbiani, D.F.; Bozzacco, L.; Keeffe, J.R.; Khouri, R.; Olsen, P.C.; Gazumyan, A.; Schaefer-Babajew, D.; Avila-Rios, S.; Nogueira, L.; Patel, R.; et al. Recurrent Potent Human Neutralizing Antibodies to Zika Virus in Brazil and Mexico. *Cell* **2017**, *169*, 597-609.e11, doi:10.1016/j.cell.2017.04.024.
55. Barba-Spaeth, G.; Dejnirattisai, W.; Rouvinski, A.; Vaney, M.C.; Medits, I.; Sharma, A.; Simon-Loriere, E.; Sakuntabhai, A.; Cao-Lormeau, V.M.; Haouz, A.; et al. Structural Basis of Potent Zika-Dengue Virus Antibody Cross-Neutralization. *Nature* **2016**, *536*, 48–53, doi:10.1038/nature18938.
56. Dai, L.; Song, J.; Lu, X.; Deng, Y.Q.; Musyoki, A.M.; Cheng, H.; Zhang, Y.; Yuan, Y.; Song, H.; Haywood, J.; et al. Structures of the Zika Virus Envelope Protein and Its Complex with a Flavivirus Broadly Protective Antibody. *Cell Host Microbe* **2016**, *19*, 696–704, doi:10.1016/j.chom.2016.04.013.
57. Prasad, V.M.; Miller, A.S.; Klose, T.; Sirohi, D.; Buda, G.; Jiang, W.; Kuhn, R.J.; Rossmann, M.G. Structure of the Immature Zika Virus at 9 Å Resolution. *Nat Struct Mol Biol* **2017**, *24*, 184–186, doi:10.1038/nsmb.3352.
58. Sevvana, M.; Long, F.; Miller, A.S.; Klose, T.; Buda, G.; Sun, L.; Kuhn, R.J.; Rossmann, M.G. Refinement and Analysis of the Mature Zika Virus Cryo-EM Structure at 3.1 Å Resolution. *Structure* **2018**, *26*, 1169-1177.e3, doi:10.1016/j.str.2018.05.006.
59. Morrone, S.R.; Chew, V.S.Y.; Lim, X.-N.; Ng, T.-S.; Kostyuchenko, V.A.; Zhang, S.; Wirawan, M.; Chew, P.-L.; Lee, J.; Tan, J.L.; et al. High Flavivirus Structural Plasticity Demonstrated by a Non-Spherical Morphological Variant. *Nat. Commun.* **2020**, *11*, 3112, doi:10.1038/s41467-020-16925-y.
60. Tyagi, A.; Ahmed, T.; Shi, J.; Bhushan, S. A Complex between the Zika Virion and the Fab of a Broadly Cross-Reactive Neutralizing Monoclonal Antibody Revealed by Cryo-EM and Single Particle Analysis at 4.1 Å Resolution. *J. Struct. Biol. X* **2020**, 100028, doi:10.1016/j.yjsbx.2020.100028.
61. Zhang, S.; Loy, T.; Ng, T.-S.; Lim, X.-N.; Chew, S.-Y.V.; Tan, T.Y.; Xu, M.; Kostyuchenko, V.A.; Tukijan, F.; Shi, J.; et al. A Human Antibody Neutralizes Different

- Flaviviruses by Using Different Mechanisms. *Cell Rep.* **2020**, *31*, 107584, doi:10.1016/j.celrep.2020.107584.
62. Long, F.; Doyle, M.; Fernandez, E.; Miller, A.S.; Klose, T.; Sevvana, M.; Bryan, A.; Davidson, E.; Doranz, B.J.; Kuhn, R.J.; et al. Structural Basis of a Potent Human Monoclonal Antibody against Zika Virus Targeting a Quaternary Epitope. *Proc. Natl. Acad. Sci.* **2019**, *116*, 1591–1596, doi:10.1073/pnas.1815432116.
63. Jiang, W.; Tang, L. Atomic Cryo-EM Structures of Viruses. *Curr. Opin. Struct. Biol.* **2017**, *46*, 122–129, doi:10.1016/j.sbi.2017.07.002.
64. Luque, D.; Castón, J.R. Cryo-Electron Microscopy for the Study of Virus Assembly. *Nat. Chem. Biol.* **2020**, *16*, 231–239, doi:10.1038/s41589-020-0477-1.
65. Grünewald, K.; Cyrklaff, M. Structure of Complex Viruses and Virus-Infected Cells by Electron Cryo Tomography. *Curr. Opin. Microbiol.* **2006**, *9*, 437–442, doi:10.1016/j.mib.2006.06.016.
66. Klasse, P.J.; Depetris, R.S.; Pejchal, R.; Julien, J.-P.; Khayat, R.; Lee, J.H.; Marozsan, A.J.; Cupo, A.; Cocco, N.; Korzun, J.; et al. Influences on Trimerization and Aggregation of Soluble, Cleaved HIV-1 SOSIP Envelope Glycoprotein. *J. Virol.* **2013**, *87*, 9873–9885, doi:10.1128/JVI.01226-13.
67. Hsieh, C.-L.; Goldsmith, J.A.; Schaub, J.M.; DiVenere, A.M.; Kuo, H.-C.; Javanmardi, K.; Le, K.C.; Wrapp, D.; Lee, A.G.; Liu, Y.; et al. Structure-Based Design of Prefusion-Stabilized SARS-CoV-2 Spikes. *Science* **2020**, *369*, 1501–1505, doi:10.1126/science.abd0826.
68. Kwong, P.D.; Wyatt, R.; Robinson, J.; Sweet, R.W.; Sodroski, J.; Hendrickson, W.A. Structure of an HIV Gp120 Envelope Glycoprotein in Complex with the CD4 Receptor and a Neutralizing Human Antibody. *Nature* **1998**, *393*, 648–659, doi:10.1038/31405.
69. Diskin, R.; Marcovecchio, P.M.; Bjorkman, P.J. Structure of a Clade C HIV-1 Gp120 Bound to CD4 and CD4-Induced Antibody Reveals Anti-CD4 Polyreactivity. *Nat. Publ. Group* **2010**, *17*, 608–613, doi:10.1038/nsmb.1796.
70. Li, F. Structure of SARS Coronavirus Spike Receptor-Binding Domain Complexed with Receptor. *Science* **2005**, *309*, 1864–1868, doi:10.1126/science.1116480.

71. Du, L.; Kou, Z.; Ma, C.; Tao, X.; Wang, L.; Zhao, G.; Chen, Y.; Yu, F.; Tseng, C.-T.K.; Zhou, Y.; et al. A Truncated Receptor-Binding Domain of MERS-CoV Spike Protein Potently Inhibits MERS-CoV Infection and Induces Strong Neutralizing Antibody Responses: Implication for Developing Therapeutics and Vaccines. *PLoS ONE* **2013**, *8*, e81587, doi:10.1371/journal.pone.0081587.
72. Zhao, H.; Fernandez, E.; Dowd, K.A.; Speer, S.D.; Platt, D.J.; Gorman, M.J.; Govero, J.; Nelson, C.A.; Pierson, T.C.; Diamond, M.S.; et al. Structural Basis of Zika Virus-Specific Antibody Protection. *Cell* **2016**, *166*, 1016–27, doi:10.1016/j.cell.2016.07.020.
73. Zhao, H.; Xu, L.; Bombardi, R.; Nargi, R.; Deng, Z.; Errico, J.M.; Nelson, C.A.; Dowd, K.A.; Pierson, T.C.; Crowe, J.E.; et al. Mechanism of Differential Zika and Dengue Virus Neutralization by a Public Antibody Lineage Targeting the DIII Lateral Ridge. *J. Exp. Med.* **2020**, *217*, doi:10.1084/jem.20191792.
74. Zhou, T.; Zhu, J.; Wu, X.; Moquin, S.; Zhang, B.; Acharya, P.; Georgiev, I.S.; Altae-Tran, H.R.; Chuang, G.-Y.; Joyce, M.G.; et al. Multidonor Analysis Reveals Structural Elements, Genetic Determinants, and Maturation Pathway for HIV-1 Neutralization by VRC01-Class Antibodies. *Immunity* **2013**, *39*, 245–258, doi:10.1016/j.immuni.2013.04.012.
75. Sanders, R.W.; Moore, J.P. Virus Vaccines: Proteins Prefer Prolines. *Cell Host Microbe* **2021**, *29*, 327–333, doi:10.1016/j.chom.2021.02.002.
76. Qiao, H.; Pelletier, S.L.; Hoffman, L.; Hacker, J.; Armstrong, R.T.; White, J.M. Specific Single or Double Proline Substitutions in the “Spring-Loaded” Coiled-Coil Region of the Influenza Hemagglutinin Impair or Abolish Membrane Fusion Activity. *J. Cell Biol.* **1998**, *141*, 1335–1347, doi:10.1083/jcb.141.6.1335.
77. Sanders, R.W.; Vesanen, M.; Schuelke, N.; Master, A.; Schiffner, L.; Kalyanaraman, R.; Paluch, M.; Berkhout, B.; Maddon, P.J.; Olson, W.C.; et al. Stabilization of the Soluble, Cleaved, Trimeric Form of the Envelope Glycoprotein Complex of Human Immunodeficiency Virus Type 1. *J VIROL* **2002**, *76*, 15.
78. Qu, P.; Zhang, W.; Li, D.; Zhang, C.; Liu, Q.; Zhang, X.; Wang, X.; Dai, W.; Xu, Y.; Leng, Q.; et al. Insect Cell-Produced Recombinant Protein Subunit Vaccines Protect against Zika Virus Infection. *Antiviral Res.* **2018**, *154*, 97–103, doi:10.1016/j.antiviral.2018.04.010.

79. Wang, Q.; Yang, H.; Liu, X.; Dai, L.; Ma, T.; Qi, J.; Wong, G.; Peng, R.; Liu, S.; Li, J.; et al. Molecular Determinants of Human Neutralizing Antibodies Isolated from a Patient Infected with Zika Virus. *Sci Transl Med* **2016**, *8*, 369ra179, doi:10.1126/scitranslmed.aai8336.
80. Dussupt, V.; Sankhala, R.S.; Gromowski, G.D.; Donofrio, G.; De La Barrera, R.A.; Larocca, R.A.; Zaky, W.; Mendez-Rivera, L.; Choe, M.; Davidson, E.; et al. Potent Zika and Dengue Cross-Neutralizing Antibodies Induced by Zika Vaccination in a Dengue-Experienced Donor. *Nat. Med.* **2020**, *26*, 228–235, doi:10.1038/s41591-019-0746-2.
81. Slon Campos, J.L.; Marchese, S.; Rana, J.; Mossenta, M.; Poggianella, M.; Bestagno, M.; Burrone, O.R. Temperature-Dependent Folding Allows Stable Dimerization of Secretory and Virus-Associated E Proteins of Dengue and Zika Viruses in Mammalian Cells. *Sci. Rep.* **2017**, *7*, 966, doi:10.1038/s41598-017-01097-5.
82. Harrison, S.C. Viral Membrane Fusion. *Virology* **2015**, *479–480*, 498–507, doi:10.1016/j.virol.2015.03.043.
83. Ackerman, M.E.; Mikhailova, A.; Brown, E.P.; Dowell, K.G.; Walker, B.D.; Bailey-Kellogg, C.; Suscovich, T.J.; Alter, G. Polyfunctional HIV-Specific Antibody Responses Are Associated with Spontaneous HIV Control. *PLOS Pathog.* **2016**, *12*, e1005315, doi:10.1371/journal.ppat.1005315.
84. Gunn, B.M.; Yu, W.-H.; Karim, M.M.; Brannan, J.M.; Herbert, A.S.; Wec, A.Z.; Halfmann, P.J.; Fusco, M.L.; Schendel, S.L.; Gangavarapu, K.; et al. A Role for Fc Function in Therapeutic Monoclonal Antibody-Mediated Protection against Ebola Virus. *Cell Host Microbe* **2018**, *24*, 221–233.e5, doi:10.1016/j.chom.2018.07.009.
85. Lu, L.L.; Suscovich, T.J.; Fortune, S.M.; Alter, G. Beyond Binding: Antibody Effector Functions in Infectious Diseases. *Nat. Rev. Immunol.* **2018**, *18*, 46–61, doi:10.1038/nri.2017.106.
86. Sapphire, E.O.; Schendel, S.L.; Gunn, B.M.; Milligan, J.C.; Alter, G. Antibody-Mediated Protection against Ebola Virus. *Nat. Immunol.* **2018**, *19*, 1169–1178, doi:10.1038/s41590-018-0233-9.

87. White, J.M.; Delos, S.E.; Brecher, M.; Schornberg, K. Structures and Mechanisms of Viral Membrane Fusion Proteins: Multiple Variations on a Common Theme. *Crit. Rev. Biochem. Mol. Biol.* **2008**, *43*, 189–219, doi:10.1080/10409230802058320.
88. Ward, A.B.; Wilson, I.A. The HIV-1 Envelope Glycoprotein Structure: Nailing down a Moving Target. *Immunol. Rev.* **2017**, *275*, 21–32, doi:10.1111/imr.12507.
89. Ozorowski, G.; Pallesen, J.; de Val, N.; Lyumkis, D.; Cottrell, C.A.; Torres, J.L.; Copps, J.; Stanfield, R.L.; Cupo, A.; Pugach, P.; et al. Open and Closed Structures Reveal Allostery and Pliability in the HIV-1 Envelope Spike. *Nature* **2017**, *547*, 360–363, doi:10.1038/nature23010.
90. Wang, H.; Barnes, C.O.; Yang, Z.; Nussenzweig, M.C.; Bjorkman, P.J. Partially Open HIV-1 Envelope Structures Exhibit Conformational Changes Relevant for Coreceptor Binding and Fusion. *Cell Host Microbe* **2018**, *24*, 579–592.e4, doi:10.1016/j.chom.2018.09.003.
91. Yang, Z.; Wang, H.; Liu, A.Z.; Gristick, H.B.; Bjorkman, P.J. Asymmetric Opening of HIV-1 Env Bound to CD4 and a Coreceptor-Mimicking Antibody. *Nat. Struct. Mol. Biol.* **2019**, *26*, 1167–1175, doi:10.1038/s41594-019-0344-5.
92. Wang, H.; Cohen, A.A.; Galimidi, R.P.; Gristick, H.B.; Jensen, G.J.; Bjorkman, P.J. Cryo-EM Structure of a CD4-Bound Open HIV-1 Envelope Trimer Reveals Structural Rearrangements of the Gp120 V1V2 Loop. *Proc. Natl. Acad. Sci. U. S. A.* **2016**, *113*, E7151–E7158, doi:10.1073/pnas.1615939113.
93. Alkhatib, G. The Biology of CCR5 and CXCR4: *Curr. Opin. HIV AIDS* **2009**, *4*, 96–103, doi:10.1097/COH.0b013e328324bbec.
94. Lee, J.H.; Andrabi, R.; Su, C.-Y.; Yasmineen, A.; Julien, J.-P.; Kong, L.; Wu, N.C.; McBride, R.; Sok, D.; Pauthner, M.; et al. A Broadly Neutralizing Antibody Targets the Dynamic HIV Envelope Trimer Apex via a Long, Rigidified, and Anionic  $\beta$ -Hairpin Structure. *Immunity* **2017**, *46*, 690–702, doi:10.1016/j.immuni.2017.03.017.
95. Gorman, J.; Soto, C.; Yang, M.M.; Davenport, T.M.; Guttman, M.; Bailer, R.T.; Chambers, M.; Chuang, G.-Y.; DeKosky, B.J.; Doria-Rose, N.A.; et al. Structures of HIV-1 Env V1V2 with Broadly Neutralizing Antibodies Reveal Commonalities That Enable Vaccine Design. *Nat. Struct. Mol. Biol.* **2016**, *23*, 81–90, doi:10.1038/nsmb.3144.

96. Walker, L.M.; Phogat, S.K.; Chan-Hui, P.-Y.; Wagner, D.; Phung, P.; Goss, J.L.; Wrin, T.; Simek, M.D.; Fling, S.; Mitcham, J.L.; et al. Broad and Potent Neutralizing Antibodies from an African Donor Reveal a New HIV-1 Vaccine Target. *Science* **2009**, *326*, 285–289, doi:10.1126/science.1178746.
97. Fera, D.; Lee, M.S.; Wiehe, K.; Meyerhoff, R.R.; Piai, A.; Bonsignori, M.; Aussedat, B.; Walkowicz, W.E.; Ton, T.; Zhou, J.O.; et al. HIV Envelope V3 Region Mimic Embodies Key Features of a Broadly Neutralizing Antibody Lineage Epitope. *Nat. Commun.* **2018**, *9*, 1111, doi:10.1038/s41467-018-03565-6.
98. Barnes, C.O.; Gristick, H.B.; Freund, N.T.; Escolano, A.; Lyubimov, A.Y.; Hartweger, H.; West, A.P.; Cohen, A.E.; Nussenzweig, M.C.; Bjorkman, P.J. Structural Characterization of a Highly-Potent V3-Glycan Broadly Neutralizing Antibody Bound to Natively-Glycosylated HIV-1 Envelope. *Nat. Commun.* **2018**, *9*, 1251, doi:10.1038/s41467-018-03632-y.
99. Scheid, J.F.; Mouquet, H.; Ueberheide, B.; Diskin, R.; Klein, F.; Oliveira, T.Y.K.; Pietzsch, J.; Fenyo, D.; Abadir, A.; Velinzon, K.; et al. Sequence and Structural Convergence of Broad and Potent HIV Antibodies That Mimic CD4 Binding. *Science* **2011**, *333*, 1633–1637, doi:10.1126/science.1207227.
100. Schoofs, T.; Barnes, C.O.; Suh-Toma, N.; Golijanin, J.; Schommers, P.; Gruell, H.; West, A.P.; Bach, F.; Lee, Y.E.; Nogueira, L.; et al. Broad and Potent Neutralizing Antibodies Recognize the Silent Face of the HIV Envelope. *Immunity* **2019**, *50*, 1513–1529.e9, doi:10.1016/j.immuni.2019.04.014.
101. Zhou, T.; Zheng, A.; Baxa, U.; Chuang, G.-Y.; Georgiev, I.S.; Kong, R.; O'Dell, S.; Shahzad-ul-Hussan, S.; Shen, C.-H.; Tsybovsky, Y.; et al. A Neutralizing Antibody Recognizing Primarily N-Linked Glycan Targets the Silent Face of the HIV Envelope. *Immunity* **2018**, *48*, 500–513.e6, doi:10.1016/j.immuni.2018.02.013.
102. Xu, K.; Acharya, P.; Kong, R.; Cheng, C.; Chuang, G.-Y.; Liu, K.; Louder, M.K.; O'Dell, S.; Rawi, R.; Sastry, M.; et al. Epitope-Based Vaccine Design Yields Fusion Peptide-Directed Antibodies That Neutralize Diverse Strains of HIV-1. *Nat. Med.* **2018**, *24*, 857–867, doi:10.1038/s41591-018-0042-6.

103. Scharf, L.; Wang, H.; Gao, H.; Chen, S.; McDowall, A.W.; Bjorkman, P.J. Broadly Neutralizing Antibody 8ANC195 Recognizes Closed and Open States of HIV-1 Env. *Cell* **2018**, 1–13, doi:10.1016/j.cell.2015.08.035.
104. Caillat, C.; Guilligay, D.; Sulbaran, G.; Weissenhorn, W. Neutralizing Antibodies Targeting HIV-1 Gp41. *Viruses* **2020**, *12*, 1210, doi:10.3390/v12111210.
105. West Jr, A.P. Structural Basis for Germ-Line Gene Usage of a Potent Class of Antibodies Targeting the CD4-Binding Site of HIV-1 Gp120. **2012**, 1–8, doi:10.1073/pnas.1208984109/-/DCSupplemental.
106. Zhou, P.; Yang, X.-L.; Wang, X.-G.; Hu, B.; Zhang, L.; Zhang, W.; Si, H.-R.; Zhu, Y.; Li, B.; Huang, C.-L.; et al. A Pneumonia Outbreak Associated with a New Coronavirus of Probable Bat Origin. *Nature* **2020**, *579*, 270–273, doi:10.1038/s41586-020-2012-7.
107. Shiakolas, A.R.; Kramer, K.J.; Wrapp, D.; Richardson, S.I.; Schäfer, A.; Wall, S.; Wang, N.; Janowska, K.; Pilewski, K.A.; Venkat, R.; et al. Cross-Reactive Coronavirus Antibodies with Diverse Epitope Specificities and Fc Effector Functions. *Cell Rep. Med.* **2021**, *2*, 100313, doi:10.1016/j.xcrm.2021.100313.
108. Chi, X.; Yan, R.; Zhang, J.; Zhang, G.; Zhang, Y.; Hao, M.; Zhang, Z.; Fan, P.; Dong, Y.; Yang, Y.; et al. A Neutralizing Human Antibody Binds to the N-Terminal Domain of the Spike Protein of SARS-CoV-2. *Science* **2020**, *369*, 650–655, doi:10.1126/science.abc6952.
109. McCallum, M.; De Marco, A.; Lempp, F.A.; Tortorici, M.A.; Pinto, D.; Walls, A.C.; Beltramello, M.; Chen, A.; Liu, Z.; Zatta, F.; et al. N-Terminal Domain Antigenic Mapping Reveals a Site of Vulnerability for SARS-CoV-2. *Cell* **2021**, *184*, 2332–2347.e16, doi:10.1016/j.cell.2021.03.028.
110. Song, G.; He, W.; Callaghan, S.; Anzanello, F.; Huang, D.; Ricketts, J.; Torres, J.L.; Beutler, N.; Peng, L.; Vargas, S.; et al. Cross-Reactive Serum and Memory B-Cell Responses to Spike Protein in SARS-CoV-2 and Endemic Coronavirus Infection. *Nat. Commun.* **2021**, *12*, 2938, doi:10.1038/s41467-021-23074-3.
111. Wang, C.; van Haperen, R.; Gutiérrez-Álvarez, J.; Li, W.; Okba, N.M.A.; Albulescu, I.; Widjaja, I.; van Dieren, B.; Fernandez-Delgado, R.; Sola, I.; et al. A Conserved Immunogenic and Vulnerable Site on the Coronavirus Spike Protein Delineated by Cross-

- Reactive Monoclonal Antibodies. *Nat. Commun.* **2021**, *12*, 1715, doi:10.1038/s41467-021-21968-w.
112. Pinto, D.; Sauer, M.M.; Czudnochowski, N.; Low, J.S.; Tortorici, M.A.; Housley, M.P.; Noack, J.; Walls, A.C.; Bowen, J.E.; Guarino, B.; et al. Broad Betacoronavirus Neutralization by a Stem Helix-Specific Human Antibody. *Science* **2021**, eabj3321, doi:10.1126/science.abj3321.
113. Sauer, M.M.; Tortorici, M.A.; Park, Y.-J.; Walls, A.C.; Homad, L.; Acton, O.J.; Bowen, J.E.; Wang, C.; Xiong, X.; de van der Schueren, W.; et al. Structural Basis for Broad Coronavirus Neutralization. *Nat. Struct. Mol. Biol.* **2021**, *28*, 478–486, doi:10.1038/s41594-021-00596-4.
114. Lv, Z.; Deng, Y.-Q.; Ye, Q.; Cao, L.; Sun, C.-Y.; Fan, C.; Huang, W.; Sun, S.; Sun, Y.; Zhu, L.; et al. Structural Basis for Neutralization of SARS-CoV-2 and SARS-CoV by a Potent Therapeutic Antibody. *Science* **2020**, *369*, 1505–1509, doi:10.1126/science.abc5881.
115. Starr, T.N.; Czudnochowski, N.; Liu, Z.; Zatta, F.; Park, Y.-J.; Addetia, A.; Pinto, D.; Beltramello, M.; Hernandez, P.; Greaney, A.J.; et al. SARS-CoV-2 RBD Antibodies That Maximize Breadth and Resistance to Escape. *Nature* **2021**, *597*, 97–102, doi:10.1038/s41586-021-03807-6.
116. Tortorici, M.A.; Czudnochowski, N.; Starr, T.N.; Marzi, R.; Walls, A.C.; Zatta, F.; Bowen, J.E.; Jaconi, S.; Di Iulio, J.; Wang, Z.; et al. Broad Sarbecovirus Neutralization by a Human Monoclonal Antibody. *Nature* **2021**, *597*, 103–108, doi:10.1038/s41586-021-03817-4.
117. Lee, E.; Lobigs, M. Substitutions at the Putative Receptor-Binding Site of an Encephalitic Flavivirus Alter Virulence and Host Cell Tropism and Reveal a Role for Glycosaminoglycans in Entry. *J. Virol.* **2000**, *74*, 8867–8875, doi:10.1128/JVI.74.19.8867-8875.2000.
118. Watterson, D.; Kobe, B.; Young, P.R.Y. 2012 Residues in Domain III of the Dengue Virus Envelope Glycoprotein Involved in Cell-Surface Glycosaminoglycan Binding. *J. Gen. Virol.* *93*, 72–82, doi:10.1099/vir.0.037317-0.

119. Chu, J.J.H.; Rajamanonmani, R.; Li, J.; Bhuvanakantham, R.; Lescar, J.; Ng, M.-L.Y. 2005 Inhibition of West Nile Virus Entry by Using a Recombinant Domain III from the Envelope Glycoprotein. *J. Gen. Virol.* **86**, 405–412, doi:10.1099/vir.0.80411-0.
120. Bhardwaj, S.; Holbrook, M.; Shope, R.E.; Barrett, A.D.T.; Watowich, S.J. Biophysical Characterization and Vector-Specific Antagonist Activity of Domain III of the Tick-Borne Flavivirus Envelope Protein. *J. Virol.* **2001**, *75*, 4002–4007, doi:10.1128/JVI.75.8.4002-4007.2001.
121. Modis, Y.; Ogata, S.; Clements, D.; Harrison, S.C. Structure of the Dengue Virus Envelope Protein after Membrane Fusion. *Nature* **2004**, *427*, 313–9, doi:10.1038/nature02165.
122. Stiasny, K.; Allison, S.L.; Marchler-Bauer, A.; Kunz, C.; Heinz, F.X. Structural Requirements for Low-PH-Induced Rearrangements in the Envelope Glycoprotein of Tick-Borne Encephalitis Virus. *J. Virol.* **1996**, *70*, 8142–8147, doi:10.1128/JVI.70.11.8142-8147.1996.
123. Stiasny, K.; Bressanelli, S.; Lepault, J.; Rey, F.A.; Heinz, F.X. Characterization of a Membrane-Associated Trimeric Low-PH-Induced Form of the Class II Viral Fusion Protein E from Tick-Borne Encephalitis Virus and Its Crystallization. *J. Virol.* **2004**, *78*, 3178–3183, doi:10.1128/JVI.78.6.3178-3183.2004.
124. Stettler, K.; Beltramello, M.; Espinosa, D.A.; Graham, V.; Cassotta, A.; Bianchi, S.; Vanzetta, F.; Minola, A.; Jaconi, S.; Mele, F.; et al. Specificity, Cross-Reactivity, and Function of Antibodies Elicited by Zika Virus Infection. *Science* **2016**, *353*, 823–6, doi:10.1126/science.aaf8505.
125. Sapparapu, G.; Fernandez, E.; Kose, N.; Bin, C.; Fox, J.M.; Bombardi, R.G.; Zhao, H.; Nelson, C.A.; Bryan, A.L.; Barnes, T.; et al. Neutralizing Human Antibodies Prevent Zika Virus Replication and Fetal Disease in Mice. *Nature* **2016**, *540*, 443–447, doi:10.1038/nature20564.
126. Deng, Y.-Q.; Dai, J.-X.; Ji, G.-H.; Jiang, T.; Wang, H.-J.; Yang, H.; Tan, W.-L.; Liu, R.; Yu, M.; Ge, B.-X.; et al. A Broadly Flavivirus Cross-Neutralizing Monoclonal Antibody That Recognizes a Novel Epitope within the Fusion Loop of E Protein. *PLOS ONE* **2011**, *6*, e16059, doi:10.1371/journal.pone.0016059.

127. Wang, J.; Bardelli, M.; Espinosa, D.A.; Pedotti, M.; Ng, T.-S.; Bianchi, S.; Simonelli, L.; Lim, E.X.Y.; Foglierini, M.; Zatta, F.; et al. A Human Bi-Specific Antibody against Zika Virus with High Therapeutic Potential. *Cell* **2017**, *171*, 229-241.e15, doi:10.1016/j.cell.2017.09.002.
128. Rouvinski, A.; Guardado-Calvo, P.; Barba-Spaeth, G.; Duquerroy, S.; Vaney, M.-C.; Kikuti, C.M.; Navarro Sanchez, M.E.; Dejnirattisai, W.; Wongwiwat, W.; Haouz, A.; et al. Recognition Determinants of Broadly Neutralizing Human Antibodies against Dengue Viruses. *Nature* **2015**, *520*, 109–113, doi:10.1038/nature14130.
129. Zhang, S.; Kostyuchenko, V.A.; Ng, T.S.; Lim, X.N.; Ooi, J.S.; Lambert, S.; Tan, T.Y.; Widman, D.G.; Shi, J.; Baric, R.S.; et al. Neutralization Mechanism of a Highly Potent Antibody against Zika Virus. *Nat Commun* **2016**, *7*, 13679, doi:10.1038/ncomms13679.
130. Dejnirattisai, W.; Jumnainsong, A.; Onsirisakul, N.; Fitton, P.; Vasanawathana, S.; Limpitikul, W.; Puttikhunt, C.; Edwards, C.; Duangchinda, T.; Supasa, S.; et al. Cross-Reacting Antibodies Enhance Dengue Virus Infection in Humans. *Science* **2010**, *328*, 745–748, doi:10.1126/science.1185181.
131. Oliphant, T.; Engle, M.; Nybakken, G.E.; Doane, C.; Johnson, S.; Huang, L.; Gorlatov, S.; Mehlhop, E.; Marri, A.; Chung, K.M.; et al. Development of a Humanized Monoclonal Antibody with Therapeutic Potential against West Nile Virus. *Nat. Med.* **2005**, *11*, 522–530, doi:10.1038/nm1240.
132. Wang, L.; Wang, R.; Wang, L.; Ben, H.; Yu, L.; Gao, F.; Shi, X.; Yin, C.; Zhang, F.; Xiang, Y.; et al. Structural Basis for Neutralization and Protection by a Zika Virus-Specific Human Antibody. *Cell Rep.* **2019**, *26*, 3360-3368.e5, doi:10.1016/j.celrep.2019.02.062.
133. Yu, L.; Wang, R.; Gao, F.; Li, M.; Liu, J.; Wang, J.; Hong, W.; Zhao, L.; Wen, Y.; Yin, C.; et al. Delineating Antibody Recognition against Zika Virus during Natural Infection. *JCI Insight* **2017**, *2*, doi:10.1172/jci.insight.93042.
134. Wahala, W.M.P.B.; Kraus, A.A.; Haymore, L.B.; Accavitti-Loper, M.A.; de Silva, A.M. Dengue Virus Neutralization by Human Immune Sera: Role of Envelope Protein Domain III-Reactive Antibody. *Virology* **2009**, *392*, 103–113, doi:10.1016/j.virol.2009.06.037.

135. Slon-Campos, J.L.; Dejnirattisai, W.; Jagger, B.W.; López-Camacho, C.; Wongwiwat, W.; Durnell, L.A.; Winkler, E.S.; Chen, R.E.; Reyes-Sandoval, A.; Rey, F.A.; et al. A Protective Zika Virus E-Dimer-Based Subunit Vaccine Engineered to Abrogate Antibody-Dependent Enhancement of Dengue Infection. *Nat. Immunol.* **2019**, *20*, 1291–1298, doi:10.1038/s41590-019-0477-z.
136. Watanabe, S.; Chan, K.W.K.; Wang, J.; Rivino, L.; Lok, S.-M.; Vasudevan, S.G. Dengue Virus Infection with Highly Neutralizing Levels of Cross-Reactive Antibodies Causes Acute Lethal Small Intestinal Pathology without a High Level of Viremia in Mice. *J. Virol.* **2015**, *89*, 5847–5861, doi:10.1128/JVI.00216-15.
137. Heinz, F.X.; Stiasny, K. Flaviviruses and Flavivirus Vaccines. *Vaccine* **2012**, *30*, 4301–4306, doi:10.1016/j.vaccine.2011.09.114.
138. Zhang, X.; Sheng, J.; Plevka, P.; Kuhn, R.J.; Diamond, M.S.; Rossmann, M.G. Dengue Structure Differs at the Temperatures of Its Human and Mosquito Hosts. *Proc. Natl. Acad. Sci.* **2013**, *110*, 6795–6799, doi:10.1073/pnas.1304300110.
139. Victora, G.D.; Nussenzweig, M.C. Germinal Centers. *Annu. Rev. Immunol.* **2012**, *30*, 429–457, doi:10.1146/annurev-immunol-020711-075032.
140. Milstein, C.; Neuberger, M.S. Maturation of the Immune Response. In *Advances in Protein Chemistry*; Richards, F.M., Eisenberg, D.E., Kim, P.S., Eds.; Academic Press, 1996; Vol. 49, pp. 451–485 ISBN 0065-3233.
141. Tiller, T.; Tsuiji, M.; Yurasov, S.; Velinzon, K.; Nussenzweig, M.C.; Wardemann, H. Autoreactivity in Human IgG<sup>+</sup> Memory B Cells. 9.
142. Davenport, T.M.; Gorman, J.; Joyce, M.G.; Zhou, T.; Soto, C.; Guttman, M.; Moquin, S.; Yang, Y.; Zhang, B.; Doria-Rose, N.A.; et al. Somatic Hypermutation-Induced Changes in the Structure and Dynamics of HIV-1 Broadly Neutralizing Antibodies. *Structure* **2016**, *24*, 1346–1357, doi:10.1016/j.str.2016.06.012.
143. Klein, F.; Mouquet, H.; Dosenovic, P.; Scheid, J.F.; Scharf, L.; Nussenzweig, M.C. Antibodies in HIV-1 Vaccine Development and Therapy. *Science* **2013**, *341*, 1199–1204, doi:10.1126/science.1241144.

144. Kwong, P.D.; Mascola, J.R. HIV-1 Vaccines Based on Antibody Identification, B Cell Ontogeny, and Epitope Structure. *Immunity* **2018**, *48*, 855–871, doi:10.1016/j.immuni.2018.04.029.
145. Klein, F.; Diskin, R.; Scheid, J.F.; Gaebler, C.; Mouquet, H.; Georgiev, I.S.; Pancera, M.; Zhou, T.; Incesu, R.-B.; Fu, B.Z.; et al. Somatic Mutations of the Immunoglobulin Framework Are Generally Required for Broad and Potent HIV-1 Neutralization. *Cell* **2013**, *153*, 126–138, doi:10.1016/j.cell.2013.03.018.
146. Wagner, S.D.; Milstein, C.; Neuberger, M.S. Codon Bias Targets Mutation. *Nature* **1995**, *376*, 732–732, doi:10.1038/376732a0.
147. Reynaud, C.-A.; Garcia, C.; Hein, W.R.; Weill, J.-C. Hypermutation Generating the Sheep Immunoglobulin Repertoire Is an Antigen-Independent Process. *Cell* **1995**, *80*, 115–125, doi:10.1016/0092-8674(95)90456-5.
148. Briney, B.S.; Willis, J.R.; Crowe, J.E. Location and Length Distribution of Somatic Hypermutation-Associated DNA Insertions and Deletions Reveals Regions of Antibody Structural Plasticity. *Genes Immun.* **2012**, *13*, 523–529, doi:10.1038/gene.2012.28.
149. Kepler, T.B.; Liao, H.-X.; Alam, S.M.; Bhaskarabhatla, R.; Zhang, R.; Yandava, C.; Stewart, S.; Anasti, K.; Kelsoe, G.; Parks, R.; et al. Immunoglobulin Gene Insertions and Deletions in the Affinity Maturation of HIV-1 Broadly Reactive Neutralizing Antibodies. *Cell Host Microbe* **2014**, *16*, 304–313, doi:10.1016/j.chom.2014.08.006.
150. Niu, X.; Yan, Q.; Yao, Z.; Zhang, F.; Qu, L.; Wang, C.; Wang, C.; Lei, H.; Chen, C.; Liang, R.; et al. Longitudinal Analysis of the Antibody Repertoire of a Zika Virus-Infected Patient Revealed Dynamic Changes in Antibody Response. *Emerg. Microbes Infect.* **2020**, *9*, 111–123, doi:10.1080/22221751.2019.1701953.
151. Gaebler, C.; Wang, Z.; Lorenzi, J.C.C.; Muecksch, F.; Finkin, S.; Tokuyama, M.; Cho, A.; Jankovic, M.; Schaefer-Babajew, D.; Oliveira, T.Y.; et al. Evolution of Antibody Immunity to SARS-CoV-2. *Nature* **2021**, *591*, 639–644, doi:10.1038/s41586-021-03207-w.
152. Wang, Z.; Muecksch, F.; Schaefer-Babajew, D.; Finkin, S.; Viant, C.; Gaebler, C.; Hoffmann, H.-H.; Barnes, C.O.; Cipolla, M.; Ramos, V.; et al. Naturally Enhanced Neutralizing Breadth against SARS-CoV-2 One Year after Infection. *Nature* **2021**, *595*, 426–431, doi:10.1038/s41586-021-03696-9.

153. Magnani, D.M.; Silveira, C.G.T.; Rosen, B.C.; Ricciardi, M.J.; Pedreno-Lopez, N.; Gutman, M.J.; Bailey, V.K.; Maxwell, H.S.; Domingues, A.; Gonzalez-Nieto, L.; et al. A Human Inferred Germline Antibody Binds to an Immunodominant Epitope and Neutralizes Zika Virus. *PLoS Negl Trop Dis* **2017**, *11*, e0005655, doi:10.1371/journal.pntd.0005655.
154. Rogers, T.F.; Goodwin, E.C.; Briney, B.; Sok, D.; Beutler, N.; Strubel, A.; Nedellec, R.; Le, K.; Brown, M.E.; Burton, D.R.; et al. Zika Virus Activates de Novo and Cross-Reactive Memory B Cell Responses in Dengue-Experienced Donors. *Sci Immunol* **2017**, *2*, doi:10.1126/sciimmunol.aan6809.
155. Gao, F.; Lin, X.; He, L.; Wang, R.; Wang, H.; Shi, X.; Zhang, F.; Yin, C.; Zhang, L.; Zhu, J.; et al. Development of a Potent and Protective Germline-like Antibody Lineage against Zika Virus in a Convalescent Human. *bioRxiv* **2019**, 661918, doi:10.1101/661918.
156. Kennedy, R.B. Current Challenges in Vaccinology. *Front. Immunol.* **2020**, *11*, 18.
157. Narkhede, Y.B.; Gonzalez, K.J.; Strauch, E.-M. Targeting Viral Surface Proteins through Structure-Based Design. *Viruses* **2021**, *13*, 1320, doi:10.3390/v13071320.
158. Burton, D.R. What Are the Most Powerful Immunogen Design Vaccine Strategies?: Reverse Vaccinology 2.0 Shows Great Promise. *Cold Spring Harb. Perspect. Biol.* **2017**, *9*, a030262, doi:10.1101/cshperspect.a030262.
159. Gebara, N.Y.; Kamari, V.E.; Rizk, N. HIV-1 Elite Controllers: An Immunovirological Review and Clinical Perspectives. 4.
160. Caskey, M.; Schoofs, T.; Gruell, H.; Settler, A.; Karagounis, T.; Kreider, E.F.; Murrell, B.; Pfeifer, N.; Nogueira, L.; Oliveira, T.Y.; et al. Antibody 10-1074 Suppresses Viremia in HIV-1-Infected Individuals. *Nat Med* **2017**, *23*, 185–191, doi:10.1038/nm.4268.
161. Courter, J.R.; Madani, N.; Sodroski, J.; Schön, A.; Freire, E.; Kwong, P.D.; Hendrickson, W.A.; Chaiken, I.M.; LaLonde, J.M.; Smith, A.B. Structure-Based Design, Synthesis and Validation of CD4-Mimetic Small Molecule Inhibitors of HIV-1 Entry: Conversion of a Viral Entry Agonist to an Antagonist. *Acc. Chem. Res.* **2014**, *47*, 1228–1237, doi:10.1021/ar4002735.
162. Vita, C.; Drakopoulou, E.; Vizzavona, J.; Rochette, S.; Martin, L.; Ménez, A.; Roumestand, C.; Yang, Y.-S.; Ylisastigui, L.; Benjouad, A.; et al. Rational Engineering of a

- Miniprotein That Reproduces the Core of the CD4 Site Interacting with HIV-1 Envelope Glycoprotein. *Proc. Natl. Acad. Sci. U. S. A.* **1999**, *96*, 13091–13096.
163. Ozorowski, G.; Torres, J.L.; Santos-Martins, D.; Forli, S.; Ward, A.B. A Strain-Specific Inhibitor of Receptor-Bound HIV-1 Targets a Pocket near the Fusion Peptide. *Cell Rep.* **2020**, *33*, 108428, doi:10.1016/j.celrep.2020.108428.
164. Fischer, W.; Giorgi, E.E.; Chakraborty, S.; Nguyen, K.; Bhattacharya, T.; Theiler, J.; Goloboff, P.A.; Yoon, H.; Abfalterer, W.; Foley, B.T.; et al. HIV-1 and SARS-CoV-2: Patterns in the Evolution of Two Pandemic Pathogens. *Cell Host Microbe* **2021**, *29*, 1093–1110, doi:10.1016/j.chom.2021.05.012.
165. Hastie, K.M.; Li, H.; Bedinger, D.; Schendel, S.L.; Dennison, S.M.; Li, K.; Rayaprolu, V.; Yu, X.; Mann, C.; Zandonatti, M.; et al. Defining Variant-Resistant Epitopes Targeted by SARS-CoV-2 Antibodies: A Global Consortium Study. *Science* **2021**, doi:10.1126/science.abh2315.
166. Letko, M.; Marzi, A.; Munster, V. Functional Assessment of Cell Entry and Receptor Usage for SARS-CoV-2 and Other Lineage B Betacoronaviruses. *Nat. Microbiol.* **2020**, *5*, 562–569, doi:10.1038/s41564-020-0688-y.
167. Jette, C.A.; Cohen, A.A.; Gnanapragasam, P.N.P.; Muecksch, F.; Lee, Y.E.; Huey-Tubman, K.E.; Schmidt, F.; Hatziioannou, T.; Bieniasz, P.D.; Nussenzweig, M.C.; et al. Broad Cross-Reactivity across Sarbecoviruses Exhibited by a Subset of COVID-19 Donor-Derived Neutralizing Antibodies. *Cell Rep.* **2021**, 109760, doi:10.1016/j.celrep.2021.109760.
168. Wec, A.Z.; Wrapp, D.; Herbert, A.S.; Maurer, D.P.; Haslwanter, D.; Sakharkar, M.; Jangra, R.K.; Dieterle, M.E.; Lilov, A.; Huang, D.; et al. Broad Neutralization of SARS-Related Viruses by Human Monoclonal Antibodies. *Science* **2020**, *369*, 731–736, doi:10.1126/science.abc7424.
169. Taylor, P.C.; Adams, A.C.; Hufford, M.M.; de la Torre, I.; Winthrop, K.; Gottlieb, R.L. Neutralizing Monoclonal Antibodies for Treatment of COVID-19. *Nat. Rev. Immunol.* **2021**, *21*, 382–393, doi:10.1038/s41577-021-00542-x.
170. Linsky, T.W.; Vergara, R.; Codina, N.; Nelson, J.W.; Walker, M.J.; Su, W.; Barnes, C.O.; Hsiang, T.-Y.; Esser-Nobis, K.; Yu, K.; et al. De Novo Design of Potent and Resilient

- HACE2 Decoys to Neutralize SARS-CoV-2. *Science* **2020**, *370*, 1208–1214, doi:10.1126/science.abe0075.
171. Bardina, S.V.; Bunduc, P.; Tripathi, S.; Duehr, J.; Frere, J.J.; Brown, J.A.; Nachbagauer, R.; Foster, G.A.; Kryzstof, D.; Tortorella, D.; et al. Enhancement of Zika Virus Pathogenesis by Preexisting Antiflavivirus Immunity. *Science* **2017**, *356*, 175–180, doi:10.1126/science.aal4365.
172. Harrison, S.C. Immunogenic Cross-Talk between Dengue and Zika Viruses. *Nat Immunol* **2016**, *17*, 1010–2, doi:10.1038/ni.3539.
173. Priyamvada, L.; Quicke, K.M.; Hudson, W.H.; Onlamoon, N.; Sewatanon, J.; Edupuganti, S.; Pattanapanyasat, K.; Chokephaibulkit, K.; Mulligan, M.J.; Wilson, P.C.; et al. Human Antibody Responses after Dengue Virus Infection Are Highly Cross-Reactive to Zika Virus. *Proc Natl Acad Sci U S A* **2016**, *113*, 7852–7, doi:10.1073/pnas.1607931113.
174. Vaughn, D.W.; Green, S.; Kalayanarooj, S.; Innis, B.L.; Nimmannitya, S.; Suntayakorn, S.; Endy, T.P.; Raengsakulrach, B.; Rothman, A.L.; Ennis, F.A.; et al. Dengue Viremia Titer, Antibody Response Pattern, and Virus Serotype Correlate with Disease Severity. *J. Infect. Dis.* **2000**, *181*, 2–9, doi:10.1086/315215.
175. Halstead, S.B. Neutralization and Antibody-Dependent Enhancement of Dengue Viruses. *Adv Virus Res* **2003**, *60*, 421–67.
176. Dejnirattisai, W.; Supasa, P.; Wongwiwat, W.; Rouvinski, A.; Barba-Spaeth, G.; Duangchinda, T.; Sakuntabhai, A.; Cao-Lormeau, V.M.; Malasit, P.; Rey, F.A.; et al. Dengue Virus Sero-Cross-Reactivity Drives Antibody-Dependent Enhancement of Infection with Zika Virus. *Nat Immunol* **2016**, *17*, 1102–8, doi:10.1038/ni.3515.
177. Wahala, W.M.; Silva, A.M. The Human Antibody Response to Dengue Virus Infection. *Viruses* **2011**, *3*, 2374–95, doi:10.3390/v3122374.
178. Alwis, R. de; Williams, K.L.; Schmid, M.A.; Lai, C.-Y.; Patel, B.; Smith, S.A.; Crowe, J.E.; Wang, W.-K.; Harris, E.; Silva, A.M. de Dengue Viruses Are Enhanced by Distinct Populations of Serotype Cross-Reactive Antibodies in Human Immune Sera. *PLOS Pathog.* **2014**, *10*, e1004386, doi:10.1371/journal.ppat.1004386.
179. Nisalak, A.; Clapham, H.E.; Kalayanarooj, S.; Klungthong, C.; Thaisomboonsuk, B.; Fernandez, S.; Reiser, J.; Srikiatkachorn, A.; Macareo, L.R.; Lessler, J.T.; et al. Forty Years

- of Dengue Surveillance at a Tertiary Pediatric Hospital in Bangkok, Thailand, 1973–2012. *Am. J. Trop. Med. Hyg.* **2016**, *94*, 1342–1347, doi:10.4269/ajtmh.15-0337.
180. SANGKAWIBHA, N.; ROJANASUPHOT, S.; AHANDRIK, S.; VIRIYAPONGSE, S.; JATANASEN, S.; SALITUL, V.; PHANTHUMACHINDA, B.; HALSTEAD, S.B. RISK FACTORS IN DENGUE SHOCK SYNDROME: A PROSPECTIVE EPIDEMIOLOGIC STUDY IN RAYONG, THAILAND: I. THE 1980 OUTBREAK. *Am. J. Epidemiol.* **1984**, *120*, 653–669, doi:10.1093/oxfordjournals.aje.a113932.
181. Katzelnick, L.C.; Narvaez, C.; Arguello, S.; Mercado, B.L.; Collado, D.; Ampie, O.; Elizondo, D.; Miranda, T.; Carillo, F.B.; Mercado, J.C.; et al. Zika Virus Infection Enhances Future Risk of Severe Dengue Disease. *Science* **2020**, *369*, 1123–1128, doi:10.1126/science.abb6143.
182. Halstead, S.B. In Vivo Enhancement of Dengue Virus Infection in Rhesus Monkeys by Passively Transferred Antibody. *J. Infect. Dis.* **1979**, *140*, 527–533, doi:10.1093/infdis/140.4.527.
183. Waggoner, J.J.; Katzelnick, L.C.; Burger-Calderon, R.; Gallini, J.; Moore, R.H.; Kuan, G.; Balmaseda, A.; Pinsky, B.A.; Harris, E. Antibody-Dependent Enhancement of Severe Disease Is Mediated by Serum Viral Load in Pediatric Dengue Virus Infections. *J. Infect. Dis.* **2020**, *221*, 1846–1854, doi:10.1093/infdis/jiz618.
184. Katzelnick, L.C.; Gresh, L.; Halloran, M.E.; Mercado, J.C.; Kuan, G.; Gordon, A.; Balmaseda, A.; Harris, E. Antibody-Dependent Enhancement of Severe Dengue Disease in Humans. *Science* **2017**, *358*, 929–932, doi:10.1126/science.aan6836.
185. Salje, H.; Cummings, D.A.T.; Rodriguez-Barraquer, I.; Katzelnick, L.C.; Lessler, J.; Klungthong, C.; Thaisomboonsuk, B.; Nisalak, A.; Weg, A.; Ellison, D.; et al. Reconstruction of Antibody Dynamics and Infection Histories to Evaluate Dengue Risk. *Nature* **2018**, *557*, 719–723, doi:10.1038/s41586-018-0157-4.
186. Cattarino, L.; Rodriguez-Barraquer, I.; Imai, N.; Cummings, D.A.T.; Ferguson, N.M. Mapping Global Variation in Dengue Transmission Intensity. *Sci. Transl. Med.* **2020**, *12*, doi:10.1126/scitranslmed.aax4144.
187. Faria, N.R.; Quick, J.; Claro, I.M.; Thézé, J.; de Jesus, J.G.; Giovanetti, M.; Kraemer, M.U.G.; Hill, S.C.; Black, A.; da Costa, A.C.; et al. Establishment and Cryptic Transmission

- of Zika Virus in Brazil and the Americas. *Nature* **2017**, *546*, 406–410, doi:10.1038/nature22401.
188. Yang, C.; Zeng, F.; Gao, X.; Zhao, S.; Li, X.; Liu, S.; Li, N.; Deng, C.; Zhang, B.; Gong, R. Characterization of Two Engineered Dimeric Zika Virus Envelope Proteins as Immunogens for Neutralizing Antibody Selection and Vaccine Design. *J. Biol. Chem.* **2019**, *294*, 10638–10648, doi:10.1074/jbc.RA119.007443.
189. Cimica, V.; Williams, S.; Adams-Fish, D.; McMahon, C.; Narayanan, A.; Rashid, S.; Stedman, T.T. Zika Virus-Like Particle (VLP) Vaccine Displaying Envelope (E) Protein CD Loop Antigen Elicits Protective and Specific Immune Response in a Murine Model. *Biochem. Biophys. Res. Commun.* **2020**, *529*, 805–811, doi:10.1016/j.bbrc.2020.05.161.
190. Tai, W.; Chen, J.; Zhao, G.; Geng, Q.; He, L.; Chen, Y.; Zhou, Y.; Li, F.; Du, L. Rational Design of Zika Virus Subunit Vaccine with Enhanced Efficacy. *J. Virol.* **2019**, *93*, e02187-18, doi:10.1128/JVI.02187-18.
191. Shanmugam, R.K.; Ramasamy, V.; Shukla, R.; Arora, U.; Swaminathan, S.; Khanna, N. Pichia Pastoris-Expressed Zika Virus Envelope Domain III on a Virus-like Particle Platform: Design, Production and Immunological Evaluation. *Pathog. Dis.* **2019**, *77*, doi:10.1093/femspd/ftz026.
192. Yang, M.; Lai, H.; Sun, H.; Chen, Q. Virus-like Particles That Display Zika Virus Envelope Protein Domain III Induce Potent Neutralizing Immune Responses in Mice. *Sci. Rep.* **2017**, *7*, 7679, doi:10.1038/s41598-017-08247-9.
193. Espinosa, D.; Mendy, J.; Manayani, D.; Vang, L.; Wang, C.; Richard, T.; Guenther, B.; Aruri, J.; Avanzini, J.; Garduno, F.; et al. Passive Transfer of Immune Sera Induced by a Zika Virus-Like Particle Vaccine Protects AG129 Mice Against Lethal Zika Virus Challenge. *EBioMedicine* **2018**, *27*, 61–70, doi:10.1016/j.ebiom.2017.12.010.
194. Cabral-Miranda, G.; Lim, S.M.; Mohsen, M.O.; Pobelov, I.V.; Roesti, E.S.; Heath, M.D.; Skinner, M.A.; Kramer, M.F.; Martina, B.E.E.; Bachmann, M.F. Correction: Zika Virus-Derived E-DIII Protein Displayed on Immunologically Optimized VLPs Induces Neutralizing Antibodies without Causing Enhancement of Dengue Virus Infection. *Vaccines* **2019**, *7*, 72. *Vaccines* **2020**, *8*, 94, doi:10.3390/vaccines8010094.

## SARS-COV-2 NEUTRALIZING ANTIBODY STRUCTURES INFORM THERAPEUTIC STRATEGIES

Barnes, C.O., Jette, C.A., **Abernathy, M.E.**, Dam, K-M.A., Esswein, S.R., Gristick, H.B., Malyutin, A.G., Sharaf, N.G., Huey-Tubman, K.E., Lee, Y.E., Robbiani, D.F., Nussenzweig, M.C., West, A.P., Bjorkman, P.J. SARS-CoV-2 neutralizing antibody structures inform therapeutic strategies. *Nature*, **588**, 682–687 (2020). <https://doi.org/10.1038/s41586-020-2852-1>

### Summary

The coronavirus disease 2019 (COVID-19) pandemic presents an urgent health crisis. Human neutralizing antibodies that target the host ACE2 receptor-binding domain (RBD) of the severe acute respiratory syndrome coronavirus-2 (SARS-CoV-2) spike protein<sup>1,2,3,4,5</sup> show promise therapeutically and are being evaluated clinically<sup>6,7,8</sup>. Here, to identify the structural correlates of SARS-CoV-2 neutralization, we solved eight new structures of distinct COVID-19 human neutralizing antibodies<sup>5</sup> in complex with the SARS-CoV-2 spike trimer or RBD. Structural comparisons allowed us to classify the antibodies into categories: (1) neutralizing antibodies encoded by the *VH3-53* gene segment with short CDRH3 loops that block ACE2 and bind only to ‘up’ RBDs; (2) ACE2-blocking neutralizing antibodies that bind both up and ‘down’ RBDs and can contact adjacent RBDs; (3) neutralizing antibodies that bind outside the ACE2 site and recognize both up and down RBDs; and (4) previously described antibodies that do not block ACE2 and bind only to up RBDs<sup>9</sup>. Class 2 contained four neutralizing antibodies with epitopes that bridged RBDs, including a *VH3-53* antibody that used a long CDRH3 with a hydrophobic tip to bridge between adjacent down RBDs, thereby locking the spike into a closed conformation. Epitope and paratope mapping revealed few interactions with host-derived *N*-glycans and minor contributions of antibody somatic hypermutations to epitope contacts. Affinity measurements and mapping of naturally occurring and in vitro-selected spike mutants in 3D

provided insight into the potential for SARS-CoV-2 to escape from antibodies elicited during infection or delivered therapeutically. These classifications and structural analyses provide rules for assigning current and future human RBD-targeting antibodies into classes, evaluating avidity effects and suggesting combinations for clinical use, and provide insight into immune responses against SARS-CoV-2.

## Introduction

Neutralizing antibodies (NAbs) against SARS-CoV-2 protect against infection in animal models<sup>1,3,4,10,11</sup> and are being evaluated for prophylaxis and as therapeutic agents in humans<sup>7,8</sup>. These antibodies target the SARS-CoV-2 spike (S) trimer<sup>3,5,10,12,13,14,15,16,17</sup>, a viral glycoprotein that mediates binding to the angiotensin-converting enzyme 2 (ACE2) receptor<sup>18,19</sup>. The S trimer comprises three copies of an S1 subunit that contains the RBD and three copies of S2, which includes the fusion peptide and transmembrane regions<sup>20,21</sup>. The RBDs of SARS-CoV-2 and other coronaviruses exhibit flexibility, such that they bind to ACE2 only when they are in an ‘up’ conformation, compared with the ‘down’ RBD conformation of the closed, prefusion S trimer<sup>20,21,22,23,24,25</sup>.

Many human NAbs isolated from COVID-19-convalescent donors target the RBD, binding to distinct, sometimes non-overlapping, epitopes<sup>3,4,5,10,12,13,14,17</sup>. A subset of these antibodies blocks viral entry by binding to the ACE2-binding site on the RBD<sup>6,11,13,15,26,27</sup>. A family of recurrent ACE2-blocking human NAbs is composed of heavy chains encoded by the *VH3-53* or *VH3-66* gene segment<sup>3,12,13,16,17,27,28,29</sup>, most of which are known or predicted<sup>15,26,28,30,31</sup> to exhibit a common RBD binding mode that results from the use of germline-encoded residues within the complementarity-determining regions 1 and 2 (CDRH1 and CDRH2) and a CDRH3 that is shorter than the average length (15 amino acids; IMGT<sup>32</sup> complementarity-determining region (CDR) definition) in human antibodies<sup>33</sup>. Other SARS-CoV-2 RBD-binding antibodies are encoded by *VH3-30*<sup>5</sup>, and these have also been isolated from donors infected with SARS-CoV<sup>34</sup>, and antibodies with a variety of the other VH gene segments<sup>3,5,10,12,13,14,15,16,17</sup>.

To classify commonalities and differences among RBD-binding human NAbs isolated from COVID-19-convalescent individuals<sup>5</sup>, we solved complexes of NAbs with stabilized (2P and 6P versions)<sup>35,36</sup> soluble S trimer. Subsequently, we used high-resolution details of the binding orientations of NAbs encoded by the *VH1-2*, *VH1-46*, *VH3-30*, *VH3-53*, *VH4-34* and *VH5-51* gene segments to determine rules for binding by four distinct anti-RBD antibody classes (Supplementary Table 2). The NAbs chosen for structures are highly potent, achieving 90% neutralization in pseudotype virus assays at concentrations ranging from 22 to 140 ng ml<sup>-1</sup> (ref. 5), and thus our structural analyses and classifications directly relate to understanding mechanisms of neutralization and potency differences between human NAbs.

## Results & Discussion

### Class 1 VH3-53 NAbs block ACE2 and bind to up RBDs

We solved Fab and Fab–RBD crystal structures of C102 (Supplementary Table 1), which we compared to our previous<sup>26</sup> cryo-electron microscopy (cryo-EM) structure of S trimer complexed with the related human NAb C105 (Extended Data Figs. 1, 2). Both C102 and C105 are VH3-53 NAbs with short (11 and 12 residues, respectively) CDRH3 loops (Extended Data Fig. 1g) that were isolated from the same donor<sup>5</sup>. They share structural similarities with each other and with other *VH3-53*-encoded short CDRH3 human NAb structures solved as complexes with RBDs<sup>12,30,37,38</sup> (Extended Data Fig. 2a). Notably, the C102–RBD structure resembled the analogous portion of the C105–S structure<sup>26</sup> (Extended Data Fig. 2a). These results establish that Fab–RBD structures can reproduce interactions with RBDs in the context of an S trimer; however, Fab–RBD structures do not reveal the state(s) of the antibody-bound RBD in the complex (up versus down) or the potential interprotomer contacts by Fabs.

Because the C105 Fab bound to either two or three up RBDs on S with no observed interactions with down RBDs or with adjacent RBDs<sup>26</sup> (Extended Data Fig. 1f), we used the higher-resolution C102 Fab–RBD structure to deduce a more accurate epitope and paratope than was possible using the C105–S cryo-EM structure with flexible up RBDs (Extended

Data Fig. 1a–e). Buried surface area calculations showed that the C102 CDRH3 region had a relatively minor role in the paratope: of 1,045 Å<sup>2</sup> of buried surface area on the antibody (786 Å<sup>2</sup> on the heavy chain; 259 Å<sup>2</sup> on the light chain), CDRH3 accounted for only 254 Å<sup>2</sup> (Extended Data Fig. 2b). This contrasts with most antibodies in which CDRH3 contributes equally or more to the interface with antigen than the sum of CDRH1 and CDRH2 contributions<sup>39</sup>. The epitopes on RBD for all available *VH3-53*-encoded short CDRH3 human NAbs span the ACE2-binding site<sup>15,26,28,30,31</sup> and show common RBD-binding interactions, represented by the C102 epitope (Extended Data Fig. 1b–e), which buried 1,017 Å<sup>2</sup> on RBD (Extended Data Fig. 2b). The ACE2-blocking epitope for these NAbs is sterically occluded in the RBD down conformation (Fig. 1b, Extended Data Fig. 1f); therefore, class 1 NAbs can only bind to up RBDs, as observed in the C105–S structure<sup>26</sup>, and as previously discussed, IgGs in this class could crosslink adjacent RBDs within a single trimer to achieve tighter binding through avidity effects<sup>26</sup>.

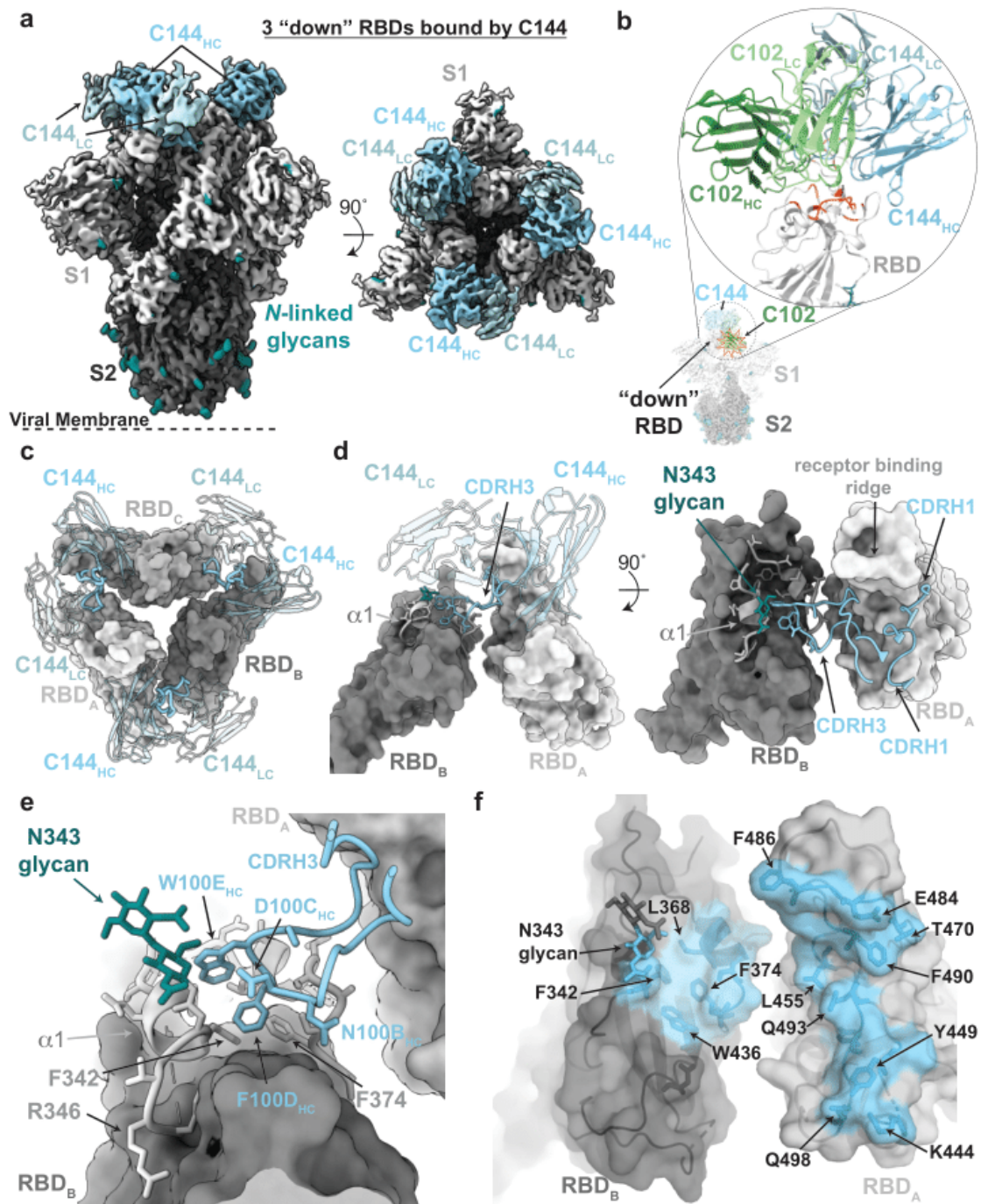


**Figure 1: Cryo-EM structure of the C144–S complex illustrates a distinct VH3-53 NAb binding mode.** **a**, 3.2 Å cryo-EM density for the C144–S trimer complex revealing C144 binding to a closed (three down RBDs) spike conformation. LC, light chain; HC, heavy chain. **b**, Overlay of C102 Fab (from C102–RBD crystal structure) (Extended Data Fig. 1) and C144 Fab (from C144–S structure) aligned on a RBD monomer. RBD residues

corresponding to the ACE2 epitope (orange-red cartoon) are shown on the same RBD for reference. C144 adopts a distinct conformation relative to the C102-like *VH3-53*-encoded short CDRH3 NAb class, allowing binding to the down RBD conformation on trimeric spike, whereas C102-like NAb can only bind to up RBDs. **c**, Quaternary epitope of C144 involving bridging between adjacent RBDs via the CDRH3 loop (illustrated as thicker ribbon). **d, e**, Close-up view of CDRH3-mediated contacts on adjacent protomer RBD (dark grey). C144 CDRH3 residues F100<sub>D</sub> and W100<sub>E</sub> are buried in a hydrophobic pocket comprising the RBD  $\alpha$ 1 helix, residue F374<sub>RBD</sub> and the N343<sub>RBD</sub> glycan. **f**, Surface representation of C144 epitope (light blue) across two adjacent RBDs. RBD epitope residues (defined as residues containing atom(s) within 4 Å of a Fab atom) are labelled in black.

### **Class 2 NAb recognize ‘up’ and ‘down’ RBDs**

In addition to the recurrent *VH3-53*-encoded short CDRH3 NAb structures, a small subset of potentially neutralizing *VH3-53*-encoded antibodies use longer CDRH3 regions<sup>5, 12</sup> (more than 15 residues, IMGT definition<sup>32</sup>) (Extended Data Fig. 1g). A recent structure of a RBD complexed with a *VH3-53*-encoded long CDRH3 human NAb (COVA2-39) revealed a different RBD binding mode<sup>38</sup>, thus confirming predictions that binding with a C102-like interaction requires a short CDRH3<sup>26,30</sup>. To further determine molecular mechanisms for binding of *VH3-53*-encoded long CDRH3 human NAb, we solved a 3.2 Å cryo-EM structure of C144 (encoded by the *VH3-53* and *VL2-14* gene segments; 25-residue CDRH3) bound to an S trimer<sup>36</sup> (Extended Data Fig. 3). Despite the ability of ligand-free stabilized S trimers to adopt up RBD conformations<sup>36</sup> and modelling suggesting the C144 binding site would be accessible on up RBDs (Fig. 1b), the C144–S structure revealed three C144 Fabs bound to a completely closed S with three down RBDs (Fig. 1a). The C144 binding mode differs from class 1 NAb, the binding orientation of which is incompatible with down RBD conformations (Fig. 1b). In addition, the binding orientation observed for C144 differs from the binding described for COVA2-39, the RBD epitope of which is predicted to be accessible only on up RBDs<sup>38</sup> owing to steric hinderances imposed on the light chain by the N343<sub>RBD</sub>-associated glycan on the adjacent RBD (Extended Data Fig. 1h). Despite differences in orientation, the RBD epitopes of C144, C102 and COVA2-39 overlap with the ACE2-binding site, which suggests a neutralization mechanism that involves direct competition with ACE2 (Fig. 1b).

Despite overlapping with the ACE2-binding site on up RBDs, an interesting feature of C144 binding is that its long CDRH3 bridges between adjacent down RBDs to lock the spike glycoprotein into a closed, prefusion conformation, providing an additional neutralization mechanism in which S cannot open to engage ACE2 (Fig. 1c, d). The formation of the C144 quaternary epitope is driven by sandwiching CDRH3 residues F100<sub>D</sub> and W100<sub>E</sub> (in which subscripts denote numbering of the CDRH3 loop) into a hydrophobic RBD cavity at the base of an *N*-linked glycan attached to N343<sub>RBD</sub>. The cavity comprises the RBD  $\alpha$ 1 helix (337–344),  $\alpha$ 2 helix (364–371), and hydrophobic residues (F374<sub>RBD</sub> and W436<sub>RBD</sub>) at the edge of the RBD five-stranded  $\beta$ -sheet (Fig. 1e, f). In contrast to the CDRH3s of class 1 *VH3-53*-encoded short CDRH3 NAbs, the C144 CDRH3 contributed to most (approximately 60%) of the paratope and buried 330 Å<sup>2</sup> of surface area on the adjacent RBD (Extended Data Fig. 2b), rationalizing observed escape at L455<sub>RBD</sub> (Fig. 1f) in C144 selection experiments<sup>40</sup>. Despite adjacent CDRH3 hydrophobic residues (F100<sub>D</sub> and W100<sub>E</sub>) likely to be solvent-exposed before antigen binding, C144 IgG showed no evidence of non-specific binding in a polyreactivity assay (Extended Data Fig. 1i).

Given the unusual binding characteristics of C144, we investigated whether antibodies that showed similar S binding orientations in low-resolution negative-stain electron microscopy reconstructions<sup>5</sup> use similar neutralization mechanisms. We characterized Fab–S cryo-EM structures (overall resolutions from 3.4 to 3.8 Å) of potent NAbs (C002, C104, C119 and C121) predicted to compete with ACE2 binding<sup>5</sup>, which varied in their use of V gene segments and CDRH3 lengths (Fig. 2, Extended Data Figs. 3, 4, Extended Data Table 1). Fab–S cryo-EM structures of these class 2 NAbs showed bound RBDs in both up or down conformations, consistent with observations of similar human NAbs from negative-stain electron microscopy<sup>5,12</sup> and single-particle cryo-EM studies<sup>10,34,41</sup>. By contrast, the C144–S structure showed Fabs bound only to down RBDs (Fig. 1), which suggests that C144 binding requires recognition of the closed S trimer, or that C144 Fab(s) initially bound to up RBD(s) could trap the closed (three RBDs down) S conformation through CDRH3-mediated interactions between adjacent RBDs.

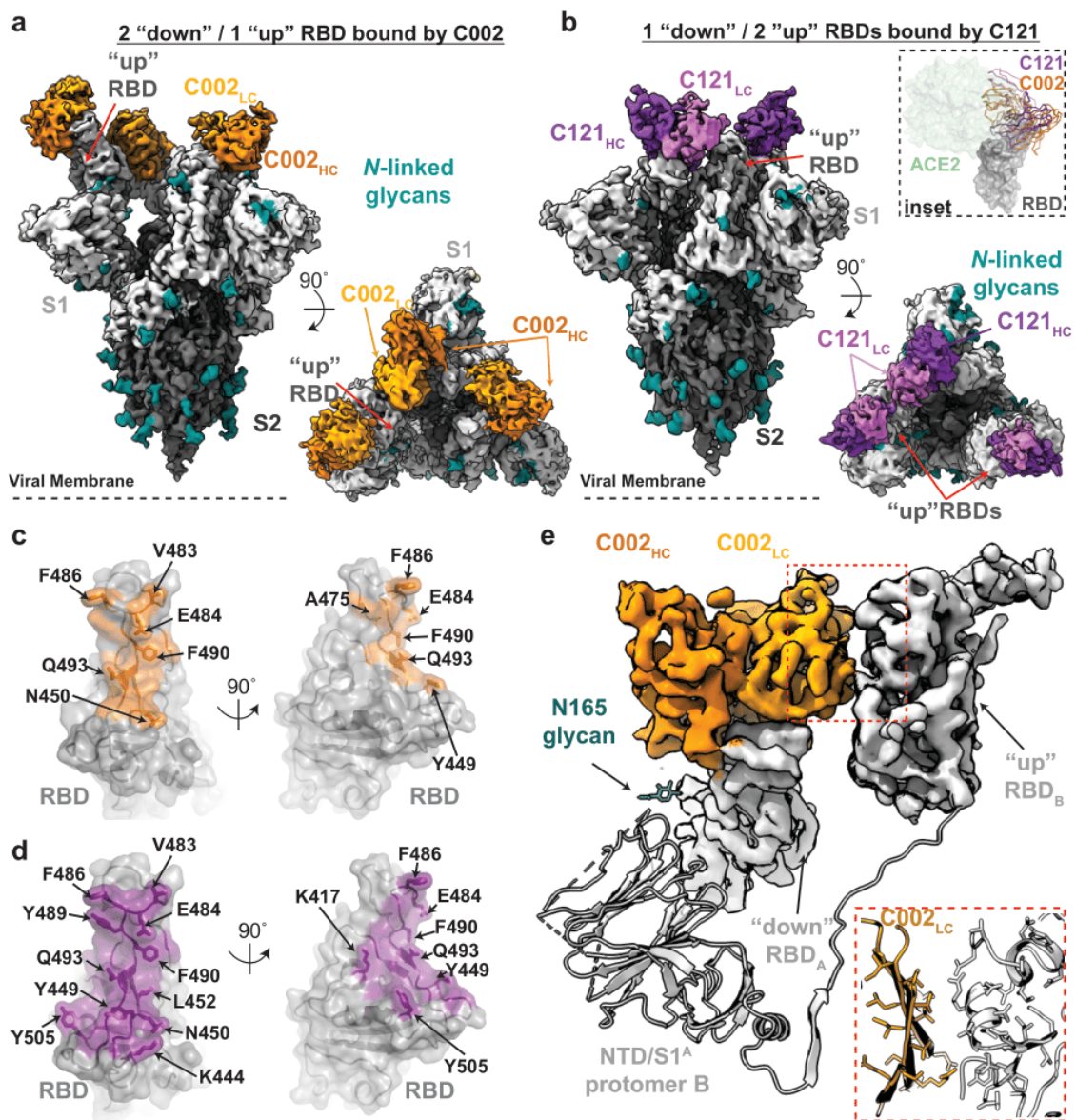


**Figure 2. Cryo-EM structures of class 2 C002 and C121 NABs show binding to up and down RBDs.** **a, b**, Cryo-EM densities for C002–S (**a**; 3.4 Å) and C121–S (**b**; 3.7 Å) complexes, revealing binding of C002 or C121 to both down and up RBDs. Inset, alignment of C002 and C121 Fabs on the same RBD. ACE2 is represented as a green surface for reference. **c, d**, Surface representations of C002 epitope (orange, **c**) and C121 epitope (purple, **d**) on the RBD surface (grey). RBD epitope residues (defined as residues containing atom(s) within 4 Å of a Fab atom) are labelled in black. **e**, C002 forms inter-protomer contacts via binding to an adjacent up RBD conformation on the surface of the trimer spike (also observed for class 2 C121–S, C119–S and C104–S structures) (Extended Data Fig. 5). Red box shows close-up of adjacent up RBD and C002 light-chain interface.

To understand commonalities of class 2 RBD epitopes better, we further analysed two additional potent human NAbs, C002 (encoded by *VH3-30* and *VK1-39* gene segments; 17-residue CDRH3, half-maximal inhibitory concentration ( $IC_{50}$ ) = 8.0 ng ml<sup>-1</sup>)<sup>5</sup> and C121 (encoded by *VH1-2* and *VL2-23* gene segments; 23-residue CDRH3,  $IC_{50}$  = 6.7 ng ml<sup>-1</sup>)<sup>5</sup>, for which cryo-EM Fab–S structures were solved to 3.4 Å and 3.6 Å, respectively (Fig. 2a, b), using crystal structures of unbound C002 and C121 Fabs for fitting (Supplementary Table 1). The C002 and C121 RBD epitopes are focused on the receptor-binding ridge, overlapping with polar and hydrophobic residues along the flat face of the RBD responsible for ACE2 interactions (Fig. 2c–e). Similar to C144, NAbs C002 and C121 buried most of their RBD epitopes against heavy-chain CDR loops, with light-chain CDR loops engaging the receptor-binding ridge (Fig. 3). Notably, Fab–S structures of C002, C121, C119 and C104 revealed a quaternary epitope involving an adjacent RBD (Extended Data Figs. 3, 4, 5a–c), albeit distinct from the quaternary binding of C144 (Fig. 1c–e). The C002/C121/C119/C104 type of secondary interaction was only observed when a Fab was bound to a down RBD and adjacent to an up RBD. The extent of secondary interactions varied depending on the antibody pose (Extended Data Fig. 5a–c). Bridging interactions between adjacent up and down RBDs would not allow the two Fabs of a single IgG to bind simultaneously to an S trimer. However, this class of antibodies could support bivalent interactions between two adjacent down RBDs (Extended Data Fig. 5h, Extended Data Table 1).

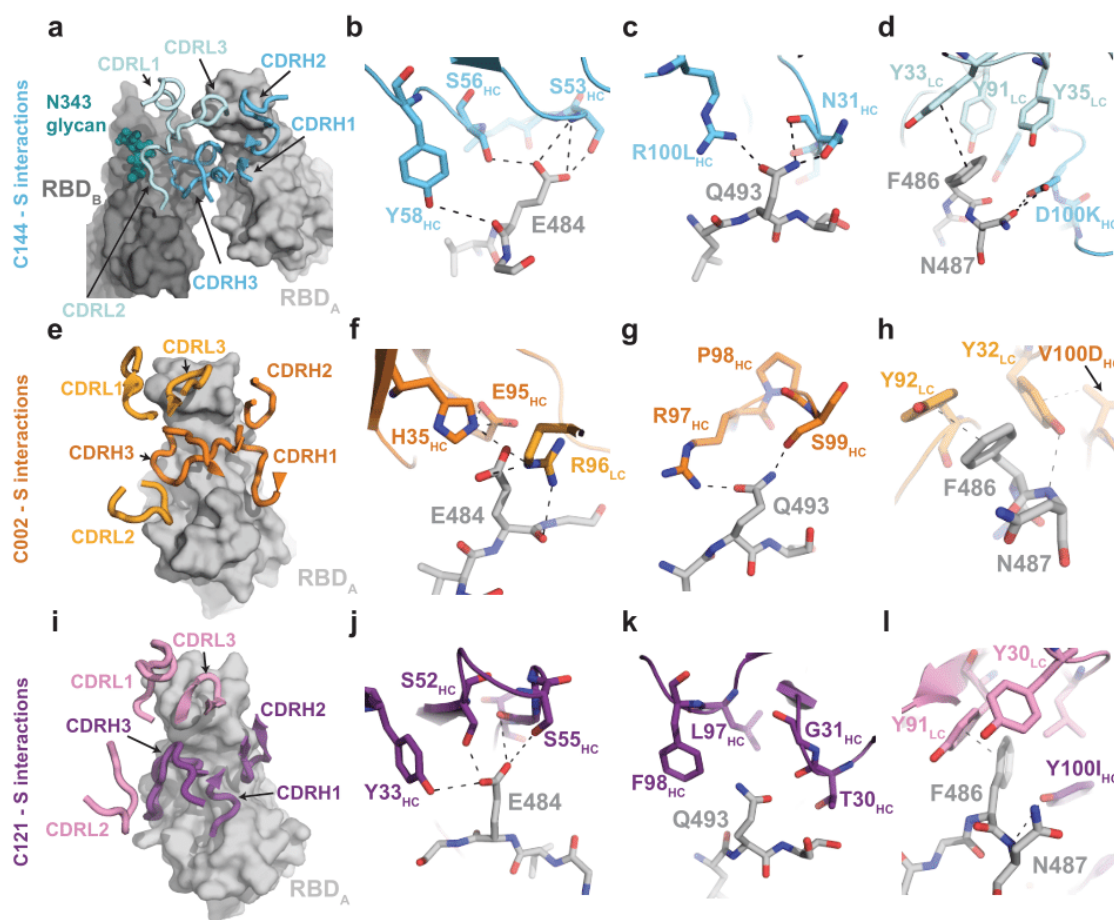


**Figure 3. Details of common RBD interactions among class 2 human NABs.** a–l, Conserved interactions between the RBD and CDRs of class 2 NABs as observed for C144 (HC, cyan; LC, sky blue) (a–d), C002 (HC, dark orange; LC, light orange) (e–h), and C121 (HC, purple; LC, pink) (i–l). Primary and secondary epitopes on adjacent down RBDs are shown for C144. Secondary epitopes for C002 and C121, which require adjacent up RBDs, are shown in Extended Data Fig. 5. RBDs are grey; potential hydrogen bonds and  $\pi$ - $\pi$  stacking interactions (d, Y33<sub>LC</sub> and F486<sub>RBD</sub>; h, Y92<sub>LC</sub> and F486<sub>RBD</sub>; l, Y91<sub>LC</sub> and F486<sub>RBD</sub>) are indicated by dashed lines.

Characterization of the highest resolution interface (C002–S structure) showed C002 light-chain framework regions 1 and 2 (FWR1 and FWR2) interfaced with the RBD residues comprising the five-stranded  $\beta$ -sheet and  $\alpha$ -helix that spans residues 440–444 (Fig. 2e), which is typically located near the three-fold axis of a closed S trimer. In addition to contacting neighbouring RBDs, inter-protomer engagement with the N165<sub>NTD</sub>-associated glycan in the N-terminal domain (NTD) was observed for the class 2 NAB BD23<sup>13</sup>. If fully

processed, the N165<sub>NTD</sub> glycan could adopt a conformation that would allow interactions with the heavy-chain FWR3 and CDRH1 (Fig. 2e). However, in the structures reported here, we did not observe N165<sub>NTD</sub> glycan density beyond the initial *N*-acetylglucosamine.

Given differences in class 2 human NAb V gene segments, CDRH3 lengths and antibody poses, we investigated sequence features that drive conserved interactions. Sequence differences between SARS-CoV-2 and SARS-CoV RBD, including at positions 486<sub>RBD</sub> and 493<sub>RBD</sub> (F and Q, respectively, in SARS-CoV-2), in the ACE2 receptor-binding motif allowed more favourable ACE2 binding to the SARS-CoV-2 RBD<sup>42</sup>. Analysis of interactions by C144, C002 and C121 revealed common interactions with these residues and also for E484<sub>RBD</sub> by both antibody heavy-chain and light-chain residues (Fig. 3). In particular, class 2 NAb interactions with F486<sub>RBD</sub> mimicked ACE2 interactions, in that F486<sub>RBD</sub> buries into a hydrophobic pocket typically involving CDRL1 or CDRL3 tyrosine residues<sup>43</sup> (Fig. 3d, h, l). Mimicking of the ACE2 F486 binding pocket by SARS-CoV-2 human NABs was observed across different light-chain V gene segments (Extended Data Table 1), which suggests that there is no restriction in light-chain V gene segment usage for class 2 NABs. Notably, a germline-encoded feature described for *VH3-53*-encoded short CDRH3 class 1 NABs, the CDRH2 SXXS motif, is also found in other class 2 NABs (for example, C121 and C119) despite different VH gene segment usage. Similar to *VH3-53* NABs C144 and COVA2-39, the C121 CDRH2 SXXS motif forms a potential hydrogen-bond network with E484<sub>RBD</sub> (Fig. 3b, j).

Overall, these results suggest a convergent mode of recognition by germline-encoded residues across diverse VH/VL gene segments for SARS-CoV-2, which may contribute to low levels of somatic hypermutation observed for these human NABs (Extended Data Fig. 4i–n, Extended Data Table 1).

### **Class 3 NABs bind outside the ACE2-binding site**

C135 is a potent NAB that showed distinct binding properties from class 1, 2 and 4 NABs, the latter of which bind a highly conserved buried epitope that is only accessible in up RBD

conformations (Extended Data Table 1). To evaluate the mechanism of C135-mediated neutralization of SARS-CoV-2, we solved the cryo-EM structure of a C135–S complex to 3.5 Å (Fig. 4a, Extended Data Fig. 6), using an unbound C135 crystal structure for fitting (Supplementary Table 1). The structure revealed three C135 Fabs bound to an S trimer with two down and one up RBD, although the C135-bound up RBD conformation was weakly resolved and therefore not modelled. C135 recognizes a similar glycopeptidic epitope to the cross-reactive SARS-CoV NAb S309<sup>34</sup>, focusing on a region of the RBD near the N343 glycan and non-overlapping with the ACE2-binding site (Fig. 4b, Extended Data Fig. 6c, d). Despite differences in binding orientations between C135 and S309, targeting of the RBD epitope was mainly VH-mediated (the surface area buried by RBD on the C135 heavy chain represented approximately 480 Å<sup>2</sup> of the 700 Å<sup>2</sup> total buried surface area) and included interactions with the core fucose moiety of the N343<sub>RBD</sub> glycan. The smaller C135 footprint relative to S309 (approximately 700 Å<sup>2</sup> versus 1,150 Å<sup>2</sup> buried surface area, respectively) (Extended Data Fig. 6c, d) focused on interactions with R346<sub>RBD</sub> and N440<sub>RBD</sub>, which are engaged by residues from heavy-chain and light-chain CDRs (Fig. 4c, d) and are not conserved between SARS-CoV-2 and SARS-CoV RBDs, rationalizing the lack of SARS-CoV cross-reactivity observed for C135<sup>5</sup>.

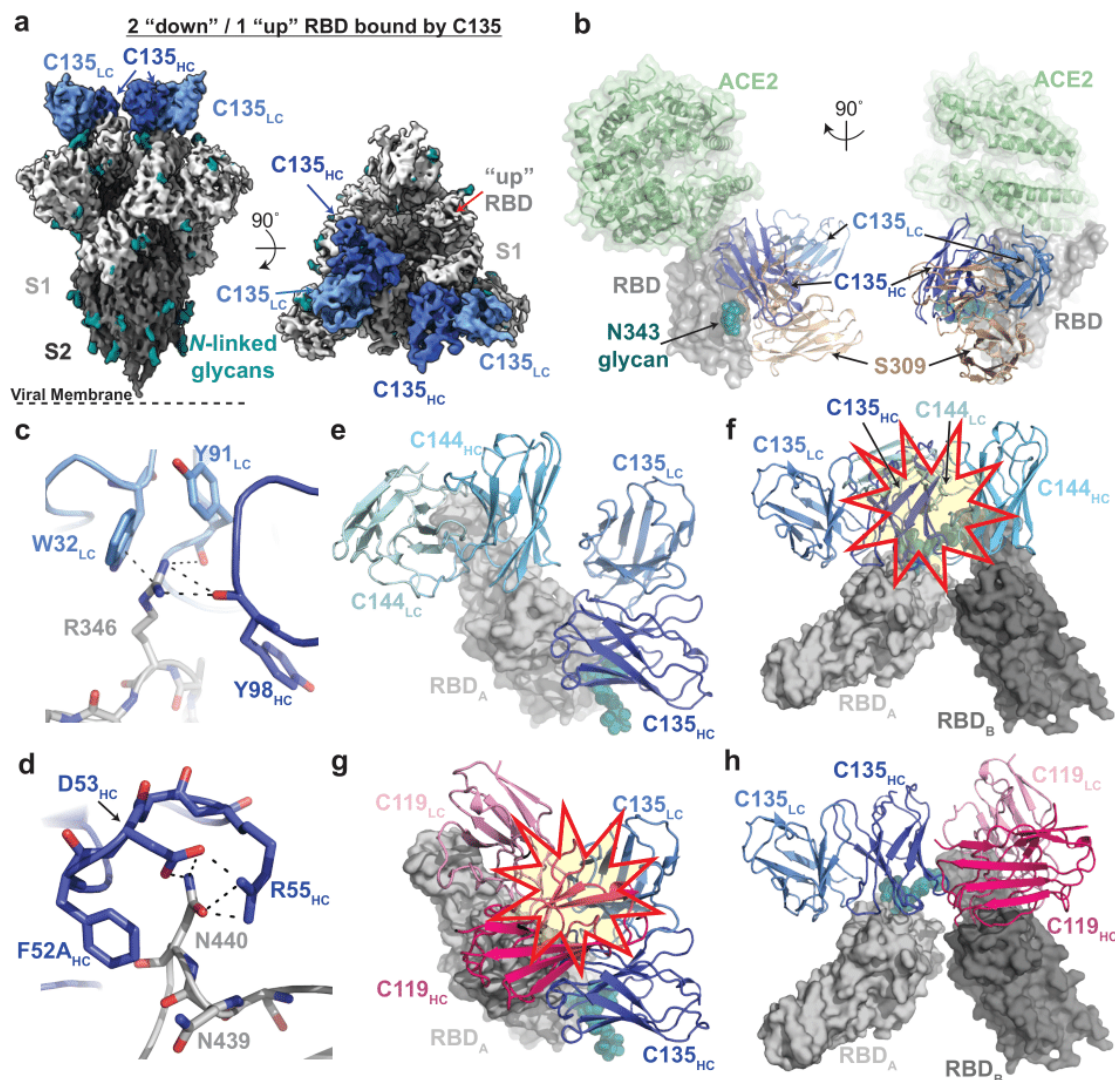


**Figure 4. Cryo-EM structure of S complexed with the class 3 (non-ACE2 blocking) human NAb C135.** **a**, 3.5 Å cryo-EM density of C135–S complex. **b**, Composite model of C135–RBD (blue and grey, respectively) overlaid with the SARS-CoV-2 NAb S309 (sand; PDB code 6WPS) and soluble ACE2 (green; PDB code 6M0J). The model was generated by aligning on 188 RBD C $\alpha$  atoms. **c**, **d**, C135 CDRH (dark blue) and CDRL (light blue) interactions with R346<sub>RBD</sub> (**c**) and N440<sub>RBD</sub> (**d**). Potential  $\pi$ – $\pi$  stacking interactions (**c**) and hydrogen bonds (**c**, **d**) are illustrated by dashed black lines. **e**, **f**, Model of RBD interactions of NAb C135 (class 3) and C144 (class 2), demonstrating that both Fabs can bind simultaneously to a single monomeric RBD (**e**), but would clash if bound to adjacent down RBDs on S trimer (**f**). Steric clashes indicated by a red and yellow star in **f**. **g**, **h**, Model of RBD interaction of NAb C135 (class 3) and C119 (class 2) demonstrating that both Fabs cannot bind simultaneously to a single monomeric RBD (**g**), but do not clash if bound to adjacent down RBDs on S trimer (**h**). Steric clashes indicated by a red and yellow star in **g**.

The discovery of class 3 NAbs such as C135 and S309 that were raised during SARS-CoV-2 or SARS-CoV natural infections, respectively, and bind outside of the ACE2-binding site, provides the potential for additive neutralization effects when combined with NAbs that block ACE2, while also limiting viral escape<sup>1,40</sup>. A pair of antibodies in human clinical trials that includes REGN10987<sup>8</sup>, a human NAb that binds distal to the ACE2-binding site, prevented SARS-CoV-2 viral escape in vitro, but did not show synergistic neutralization<sup>6</sup>. Comparison of C135 and REGN10987 interactions with S showed similarities in epitopes (interactions focused on R346<sub>RBD</sub> and N440<sub>RBD</sub>) (Extended Data Fig. 7c, f). However, REGN10987 binding would sterically hinder ACE2 interactions, whereas C135 binding does not (Fig. 4b, Extended Data Fig. 6b). Notably, a structure of S complexed with C110 (encoded by the *VH5-51* and *VK1-5* gene segments), isolated from the same donor as the C102 and C105 (class 1) and C119 and C121 (class 2) NAbs<sup>5</sup>, showed a binding pose that resembled that of REGN10987 (Extended Data Fig. 6b, e, f). The C110 epitope showed similarities with both class 3 and class 2 NAbs, binding distal to the ACE2-binding motif, but like REGN10987, could potentially sterically interfere with ACE2 (Extended Data Fig. 7). For each of these class 3 NAbs, the Fab binding pose suggests that inter-protomer crosslinking by a single IgG is not possible (Extended Data Table 1).

Class 3 human NAbs add to the anti-SARS-CoV-2 antibody repertoire and could probably be effectively used in therapeutic combinations with class 1 or 2 NAbs. However, when using structures to predict whether NAbs have overlapping epitopes, it is sometimes not sufficient to only examine Fab–RBD structures or even static images of the S trimer because of the dynamic nature of the spike. Thus, what might appear to be non-overlapping epitopes on an isolated RBD could overlap in some (Fig. 4e, f), but not all (Extended Data Fig. 7), scenarios on a spike trimer, complicating interpretation of competition experiments using monomeric RBDs and S trimers. The opposite can also be true; that is, two Fabs predicted to be accommodated on a trimer could clash on an RBD monomer (Fig. 4g, h). Finally, adjacent monomers in different orientations could accommodate different antibodies that target overlapping sites (Extended Data Fig. 7).

### **RBD substitutions affect NAb binding**

Vesicular stomatitis virus (VSV) reporter viruses pseudotyped with the SARS-CoV-2 S protein can escape by mutation(s) from the C121, C135 or C144 NAbs<sup>40</sup> that we used for structural studies. RBD mutations that were selected in response to antibody pressure correlated with the epitopes mapped from the structures of their Fabs complexed with the S trimer (Figs. 1, 2, 4).

To further assess the effects of these mutations and other RBD substitutions, we assayed NAbs for which we obtained structural information (eight from this study; C105–S complex previously described<sup>26</sup>) for binding to mutated RBD proteins. The RBD mutants included two that induced escape from the class 3 hNAb C135 (R346S and N440K)<sup>40</sup> (Fig. 4c, d), one found in circulating isolates<sup>44</sup> that conferred partial resistance to C135 (N439K)<sup>40</sup> (Fig. 4d), a circulating variant (A475V) that conferred resistance to class 1 and 2 VH3-53 NAbs<sup>44</sup>, two that induced escape from C121 or C144 (E484K and Q493R)<sup>40</sup> (Fig. 3), and a circulating variant that conferred partial resistance to C121 (V483A)<sup>40</sup>. Kinetic and equilibrium constants for the original and mutant RBDs were derived from surface plasmon resonance (SPR) binding assays in which RBDs were injected over immobilized IgGs. Loss of binding affinity was consistent with RBD mutations that conferred escape (Extended Data Fig. 8). Comparing effects of point mutations between NAb classes showed that point mutations leading to a loss of binding for NAbs within one class did not affect NAbs in a different class, indicating that antibody pressure that leads to escape from one NAb class would be unlikely to affect a different class. These results suggest a therapeutic strategy involving human NAbs of different classes for monoclonal NAb treatment of individuals infected with SARS-CoV-2.

### **Conclusions**

Here we report structural, biophysical and bioinformatics analyses of SARS-CoV-2 NAbs (Extended Data Fig. 9), providing information for interpreting correlates of protection for clinical use. The structures reveal a wealth of unexpected interactions of NAbs with the spike protein, including five antibodies that reach between adjacent RBDs on the protomers of a

single trimer. A notable example of bridging between spike protomers involved the human C144 NAb that uses a long CDRH3 with a hydrophobic tip to reach across to an adjacent RBD, resulting in all three RBDs on the spike trimer being locked into a closed conformation. This example, and four other NAb that contact adjacent RBDs, demonstrates that crystal structures of Fab–monomeric RBD complexes, although informative for defining primary epitopes on one RBD, do not reveal how antibodies recognize the flexible up or down RBD conformations on the spike trimer that are targeted for neutralization on a virus. Indeed, our cryo-EM structures of Fab–spike trimer complexes showed all possible up and down combinations of recognized RBDs, with structures showing either three or two Fabs bound per trimer. By analysing approach angles of Fabs bound to RBDs on spike trimers, we predicted whether an IgG can bind to a single spike trimer to gain potency through avidity, which would also render the antibody more resistant to spike mutations. In addition, structural information allowed us to assess RBD mutants that arose in circulating viral isolates and/or were obtained by in vitro selection. Together, this study provides a blueprint for the design of antibody cocktails for therapeutic agents and potential spike-based immunogens for vaccines.

## **Methods**

No statistical methods were used to predetermine sample size. The experiments were not randomized, and investigators were not blinded to allocation during experiments and outcome assessment.

### **Cell lines**

Expi293F cells (GIBCO) for protein expression were maintained at 37 °C and 8% CO<sub>2</sub> in Expi293 Expression medium (GIBCO), transfected using Expi293 Expression System Kit (GIBCO) and maintained under shaking at 130 rpm. Cell lines were not specifically authenticated, but lines tested negative for contamination with mycoplasma.

### Protein expression

Expression and purification of SARS-CoV-2 ectodomains were conducted as previously described<sup>26</sup>. In brief, constructs encoded the SARS-CoV-2 S ectodomain (residues 16–1206 of the early SARS-CoV-2 GenBank MN985325.1 sequence isolate with 2P<sup>35</sup> or 6P<sup>36</sup> stabilizing mutations, a mutated furin cleavage site between S1 and S2, a C-terminal TEV site, foldon trimerization motif, octa-His tag, and AviTag) were used to express soluble SARS-CoV-2 S ectodomains. Constructs encoding the SARS-CoV-2 RBD from GenBank MN985325.1 (residues 331–524 with C-terminal octa-His tag and AviTag) and mutant RBDs were made as described<sup>26</sup>, SARS-CoV-2 2P S, 6P S, and RBD proteins were purified from the supernatants of transiently transfected Expi293F cells (Gibco) by nickel affinity and size-exclusion chromatography<sup>26</sup>. Peak fractions were identified by SDS–PAGE, and fractions corresponding to S trimers or monomeric RBDs were pooled and stored at 4 °C. Fabs and IgGs were expressed, purified, and stored as previously described<sup>45,46</sup>.

### X-ray crystallography

Crystallization trials were carried out at room temperature using the sitting drop vapour diffusion method by mixing equal volumes of a Fab or Fab–RBD complex and reservoir using a TTP LabTech Mosquito robot and commercially available screens (Hampton Research). Crystals were obtained in 0.2 M ammonium sulfate, 20% (w/v) PEG 3350 (C102 Fab), 0.2 M sodium citrate tribasic, 20% (w/v) PEG 3350 (C102–RBD), 0.2 M lithium sulfate monohydrate, 20% (w/v) PEG 3350 (C002 Fab), 0.04 M potassium phosphate, 16% (w/v) PEG 8000, 20% (v/v) glycerol (C135 Fab), 0.2 M ammonium citrate pH 5.1, 20% PEG 3350 (C121 Fab), or 0.2 M sodium tartrate dibasic dihydrate pH 7.3, 20% (w/v) PEG 3350 (C110 Fab). A C135 Fab crystal was directly looped and cryopreserved in liquid nitrogen. Other crystals were quickly cryoprotected in a mixture of well solution with 20% glycerol and then cryopreserved in liquid nitrogen.

X-ray diffraction data were collected for Fabs and the Fab–RBD complex at the Stanford Synchrotron Radiation Lightsource (SSRL) beamline 12-1 on a Eiger X 16 M pixel detector (Dectris) at a wavelength of 1.0 Å. Data from single crystals of C121 Fab and C110 Fab were

indexed and integrated in XDS<sup>47</sup> and merged using AIMLESS v.0.7.4 in CCP4<sup>48</sup> v.7.0.6 (Supplementary Table 1). Data from single crystals of C102 Fab, C135 Fab and C002 Fab were indexed and integrated using XDS<sup>47</sup> and merged in Phenix<sup>49</sup> (v.1.18). Data from a single crystal of C102 Fab–RBD complex were indexed and integrated using XIA2<sup>50</sup> v.0.3.8 implementing DIALS<sup>51,52</sup> v.2.2 and merged using AIMLESS in CCP4<sup>48</sup>. For C110 Fab and C121 Fabs, structures were determined by molecular replacement in PHASER<sup>53</sup> v.2.8.2 using the coordinates for B38 (PDB 7BZ5) or an inferred germline form of the HIV-1 NAb IOMA<sup>54</sup> inferred germline (unpublished), respectively, after removing CDR loops as a search model. For C002 Fab, C102 Fab, C102 Fab–RBD and C135 Fab, structures were determined by molecular replacement in PHASER<sup>53</sup> using B38 Fab coordinates (PDB 7BZ5) after trimming heavy and light chain variable domains using Sculptor<sup>55</sup> v.2.0 (and for the C102 Fab–RBD data, also RBD coordinates from PDB code 7BZ5) as search models. Coordinates were refined using Phenix<sup>49</sup> and cycles of manual building in Coot<sup>56</sup> (Supplementary Table 1).

#### Cryo-EM sample preparation

Purified Fabs were mixed with the SARS-CoV-2 S 2P trimer<sup>35</sup> or SARS-CoV-2 S 6P trimer<sup>36</sup> (1.1:1 molar ratio Fab per protomer) to a final Fab–S complex concentration of 2–3 mg ml<sup>-1</sup> and incubated on ice for 30 min. Immediately before deposition of 3 µl of complex onto a 300 mesh, 1.2/1.3 UltrAuFoil grid (Electron Microscopy Sciences) that had been freshly glow-discharged for 1 min at 20 mA using a PELCO easiGLOW (Ted Pella), a 0.5% (w/v) octyl-maltoside, fluorinated solution (Anatrace) was added to each sample to a final concentration of 0.02%. Samples were vitrified in 100% liquid ethane using a Mark IV Vitrobot (Thermo Fisher) after blotting at 22 °C and 100% humidity for 3 s with Whatman No. 1 filter paper.

#### Cryo-EM data collection and processing

Single-particle cryo-EM data were collected on a Titan Krios transmission electron microscope (Thermo Fisher) operating at 300 kV for all Fab–S complexes except for C144–S, which was collected on a Talos Arctica (Thermo Fisher) operating at 200 kV. Movies

were collected using SerialEM v.3.7 automated data collection software<sup>57</sup> with beam-image shift over a 3-by-3 pattern of 1.2  $\mu\text{m}$  holes with 1 exposure per hole. Movies were recorded in super-resolution mode on a K3 camera (Gatan) for the C144–S dataset on the Arctica (0.435 $\text{\AA}$  per pixel) or on a K3 behind BioQuantum energy filter (Gatan) with a 20 eV slit on the Krios (0.418  $\text{\AA}$  per pixel) for all other datasets. Data collections parameters are summarized in Supplementary Table 2. In general, the data processing workflow described below was performed for all datasets in cryoSPARC v.2.15<sup>58</sup>.

Cryo-EM movies were patch motion corrected for beam-induced motion including dose weighting within cryoSPARC<sup>58</sup> after binning super-resolution movies. The non-dose-weighted images were used to estimate CTF parameters using CTFFIND4<sup>59</sup> v.4.1.14 or with cryoSPARC implementation of the Patch CTF job, and micrographs with power spectra that showed poor CTF fits or signs of crystalline ice were discarded. A subset of images were randomly selected and used for reference-free particle picking using Blob picker in cryoSPARC<sup>58</sup>. Particles were subjected to 2D classification and the best class averages that represented different views were used to generate 3 ab initio models. The particles from the best classes were used in another 2D classification job, and the best set of unique views was used as templates for particle picking on the full set of images. Initial particle stacks were extracted, downsampled twice, and used in heterogeneous refinement against the three ab initio volumes generated with the smaller dataset (ab initio volumes used were interpreted as a Fab–S complex, free Fab or dissociated S protomers, and junk/noise class). Particles assigned to the Fab–S volume were further cleaned via iterative rounds of 2D classification to select class averages that displayed unique views and secondary structural elements. Resulting particle stacks were homogeneously refined before being split into nine individual exposure groups based upon collection holes. Per particle CTF and aberration corrections were performed and the resulting particles further 3D refined. Additional processing details are summarized in Supplementary Table 2.

Given the known heterogeneity of spike trimers<sup>20,21</sup>, homogeneously refined particles were used for 3D classification in cryoSPARC<sup>58</sup> (ab initio job:  $k = 4$  classes, class

similarity = 0.3). This typically resulted in one or two majority Fab–S complexes, with the other minority populated classes representing junk or unbound S trimer. Particles from the good class(es) were further subjected to 3D classification (ab initio job:  $k = 4$ , class similarity = 0.7) to attempt to separate various Fab–S complex states. If several states were identified (as observed for the C002–S and C121–S complexes), particles were heterogeneously refined, followed by re-extraction without binning (0.836 Å per pixel) before homogeneous refinement of individual states. For all other datasets, most particles represented one state that was homogeneously refined after re-extraction without binning.

Particle stacks for individual states were non-uniformly refined with  $C1$  symmetry and a dynamic mask. To improve resolution at the Fab–RBD interfaces, volumes were segmented in Chimera<sup>60</sup> and the regions corresponding to the NTD and RBD domains of the S1 subunit and the Fab VH–VL domains were extracted and used to generate a soft mask (5-pixel extension, 10-pixel soft cosine edge). Local refinements with the mask resulted in modest improvements of the Fab–RBD interface, which allowed for fitting and refinement of this region. The particles were then subjected to CTF refinement and aberration correction, followed by a focused, non-uniform refinement with polished particles imposing  $C1$  symmetry (except for the C144–S complex, in which  $C3$  symmetry was used). Final overall resolutions were according to the gold-standard FSC<sup>61</sup>. Details of overall resolution and locally refined resolutions according to the gold-standard FSC<sup>61</sup> can be found in Supplementary Table 2.

#### Cryo-EM structure modelling and refinement

Coordinates for initial complexes were generated by docking individual chains from reference structures into cryo-EM density using UCSF Chimera<sup>62</sup> v.1.13. The following coordinates were used: SARS-CoV-2 S trimers: PDB codes 6VXX, 6VYB and 6XKL, up RBD conformations: PDB codes 7BZ5 or 6W41, and unbound C102, C002, C110, C121, C135 Fab structures (this study) (Supplementary Table 1). Initial models were then refined into cryo-EM maps using one round of rigid body refinement followed by real space refinement. Sequence-updated models were built manually in Coot<sup>56</sup> v.0.8.9 and then refined

using iterative rounds of refinement in Coot<sup>56</sup> and Phenix<sup>49</sup>. Glycans were modelled at potential *N*-linked glycosylation sites in Coot<sup>56</sup> using ‘blurred’ maps processed with a variety of B-factors<sup>63</sup>. Validation of model coordinates was performed using MolProbity<sup>64</sup> (Supplementary Table 2).

### Structural analyses

CDR lengths were calculated based on IMGT definitions<sup>32</sup>. Structure figures were made with PyMOL (v.2.2 Schrodinger, LLC) or UCSF ChimeraX<sup>60</sup> v.1.0. Local resolution maps were calculated using cryoSPARC v.2.15<sup>58</sup>. Buried surface areas were calculated using PDBePISA v.1.48<sup>65</sup> and a 1.4 Å probe. Potential hydrogen bonds were assigned as interactions that were less than 4.0 Å and with an A-D-H angle above 90°. Potential van der Waals interactions between atoms were assigned as interactions that were less than 4.0 Å. Hydrogen bond and van der Waals interaction assignments are tentative due to resolution limitations. r.m.s.d. calculations following pairwise C $\alpha$  alignments were done in PyMOL without rejecting outliers. Criteria for epitope assignments are described in figure legends.

To evaluate whether intra-spike crosslinking by an IgG binding to a single spike trimer was possible (Extended Data Table 1), we first measured the C $\alpha$  distance between a pair of residues near the C termini of adjacent Fab CH1 domains (residue 222 of the heavy chain on each Fab) (Extended Data Fig. 5h). We compared this distance to the analogous distances in crystal structures of intact IgGs (42 Å, PDB code 1HZH; 48 Å, PDB code 1IGY; 52 Å, PDB code 1IGT). To account for potential influences of crystal packing in these measurements, as well as flexibility in the VH–VL/CH1–CL elbow bend angle and uncertainties in CH1–CL domain placement in Fab–S cryo-EM structures, we set a cut-off of  $\leq 65$  Å for this measured distance as possibly allowing for a single IgG to include both Fabs. Entries in the ‘potential IgG intra-spike binding’ column in Extended Data Table 1 are marked ‘no’ if all of the adjacent Fabs in cryo-EM classes of that structure are separated by more than 65 Å for this measured distance. Entries in the ‘potential IgG intra-spike binding’ column in Extended Data Table 1 are marked as ‘yes’ if at least one pair of the adjacent Fabs in cryo-EM classes of that structure are separated by  $\leq 65$  Å for this measured distance.

### SPR binding experiments

SPR experiments were performed using a Biacore T200 instrument (GE Healthcare). IgGs were immobilized on a CM5 chip by primary amine chemistry (Biacore manual) to a final response level of approximately 3,000 resonance units. Concentration series of the original SARS-CoV-2 RBD and RBD mutants (six fourfold dilutions starting from a top concentration of 1,000 nM) were injected at a flow rate of 30  $\mu\text{l min}^{-1}$  over immobilized IgGs for a contact time of 60 s, followed by an injection of 0.01 M HEPES, pH 7.4, 0.15 M NaCl, 3 mM EDTA, 0.005% (v/v) surfactant P20 buffer for a dissociation time of 300 s. Binding reactions were allowed to reach equilibrium, and  $K_d$  values were calculated from the ratio of association and dissociation rates ( $K_d = k_d/k_a$ ) derived from a 1:1 binding model (C002, C102, C105, C110 and C119 (except for C119 mutant E484K)), C121, C135 and C144), or from a two-state binding model ( $K_d = k_{d1}/k_{a1} \times k_{d2}/[k_{d2} + k_{a2}]$ ) (C104 and C119 mutant E484K). Kinetic constants were calculated using Biacore T200 Evaluation Software v.3.2 using a global fit to all curves in each dataset. Flow cells were regenerated with 10 mM glycine, pH 2.0, at a flow rate of 90  $\mu\text{l min}^{-1}$ .

### Polyreactivity assays

IgGs were evaluated for off-target interactions by measuring binding to baculovirus extracts containing non-specific proteins and lipids as described<sup>59</sup>. The assays were automated on a Tecan Evo2 liquid handling robot fitted with a Tecan Infinite M1000 plate reader capable of reading luminescence. Maxisorb 384-well plates (Nunc) were adsorbed overnight with a 1% preparation of recombinant baculovirus particles generated in Sf9 insect cells<sup>66</sup>. The adsorbed plate was blocked with 0.5% bovine serum albumin (BSA) in PBS, then incubated with 20  $\mu\text{l}$  of a 1.0  $\mu\text{g ml}^{-1}$  solution of IgG in PBS for 3 h. Polyreactivity was quantified by detecting bound IgG using an HRP-conjugated anti-human IgG secondary antibody (SouthernBiotech) at a 1:5,000 dilution and SuperSignal ELISA Femto Maximum Sensitivity Substrate (Thermo Scientific). RLUs were measured at 475 nm in the integrated plate reader. Engineered human anti-HIV-1 IgGs previously demonstrated to exhibit high levels of polyreactivity (NIH45-46(G54W) and 45-46m2)<sup>60,61</sup> were used as positive controls. NIH45-46, which exhibited intermediate polyreactivity<sup>62</sup>, was also evaluated for

comparisons. Negative control IgGs with low polyreactivity included the human HIV-1 antibodies N6<sup>63</sup> and 3BNC117<sup>62</sup> and BSA. RLU values were plotted in GraphPad Prism v8.4.3 and presented as the mean and standard deviation of triplicate measurements ( $n = 3$  biological replicates) with results for individual experiments shown as circles in Extended Data Fig. 1i.

### **Data availability**

The atomic models generated from X-ray crystallographic studies of the C102–RBD complex, C102 Fab, C002 Fab, C110 Fab, C121 Fab and C135 Fab have been deposited at the Protein Data Bank (PDB) under accession codes 7K8M, 7K8N, 7K8O, 7K8P, 7K8Q and 7K8R, respectively. The atomic models and cryo-EM maps generated from cryo-EM studies of the C002–S 2P (state 1), C002–S 2P (state 2), C104–S 2P, C110–S 2P, C119–S 2P, C121–S 2P (state 1), C121–S 2P (state 2), C135–S 2P and C144–S 6P complexes have been deposited at the PDB and the Electron Microscopy Data Bank (EMDB) under the following accession codes: PDB 7K8S, 7K8T, 7K8U, 7K8V, 7K8W, 7K8X, 7K8Y, 7K8Z and 7K90; EMD EMD-22729, EMD-22730, EMD-22731, EMD-22732, EMD-22733, EMD-22734, EMD-22735, EMD-22736 and EMD-22737.

### **Acknowledgements**

We thank J. Vielmetter, P. Hoffman, and the Protein Expression Center in the Beckman Institute at Caltech for expression assistance, J. Vielmetter and J. Keeffe for setting up automated polyreactivity assays, J. Keeffe for construct design, and N. Koranda for help with cloning and protein purification. Electron microscopy was performed in the Caltech Beckman Institute Resource Center for Transmission Electron Microscopy with assistance from S. Chen. We thank the Gordon and Betty Moore and Beckman Foundations for gifts to Caltech to support the Molecular Observatory (J. Kaiser, director), and S. Russi, A. Cohen and C. Smith and the beamline staff at SSRL for data collection assistance. Use of the Stanford Synchrotron Radiation Lightsource, SLAC National Accelerator Laboratory, is supported by the US Department of Energy, Office of Science, Office of Basic Energy

Sciences under contract no. DE-AC02-c76SF00515. The SSRL Structural Molecular Biology Program is supported by the DOE Office of Biological and Environmental Research, and by the National Institutes of Health, National Institute of General Medical Sciences (P41GM103393). The contents of this publication are solely the responsibility of the authors and do not necessarily represent the official views of NIGMS or NIH. This work was supported by NIH grant P01-AI138938-S1 (P.J.B. and M.C.N.), the Caltech Merkin Institute for Translational Research (P.J.B.), NIH grant P50 8 P50 AI150464-13 (P.J.B.), and a George Mason University Fast Grant (P.J.B.). C.O.B was supported by the Hanna Gray Fellowship Program from the Howard Hughes Medical Institute and the Postdoctoral Enrichment Program from the Burroughs Wellcome Fund. M.C.N. is a Howard Hughes Medical Institute Investigator.

## References

1. Baum, A. et al. REGN-COV2 antibody cocktail prevents and treats SARS-CoV-2 infection in rhesus macaques and hamsters. *Science*. <https://doi.org/10.1126/science.abe2402> (2020).
2. Baum, A. et al. Antibody cocktail to SARS-CoV-2 spike protein prevents rapid mutational escape seen with individual antibodies. *Science* **369**, 1014–1018 (2020).
3. Rogers, T. F. et al. Isolation of potent SARS-CoV-2 neutralizing antibodies and protection from disease in a small animal model. *Science* **369**, 956–963 (2020).
4. Zost, S. J. et al. Potently neutralizing and protective human antibodies against SARS-CoV-2. *Nature* **584**, 443–449 (2020).
5. Robbiani, D. F. et al. Convergent antibody responses to SARS-CoV-2 in convalescent individuals. *Nature* **584**, 437–442 (2020).
6. Hansen, J. et al. Studies in humanized mice and convalescent humans yield a SARS-CoV-2 antibody cocktail. *Science* **369**, 1010–1014 (2020).
7. US National Library of Medicine. A study of LY3819253 (LY-CoV555) in preventing SARS-CoV-2 infection and COVID-19 in nursing home residents and staff (BLAZE-2). ClinicalTrials.gov <https://clinicaltrials.gov/ct2/show/NCT04497987> (2020).
8. NIH. Clinical trials of monoclonal antibodies to prevent COVID-19 now enrolling. <https://www.nih.gov/news-events/news-releases/clinical-trials-monoclonal-antibodies-prevent-covid-19-now-enrolling> (2020).
9. Yuan, M. et al. A highly conserved cryptic epitope in the receptor binding domains of SARS-CoV-2 and SARS-CoV. *Science* **368**, 630–633 (2020).
10. Liu, L. et al. Potent neutralizing antibodies against multiple epitopes on SARS-CoV-2 spike. *Nature* **584**, 450–456 (2020).
11. Kreye, J. et al. A SARS-CoV-2 neutralizing antibody protects from lung pathology in a COVID-19 hamster model. Preprint at <https://doi.org/10.1101/2020.08.15.252320> (2020).
12. Brouwer, P. J. M. et al. Potent neutralizing antibodies from COVID-19 patients define multiple targets of vulnerability. *Science* **369**, 643–650 (2020).

13. Cao, Y. et al. Potent neutralizing antibodies against SARS-CoV-2 identified by high-throughput single-cell sequencing of convalescent patients' B cells. *Cell* **182**, 73–84 (2020).
14. Kreer, C. et al. Longitudinal isolation of potent near-germline SARS-CoV-2-neutralizing antibodies from COVID-19 patients. *Cell* **182**, 843–854 (2020).
15. Shi, R. et al. A human neutralizing antibody targets the receptor-binding site of SARS-CoV-2. *Nature* **584**, 120–124 (2020).
16. Zost, S. J. et al. Rapid isolation and profiling of a diverse panel of human monoclonal antibodies targeting the SARS-CoV-2 spike protein. *Nat. Med.* **26**, 1422–1427 (2020).
17. Seydoux, E. et al. Analysis of a SARS-CoV-2-infected individual reveals development of potent neutralizing antibodies with limited somatic mutation. *Immunity* **53**, 98–105 (2020).
18. Hoffmann, M. et al. SARS-CoV-2 cell entry depends on ACE2 and TMPRSS2 and is blocked by a clinically proven protease inhibitor. *Cell* **181**, 271–280 (2020).
19. Wang, Q. et al. Structural and functional basis of SARS-CoV-2 entry by using human ACE2. *Cell* **181**, 894–904 (2020).
20. Walls, A.C. et al. Structure, function, and antigenicity of the SARS-CoV-2 spike glycoprotein. *Cell* **181**, 281–292 (2020).
21. Wrapp, D. et al. Cryo-EM structure of the 2019-nCoV spike in the prefusion conformation. *Science* **367**, 1260–1263 (2020).
22. Walls, A. C. et al. Cryo-electron microscopy structure of a coronavirus spike glycoprotein trimer. *Nature* **531**, 114–117 (2016).
23. Yuan, Y. et al. Cryo-EM structures of MERS-CoV and SARS-CoV spike glycoproteins reveal the dynamic receptor binding domains. *Nat. Commun.* **8**, 15092 (2017).
24. Kirchdoerfer, R. N. et al. Pre-fusion structure of a human coronavirus spike protein. *Nature* **531**, 118–121 (2016).
25. Li, Z. et al. The human coronavirus HCoV-229E S-protein structure and receptor binding. *eLife* **8**, e51230 (2019).
26. Barnes, C.O. et al. Structures of human antibodies bound to SARS-CoV-2 spike reveal common epitopes and recurrent features of antibodies. *Cell* **182**, 828–842 (2020).
27. Ju, B. et al. Human neutralizing antibodies elicited by SARS-CoV-2 infection. *Nature*

**584**, 115–119 (2020).

28. Wu, Y. et al. A noncompeting pair of human neutralizing antibodies block COVID-19 virus binding to its receptor ACE2. *Science* **368**, 1274–1278 (2020).

29. Chi, X. et al. A neutralizing human antibody binds to the N-terminal domain of the Spike protein of SARS-CoV-2. *Science* **369**, 650–655 (2020).

30. Yuan, M. et al. Structural basis of a shared antibody response to SARS-CoV-2. *Science* **369**, 1119–1123 (2020).

31. Hurlburt, N. K. et al. Structural basis for potent neutralization of SARS-CoV-2 and role of antibody affinity maturation. Preprint at <https://doi.org/10.1101/2020.06.12.148692> (2020). 32. Lefranc, M. P. et al. IMGT®, the international ImMunoGeneTics information system® 25 years on. *Nucleic Acids Res.* **43**, D413–D422 (2015).

33. Briney, B., Inderbitzin, A., Joyce, C. & Burton, D. R. Commonality despite exceptional diversity in the baseline human antibody repertoire. *Nature* **566**, 393–397 (2019).

34. Pinto, D. et al. Cross-neutralization of SARS-CoV-2 by a human monoclonal SARS-CoV antibody. *Nature* **583**, 290–295 (2020).

35. Pallesen, J. et al. Immunogenicity and structures of a rationally designed prefusion MERS-CoV spike antigen. *Proc. Natl Acad. Sci. USA* **114**, E7348–E7357 (2017).

36. Hsieh, C. L. et al. Structure-based design of prefusion-stabilized SARS-CoV-2 spikes. *Science* **369**, 1501–155 (2020).

37. Wu, F. et al. Neutralizing antibody responses to SARS-CoV-2 in a COVID-19 recovered patient cohort and their implications. Preprint at <https://doi.org/10.1101/2020.03.30.20047365> (2020).

38. Wu, N. C. et al. An alternative binding mode of IGHV3-53 antibodies to the SARS-CoV-2 receptor binding domain. *Cell Rep.* <https://doi.org/10.1016/j.celrep.2020.108274> (2020).

39. Marillet, S., Lefranc, M. P., Boudinot, P. & Cazals, F. Novel structural parameters of Ig-Ag complexes yield a quantitative description of interaction specificity and binding affinity. *Front. Immunol.* **8**, 34 (2017).

40. Weisblum, Y. et al. Escape from neutralizing antibodies by SARS-CoV-2 spike protein

- variants. Preprint at <https://doi.org/10.1101/2020.07.21.214759> (2020).
41. Wang, B. et al. Bivalent binding of a fully human IgG to the SARS-CoV-2 spike proteins reveals mechanisms of potent neutralization. Preprint at <https://doi.org/10.1101/2020.07.14.203414> (2020).
  42. Shang, J. et al. Structural basis of receptor recognition by SARS-CoV-2. *Nature* **581**, 221–224 (2020).
  43. Yan, R. et al. Structural basis for the recognition of SARS-CoV-2 by full-length human ACE2. *Science* **367**, 1444–1448 (2020).
  44. Li, Q. et al. The impact of mutations in SARS-CoV-2 spike on viral infectivity and antigenicity. *Cell* **182**, 1284–1294.e9 (2020).
  45. Scharf, L. et al. Broadly neutralizing antibody 8ANC195 recognizes closed and open states of HIV-1 Env. *Cell* **162**, 1379–1390 (2015).
  46. Schoofs, T. et al. Broad and potent neutralizing antibodies recognize the silent face of the HIV envelope. *Immunity* **50**, 1513–1529 (2019).
  47. Kabsch, W. XDS. *Acta Crystallogr. D* **66**, 125–132 (2010).
  48. Winn, M. D. et al. Overview of the CCP4 suite and current developments. *Acta Crystallogr. D* **67**, 235–242 (2011).
  49. Adams, P. D. et al. PHENIX: a comprehensive Python-based system for macromolecular structure solution. *Acta Crystallogr. D* **66**, 213–221 (2010).
  50. Winter, G. xia2: an expert system for macromolecular crystallography data reduction. *J. Appl. Crystallogr.* **43**, 186–190 (2010).
  51. Beilsten-Edmands, J. et al. Scaling diffraction data in the DIALS software package: algorithms and new approaches for multi-crystal scaling. *Acta Crystallogr. D* **76**, 385–399 (2020).
  52. Winter, G. et al. DIALS: implementation and evaluation of a new integration package. *Acta Crystallogr. D* **74**, 85–97 (2018).
  53. McCoy, A. J. et al. Phaser crystallographic software. *J. Appl. Crystallogr.* **40**, 658–674 (2007).
  54. Gristick, H. B. et al. Natively glycosylated HIV-1 Env structure reveals new mode for antibody recognition of the CD4-binding site. *Nat. Struct. Mol. Biol.* **23**, 906–915 (2016).

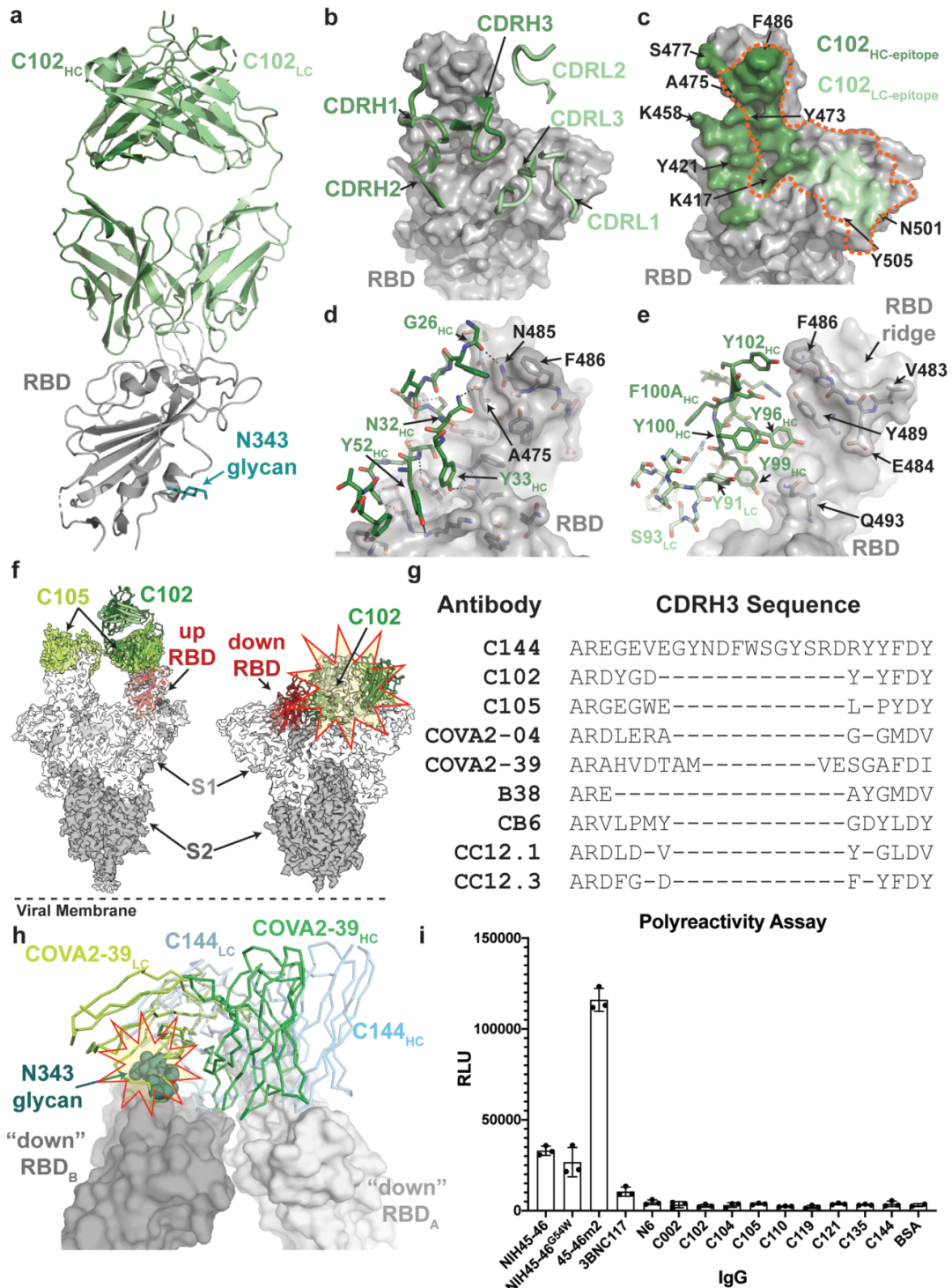
55. Bunkóczi, G. & Read, R. J. Improvement of molecular-replacement models with Sculptor. *Acta Crystallogr. D* **67**, 303–312 (2011).
56. Emsley, P., Lohkamp, B., Scott, W. G. & Cowtan, K. Features and development of Coot. *Acta Crystallogr. D* **66**, 486–501 (2010).
57. Mastronarde, D. N. Automated electron microscope tomography using robust prediction of specimen movements. *J. Struct. Biol.* **152**, 36–51 (2005).
58. Punjani, A., Rubinstein, J. L., Fleet, D. J. & Brubaker, M. A. cryoSPARC: algorithms for rapid unsupervised cryo-EM structure determination. *Nat. Methods* **14**, 290–296 (2017).
59. Rohou, A. & Grigorieff, N. CTFFIND4: fast and accurate defocus estimation from electron micrographs. *J. Struct. Biol.* **192**, 216–221 (2015).
60. Goddard, T. D. et al. UCSF ChimeraX: meeting modern challenges in visualization and analysis. *Protein Sci.* **27**, 14–25 (2018).
61. Bell, J. M., Chen, M., Baldwin, P. R. & Ludtke, S. J. High resolution single particle refinement in EMAN2.1. *Methods* **100**, 25–34 (2016).
62. Goddard, T. D., Huang, C. C. & Ferrin, T. E. Visualizing density maps with UCSF Chimera. *J. Struct. Biol.* **157**, 281–287 (2007).
63. Terwilliger, T. C., Adams, P. D., Afonine, P. V. & Sobolev, O. V. A fully automatic method yielding initial models from high-resolution cryo-electron microscopy maps. *Nat. Methods* **15**, 905–908 (2018).
64. Chen, V. B. et al. MolProbity: all-atom structure validation for macromolecular crystallography. *Acta Crystallogr. D* **66**, 12–21 (2010).
65. Krissinel, E. & Henrick, K. Inference of macromolecular assemblies from crystalline state. *J. Mol. Biol.* **372**, 774–797 (2007).
66. Davis, M. I., Bennett, M. J., Thomas, L. M. & Bjorkman, P. J. Crystal structure of prostate-specific membrane antigen, a tumor marker and peptidase. *Proc. Natl Acad. Sci. USA* **102**, 5981–5986 (2005).
67. Liu, H. et al. Cross-neutralization of a SARS-CoV-2 antibody to a functionally conserved

site is mediated by avidity. Preprint at <https://doi.org/10.1101/2020.08.02.233536> (2020).

68. Zhou, D. et al. Structural basis for the neutralization of SARS-CoV-2 by an antibody from a convalescent patient. *Nat. Struct. Mol. Biol.* **27**, 950–958 (2020).

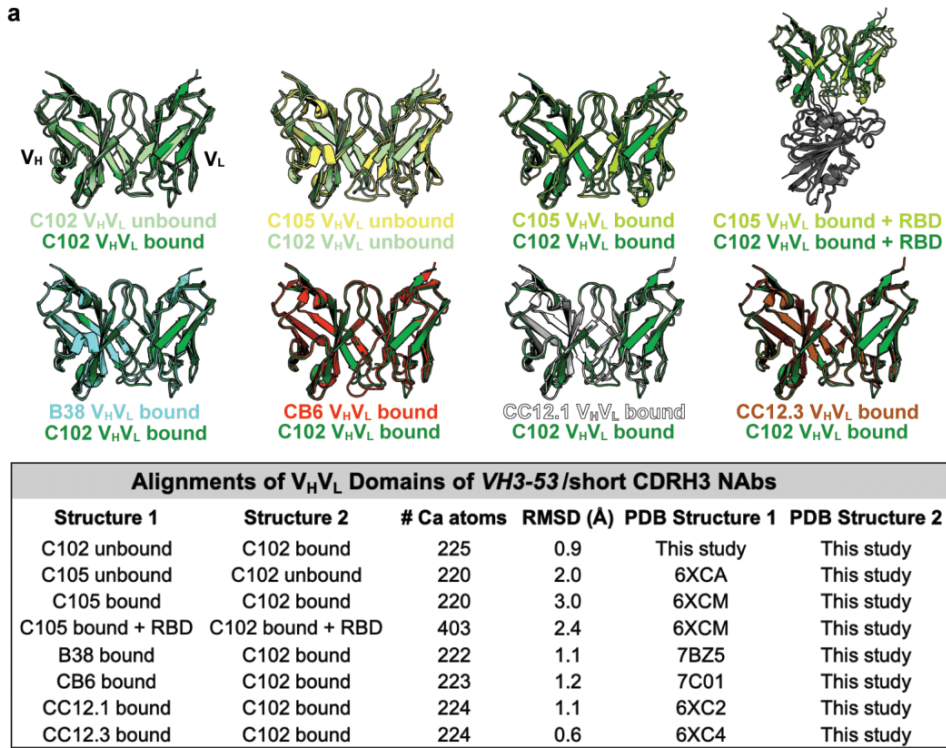
69. Piccoli, L. et al. Mapping neutralizing and immunodominant sites on the SARS-CoV-2 spike receptor-binding domain by structure-guided high-resolution serology. *Cell* **183**, 1024–1042 (2020).

## Extended Data Figures and Tables



**Extended Data Fig. 1 X-ray structure and epitope mapping of VH3-53 NAb C102. a,** X-ray structure of the C102 Fab–RBD<sub>331–518</sub> complex. **b,** C102 CDR loops mapped on the RBD surface. **c,** Surface representation of C102 epitope coloured by C102 heavy chain (dark

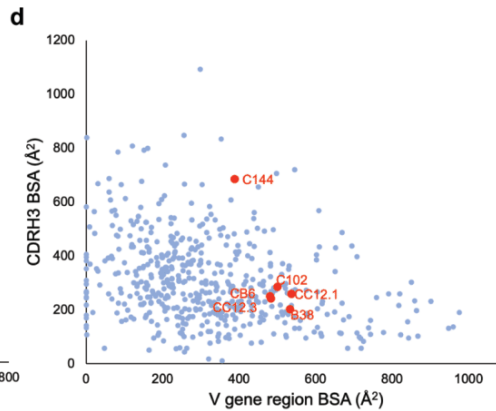
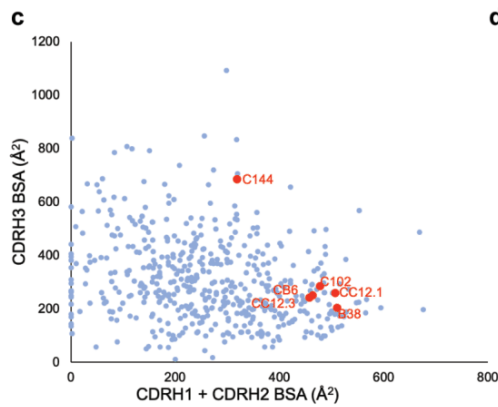
green) and light chain (light green) interactions. **d, e**, CDRH1, CDRH2 (**d**) and CDRH3 (**e**) interactions with RBD residues. Potential hydrogen-bond contacts are illustrated as dashed lines. **f**, Left, overlay of C102–RBD crystal structure (cartoon) with C105–S trimer cryoEM density (PDB 6XCM, EMD-22127) illustrating conserved binding to RBD epitope in an up conformation. Right, the C102 epitope is sterically occluded when aligned to a down RBD conformation (red and yellow star). SARS-CoV-2 S domains are dark grey (S2 domain) and light grey (S1 domain); the C105 Fab is yellow-green. **g**, Alignment of selected CDRH3 sequences for *VH3-53*- or *VH3-66*-encoded SARS-CoV-2 neutralizing antibodies (IMGT definition<sup>32</sup>). **h**, Overlay of NAb COVA2-39 Fab<sup>38</sup> (lime green and lemon, from COVA2-39–RBD structure, PDB 7JMP) and C144 Fab (blue, from C144–S structure) aligned on a RBD<sub>A</sub> of C144 epitope. COVA2-39 adopts a distinct conformation relative to the C102-like *VH3-53*-encoded short CDRH3 NAb class and to C144, recognizing its RBD epitope only in an up RBD conformations owing to steric clashes (red and yellow star) with the N343-associated glycan on the adjacent RBD. **i**, Polyreactivity assay. IgGs were evaluated for binding to baculovirus extracts to assess non-specific binding. Polyreactive positive control IgGs were NIH45-46, 45-46<sup>G54W</sup> and 45-46m2. Negative controls were bovine serum albumin (BSA) and IgGs N6 and 3BNC117. Relative light unit (RLU) values are presented as the mean and s.d. of triplicate measurements ( $n = 3$  biological replicates) with results for individual experiments shown as circles.



**b**

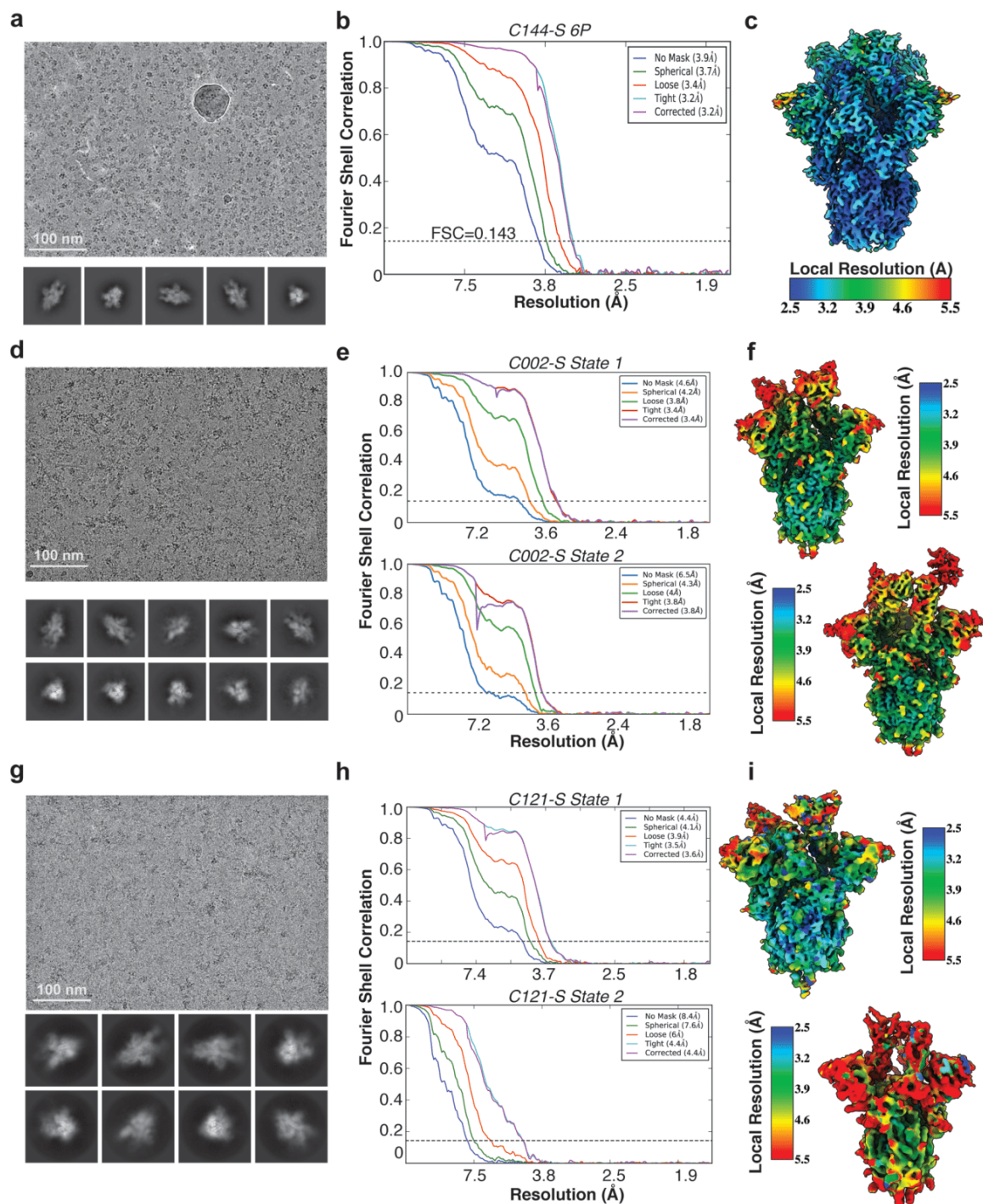
**Interface Buried Surface Area ( $\text{\AA}^2$ )**

Structure	Interface Buried Surface Area ( $\text{\AA}^2$ )						C144 Fab/RBD	
	C102 Fab/RBD	B38 Fab/RBD	CB6 Fab/RBD	CC12.1 Fab/RBD	CC12.3 Fab/RBD	this study		
PDB	7BZ5	7C01	6XC2	6XC4	RBD A		RBD B	
$VH$ gene usage	$VH3-53$ /short	$VH3-53$ /short	$VH3-53$ /short	$VH3-53$ /short	$VH3-53$ /short	$VH3-53$ /long	$VH3-53$ /long	
<b>Heavy Chain Paratope</b>	796	735	732	786	721	707	367	
FWRH1	29	22	17	23	25	6	0	
CDRH1	275	267	211	223	217	161	0	
FWRH2	0	0	0	0	0	0	0	
CDRH2	199	203	210	215	204	127	0	
FWRH3	34	40	43	82	42	95	0	
CDRH3	259	203	251	243	233	318	367	
FWRH4	0	0	0	0	0	0	0	
<b>Light Chain Paratope</b>	257	485	355	559	164	87	20	
FWRL1	0	15	0	18	1	0	0	
CDRL1	217	239	127	262	111	51	0	
FWRL2	0	0	0	0	0	0	0	
CDRL2	0	0	0	0	0	0	0	
FWRL3	0	35	1	48	0	0	20	
CDRL3	40	196	227	231	52	36	0	
FWRL4	0	0	0	0	0	0	0	
<b>Total Paratope</b>	1052	1220	1087	1345	885	794	387	
<b>Heavy Chain Epitope</b>	797	689	736	763	677	722	330	
<b>Light Chain Epitope</b>	225	504	313	574	186	100	22	
<b>Total Epitope</b>	1022	1193	1049	1337	863	822	351	



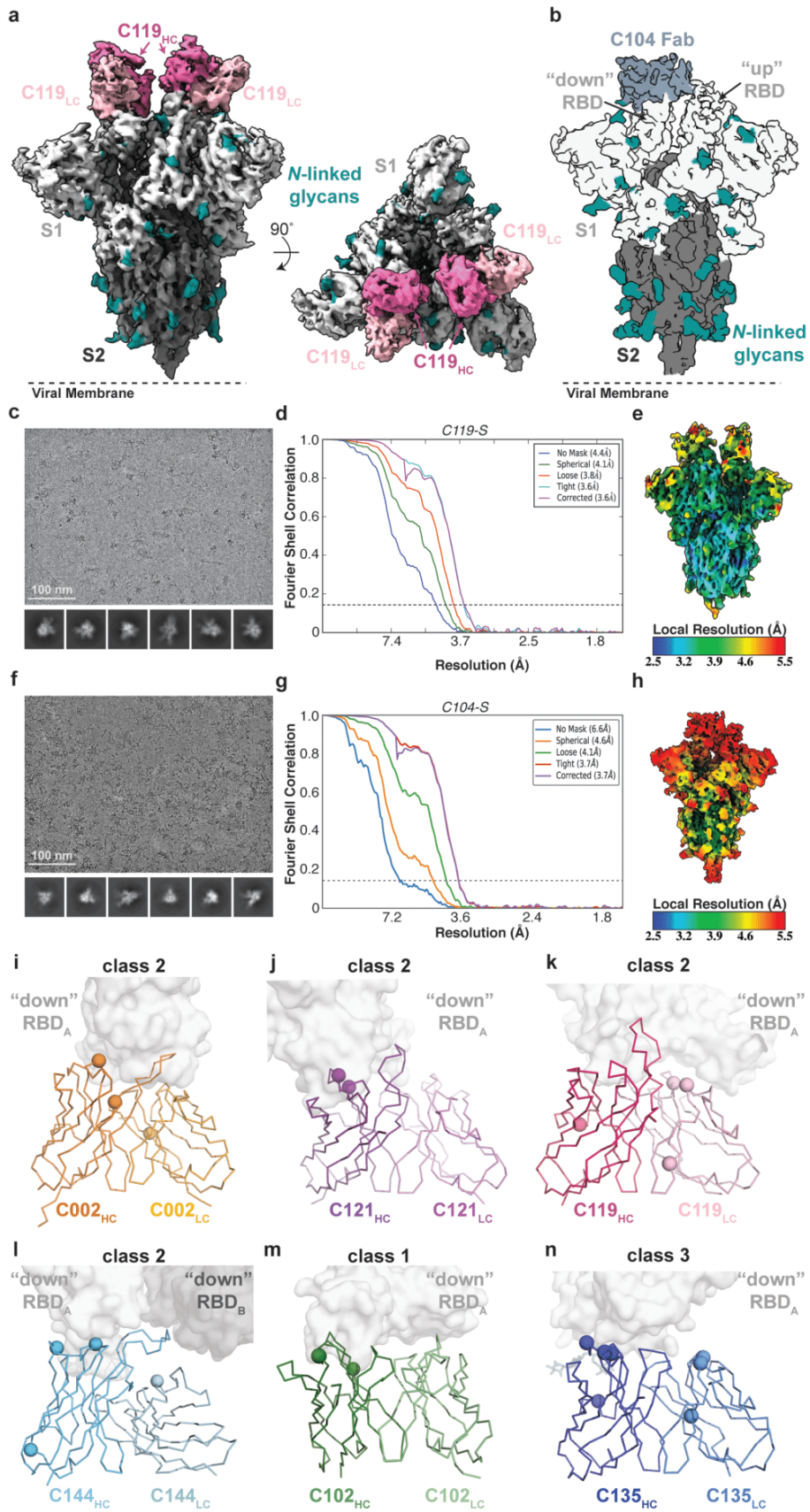
**Extended Data Fig. 2 Overview of *VH3-53/VH3-66*-encoded human NAb structures.**

**a**, Superimposition of VH and VL domains of C102 with other *VH3-53*- or *VH3-66*-encoded NAbs (top) and root mean square deviation (r.m.s.d.) calculations (bottom). **b**, Buried surface area comparisons for the indicated Fab–RBD structures. Buried surface areas were calculated using PDBePISA<sup>65</sup> and a 1.4 Å probe. **c, d**, Heavy-chain buried surface areas of anti-SARS-CoV-2 antibodies plotted as CDRH1 (IMGT residues 27–38) plus CDRH2 (residues 56–67\*) versus CDRH3 (residues 105–117) (**c**), and V gene segment region (residues 1–105) versus CDRH3 (residues 106\*–117) (**d**, asterisk indicates differences from IMGT definition). Blue data points represent 501 human antibodies complexed with protein antigens. IMGT-numbered structures (resolutions of 3.5 Å or better) were downloaded from the Structural Antibody Database (SAbDab)<sup>70</sup> and buried surface area were calculated using PISA<sup>65</sup>. Buried surface areas from antibody structures with identical or near-identical heavy chain sequences were averaged to give a single point on the graph.

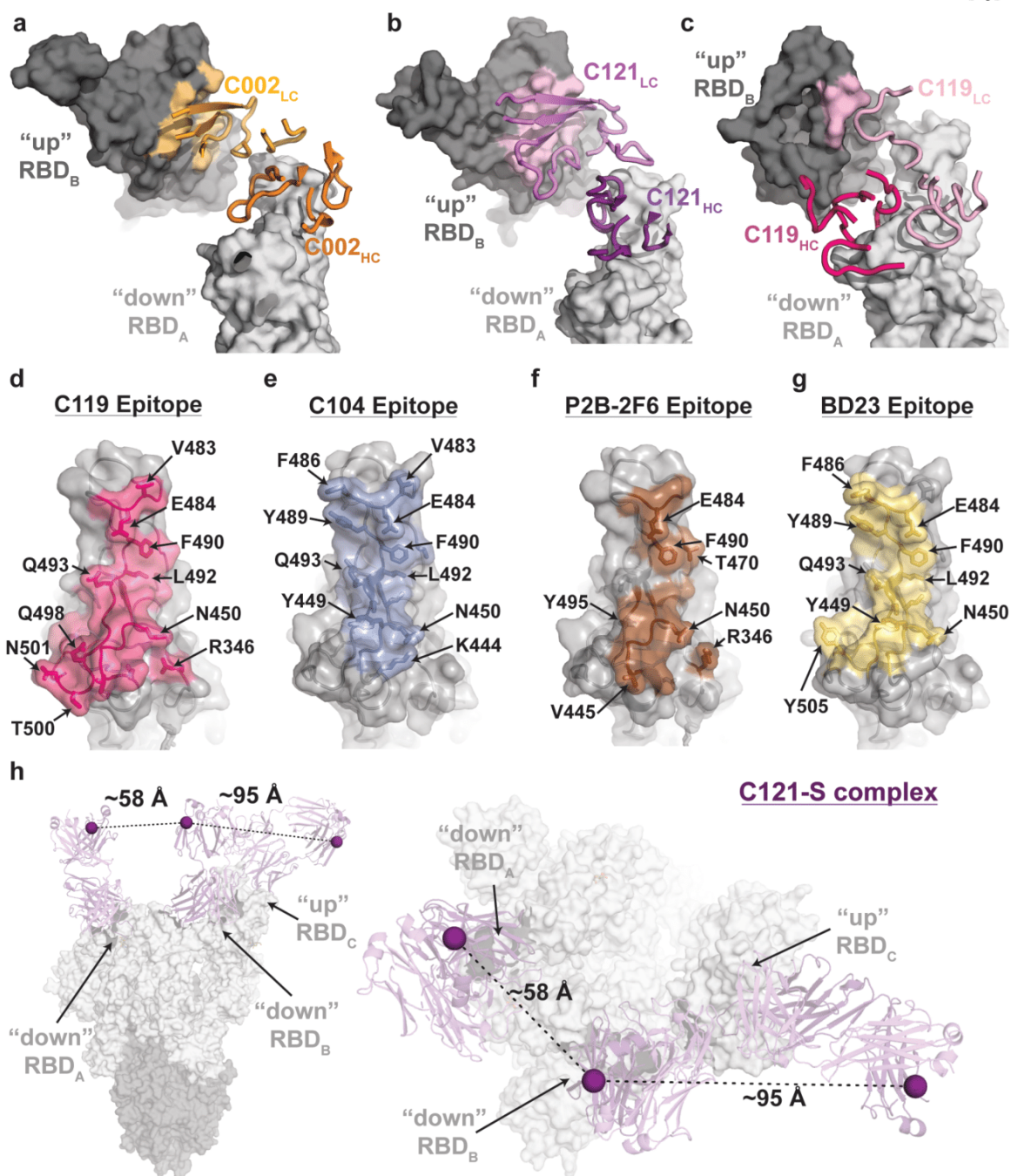


**Extended Data Fig. 3 Cryo-EM data processing and validation for C144-S, C002-S and C121-S complexes.** a–i, Representative micrograph selected from total dataset (Supplementary Table 2), 2D class averages, gold-standard Fourier shell correlation (FSC) plots, and local resolution estimations for C144-S 6P (a–c), C002-S 2P (d–f) and C121-S 2P (g–i). Scale bars, 100 nm. For the C002-S dataset, two classes were resolved: state 1,

C002 Fabs bound to three down RBDs, and state 2, C002 Fabs bound to two down and one up RBD. For the C121-S 2P dataset, two classes were resolved: state 1, C121 Fabs bound to two down and one up RBD and state 2, C121 Fabs bound to one down, two up RBDs.

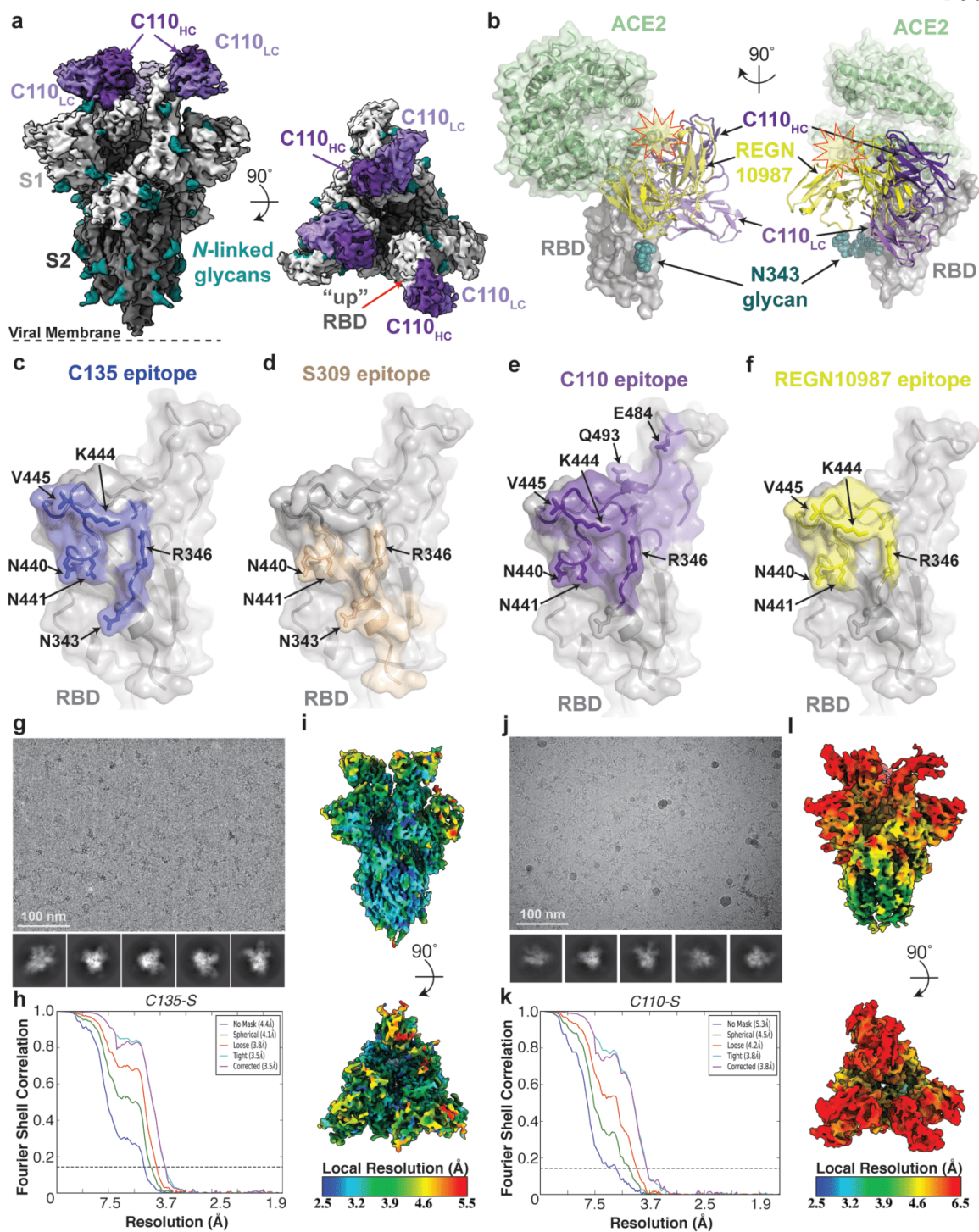


**Extended Data Fig. 4 Cryo-EM processing, validation and reconstruction for C119-S and C104-S complexes.** **a**, 3.6 Å cryo-EM reconstruction for a C119-S trimer complex. **b**, 3.7 Å cryo-EM reconstruction for a C104-S trimer complex. Representative micrograph selected from the total dataset (Supplementary Table 2), 2D class averages, gold-standard FSC plot, and local resolution estimation for C119-S2P (**c-e**) and C104-S (**f-h**). Scale bars, 100 nm. Both complexes revealed binding of Fabs to both down and up RBD conformations. **i-n**, Somatic hypermutations in heavy- and light-chain V gene segments for C002 (**i**), C121 (**j**), C119 (**k**), C144 (**l**), C102 (**m**) and C135 (**n**) are shown as spheres on the antibody VH and VL domains (ribbon representations). The primary RBD epitope is shown as a light grey surface; secondary RBD epitope for C144 is in dark grey.



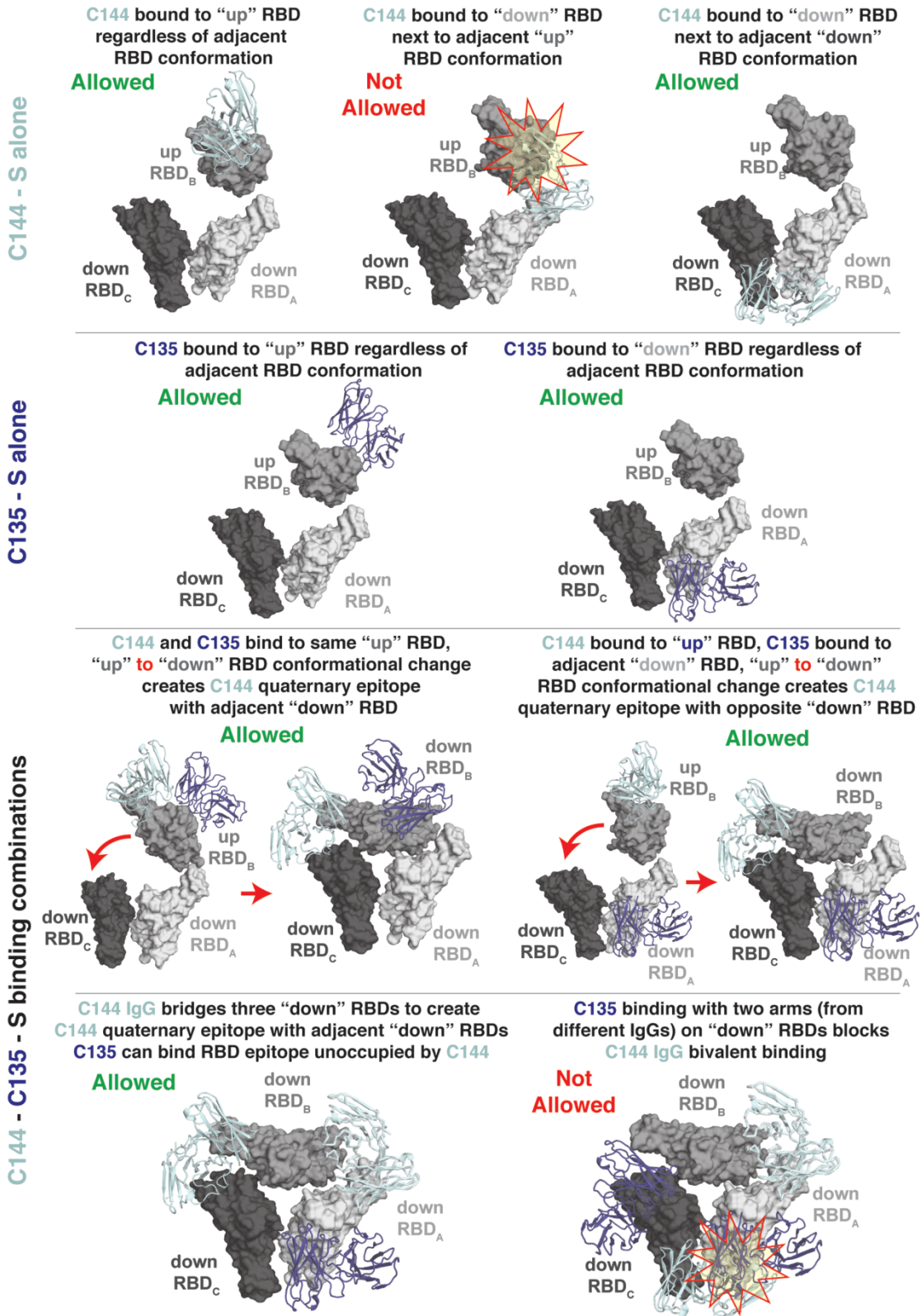
**Extended Data Fig. 5 Primary and secondary epitopes of class 2 human NAbs.** a–c, Primary epitopes for C002 (a), C121 (b), and C119 (c) on down RBD. A secondary epitope is observed if a Fab is bound to an adjacent up RBD for these NAbs. Antibody paratopes are represented as cartoons. A similar interaction in the C104–S structure is not shown owing to low local resolution on the up RBD. d–g, Primary epitopes for C119 (d), C104 (e), P2B-2F6 (f; PDB 7BWJ), and BD23 (g; PDB 7BYR). The existence of secondary epitopes for P2B-2F6 and BD23 cannot be determined because the P2B-2F6 epitope was determined from a

crystal structure with an RBD<sup>27</sup>, and the BD23–S cryo-EM structure showed only one bound Fab<sup>13</sup>. **h**, Measurement of C $\alpha$  distance between the C termini of adjacent C121 CH1 domains (residue 222 of the heavy chain on each Fab). Measurements of this type were used to evaluate whether intra-spike crosslinking by an IgG binding to a single spike trimer was possible for human NAbS in Extended Data Table 1.

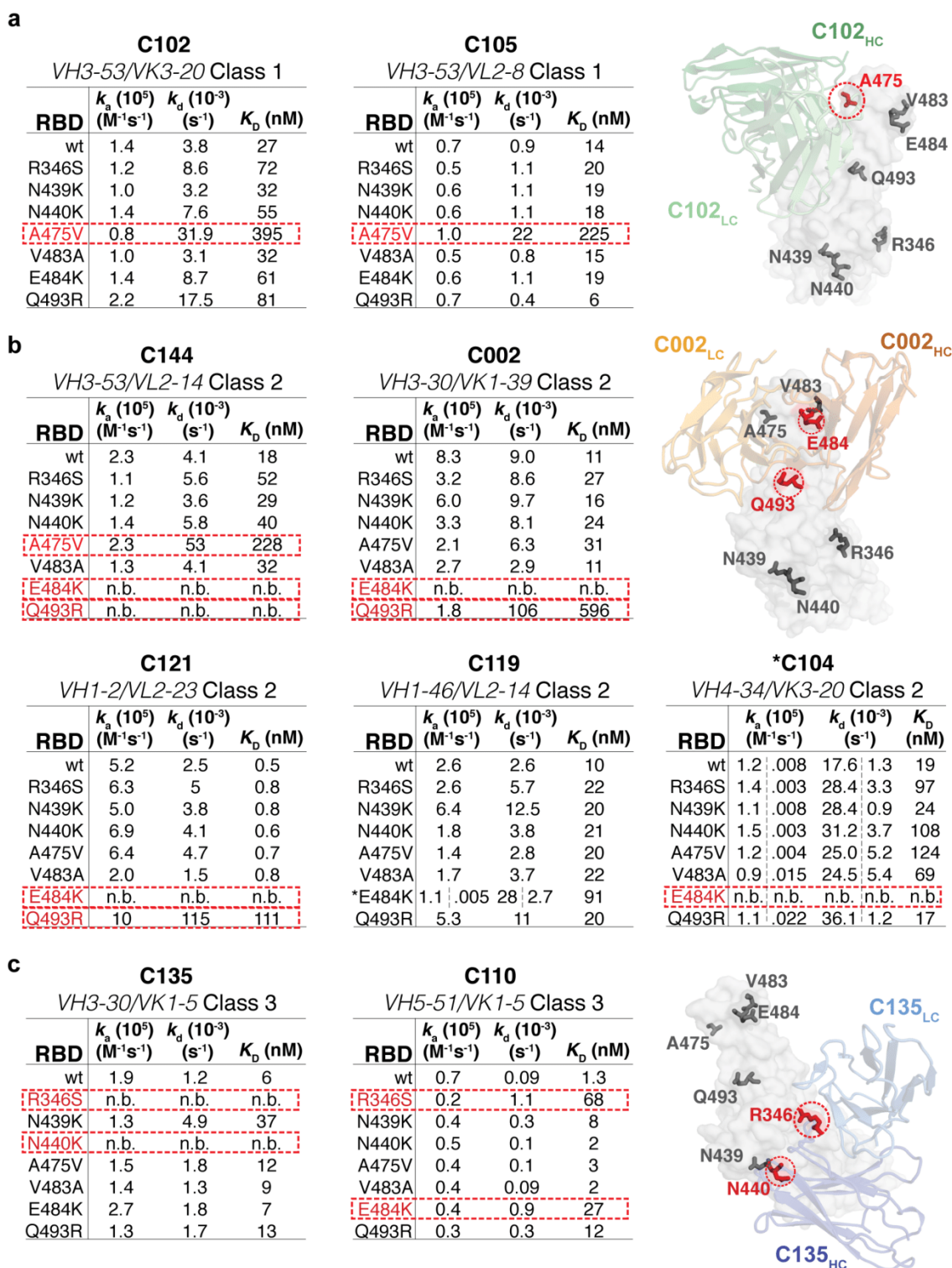


**Extended Data Fig. 6 Cryo-EM structure of C110-S complex and epitope mapping. a,** 3.8 Å cryo-EM reconstruction of the C110-S trimer complex. **b,** Composite model of C110-RBD (purple and grey, respectively) overlaid with the SARS-CoV-2 NAb REGN-10987 (yellow, PDB 6XDG) and soluble ACE2 (green, PDB 6M0J). Model was generated by aligning structures on 188 RBD C $\alpha$  atoms. **c-f,** Surface representation of RBD epitopes for

C135 (blue) (c), S309 (brown, PDB 6WSP) (d), C110 (purple) (e) and REGN-10987 (yellow, PDB 6XDG) (f). Given the low resolution of the antibody–RBD interface, epitopes were assigned by selection of any RBD residue within 7 Å of any antibody C $\alpha$  atom. Mutation sites found in sequence isolates<sup>44</sup> (green) and in laboratory selection assays<sup>40</sup> (red) are shown. Representative micrograph selected from total dataset (Supplementary Table 2), 2D class averages, gold-standard FSC plot, and local resolution estimation for C135–S 2P (g–i) and C110–S 2P (j–l). Scale bars, 100 nm. Both complexes revealed binding of Fabs to both two-down and one-up RBD conformations.

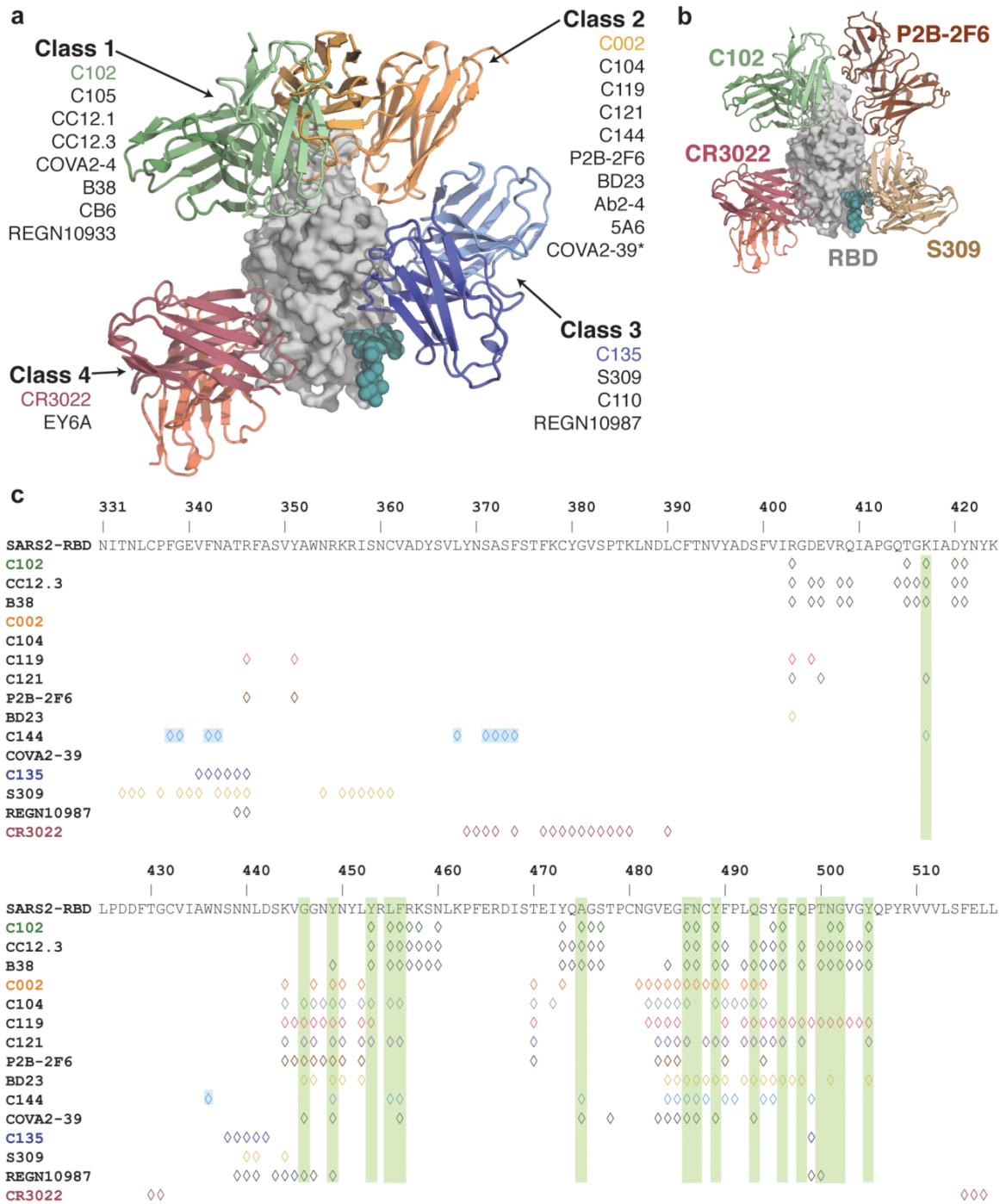


**Extended Data Fig. 7 Possibilities for simultaneous engagement of C144 and C135 on spikes with different combinations of up and down RBDs.** Modelling of C144 (light blue) and C135 (dark blue) VH–VL domains on different RBD conformations. Steric clashes are shown as a red and yellow star.



**Extended Data Fig. 8 SPR binding data for NAbs. a–c,** Kinetic and equilibrium constants for binding to unaltered RBD (indicated as wild type, wt) and mutant RBDs are shown in

tables beside structures of a representative NAb–RBD complex for each class. Residues that were mutated are highlighted as coloured side chains on a grey RBD surface. Antibody VH–VL domains are shown as cartoons. Kinetic and equilibrium constants for NAbs that contact adjacent RBDs on the S trimer (C144, C002, C119 and C121) do not account for contacts to a secondary RBD because binding was assayed by injected monomeric RBDs over immobilized IgGs. Asterisk indicates kinetic constants determined from a two-state binding model.



**Extended Data Fig. 9 Summary of NABs.** **a**, Structural depiction of a representative NAb from each class binding its RBD epitope. **b**, Composite model illustrating non-overlapping epitopes of NABs from each class bound to a RBD monomer. **c**, Epitopes for SARS-CoV-2 NABs. RBD residues involved in ACE2 binding are boxed in green. Diamonds represent RBD residues contacted by the indicated antibody.

Antibody	Reference	IGHV (# of aa SHM)	CDRH3 length (aa) <sup>^</sup>	IGLV (# of aa SHM)	CDRL3 length (aa) <sup>^</sup>	IC <sub>50</sub> /IC <sub>90</sub> (ng/mL) <sup>†</sup>	Potential IgG intra- spike binding <sup>§</sup>	Contacts adjacent RBD	Structural Information
<u>Class 1: Blocks ACE2, accessibility of RBD epitope only in "up" conformation</u>									
C102	this study	VH3-53 (2)	11	VK3-20 (0)	9	34 / 143	???	???	3.0 Å Fab-RBD
C105	Barnes, et al. <sup>26</sup>	VH3-53 (0)	12	VL2-8 (1)	11	26.1 / 134	Yes	No	3.4 Å Fab-S, PDB 6XCM
B38	Wu, et al. <sup>28</sup>	VH3-53 (1)	9	VK1-9 (2)	10	117 / NA	???	???	1.8 Å Fab-RBD, PDB 7BZ5
CC12.3	Yuan, et al. <sup>30</sup>	VH3-53 (3)	12	VK3-20 (1)	9	20 / NA	???	???	2.9 Å Fab-RBD, PDB 6XC7
<u>Class 2: Blocks ACE2, accessibility of RBD epitope in "up"/"down" conformations</u>									
C002	this study	VH3-30 (1)	17	VK1-39 (1)	9	8.9 / 37.6	Yes	Yes	3.4 Å Fab-S
C104	this study	VH4-34 (6)	17	VK3-20 (3)	9	23.3 / 140	Yes	Yes	3.7 Å Fab-S
C119	this study	VH1-46 (1)	20	VL2-14 (3)	11	9.1 / 97.8	Yes	Yes	3.5 Å Fab-S
C121	this study	VH1-2 (2)	22	VL2-23 (0)	10	6.7 / 22.3	Yes	Yes	3.6 Å Fab-S
C144	this study	VH3-53 (3)	25	VL2-14 (1)	10	6.9 / 29.7	Yes	Yes	3.3 Å Fab-S
COVA2-39	Wu, et al. <sup>38</sup>	VH3-53 (3)	17	VL2-23 (1)	10	36 / NA	???	???	1.7 Å Fab-RBD, PDB 7JMP
5A6	Wang, et al. <sup>41</sup>					75.5 / NA	Yes	Yes	2.4 Å Fab-S
P2B-2F6	Ju, et al. <sup>27</sup>	VH4-38*02 (2)	20	VL2-8 (0)	10	50 / NA	???	???	2.9 Å Fab-RBD, PDB 7BWJ
Ab2-4	Liu, et al. <sup>10</sup>	VH1-2 (3)	15	VL2-8 (0)	10	394 / NA	Yes	No	3.2 Å Fab-S, PDB 6XEY
BD23	Cao, et al. <sup>13</sup>	VH7-4*02 (0)	19	VK1-5*03 (0)	9	4800 / NA	No	No	3.8 Å Fab-S, PDB 7BYR
<u>Class 3: Does not overlap with ACE2 binding site, accessibility of RBD epitope in "up"/"down" conformations</u>									
C135	this study	VH3-30 (4)	12	VK1-5 (3)	9	16.6 / 48.9	No	No	3.5 Å Fab-S
S309	Pinto, et al. <sup>34</sup>	VH1-18 (6)	20	VK3-20 (3)	8	79* / NA	No	No	3.1 Å Fab-S, PDB 6WPS
C110	this study	VH5-51 (2)	21	VK1-5 (3)	9	18.4 / 77.3	No	No	3.8 Å Fab-S
REGN10987	Hansen, et al. <sup>6</sup>	VH3-30 (4)	13	VL2-14 (6)	10	6.1 / NA	???	???	3.9 Å Fab-RBD, PDB 6XDG
<u>Class 4: Does not overlap with ACE2 binding site, accessibility of RBD epitope only in "up" conformation</u>									
CR3022	Yuan, et al. <sup>9</sup>	VH5-51 (8)	12	VK4-1 (3)	9	>10,000 / NA	???	???	3.1 Å Fab-RBD, PDB 6W41
COV1-16	Liu, et al. <sup>69</sup>	VH1-46 (1)	20	VK1-33 (3)	10	130 / NA	???	???	2.9 Å Fab-RBD
EY6A	Zhou, et al. <sup>70</sup>	VH3-30*18 (3)	14	VK1-39 (0)	10	70-20,000**/ NA	No	Yes	3.7 Å Fab-S, PDB 6ZDH
S304	Pinto, et al. <sup>34</sup>	VH3-13 (5)	14	VK1-39 (6)	10	>5,000 / NA	No	Yes	4.3 Å Fab-S, PDB 7JW0
S2A4	Piccoli, et al. <sup>71</sup>	VH3-7 (2)	?	VL2-23 (0)	?	3,500 / NA	No	Yes	3.3 Å Fab-S, PDB 7JVC

**Extended Data Table 1. Classification and structural properties of SARS-CoV-2 RBD-specific antibodies.**

PDB ID	C102		C002 Fab	C110 Fab	C121 Fab	C135 Fab
	SARS-CoV-2 RBD	C102 Fab				
	7K8M	7K8N	7K8O	7K8P	7K8Q	7K8R
<b>Data collection<sup>a,b</sup></b>						
Space group	P2 <sub>1</sub> 2 <sub>1</sub> 2 <sub>1</sub>	P6 <sub>3</sub> 22	P3 <sub>1</sub> 21	P2	P6 <sub>3</sub> 22	P4 <sub>1</sub>
Cell Dimensions						
<i>a</i> , <i>b</i> , <i>c</i> (Å)	54.6, 89.3, 175.1	88.8, 88.8, 218.9	92.3, 92.3, 130.9	48.5, 62.7, 78.4	71.3, 71.3, 404.8	102.3, 102.3, 53.3
$\alpha$ , $\beta$ , $\gamma$ (°)	90, 90, 90	90, 90, 120	90, 90, 120	90, 97.5, 90	90, 90, 120	90, 90, 90
Resolution (Å)	48.85-3.2 (3.31-3.20)	37.9-1.65 (1.71-1.65)	34.1-1.95 (2.02-1.95)	38.7 - 1.80 (1.86-1.80)	39.1-2.0 (2.05-2.0)	45.7-2.0 (2.07-2.0)
R <sub>merge</sub> (%)	16.0 (44.5)	9.58 (148)	7.06 (176)	8.7 (107)	58.1 (136)	8.49 (213)
R <sub>pin</sub> (%)	6.8 (19.9)	2.27 (33.4)	2.36 (59.0)	4.1 (81.9)	11.4 (81)	3.50 (88.9)
CC <sub>1/2</sub> (%)	98.7 (90.3)	99.8 (80.7)	99.9 (88.7)	99.6 (78.2)	99.5 (24.8)	99.9 (68.4)
<I/σI>	6.1 (0.86)	15.3 (1.6)	13.5 (1.11)	7.7 (2.0)	8.4 (0.6)	10.5 (0.76)
Completeness (%)	99.7 (99.5)	100 (100)	99.3 (99.5)	98.8 (99.2)	99.2 (97.7)	99.4 (98.4)
Redundancy	6.5 (6.0)	19.2 (19.3)	10.0 (9.9)	4.7 (2.0)	26.3 (26.8)	6.8 (6.6)
Wilson <i>B</i> -factor	77.8	28.5	48.6	23.8	44.3	52.6
<b>Refinement and Validation</b>						
Resolution (Å)	48.9 - 3.2	37.9 - 1.65	34.1-1.95	38.9 - 1.80	36.4 - 2.0	45.7 - 2.0
Unique Reflections	14,722 (1413)	62,121 (6095)	47459 (4652)	42,891 (4,284)	42,233 (2,989)	37,324 (3071)
Number of atoms						
Protein	4,731	3,256	3,337	3,345	3,269	3,315
Ligand	14	58	53	n/a	14	18
Waters	0	101	63	172	12	30
R <sub>work</sub> /R <sub>free</sub> (%)	17.6/23.4	19.7/20.7	20.4/23.7	20.9/23.4	20.7/23.9	19.5/23.7
R.m.s. deviations						
Bond lengths (Å)	0.005	0.015	0.005	0.01	0.005	0.013
Bond angles (°)	0.73	1.48	0.72	1.1	0.7	1.17
Poor rotamers (%)	0.76	0.82	1.84	0	0.8	1.60
Ramachandran plot						
Favored (%)	93.5	98.3	97.9	97.9	97.5	96.5
Allowed (%)	6.3	1.7	2.1	2.1	2.5	3.5
Disallowed (%)	0.2	0	0	0	0	0
Average <i>B</i> -factor (Å)	73.3	41.5	72.14	32.8	53.5	59.9

<sup>a</sup>For each structure reported, data were derived from a single crystal.

<sup>b</sup>Numbers in parentheses correspond to the highest resolution shell

**Supplementary Table 1. X-ray Crystallography Data Collection and Refinement Statistics.**

Supplementary Table 2. cryo-EM data collection and refinement statistics.

	C002		C104	C110	C119	C121	C121	C135	C144
	SARS-CoV-2 S 2P	SARS-CoV-2 S 6P							
	(state 1)	(state 2)	(open state)	(open state)	(open state)	(state 1)	(state 2)	(open state)	(closed state)
<b>PDB</b>	7K8S	7K8T	7K8U	7K8V	7K8W	7K8X	7K8Y	7K8Z	7K90
<b>EMD</b>	22729	22730	22731	22732	22733	22734	22735	22736	22737
<b>Data collection conditions</b>									
Microscope	Titan Krios	Talos Arctica							
Camera	Gatan K3 Summit								
Magnification	105,000x	45,000x							
Voltage (kV)	300	300	300	300	300	300	300	300	200
Recording mode	counting								
Dose rate (e <sup>-</sup> /pixel/s)	22.1	22.1	23.1	22.1	22.1	23.1	22.1	23.5	15.28
Elektron dose (e <sup>-</sup> /Å <sup>2</sup> )	60	60	61	60	60	60	60	60	60
Defocus (µm)	1.0 - 2.5	1.0 - 2.5	1.0 - 2.6	1.0 - 2.5	1.0 - 2.5	1.0 - 2.5	1.0 - 2.5	1.0 - 2.5	0.8 - 2.2
Pixel size (Å)	0.836	0.836	0.836	0.836	0.836	0.836	0.836	0.836	0.869
Micrographs collected	3,471	3,471	3,383	4,995	3,626	5,481	5,481	3,882	2,530
Micrographs used	3,105	3,105	2,668	2,923	3,069	3,671	3,671	3,184	2,184
Total extracted particles	1,691,930	1,691,930	1,181,957	840,293	1,381,582	892,954	892,954	634,621	376,586
Refined particles	51,915	49,238	40,469	43,981	140,378	40,489	14,999	101,114	212,876
Symmetry imposed	C1	C3							
<b>Refinement and Validation</b>									
Initial model used	6VXX	6VYB	6XXL						
Number of atoms									
Protein	28,865	28,871	23,852	25,365	25,662	27,399	25,098	23,436	28,466
Ligand	795	779	671	649	837	357	262	789	627
MapCC (global/local)	0.83/0.82	0.86/0.81	0.86/0.82	0.80/0.72	0.74/0.73	0.78/0.74	0.79/0.78	0.81/0.82	0.8/0.77
Map sharpening B-factor	88	79.1	135.1	98.4	80.7	58.1	42.4	71.4	66.9
R.m.s. deviations									
Bond lengths (Å)	0.01	0.01	0.01	0.01	0.01	0.003	0.002	0.006	0.003
Bond angles (°)	0.81	0.9	0.84	0.81	1	0.6	0.5	0.8	0.6
MolProbity score	2.56	2.14	2.27	2.33	2.46	2.06	2	2.3	2.37
Clashscore (all atom)	16.5	15.2	18.9	19.7	18.1	11.2	20.9	16.3	9.7
Poor rotamers (%)	0	0	0	2.1	2.4	2.4	0	0.2	1.3
<b>Ramachandran plot</b>									
Favored (%)	92.6	92.9	91.7	95.9	93.7	96.7	97.1	97.2	94
Allowed (%)	6.9	6.5	8.3	4.1	6.3	3.2	2.7	12.4	5.6
Disallowed (%)	0.5	0.6	0	0	0	0.1	0.2	0.4	0.4

Supplementary Table 2. Cryo-EM Data Collection and Refinement Statistics.